Seismic characterisation of fluid flow in fractured reservoirs

Serafeim Vlastos

Thesis submitted for the degree of Doctor of Philosophy

School of GeoSciences

University of Edinburgh

2005

It is the mark of an instructed mind to rest satisfied with the degree of precision which the nature of the subject admits and not to seek exactness when only an approximation of the truth is possile.

Aristotle

Abstract

A variety of approaches are available for modelling wave propagation in fractured rock. Analytical solutions for the diffracted seismic wavefield produced by a fracture are only available for single cracks with simple geometries, i.e. circular or elliptical, and in most cases are only valid in the far field. The use of numerical approaches is essential in order to simulate the diffracted wavefield produced by any realistic distribution of fractures. In the first part of this thesis we introduce a new numerical method that combines a numerical method with an analytical method. The numerical method we implement is the pseudospectral method and the analytical method is the equivalent medium theory. The method is applicable for both P and S waves. We model the seismic wave propagation in fractured rock using the pseudospectral method. The fractures are treated as planes of weakness using the concept of the linear slip deformation or displacement discontinuity model. The implementation of fractures with a vanishing width in the finite difference grid is done using an equivalent medium theory.

The objective is to investigate the effects of lengthscale (size) and spatial distributions of fractures on the characteristics of propagating waves. We demonstrate that the waveforms can be significantly affected by the presence of fractures with different lengthscales relative to the wavelength, and we also show that different spatial distributions of fractures can give characteristic features on the wavefields, implying that information about fracture distributions in natural rock may be obtained directly from seismic data.

An important effect of the presence of fractures on wave propagation is seismic attenuation. Seismic attenuation is recognised as a potentially important quantity in reservoir characterisation. Seismic attenuation is, in general, a combined effect of absorption (intrinsic attenuation), which is affected by lithological parameters, and scattering (apparent) attenuation, which is related to structural parameters. Which of these two mechanisms dominates in any given situation depends on the relative wavelengths of the seismic wave and the heterogeneities of the fracture system. In the second part of the thesis, we deal exclusively with scattering attenuation. Synthetic modelling studies with and without intrinsic attenuation show that the contribution of scattering attenuation is significant. Scattering involves no energy loss, but produces a more extended, lower amplitude wavetrain by the resulting interference. It is dependent on the nature of small-scale fluctuations in the earth parameters and is found to be frequency dependent. For the numerical simulations we use the method introduced in the thesis that can accurately model the effects of scattering in a fractured network. The various fracture patterns examined are patterns of development of a population of fractures involving nucleation, growth, branching, interaction and coalescence created by a multiscale cellular automaton model.

The objective of this thesis is to examine the behaviour of scattering attenuation at different fracture patterns characterised by different statistical properties, fracture population geometry and criticality. We examine scattering attenuation in a range of frequencies for each one of the fracture patterns and demonstrate the frequency dependence. The comparison of the pattern of scattering attenuation with frequency between different fracture patterns shows that there is a change that can be attributed to the changes in the statistical properties of the fracture population. We conclude by examining the existence of direct links between fracture properties and scattering attenuation patterns, that scattering attenuation can be used for the characterisation of a fractured reservoir.

In the final part of the thesis, we concentrate on seismic attributes that respond directly to the fluid presence, and in particular on static fluid effects on the compliances of the porous and fractured rocks. We simulate the fluid movement in the fractured medium with a model of pore fluid pressure diffusion. From the simulation we can monitor the pore pressure changes in the medium at consecutive times. As a result of the changes in pore pressure the effective stress will change in the medium. We use an empirical relationship to estimate the changes in compliances of the fractured rock due to the effective stress changes, and use a 2-D finite difference method to model the wave propagation in the medium before and during the fluid injection. The objective is to examine if there is clear indication of the pore pressure changes in the synthetic seismograms. We conclude from this study that P-waves are not sensitive to pore pressure changes, as opposed to S and coda waves that are very sensitive. Also pore pressure increase seems to cause a shift of energy towards lower frequencies. Finally, the fluid effects on the wavefield vary significantly with the source-receiver direction and a similar dependence is noticed in the frequency shift.

Acknowledgements

Contents

8 Single-phase flow in porous media: Theory and numerical modelling

Notations and conventions

In this section all the mathematical variables and other abbreviations that are used throughout the thesis are explained. They are arranged by chapters in the order of their appearance.

Chapter 2

Symbol	Meaning
ρ	density
u_i	displacement
σ_{ij}	stress
f_i	forcing
e_{kl}	strain
c_{ijkl}	elastic stiffness
t	time
k	spatial wavenumber
$\tilde{f}(k)$	Fourier transform of function f(x)
$k(N_x)$	Nyquist wavenumber
N_x	number of grid points
$\gamma(x)$	reduction function
τ	traction acting across a fracture
Z_N	normal fracture compliance tensor
Z_T	tangential fracture compliance tensor

Chapter 3

Symbol	Meaning
p(x,z,t)	amplitude of the wavefield
x	horizontal distance
z	vertical distance
ν	velocity
ω	angular frequency
f	source frequency
λ	wavelength
V_P	P-wave velocity
V_S	S-wave velocity
dx	grid spacing in the horizontal direction
dz	grid spacing in the vertical direction

Chapter 4

Symbol	Meaning
s(t)	source time function

Chapter 5

Symbol	Meaning
α	fracture semi-length
C(r)	two-point correlation function
N	total number of grid points
N_d	number of pairs of points whose distance is less than r
k_P	P-wave spatial wavelength
k_S	S-wave wavelength

Symbol	Meaning
$< \alpha >$	mean length of fractures
ε	fracture density
N_f	number of fractures
S	surface of medium

Chapter 6

Symbol	Meaning
σ_1	North-South principal stress
σ_2	vertical principal stress
σ_3	East-West principal stress
θ	angle from the maximum compressive stress
μ	coefficient of internal friction
$Q_s^{-1}(\omega)$	scattering attenuation
$Q_c^{-1}(\omega)$	coda wave attenuation
$Q_i^{-1}(\omega)$	anelastic or intrinsic attenuation
$A(\omega)$	amplitude spectrum of a wave
$A_o(\omega)$	amplitude spectrum of a source
α	wave speed
K	susceptibility
L(y)	maximised logarithm likelihood
n	number of data points
p	number of unknown parameters
S_R^2	residual sum of squares
y_i	data points
$\gamma(x_i)$	calculated values of data points based on a polynomial fit

Chapter 7

Symbol	Meaning
$p(\alpha)$	probability density
$n(x)$	refractive index
u_o	incident wave
u_s^j	scattered wave from the j-th crack
u^j	external displacement field acting upon the j-th crack
Ψ_s^j	operator that determines the scattering property of the j-th crack
r_j	location of the centre of the j-th crack
θ_j	orientation of the j-th crack
n	number density of the crack distribution
E	peak strain energy stored in a volume
$-\Delta E$	energy loss
β	acoustic wave speed
k_α	normalised wavenumber

Chapter 8

Symbol	Meaning
k_v	vertical permeability
k_h	horizontal permeability
ϕ	porosity
η	viscosity
c	compressibility
P	pressure
$\hat{Q}$	volumetric flow rate

Symbol	Meaning
L	length
A	cross-sectional area
ΔP	pressure drop
K	absolute permeability
$\vec{V}$	fluid flow rate vector
g	gravity acceleration
Re	Raynolds number
D	depth
q	mass rate of injection per unit volume of reservoir
$\dot{\epsilon}_{ij}$	strain rate
f(i,j)	Boolean function
D_{ij}	diffusion tensor
$e_{a)}$	lattice vector
λ_a	relaxation parameter
P_a^{eq}	local equilibrium pressure
C	cohesion
σ_{ij}^{eff}	effective stress
τ	friction
α	Terzaghi coefficient
ζ	proportion of deviatoric stress still present after rupture
t_r	relaxation time
t_r^*	dimensionless timescale
τ_s	static friction
τ_d	dynamic friction
γ	ratio between differential stress and cohesion
χ	ration between isotropic stress and pore fluid pressure
ψ	parameter that determines how far the medium is from rupture

Chapter 9

Symbol	Meaning
s^b_{ijkl}	elastic compliance tensor of the background medium
s^f_{ijkl}	excess compliance tensor due to the presence of fractures
S_q	surface area of the qth displacement discontinuity
$[u_i]$	local displacement discontinuity across the surface
n_i	local normal to the fracture surface
φ	polar angle
θ	azimuthal angle
$\tau_\perp$	normal component of traction
Δ_{t_d}	required time step for diffusion process
D_1	diffusivity along a fracture
D_2	diffusivity normal to a fracture
C(x)	cohesion

Appendix A

Symbol	Meaning
Z_{max}	maximum value of compliance
x	x-coordinate of a point in a fracture
l	half-length of a fracture

Appendix C

Symbol	Meaning
$\eta(c)$	mixing viscosity
η_s	solvent viscosity
η_o	oil viscosity
S_w	water saturation
S_o	oil saturation
S_g	gas saturation
S_{or}	residual oil saturation
P_c	capillary pressure
λ	mobility of a fluid phase
f_w	water fractional flow
f_o	oil fractional flow
k_r	relative permeability
Q_t	total volumetric injection rate

INTRODUCTION

1.1 Research Motivation and Objectives

Fractures and fracture systems are crucial for hydrocarbon production. In order to produce oil and gas economically from a fractured reservoir, it is critical that a thorough investigation of the fracture network is made. From a strictly geomechanical point of view a fracture is the surface in which a loss of cohesion has taken place. In general, a fracture in which relative displacement has occured can be defined as a fault, while a fracture in which no noticeable displacement has occurred can be defined as a joint. A fracture can also be defined, in a more general way, as the discontinuity which breaks the rock beds into blocks along cracks, fissures or joints, and along which there is no displacement parallel with the planes of discontinuity. Basically, whether a fracture is considered a joint or a fault depends on the scale of investigation, but in general, that which is called a fracture corresponds to a joint. When there are fracture-controlled reservoirs, understanding the subsurface networks is important, for instance to optimize well planning and production. A large portion of oil and natural gas in the world is trapped in tight reservoirs (Nelson, 1985). In such formations, often the only practical means of extracting the gas/oil is to use the increased drainage surface provided by natural fractures, which controls fluid storage and mobility.

The reverse effect is that fractures can provide the paths for the injected steam or water to bypass the matrix pores, and cause the slow-down or termination of hydrocarbon production (Massonnat et al., 1994). In both situations, locating the subsurface fractured zones and obtaining the fractures physical properties, such as fracture orientation and density will help to optimise the field development plan.

Fractures found in reservoirs can have a wide range of scales (from microcracks to formation-scale fractures and large faults). They can act both as permeable pathways to fluid migration and also as significant storage. As low permeability reservoirs, particularly carbonates, are exploited the need to adequately characterise the distribution and properties of fractures within the subsurface will increase. One of the key issues in attempting to characterise fracture systems is to identify the "hydraulic backbone" of the system. Fractured reservoir rocks are made up of two porosity systems. One is the intergranular formed by void spaces between the grains of the rock, and a second is formed by void spaces of fractures and vugs. In compact, brittle rock of relatively low intergranular porosity, such as compact limestones, shales, shaly sandstones, schists, etc, porosity is normally caused by rock fracturing. In such an environment, a good knowledge of the fracture network will give us an insight in the possible directions of fluid flow. The knowledge of possible fluid flow paths gives us the "hydraulic backbone" of the system. Many studies have shown that relatively few large fractures may contribute to flow within a system and so the accurate characterisation of this hydraulic subset is of vital importance to optimise production in these heterogeneous and complex reservoir systems.

Although many logging tools and log-analysis methods, have been designed to view the subsurface fractures cutting through a borehole, their usage is limited by the high cost and small sampling area. The information obtained is very valuable about the subsurface fracture geometry (borehole teleview), fluid content, spac-

ing, and connectivity. However, the interpolation of fracture-network properties over a field is inevitably inaccurate when there are only a few wells with fracture information.

Seismic methods are the most commonly used tools in hydrocarbon prospecting to infer fracture patterns and fracture properties. A seismic survey has the advantage of low cost, wide coverage, and deep penetration. Theoretical and laboratory studies (Nur, 1971; Crampin and Bamford, 1977; Hudson, 1980, 1981, 1990, 1994) have shown that fractures can induce anisotropy into seismic properties of the rock. The seismic survey has the potential to be a powerful tool to detect and characterise subsurface fractures. One of the most popular methods in seismic fracture detection uses the shear-wave splitting techniques. These techniques have been used successfully in locating the fractured zones in many field studies (Queen and Rizer, 1990; Liu et al., 1991). Another method of estimating fracture parameters is from azimuthal P-wave data. That is based on the fact that P-waves show azimuthal variations in propagation attributes i.e. velocity, reflectivity, amplitude, as a function of rock properties such as fracture-induced seismic anisotropy. P-waves are cheaper to acquire, have higher signal-to-noise ratio, and are more commonly available in 3D than shear wave data. However, the use of P-wave data in fracture detection and characterisation is not fully exploited. There has been both theoretical work and field observations showing the correlation between the fractured zones and the azimuthal variations in P-wave amplitude and velocity (Crampin and Bamford, 1977; Lynn et al., 1996; Rueger, 1996). The outputs of these studies often took the form of anisotropy mapped over the survey areas. Some authors converted the amount of anisotropy to crack density, according to the penny-shaped crack model (Hudson, 1980, 1981, 1990, 1994). However, they did not take into account realistic in-situ physical conditions, including subsurface temperature, pressure, nature of fracture filling material, seismic frequency, and the hydraulic interaction between fractures.

Critical problems remain in estimating the subsurface fracture properties under in-situ reservoir conditions. Gaps also exist in integrating all the information measured at core, log and seismic (including P- and S-wave surveys) scales for fracture characterisation.

The key issue in seismic monitoring experiments is to interpret the information we get, and estimate fracture properties, i.e. fracture density, spatial distribution and fracture lengthscale. In order to explain the characteristics of seismic waves recorded during seismic surveys, we need to have better understanding of the effects of fractures on seismic waves. There are available theoretical approaches that describe the response of seismic waves to fractures. Such theoretical models are available for the short and the long wavelength cases. The range of wavelengths used in most seismics is from $\lambda = 1cm$ to $\lambda = 1km$. Scalelengths in a reservoir can vary from large basin description (described as megascale) relating to the field wide variability across depositional systems; to the macroscale, where distributions of lithofacies on the well-to-well scale and the geometric distribution of reservoir compartments is important, the cross-bed mesoscale with features such as ripple laminations; to the smallest microscale which includes grains, pores, crystals, minerals or even pore throats. When the wavelength is smaller than the lengthscale of the fracture (short wavelength) we have the ray theory, single scattering (e.g. Knopoff and Hudson, 1964; Aki and Richards, 2002; Barley et al., 1982) and multiple scattering theories (e.g. Landers and Clearbout, 1972; Hudson, 1980b; Wu, 1994; Wesley, 1965; Ryzhik et al., 1996). That is the range at which traditional seismic experiments image structures at large scalelengths and they obey the inequality $\alpha/\lambda > 1/4$, where α is the size of the fracture and λ is the wavelength. When the wavelength is much greater than the lengthscale of the fractures (long wavelength), we can use an equivalent medium theory where we consider fractured blocks as equivalent anisotropic solids (e.g. O'Connell and Budiansky, 1974; Hudson, 1980; Schoenberg, 1980; Nishizawa, 1982). Equivalent

medium theory has a range of validity to the left of the operative seismic wavelength with a limit of $\alpha/\lambda < 1/8$, so that features with scalelengths smaller than the seismic wavelength are resolved. In principle, it seems that the role of equivalent medium theory could be to fill the lower scalelength portion of the seismic resolution, and so provide information on a complete spectrum of reservoir features. However, those methods are valid for small disorder but they fail at large disorder (i.e. high fracture density, complicated fracture networks). That introduces serious limitations in the application of the methods for the examination of fractured networks.

More recently, it has been realised that seismic waves can be used to monitor changes in an oil or gas reservoir as a function of time. The influence of porosity, permeability, and fluid properties on the elastic characteristics of rocks was studied by Terzagi (1943), Frenkel (1944) and Biot (1941), Biot (1956a), Biot (1956b). Those research results are employed, either in their qualitative or quantitative form, in a number of seismic exploration technologies. When used in conjunction with reservoir simulations, seismic monitoring will probably become a powerful tool in reservoir management.

Field monitoring experiments had some success in some cases. However, that does not mean that we fully understand the effects of fluids and transport properties on seismic wavefields. Also such results indicate that the petrophysical models used in the monitoring of fluid flow are good approximations. That may be true in a number of cases, but we have not achieved yet models that can describe with sufficient accuracy and reliability a variety of cases, especially complicated ones. A deeper insight into the process of wave propagation in rocks, as well as the development of a set of quantitative petrophysical models for a variety of reservoir environments is needed. It is obvious from the above mentioned that there are still gaps between the theoretical predictions of rock properties and the actual measured ones.

One of the objectives of the thesis is to examine the effect of fracture parameters on seismic waves. We realised that there are limitations on the equivalent medium theory, in both cases of short and long wavelength, when it is used for fracture characterisation, based on the concept of seismic anisotropy. The limitations are that it cannot provide information about fracture size, length distribution and spatial distribution. We propose to use numerical methods to model discrete fractures. Numerical methods are not restricted in any way. For the numerical modelling we use the pseudospectral method. Discrete fractures are implemented in the finite difference grid using the equivalent medium theory. The combination of a numerical method with the equivalent medium theory, overcomes the limitations of the equivalent medium representation of the medium, gives accurate representation of the fractures, and produces reliable synthetic seismograms. We use the synthetic seismograms for a detailed examination of the effect of fracture size, length distribution and spatial distribution on seismic waves.

The other objective of the thesis is the examination of the effect of fluid flow on seismic waves and the identification of characteristic features on seismic signatures that can be attributed to fluid flow. Despite recent theoretical developments in the field of rock physics, there is usually no actual link between the seismic response of fractured reservoirs and the fluid properties in the fractures. We use an empirical relationship that describes fracture compliance changes as the traction on the fractures changes due to pore pressure changes, while properties of the intact background rock are assumed constant. We simulate the fluid movement in the fractured network with a model of pore fluid pressure diffusion. We use the 2-D finite difference method presented in the previous chapters of the thesis to model the wave propagation before and during fluid injection. The aim is to examine any direct indication of pore pressure changes in the synthetic seismograms for a common fracture network

1.2   Description of this thesis

In this thesis we present the theoretical background and the implementation of a new numerical modelling technique. This technique is used to examine wave propagation in a fractured network with discrete fractures of different sizes and of various spatial distributions. Also we present a simulation of fluid flow in the fractured network, and we investigate the link between pore pressure changes and seismic signatures of fractures. In the first section of Chapter 2 we describe the methods that are used to simulate wave propagation in a fractured network. There are a number of theoretical methods depending on the size of the fractures compared to the wavelength. Analytical solutions are available for the short and long wavelength cases. When the wavelength is smaller than the scale length, wave propagation is described by the ray theory, single scattering and multiple scattering theories. When the wavelength is much greater than the length scale of the fractures, finite fracture openings and details of the spatial distributions of fractures can be neglected and fractured blocks can be considered as equivalent or effective anisotropic solids, thus applying the effective medium theories.

In the following section, we present the pseudospectral method that is used in the numerical simulation of wave propagation. We describe the implementation of the wave equation in the finite difference grid, the representation of the medium in each grid cell and the absorbing boundary conditions.

In the final section, we describe the implementation of fractures in the isotropic background medium, which is the key issue of our method. We use an effective medium theory to calculate the elastic parameters for the cells that are intersected by fractures. The linear slip interface model (Schoenberg and Sayers, 1995) is used to calculate the effective compliance of the medium for each grid cell. The theoretical background of the implementation in a fractured network, is presented in details.

In Chapter 3 we examine the accuracy of the modelling technique presented in Chapter 2. We begin by considering some general limitations introduced by the pseudospectral technique and the implementation of fractures using an equivalent medium theory. In the next section, we present a detailed examination of the limitations in grid spacing related to the frequency and the size of the fractures. We continue with an examination of the vertical and the lateral resolution of the model, and in the final sections we present the results of three numerical examples where we show the accuracy of the modelling technique.

After introducing the modelling technique in Chapter 2 and examining its accuracy and validity in Chapter 3, in Chapter 4 we apply the model to examine the effect of fracture parameters on seismic wave propagation. Firstly, we examine the effect of fracture size. The aim of this section is to understand the behaviour of the fractures in three main cases, when fractures are larger than the wavelength, when fractures have the same size with the wavelength, and when fractures are smaller than the wavelength. Secondly, we examine the spatial distribution of fractures. We present the cases of uniform, Gaussian, exponential and gamma distributions of fractures that have the same size. This examination shows the effect of spatial distribution on wave propagation, both on synthetic seismograms and the frequency content. Finally, we discuss the case of fractures having various scalelengths, which is usually the case in earth, and we also present the results for a power-law size distribution.

In Chapter 5 we introduce a realistic fracture model and we examine multiple scattering in a medium with a complicated fracture network. We use the results of a multiscale cellular automaton (Narteau, in press) to create a fractured medium that attempts to model the natural rock. Basically, it is a model of rupture whose outputs can be compared with different aspects of the structural patterns observed in the formation and evolution of a population of strike-slip fractures. Fracture formation and evolution is a result of fracture interaction and

pre-existing material heterogeneity. In natural data, there is a growing body of evidence that indicates that neighbouring fractures interact and that fracturing processes at every scale are strongly dependent on the interrelated evolution of pre-existing faults. The model describes important generic characteristics of the faulting patterns generated during the formation and evolution of fractures. We model the wave propagation at each stage of the evolution of the fracture network, and examine scattering attenuation of P-waves. Therefore we are able to inspect the interaction of each individual feature of the fractures that are examined in Chapter 4 and their joint effect on the wavefield.

In Chapter 6 we use a meanfield theory to continue the examination of scattering attenuation, and investigate different aspects of wave propagation. In the meanfield theory the variations of the properties of the wavefield are averaged, thus we obtain a mean effect of the fractures. We present the theoretical background for the estimation of scattering attenuation. We use different realisations of random distributions of fractures and estimate the mean wavefield for all the realisations. We consider different fracture sizes and the results are compared with the results presented in Chapter 5. In order to obtain more accurate results, we select a window to keep only the first arrivals. We examine the effect of travel distance and angle of scattering on the estimation of scattering attenuation.

Until Chapter 6, when we refer to fractures we assume that fractures are dry. In real earth fractures may be filled with fluid, and they are the main path that fluid flows through. In Chapter 7 we present the fundamentals of fluid flow. In the first section, we give a brief presentation of the various modelling techniques of fluid flow. In the next section, we introduce the two basic flow models, the equivalent continuum and the discrete network model. We briefly describe phase, viscosity and compressibility, and present some typical values of those parameters. We present the single phase properties, that is permeability, porosity, saturation, capillary pressure, mobility and fractional flow. We describe the basic parameters

that control fluid flow, and explain how those parameters are linked to describe fluid flow in the form of differential equations. Finally, we describe Darcy's law and based on that we get a general equation for single-phase flow.

In Chapter 8, after presenting in Chapter 7 the basic concepts of fluid flow, we examine the dual simulation of fluid flow and seismic wave propagation in a fractured medium. In the first section we refer to the theoretical model. We explain how the solid phase and the fluid phase are implemented in the model. In the next section, we give a detailed description of the BGK model that we use for the numerical modelling of fluid flow. We concentrate on single phase fluid. In the following section, we present the interaction between the solid and the fluid phases and the basic assumptions applied in the numerical modelling. The flow of fluid through fractures will effect the elastic properties of the medium as well as the stress distribution. In the next section, we give a detailed description of fracture compliance variations due to pore pressure changes. Following that, we consider effective static stress changes due to pore pressure changes, and the possible evolution of the fracture network. We apply the above for simplicity in the case of vertical fractures under anisotropic stress. Finally, we present numerical examples based on the theoretical model. We use the fluid flow simulator to generate pore pressure maps at consecutive stages. The pore pressure variations, result in variations in the elastic properties, following the theoretical model presented in the previous section. For each one of the consecutive stages, we simulate wave propagation using the modelling technique presented in Chapters 2 and Chapter 3. We examine the case of single and multiple azimuths, and discuss the possibility of establishing a direct link between pore pressure changes and seismic wave properties, such as amplitude, arrival time or frequency spectra.

Wave propagation in fractured media: Equivalent medium theories and numerical simulations

2.1 Introduction

Fracture systems have been actively studied for the last 25 years. That interest was motivated to a large extent by the siting of hazardous waste disposal sites in crystalline rocks, by the problems of multiphase flow in fractured hydrocarbon reservoirs, and by earthquake hazards and the possibility of prediction. According to different points of view various definitions can be given to a fracture, but from a strictly geo-mechanical point of view a fracture is the surface in which a loss of cohesion has taken place. Since rupture refers to a process which results in the loss of cohesion of a given material, a fracture is then the result of a rupture. In general, a fracture in which relative displacement has occurred can be defined as a fault, while a fracture in which no noticeable displacement has occurred can be defined as a joint. A fracture can be defined, in a general way, as the discontinuity which breaks the rock beds into blocks along cracks, fissures, joints or whatever they may be referred to as, and along which there is no displacement parallel with the planes of discontinuity. Fractures exist on a wide range of scales from

microns to hundreds of kilometers, and it is known that throughout this scale range they have a significant effect on processes in the Earth's crust including fluid flow and rock strength.

Fractures are a result of a variety of geological processes (Menéndez et al., 1999), including thermal gradients, mechanical effects of an ambient stress field, combined effects of a stress concentration at the crack tips and chemical weakening of molecular bonds ahead of the crack tip by the mechanism of stress corrosion (Atkison, 1984; Atkinson and Meredith, 1987). From the examination of fractured reservoir case histories (Stearns and Friedman, 1972), the most probable fractured reservoirs are expected to occur in brittle reservoir rock of low porosity where favourable tectonic events have developed. In this case the resulting fractures are large and very extended and are, therefore, called macrofractures. Such reservoirs are in fractured basements, where the oil and gas in place may be held within an extensive fracture network rather than within the matrix porosity of the formation. Most basement rocks are hard and brittle with very low matrix porosity and permeability. In basement reservoirs matrix porosity is effectively close to zero and most of the storage capacity and permeability is due to fractures. Such reservoirs are the Edison and Mountain View Fields in the San Joaquin Valley of California; the El Segundo, Wilmington and Playa Del Rey Fields in the Los Angeles Basin (Eggleston, 1948; McNaughton, 1953); the La Paz-Mara Fields in Venezuela (Smith, 1951); and the Amal Field in Libya. If the rock is less brittle and has a high intergranular porosity, the fractures are generally of limited extend and with relatively small openings and are, therefore, called microfractures. In the thesis, we mainly consider fractured carbonate reservoirs. Such reservoir is the Mara-LaPaz fields of Venezuela, where matrix porosity does not exceed 3% and permeability is $0.1md$. Production was, in this case, the result of fracture permeability. Another example is the Selma fractured chalk reservoir of the Gilbertown field in Alabama, where fracture porosity existed as a secondary trap

for oil migrating from the older Eutaw sands.

The variations of fracture characteristics is so irregular and complicated, that the description of a fractured reservoir is very difficult. Such characteristics are the opening (width), size and nature of fracture. If the single fracture is associated with the reservoir environment, another essential characteristic, the fracture orientation, will result. For a multi-fracture network important parameters are the fracture density and distribution. All those characteristics are critical for successful fracture detection and evaluation. Variations on those parameters will affect seismic waves traveling in the reservoir. In order to interpret seismic reflection data from such a reservoir, we need theoretical models that can relate fracture properties to characteristics of the seismic data.

2.2   Analytical methods

In the Earth's crust there are fractures of all lengthscales (Yielding et al., 1992). Fractures will respond in a different way depending on the wavelength scale of seismic waves. Analytical solutions that describe seismic wave response are available for the short and the long wavelength cases.

For the case that the wavelength is smaller than the lengthscale of the fractures we have the ray theory, single scattering and multiple scattering theories. For the ray theory to be applicable wavelengths should be much smaller than the lengthscale of spatial variations in material properties. However, ray theory is not capable of describing diffraction effects. A theory that can describe accurately single scattering is the Born approximation (Knopoff and Hudson, 1964; Aki and Richards, 2002). It has been applied successfully to scattering Rayleigh waves (Hudson, 1967), and when the amplitude of the source signal is relatively small, so limited scattering becomes significant (Barley et al., 1982). However, that the-

ory is not applicable to multiple scattering cases. Theories that describe multiple scattering are the parabolic approximation (Landers and Clearbout, 1972; Hudson, 1980b), the "complex-screen" (Wu, 1994) and the diffusion approximation (Wesley, 1965; Ryzhik et al., 1996). In addition to multiple scattering, diffraction effects can be described by the parabolic approximation or by the geometrical theory of diffraction (Achenbach et al., 1982). Nevertheless, the special case of P to S scattering, or vice versa, cannot be described accurately by the parabolic theory (McCoy, 1977).

When the wavelength is much greater than the lengthscale of the fractures, we can neglect finite fracture openings and details of the spatial distributions of fractures and can consider fractured blocks as equivalent or effective anisotropic solids. The parameters of such an effective model will depend on the orientation and intensity of the fracture set(s) and the properties of the material filling the fractures, as well as on the elastic coefficients of the host rock. At the core of that approach is the idea that a heterogeneous medium can be seen as an equivalent homogeneous medium, i.e. its properties are the same as those of a homogeneous medium. This strategy is valid for small disorder but is bound to fail at large disorder. A number of authors have presented effective medium theories that give the overall properties of elastic material that have fractures (e.g. O'Connell and Budiansky, 1974; ?; Nishizawa, 1982). All those techniques, although each one is using a different approach, they all need to calculate the response of a single fracture. This can be calculated in the limit in which the thickness of the crack vanishes (Walsh, 1965; Garbin and Knopoff, 1973; O'Connell and Budiansky, 1974; ?). Fractures are either assumed to be dry (Walsh, 1965; Garbin and Knopoff, 1973; O'Connell and Budiansky, 1974; Hudson, 1981), fluid-filled (Anderson et al., 1974; Garbin and Knopoff, 1975; O'Connell and Budiansky, 1977; Hudson, 1981), or partially saturated (Hudson, 1988). Although usually fractures are described as circular ("penny-shaped"), there is a number of other

implementations. Budiansky and O'Connell (1976) introduced elliptical fractures. Spheroids of a non-zero thickness were studied by some authors (Eshelby, 1957; Anderson et al., 1974; Kuster and Toksoz, 1974; Nishizawa, 1982; Sayers, 1988; Hudson, 1994), and non-elliptical thin fractures have also been examined (Mavko and Nur, 1978; Walsh and Grosenbaugh, 1979).

2.3   Numerical methods

Seismic numerical modelling is a technique for simulating wave propagation in the earth. The objective is to predict the seismogram that a set of sensors would record, given an assumed structure of the subsurface. The computation of synthetic seismograms is an essential component of full waveform inversion schemes for determining subsurface earth structures. There are many approaches to seismic modeling. Carcione et al. (2002) classify them into three main categories: direct methods, integral-equation methods, and ray-tracing methods.

To solve the wave equation by direct methods, the geological model is approximated by a numerical mesh, that is, the model is discretised in a finite numbers of points. These techniques are also called grid methods and full-wave equation methods, the latter since the solution implicitly gives the full wavefield. Direct methods do not have restrictions on the material variability and can be very accurate when a sufficiently fine grid is used. Furthermore, the technique can handle the implementation of different rheologies and is well suited for the generation of snapshots which can be an important aid in the interpretation of the results. A disadvantage of these general methods, however, is that they can be more expensive than analytical and ray methods in terms of computer time.

Integral-equation methods are based on integral representations of the wavefield in terms of waves, originating from point sources. These methods are based on

Huygens' principle, formulated by Huygens in 1960 in a rather heuristic way. When examining Huygens' work closer, we can see that he states that the wave-field can, in some cases, be considered as a superposition of wavefields due to volume point sources and, in other cases, as a superposition of waves due to point sources located on a boundary. Both forms of Huygens' principle are still in use today and we have both volume integral equations and boundary integral equations, each with their own applications. These methods are somewhat more restrictive in their application than the above direct methods. However, for specific geometries, such as bounded objects in a homogeneous embedding, boreholes, or geometries containing many small-scale cracks or inclusions, integral equation methods have shown to be very efficient and to give accurate solutions. Due to their somewhat more analytic character, they have also been useful in the derivation of imaging methods based on the Born approximation (i.e. Cohen et al., 1986 and Bleistein et al., 2001).

Asymptotic methods or ray-tracing methods are very frequently used in seismic modeling and imaging. These methods are approximate, since they do not take the complete wavefield into account. On the other hand, they are perhaps the most efficient compared with the rest of the methods. Especially for large, three-dimensional models the speedup in computer time can be significant. In these methods, the wavefield is considered as an ensemble of certain events, each arriving at a certain time (traveltime) and having a certain amplitude. Asymptotic methods, due to their efficiency, have played a very important role in seismic imaging based on the Born approximation for heterogeneous reference velocity models. Another important application of these methods is the modeling and identification of specific events on seismic records.

2.4   Comparison of modeling methods

After presenting the various techniques that approximate the solution of the wave
equation, I continue with a comparison of those techniques. In general the direct
methods presented do not have restrictions on the type of constitutive equation,
boundary conditions, and source type, and allow general material variability.
For instance, the numerical solution of wave propagation in an anisotropic poro-
viscoelastic medium, which is suitable to describe a reservoir environment, is
not particularly difficult in comparison with simple cases, such as the acoustic
wave equation that describes the propagation of dilatational waves. In order to
handle such complex constitutive equations using an integral-equation method or
an asymptotic method, we need to make simplifying assumptions. On the other
hand, direct methods are certainly more expensive in terms of computer time and
storage requirements.

Finite differences are simple to program and when the accuracy required is
moderate they are very efficient compared to other methods. A good choice
can be an FD algorithm which is second order in time and fourth order in space.
Pseudospectral methods on the contrary may be computationally more expensive,
that is the computation time is longer than the equivalent FD computation,
but have much higher accuracy and relatively lower background noise especially
when staggered differential operators are used. These operators are also suitable
when in the model we have large variations of Poisson's ratio (e.g. a fluid-solid
interface). In 3-D cases, pseudospectral methods give very high accuracy and
need only a minimum number of grid points, so they are the best choice when
there are limitations in the computer storage required. However, when we need
a dense grid of points, as in the case of fine-layering, scattering inhomogeneities,
the FD method is more convenient.

When we are interested in modeling surface topography and curved interfaces,

the method that gives us the best results is the finite element method. The method's accuracy and stability can compete with the other techniques. However, finite element methods become unstable when Poisson's ratio varies greatly. In general, FE methods are suitable for engineering problems, where interfaces are well defined in contrast with geological interfaces. In these interfaces for accurate modeling we require nonstructured grids. That is one of the main advantages of FE, especially when we are dealing with complicated 3D models. Despite of that, generally FE methods are preferred for seismic problems that involve the propagation of surface waves in complex topographies.

Integral equations contains a Green's function that describes the wave propagation in the embedding medium. For certain geometries, such as boreholes or other boundaries, media containing cracks, and inclusions of bounded extent, these methods are relatively efficient compared to direct methods. The reason for this efficiency is that the number of unknown functions to be determined is confined to a bounded region. The price to pay for this reduction in unknowns is the fact that the system matrix is full, whereas direct methods usually have sparse system matrices that can be solved in an efficient way. Since integral-equation methods can explicitly account for the boundary conditions at crack boundaries or borehole walls, these methods can provide accurate results for the specific geometries mentioned. Also, for deriving analytical imaging methods, integral-equation techniques are very well suited, and are often used together with asymptotic methods.

Asymptotic methods aim at the calculation of approximate solutions for the wave equation that are valid for high frequencies. Asymptotic methods calculate the solution up to a smooth error. In fact, they calculate only the most singular part of the solution, which is characterized by a traveltime function and an amplitude function. The traveltime function is a solution of the eikonal equation; the amplitude function is a solution of the transport equation. Due to their com-

putational efficiency, asymptotic methods are widely applied in the generation
of synthetic seismograms and the solution of inverse problems such as traveltime
tomography and migration.

2.5 Boundary conditions

The simulation of waves by direct methods in unbounded domains requires a
special treatment for the boundaries of the necessarily truncated computational
domain. The imposition of artificial boundaries introduces spurious reflections
which will affect the accuracy of numerical solutions. Although we can overcome
the problem by increasing the size of the model, it is not always feasible because
of the large amount of computer memory required for long-time solutions. It
is thus highly desirable to eliminate these reflections. Two solutions have been
proposed for this purpose: absorbing boundary conditions (ABCs) and absorbing
layers.

The ABCs consist of introducing some suitable local boundary conditions that
simulate the outgoing nature of the waves impinging on the borders. Smith (1974)
proposed an ABC for finite-difference and finite element methods. In this method,
the Dirichlet and Neumann conditions are used alternatively, and the solutions
from these two conditions are superimposed. Although easy to implement, this
method greatly increases the computation time. A widely used ABC in seismic
modeling proposed by Clayton and Engquist (1977) is the one-way wave equa-
tion based on the paraxial approximations of the acoustic or elastic equations.
Similar approaches were proposed by several authors, including Reynolds (1978).
Although effective for small incidence angles, these absorbing boundary condi-
tions degrade for large angles of incidence. Furthermore, they are known to have
instability problems when the Poisson's ratio is greater than 2.0 (Mahrer (1986);
Stacey (1988)). Another approach is to add a spatial filter or damping taper to

the boundaries (Cerjan et al. (1985); Kosloff and Kosloff (1986)). In this so-called
sponge absorber method, the transition zone from the inner region to the outer
boundary should be thick and smooth. Liao et al. (1984) developed an ABC
based on the principle of plane wave and interpolation. Although effective even
for perpendicular inhomogeneous boundary intersecting the absorbing boundary,
Liao's ABC requires double precision for stability.

Layer models are an alternative to ABCs. The idea is to surround the do-
main of interest by some artificial absorbing layers in which waves are trapped
and attenuated. For elastic waves, several models have been proposed. For in-
stance, Sochacki et al. (1987) suggest adding inside the layers some attenuation
term, proportional to the first time derivative of the elastodynamic equations.
The main difficulty is that when entering the layers, the wave "sees" the change
in impedance of the medium and then is reflected artificially into the domain
of interest. The use of smooth and not too high attenuation profiles allows us
to weaken the difficulty but requires the use of thick layers (Israeli and Orszag,
1981). Berenger (1994) proposed a highly effective perfectly matched layer (PML)
as an absorbing boundary condition for electromagnetic waves. It has since been
widely used for finite-difference and finite element methods (e.g., Chew and Wee-
don (1994); Liu (1997)). Chew and Liu (1996) first proved that such a perfectly
matched layer also exists for elastic waves in spite of the coupling of S- and
P-waves at an elastic interface. In the continuous limit, the PML has zero reflec-
tion to the regular elastic medium, although a small reflection can result from
discretization in the PML scheme. Hastings et al. (1996) independently imple-
mented the PML ABC for two-dimensional problems using potentials. The PML
ABC has also been extended to model acoustic waves and electromagnetic waves
in lossy media (Liu (1997); Liu and Tao (1997)) as well as electromagnetic and
elastic waves in cylindrical and spherical coordinates (Liu (1999); He and Liu
(1999)). The previous works, however, have been developed for electromagnetic,

acoustic, and elastic waves in solids. Currently there is limited work done for
the implementation of the PML to elastic waves in porous media. Such is the
work of Collino and Tsogka (2001) where they incorporate the PMLs into the
stress-velocity formulation. Also Zeng et al. (2001) extended the PML to trun-
cate unbounded poroelastic media for numerical solutions using a finite-difference
method. They adopted the method of complex coordinates (Chew and Weedon
(1994); Liu (1997); Liu and Tao (1997)) to formulate the PML for poroelastic
media.

2.6 Simulation of wave propagation using a pseudospectral method

2.6.1 Wave propagation in anisotropic media

The wave equation for an inhomogeneous anisotropic medium is :

$$\rho \ddot{u}_i = \sigma_{ij,j} + f_i, \qquad (2.1)$$

where ρ, u, σ, and f represent density, displacement, stress and forcing, respec-
tively (Wu and Lees, 1997). Stress σ and strain e are related by Hooke's law

$$\sigma_{ij} = c_{ijkl} e_{kl}, \qquad (2.2)$$

where c_{ijkl} are the elements of the elastic fourth-rank stiffness tensor. It obeys the
laws of tensor transformation and has a total of eighty-one components. However,
not all eighty-one components are independent. In those equations Einstein's
summation convention is implied. If we combine equations (2.1) and (2.2), we
obtain the wave equation in an analytic form:

$$\rho \frac{\partial^2 u_i}{\partial t^2} = \frac{\partial}{\partial x_j} \left(c_{ijkl} \frac{\partial u_k}{\partial x_l} \right) + f_i \qquad (2.3)$$

In the models we examine, we have isotropic mediums in which anisotropy is introduced by the presence of fractures. Equation (2.3) is the equation that describes the wave propagation in general heterogeneous anisotropic media.

2.6.2   The pseudospectral method

Finite difference modeling of wave equations in the seismic context began around 1970. Alford et al. (1974) note that fourth-order FD is superior to the second-order FD for the 2-D acoustic ($\mu = 0$) wave equation. Many production codes for solving the elastic wave equation were upgrated from second-order to fourth-order FD around 1986. The numerical techniques employed so far to study seismic wave scattering problems include the Maslov theory (Chapman and Drummond, 1982), the finite-difference method (FD) (VanBaren et al., 2001; Saenger and Shapiro, 2002), the pseudospectral method (PS) (Fornberg, 1988), the finite-element method (FE) (Lysmer and Drake, 1972), the boundary element method (Benites et al., 1992; Pointer et al., 1998; Liu and Zhang, 2001) and the spectral finite-difference method (Mikhailenko, 2000).

In this study we use the pseudospectral method to simulate wave propagation in media with discrete distributions of fractures. PS methods originally were not used extensively, but gradually received much attention in the literature. Kosloff and Baysal (1982) test a Fourier-PS method on two 2-D acoustic model problems and find it more effective than a FD scheme. Johnson (1984) applies the Fourier-PS method to a 3-D acoustic problem, and Kosloff et al. (1984) to a 2-D elastic problem. After comparing second-order and fourth-order FD against Fourier-PS on a number of 2-D elastic problems (Fornberg, 1987) (as shown in Figure 2.1), it became clear that PS method would decidedly outperform second-order and fourth-order FD methods. The result of the comparison is not model dependant. Equivalent resuls were found by other researchers too.
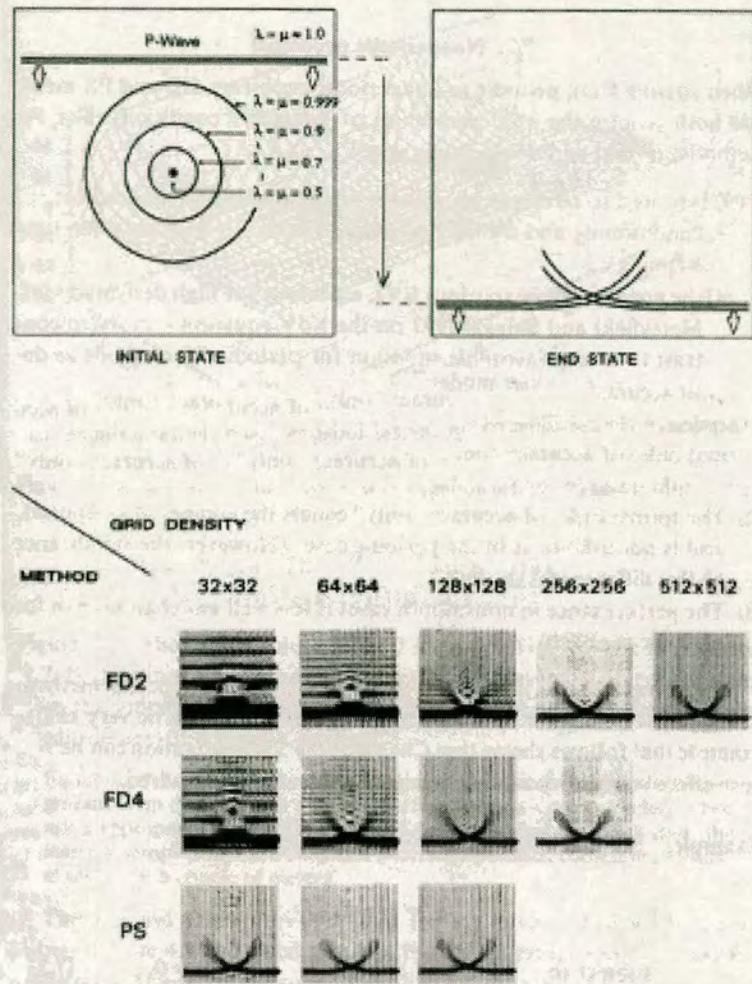
Figure 2.1: Contour curves for the variable medium, schematic illustrations of the
initial and end states of the test runs, and numerical results for the test
problem (variable f displayed); comparison between different methods
and grid sizes (Fornberg, 1987)

Figure 2.2 shows the computation geometry with the absorbing boundaries in

the PS computation. While FD approximates spatial derivatives of field vari-

ables by differences, the pseudospectral method uses the derivative property of

the Fourier transform, namely that the differentiation in space domain is a multi-

plication of the Fourier transform in the wavenumber domain by ik, where k is the

spatial wavenumber (Wu and Lees, 1997). The equations for the differentiation

in the 2-D case are

$$
\begin{aligned}
\frac{\partial u(x,z)}{\partial x} &\rightarrow ik_x U(k_x, k_z), \\
\frac{\partial u(x,z)}{\partial z} &\rightarrow ik_z U(k_x, k_z), \\
\frac{\partial^2 u(x,z)}{\partial x \partial z} &\rightarrow -k_x k_z U(k_x, k_z), \\
\frac{\partial^2 u(x,z)}{\partial^2 x} &\rightarrow -k_x^2 U(k_x, k_z), \\
\frac{\partial^2 u(x,z)}{\partial^2 z} &\rightarrow -k_z^2 U(k_x, k_z).
\end{aligned}
\tag{2.4}
$$
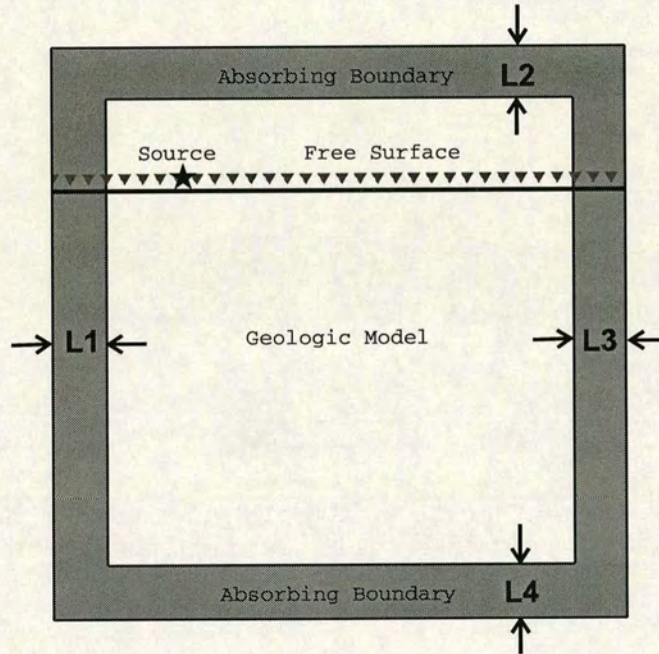
Figure 2.2: Schematic representation of the computational grid used in the application of the pseudospectal method. The shaded area is the absorbing boundary

The effect of this change is equivalent to an infinite-order (limited by grid size) difference scheme (Fornberg, 1987) and is accurate for all the Fourier components with the possible exception of the Nyquist frequency. Using this idea, we substitute the spatial difference scheme with a Fourier and inverse Fourier transform pair. A minimum of two nodes per wavelength (theoretically) is needed to get an accurate derivative, compared with FD that normally requires 10-20 nodes per

wavelength (Alford et al., 1974). So if we have limited computer memory, we can
obtain much higher frequencies or, equivalently, can accommodate much larger
models. Also accuracies of FD methods are measured by the order of polynomi-
als that are approximated exactly, whereas PS methods are measured by which
frequency components are best approximated. PS methods thus seem to be more
natural than FD methods in dealing with waveform propagation containing sinu-
soidal elements.

There are, however, some disadvantages to PS methods, namely that a periodic
medium and a periodic source is implicitly assumed. This results in a wraparound
effect that is difficult to estimate and remove. Signals with frequencies higher than
Nyquist may arise from heterogeneous structural variations, source function, and
source spatial distribution, and thus aliasing effects on the wavefield can become
significant. We try to mitigate those unwanted effects by introducing absorbing
boundary conditions, and by having a large model space.

Summarizing, the main advantage of the pseudospectral method is that it is
numerically very stable, and for a given accuracy, requires fewer grid points per
wavelength than traditional finite differencing (Fornberg, 1987). So for a desired
accuracy it makes less computations and therefore it is faster than the FD meth-
ods, and also has much less memory requirements. On the other hand, the use of
PS methods introduces wraparound effect and the use of an absorbing boundary
is necessary to remove it.

2.6.3   Calculation of spatial derivatives

The pseudospectral methods used in forward modeling of seismic waves are mainly
based on the Fourier and Chebyshev differential operators. Gazdag (1981) first
and Kosloff and coworkers later applied this technique to seismic exploration
problems (e.g., Kosloff and Baysal, 1982; Reshef et al., 1988). Mikhailenko (1985)

combined transform methods (e.g., Bessel transformations) with FD and analytical techniques.

The sampling points of the Fourier method are $x_j = j \ dx = jx_{max}/(N_x - 1)$ $(j = 0, \ldots, N_x - 1)$, where x_{max} is the maximum distance and N_x is the number of grid points. For a given function $f(x)$, with Fourier transform $\tilde{f}(k)$, first and second derivatives are computed as

$$\widetilde{\frac{\partial f}{\partial x}} = ik\tilde{f}, \qquad \widetilde{\frac{\partial^2 f}{\partial x^2}} = -k^2\tilde{f}, \qquad (2.5)$$

where k is the discrete wavenumber. The transform f to the wavenumber domain and the transform back to the space domain are calculated by the fast Fourier transform (FFT). The derivatives of two real functions - two adjacent grid lines of the computational mesh - can be computed by two complex (direct and inverse) FFTs. The two functions are put into the real and imaginary parts, the FFT is performed, the result is multiplied by ik, and the inverse FFT gives the derivatives in the real and imaginary parts. Staggered operators that evaluate first derivatives between grid points are given by

$$D_x^{\pm}\phi = \sum_{k=0}^{k(N_x)} ikexp(\pm ikdx/2)\phi(k)exp(ikx), \qquad (2.6)$$

where $k(N_x) = \pi/dx$ is the Nyquist wavenumber. The standard differential operator requires the use of odd-based FFTs (i.e., N_x should be an odd number). This is because even transforms have a Nyquist component which does not possess the Hermitian property of the derivative (Kosloff and Kessler, 1989). The approximation (2.4) is accurate up to the Nyquist wavenumber. If the source spectrum is negligible beyond the Nyquist wavenumber, we can consider that there is no significant numerical dispersion due to the spatial discretisation. Hence, the dispersion relation is given by

$$\frac{2}{dt}sin(\frac{\bar{\omega}dt}{2}) = ck\sqrt{1 - 2\sum_{l=2}^{L}(-1)^l\frac{(ckdt)^{2l-2}}{(2l)!}}, \qquad (2.7)$$

which for a second-order time integration can be written as

$$\bar{\omega} = \frac{2}{dt} sin^{-1}(\frac{ckdt}{2}).$$

(2.8)

Because k should be real to avoid exponentially growing solutions, the argument
of the inverse sine must be less than one. This implies the stability condition
$k_{max}cdt/2 \leq 1$, which leads to $\alpha \equiv cdt/dt \leq 2/\pi$, since $k_{max} = \pi/dx$ (α is called
the Courant number). Generally, a criterion $\alpha < 0.2$ is used to chose the time
step (Kosloff and Baysal, 1982). The Fourier method has periodic properties. In
terms of wave propagation this means that a wave impinging on the left boundary
of the grid will return from the right boundary (the numerical artifact called
wraparound).

The Chebyshev method is mainly used in the velocity-stress formulation to
model free surface, rigid and nonreflecting boundary conditions at the boundaries
of the mesh. Chebyshev transforms are generally computed with the FFT, with
a length twice of that used by the Fourier method (Gottlieb and Orszag, 1977).
Since the sampling points are very dense at the edges of the mesh, the Chebyshev
method requires 1-D stretching transformation to avoid very small time steps.
Because the grid cells are rectangular, mapping transformations are also used
for modeling curved interfaces to obtain an optimal distribution of grid points
(Fornberg, 1988; Carcione, 1994) and model surface tomography (Tessmer and
Kosloff, 1994).

The Fourier and Chebyshev methods are accurate up to the maximum wavenum-
ber of the mesh that corresponds to a spatial wavelength of two grid points (at
maximum grid spacing for the Chebyshev operator). This fact makes these meth-
ods very efficient in terms of computer storage (mainly in 3-D space).

2.6.4   Absorbing Boundary Conditions

Previous studies have shown that reduction of both amplitude and time derivative of a physical quantity in a boundary layer effectively attenuates the physical quantity in consecutive computations, leaving no reflected and transmitted disturbances (Cerjan et al., 1985). The process for modifying the physical quantity u is

$$u^{(new)} \quad = \quad \gamma u^{(old)} \tag{2.9}$$

where $\gamma = \gamma(x)$ or $\gamma = \gamma(z)$, is the reduction function that departs from zero only in a restricted boundary layer on the grid perimeter as shown in Figure 2.2. The coordinates x and z are measured from the edge of the computational grid. As we mentioned before PS methods intrinsically treat all physical quantities as spatially periodic and, as a result, all energy transmitted and reflected through the boundary will travel (wrap) back into the grid. This symmetry consideration requires that γ should be symmetrical with respect to its central line (at grid boundary), since it should perform identically for waves incident from either side. The ideal reduction function will be as smooth as possible with values large enough to eliminate transmission and derivatives small enough to reduce reflections, and with a boundary layer as thin as possible. The reduction function

we use in the 128×128 computational grid for the modelling is :

For the left and top boundaries

$$\gamma(x) = exp\left\{-\left[0.025\left(L_i - x\right)\right]^2\right\},$$

$$\gamma(z) = exp\left\{-\left[0.025\left(L_i - z\right)\right]^2\right\}, (2.10)$$

where i=1, 2

For the right and bottom boundaries

$$\gamma(x) = exp\left\{-\left[0.025\left(x - L_j\right)\right]^2\right\}$$

$$\gamma(z) = exp\left\{-\left[0.025\left(z - L_j\right)\right]^2\right\} (2.11)$$

where j=3, 4

For the left and top boundaries we use $L_1 = L_2 = 16$, and for the right and
bottom boundaries $L_3 = L_4 = 111$.

2.6.5   Implementation of fractures

Liu et al. (2000) examined the published fracture models and classified them
into three broad groups, which are schematically shown in Figure 2.3. Model
(a) portrays a plane distribution of small cracks and model (b) portrays a plane
distribution of contacts. Both models can be replaced with an equivalent fracture
of constant aperture with appropriate material infill as demonstrated by Hudson
and Liu (1999) in model (c).

To obtain the effective parameters of fractured media, fractures are treated as
infinitely thin highly compliant interfaces inside a solid rockmass. Following the
concept of the linear slip deformation or displacement discontinuity model of
(Schoenberg, 1980), a fracture can be represented as a boundary across which
the displacements are discontinuous whereas the stresses remain continuous. To
first order the displacement discontinuity and the tractions are linearly related,

that is,

$$[u] = Z\tau, \tag{2.12}$$

where $[u]$ is the average displacement discontinuity, τ is the traction acting across the fracture, and Z is called the fracture compliance tensor, which is an elastic parameter of the medium. This linear relationship is consistent with the usual seismic approximation of infinitesimal strain. In addition, there has been some experimental verification of the DDM model by Pyrak-Nolte et al. (1990) and Hsu and Schoenberg (1993). Essentially Equation (2.12) is a boundary condition of the fracture surfaces. In a finite difference algorithm, the relationship can be implemented by requiring a displacement jump across grid points on either side of the interface, proportional to the local (continuous) stress traction. The implementation of the displacement jump is relatively simple, even with Z being a function of position on the fault plane, providing the interface lies along a given plane of the finite difference grid. In nature, fractures have finite length. To implement a finite fracture we take $Z = 0$ at locations on the plane exterior to the fracture. The question that remains is how to implement the constraint that

(a) Plane distribution of small cracks
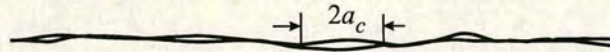
(b) Plane distribution of contacts
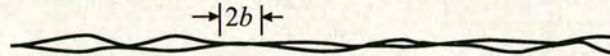
(c) Thin layer of weak material infills
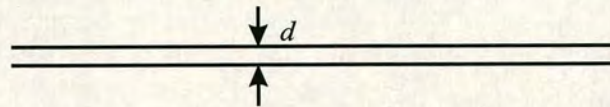
Figure 2.3: Schematic illustration of three fracture models. (a) A plane distribution of small cracks; (b) a plane distribution of contacts, and (c) a thin layer of weak solid material with a constant aperture (Liu et al., 2000)

$Z \to 0$ on the tips of the fracture. We taper off the value of Z following the
formulation of the crack opening displacement introduced by Kashanov (1984).
The value of Z has its maximum value in the centre of the fracture and reduces
to 0 at both fracture tips following a hyperbolic pattern. The rate at which the
value of compliance reduces depends strongly on the length of the fracture.

In the pseudospectral method, the medium is discretised into small rectangular
grids and we find the elastic parameters of the equivalent medium for each grid
cell. For each grid intersected by a fracture (or portion of fracture), the elastic
medium within the cell surrounding the fracture, together with the embedded
segment of the fracture, are replaced by an equivalent anisotropic medium. Muir
et al. (1992) showed how the elastic parameters could be found for a cell enclosing
an interface between two elastic media.

The discretisation of the fracture in the finite difference grids is shown schemati-
cally in Figure 2.4. This method was first used by Coates and Schoenberg (1995).
In Figure 2.4(a) we show the whole fractured medium. Then we take a very small
area of the medium in Figure 2.4(b), to show how the fractures are represented
in the finite difference grid. Figure 2.4(c) shows the discretisation of the fractures
in the grid, where the shaded areas are the finite difference grid cells intersected
by one or more fractures, whilst the plain areas are the cells which include only
the background rock. Finally, in Figure 2.4(d) we show the whole medium again,
but this time each cell is either shaded or plain, depending on whether fractures
are present. By comparing Figure 2.4(d) with Figure 2.4(a), where we have the
medium with the actual fractures, we can see that the discretisation of the frac-
tures is very accurate. The grid cell size is very important for the discretisation
of the fractures. To achieve high accuracy, we choose grid sizes smaller or equal
to the size of the smallest fractures. Thus any size of fracture can be represented
accurately by the elastic parameters of the effective medium in each finite dif-
ference grid cell. The variables required for the effective medium calculation in

each cell are the length of the fracture, its orientation, and the local value of the
fracture compliance tensor. In the numerical models that will be presented later,
fractures are represented as finite lines of which we know the starting and the
ending points. Using simple algebra we can define the equation of any line that
passes between two points. Knowing the equation that describes each fracture,
we can locate the intersections of the fractures with the horizontal and vertical ·
boundaries of each cell (if any) and calculate the length and orientation of the
fracture segment lying in each cell. The effective medium for each cell may then
be calculated using these values and the method for estimating the fracture com-
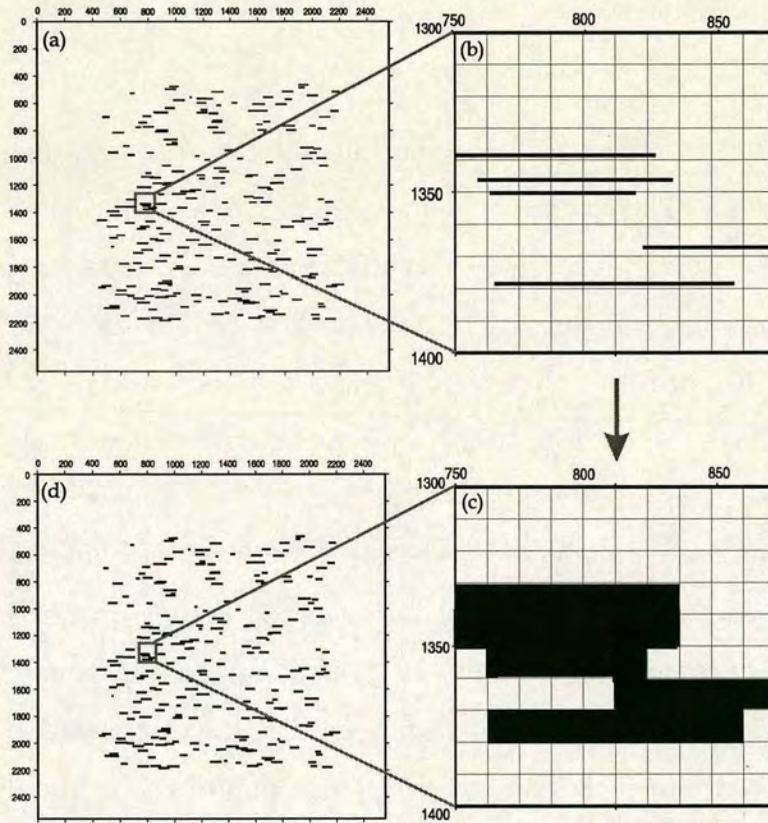
Figure 2.4: Schematic illustration of fracture discretisation in the finite difference
grid. In (a) we show the fractured medium that we want to examine. In
(b) we present a very small area of the whole model, and (c) shows the
same area discretised in the FD grid. Finally, (d) shows again the whole
medium where, this time, the fractures are discretised. By comparing
figures (a) and (d), we can see the high accuracy of the discretisation.

pliance tensor outlined in the following section. The tapering of the value of the
fracture compliance Z is explained in detail in Appendix A.

2.6.6   Comparison of 2D and 3D simulation

In the following chapters we concentrate on 2D numerical modelling for the ex-
amination of fracture parameters and their effect on seismic waves. However, in
real earth both the geological structures as well as the sources of the waves are
3D. In this section we discuss the differences in the waveforms due to this. To
do so, we examine the amplitude of the waves at a distance from the source, and
compare the two cases. Let's take first the case of a point source in an infinite
homogeneous medium, which is the case in 3D. Let's imagine two wave fronts,
which make two spherical shells whose centres are the coincided location of the
source. The radius to the outer shell is r_2, which is greater than that of the radius
of the inner shwll r_1. Thus, the surface areas of the outer and inner shells are $4\pi r_2^2$
and $4\pi r_1^2$, respectively. By energy conservation, the total energy flowing through
the outer shell and the inner shell at a given time should be kept the same so
that we have $E_2 = E_1$, where E is the energy. From that we have $I_2 S_2 = I_1 S_1$,
$I_2 4\pi r_2^2 = I_1 4\pi r_1^2$ and $I_2 = (r_1/r_2)^2 I_1$, where I is the energy intensity. If we
substitute energy intensity by its equivalent we have $\frac{1}{2}\rho\omega^2 u_2^2 = (r_1/r_2)^2 \frac{1}{2}\rho\omega^2 u_1^2$,
which leads to $u_2 = (r_1/r_2)u_1$, where ρ is the density, ω the frequency, and u
is the amplitude. To generalise this relation with the inner shell becoming a
constant reference shell closer to the source and the outer shell a generic one we
have $u = (r_o/r)u_o$. This states that the amplitude is decaying against $1/r$ for the
waves generated by a point source. Since the shape of the wavefront is spherical,
this is generally referred as the geometric spreading for spherical waves.

For an infinitely long line source, that is the case in 2D, the shape of the wave-
front is cylinder, and that is called the cylindrical wave. Following once more en-

ergy conservation we have $E_2 = E_1$. From that we have $I_2 S_2 = I_1 S_1$, $I_2 4\pi r_2 L =$
$I_1 4\pi r_1 L$ and $I_2 = (r_1/r_2)I_1$, where L is the length of the cylinder axis. If we sub-
stitute energy intensity by its equivalent we have $\frac{1}{2}\rho\omega^2 u_2^2 = (r_1/r_2)\frac{1}{2}\rho\omega^2 u_1^2$, which
leads to $u_2 = \sqrt{r_1/r_2}u_1$. To generalise this relation with the inner shell becom-
ing a constant reference shell closer to the source and the outer shell a generic
one we have $u = \sqrt{r_o/r}u_o$. This state that the amplitude is decaying against
$1/\sqrt{r}$ for waves generated by a line source. Since the shape of the wavefront
is cylindrical this is generally referred as the geometric spreading for cylindrical
waves. It is clear from the above discussion that when we use 2D numerical mod-
elling, we have some incosistency in the amplitude of the wave due to geometrical
spreading. In addition to that, there is the issue of the structures being three
dimensional.In 2D modelling information on connectivity is lost resulting in a
higher fraction of isolated and dead end pores, thus leading to lower connectivity
values (Carmeliet et al., 2004). Also the flow mechanism has a 3D character,
which cannot be represented accurately by a 2D model Finally, 2D modelling as-
sumes a constant height, predicting width and length. Since experience indicates
height growth occurs in many reservoirs, this is a limitation of 2D modelling that
leads to overly optimistic fracture lengths and poor transport predictions. 3D
modelling can be more accurate, but more input data is needed. It matches both
pressure behaviour and fracture geometry.

2.6.7 Effective compliance of a fractured medium

Effective medium calculus is used to calculate the elastic parameters that are
associated with a given cell through which a fracture passes. In the simple case
of an unfractured cell, where the cell is occupied only by the background rock,
the calculation of the compliance tensor is straightforward. Assuming that we
know the elastic parameters of the host rock, we calculate the compliance tensor

s^0_{ijkl} as follows :

$$\mu = \rho V_s^2, \tag{2.13}$$

$$\lambda = \rho \left(V_P^2 - 2V_S^2 \right), \tag{2.14}$$

$$(s^0_{ijkl})^{-1} = c_{ijkl} = \begin{bmatrix} \lambda + 2\mu & \lambda & \lambda & 0 & 0 & 0 \\ \lambda & \lambda + 2\mu & \lambda & 0 & 0 & 0 \\ \lambda & \lambda & \lambda + 2\mu & 0 & 0 & 0 \\ 0 & 0 & 0 & \mu & 0 & 0 \\ 0 & 0 & 0 & 0 & \mu & 0 \\ 0 & 0 & 0 & 0 & 0 & \mu \end{bmatrix}, \tag{2.15}$$

where V_P and V_S are the P-wave and S-wave velocities in the medium, respectively, c_{ijkl} is the 6×6 matrix form of the stiffness tensor for the unfractured medium, and λ, μ are the Lamé constants.

That way the only unknown elastic parameters are the ones from the cells that are intersected by the fracture. According to Coates and Schoenberg (1995) equivalent medium calculus is used to calculate the elastic parameters that are associated with a given cell through which the fracture passes. From knowledge of the equivalent medium in each cell, we define the appropriate elastic parameters at each point of the finite-difference grid. Muir et al. (1992) showed how the elastic parameters could be found for a cell enclosing an interface between two elastic media. The idea was to use the equivalent layered medium for the cell, where the layers were assumed parallel to the interface and the relative amounts of each constituent are propotional to the amount of that constituent within the cell.

In the presence of fractures the average strain ϵ in an elastic homogeneous solid with volume V containing N_f fractures with surfaces S_r (r = 1,2,$\cdots$, N_f) can be written as

$$\epsilon_{ij} = \left(s^0_{ijkl} + s^f_{ijkl} \right) \sigma_{kl}, \tag{2.16}$$

where σ is the average stress tensor, s_{ijkl}^0 is the matrix compliance tensor in the absence of the fractures, and s_{ijkl}^f is the extra compliance tensor resulting from the fractures. The additional strain is given by (Hill, 1963; Hudson and Knopoff, 1989),

$$s_{ijkl}^f \sigma_{kl} = \frac{1}{2V} \sum_{r=1}^{N_f} \int_{S_r} \left([u_i] \, n_j + [u_j] \, n_i \right) dS, \qquad (2.17)$$

where u_i is the ith component of the displacement discontinuity on S_r and n_i is the ith component of the fracture normal. If all fractures are aligned with fixed normal n, we may replace each fracture in V by an average fracture having a surface area S and a smoothed linear slip boundary condition given by

$$[\overline{u_i}] = Z_{ip}\tau_p, \qquad (2.18)$$

where τ_p is the traction on the fracture, $[\overline{u_i}]$ is the average displacement discontinuity on the fracture, and the quantities $\{Z_{ip}\}$ depend on the interior conditions and infill of the fracture (Schoenberg and Sayers, 1995; Sayers and Kachanov, 1995). The traction τ_p is linearly related to the imposed mean stress σ or, more precisely, to the traction $\sigma_{pq}n_q$ which would exist on the crack face if the displacements were constrained to be zero.

Liu et al. (2000) used a model of a simple fracture in an unbounded medium and proposed that the traction can be written as

$$\tau_p = \sigma_{pq}n_q, \qquad (2.19)$$

Equation (2.18) becomes

$$[\overline{u_i}] = Z_{ip}\sigma_{pq}n_q. \qquad (2.20)$$

Inserting (2.20) into (2.17) and after some tensor algebra, we get,

$$s_{ijkl}^f \sigma_{kl} = \frac{N_f S}{4V} \left(Z_{ik}n_l n_j + Z_{jk}n_l n_i + Z_{il}n_k n_j + Z_{jl}n_k n_i \right) \sigma_{kl}, \qquad (2.21)$$

where S is the mean area of fracture; so the fracture induced excess compliance s_{ijkl}^f is

$$s_{ijkl}^f = \frac{D_f}{4} \left(Z_{ik}n_l n_j + Z_{jk}n_l n_i + Z_{il}n_k n_j + Z_{jl}n_k n_i \right), \qquad (2.22)$$

where D_f is

$$D_f = \frac{N_f S}{V}. \tag{2.23}$$

If the fracture set is statistically invariant under rotations about n, only two terms in Z are required (Schoenberg and Sayers, 1995); a normal fracture compliance Z_N and a tangential compliance Z_T. Thus

$$Z_{ij} = Z_N n_i n_j + Z_T \left(\delta_{ij} - n_i n_j\right) = Z_T \delta_{ij} + \left(Z_N - Z_T\right) n_i n_j, \tag{2.24}$$

where δ_{ij} is the Kroneker delta. By inserting (2.24) into (2.22), we have

$$s^f_{ijkl} = \frac{D_f}{4} \left[Z_T \left(\delta_{ik} n_l n_j + \delta_{jk} n_l n_i + \delta_{il} n_k n_j + \delta_{jl} n_k n_i\right) + 4 \left(Z_N - Z_T\right) n_i n_j n_k n_l\right]. \tag{2.25}$$

Following Coates and Schoenberg (1995), in the case of 2-D media in a grid cell intersected by a fracture, equation (2.23) becomes

$$D_f = \frac{N_f \Delta l}{\Delta A}, \tag{2.26}$$

where Δl is the length of the segment of the fracture lying within the cell, and ΔA is the area of the 2-D cell. If L is defined for each cell intersected by a fracture so that,

$$\frac{1}{L} \equiv \frac{\Delta l}{\Delta A}, \tag{2.27}$$

then equation (2.25) finally becomes :

$$s^f_{ijkl} = \frac{N_f}{4L} \left[Z_T \left(\delta_{ik} n_l n_j + \delta_{jk} n_l n_i + \delta_{il} n_k n_j + \delta_{jl} n_k n_i\right) + 4 \left(Z_N - Z_T\right) n_i n_j n_k n_l\right], \tag{2.28}$$

which is the equation we use for the calculation of the excess compliance tensor. So the induced excess compliance tensor of a cell depends on the normal Z_N and the tangential Z_T fracture compliance, the number N_f of the fractures inside the cell, the length Δl of each fracture (or segment of fracture), and the orientation of each fracture estimated by the normals n. The total compliance tensor for the fractured cells is the effective compliance tensor s^{eff}_{ijkl}, which characterises the cell and is

$$s^{eff}_{ij} = s^0_{ijkl} + s^f_{ijkl}. \tag{2.29}$$

If we want to determine the stiffness c_{ijkl}, we transform the s_{ijkl} to the conventional (two-subscript) condensed 6×6 matrix notation, $11 \rightarrow 1$, $22 \rightarrow 2$, $33 \rightarrow 3$, $23 \rightarrow 4$, $13 \rightarrow 5$, $12 \rightarrow 6$, with factors 2 and 4 introduced as follows : $s_{ijkl} \rightarrow s_{pq}$ when both of p, q are 1, 2, or 3; $2s_{ijkl} \rightarrow s_{pq}$ when one of p, q is 4, 5, or 6; and $4s_{ijkl} \rightarrow s_{pq}$ when p, q are any of 1, 2, 3, 4, 5, or 6. The inverse of the compliance matrix s_{pq} gives the effective elastic constants or stiffness matrix c_{pq}. Using the same transformation as for the compliance, we transform the stiffness from the condensed (two-subscript) to the normal notation ($c_{pq} \rightarrow c_{ijkl}$).

To summarise the general course of action we follow to represent a fracture medium using the equivalent medium theory is the following. Firstly, we calculate the elastic parameters (elastic stiffness or compliance) for the cells of the medium that are not intersected by the fracture. Secondly, to calculate the stiffness tensor for the fractured cells we take into account the effect of the existence of the fracture. So, we invert the c_{ijkl} stiffness tensor of the background medium to find the respective compliance matrix s_{ijkl}^{b}, where the subscript b denotes the background compliance. Thirdly, we add to this the excess compliance s_{ijkl}^{f} of the fractured rock occupying the same cell, where the subscript f denotes the excess compliance of the cell as a result of the existence of the fracture surface. Finally, if we want to get the stiffness tensor of the fractured cells we invert the compliances. It is very important that all compliances and stiffnesses refer to the fracture coordinate system.

2.7 Summary

In this chapter, we described the method used to model wave propagation in a fractured medium, and also the implementation of fractures in the finite difference grid. To solve the wave equation in an elastic medium, there are analytical

methods and numerical methods. Analytical methods are available only for the
short and long wavelength cases. On the contrary numerical methods do not have
significant limitations. Numerical methods are classified into direct methods, in-
tegral equation methods and ray tracing methods. Direct methods approximate
the geological model by a numerical mesh, integral-equation methods are based on
integral representations of the wavefield, while in ray-tracing methods the wave-
field is considered as an ensemble of certain events. We compared the methods
and concluded that for the case of complicated fractured medium direct methods
are most suitable for the modelling. We chose to use the pseudospectral method
among the direct methods, because it gives the most accurate results especially
in complicated cases. In order to simulate waves in an unbounded medium in
a computational domain, we need to use boundary conditions. We presented a
review of the two basic boundary conditions, the absorbing boundary condition
and the absorbing layers. In this thesis, for the modelling of wave propagation in
a fractured medium we used the pseudospectral method. The wave equation for
an inhomogeneous medium is solved by an approximation that uses the derivative
property of the Fourier transform. We gave a detailed description of the calcula-
tion of spatial derivatives by the pseudospectral method. We used an absorbing
boundary condition in order to deal with reflected and transmitted disturbances.
The fractures were implemented using an effective medium formula. We used
the linear slip deformation or displacement discontinuity model. According to
that model a fracture is represented as a boundary across which the displace-
ments are discontinuous, whereas the stresses remain continuous. We discretised
the medium into small finite difference grids and applied the effective medium
in each grid cell. The effective medium is described by the stiffness tensor or
its inverse, the compliance tensor. For the unfractured grid cell the calculation
of the tensor is straightforward, directly from the elastic parameters of the host
rock. For the fractured grid cells, for the calculation of the tensor we take into
account the host rock tensor and an excess tensor due to the fractures. The excess

compliance tensor depends on the normal and the tangential fracture compliance, the number of fractures inside the grid cell, the length of each fracture segment inside the grid cell, and the orientation of each fracture segment estimated by the normals on the fracture. We concluded by giving a detailed description of the calculation of the effective medium for each grid cell.

CHAPTER 3

Accuracy of fracture modelling using the pseudospectral (PS) method

3.1 Introduction

Modelling synthetic seismograms may have different purposes - for instance, to design a seismic experiment (Ozdenvar et al., 1996), to provide for structural interpretation (Fagin, 1992) or to perform a sensitivity analysis related to the detectability of a petrophysical variable, such as porosity, fluid type, fluid saturation, etc. Modelling algorithms can also be part of inversion and migration algorithms. In Chapter 2, we introduced a technique for modelling wave propagation through a complicated fractured medium. The wave equation is solved using the pseudospectral method and the fractures are implemented in the finite difference grid using an equivalent medium theory. Although there are available analytical methods for complicated earth structures such as fractured reservoirs, which are the cases I will examine, analytical methods are intractable. Only fully numerical methods are capable of accounting for the whole wavefield. However, the precision of the numerical methods is restricted by the numerical model and numerical dispersion. The PS method that is used for the modelling, has no

49

spatial truncation errors for Fourier components of the grid, so truncation errors depend only on the chosen time integration. This is a significant improvement over other methods (Gazdag, 1981). Even though PS methods require more computation per grid element than finite difference (FD) methods, the increase in accuracy more than compensates for this because the number of grid points per wavelength can be reduced radically (Wu and Lees, 1997). It has been shown that the PS approximation is the limit of a finite-difference approximation of increasing (to infinite) orders of periodic functions (Fornberg, 1987).

In this chapter we examine the issue of accuracy of the solution of the wave equation by the pseudospectral method, and the modelling of wave propagation based on that. We discuss two important sources of error, the truncation error and the aliasing effect. We also consider the limitations of the PS technique. We examine the constraints in grid spacing related to signal frequency and related to the size of the fractures. Those limitations are very important for the accuracy of the modelling and they are necessary to have clearly distinguished wavelets.

3.2   Accuracy of PS method

Depending upon the method employed, the grid size must be considerably smaller than the half-wavelength of the shortest wave component for reliable computations. This is a consequence of truncation errors, which are particularly large for the shortest waves due to approximation of the continuum space derivative terms by finite-difference expressions. These errors can be minimised by computing the space derivatives with high accuracy for all wavelengths. A condition for accuracy is that the data be band-pass limited by the highest (Nyquist) spatial frequencies that can be represented on the computational grid. The Nyquist frequency ν_N is half the sampling frequency of the signal. Any frequency present in the signal that is greater than the Nyquist frequency by the amount $\Delta\nu$ will be indistin-

guishable from the lower frequency $\nu_N - \Delta\nu$. Thus we have alias signals that fall within the frequency band in which we are primarily interested and appear to be legitimate signals. To avoid this, filters are used before sampling to remove frequency components higher than the Nyquist frequency. This must be done before sampling because afterwards the alias signals cannot be recognised.

The truncation error is a result of the Taylor series type of derivation, where the error comes from the truncation of the series. The form of the error is written in terms of some high-order derivatives. Using a model of uniform velocity Gazdag (1981) established criteria for stability and estimated the truncation errors. He found that there is no interaction between Fourier modes, and thus each Fourier component maintains its identity; only its phase angle changes with increasing time.

Let us consider the two-dimensional acoustic wave equation for a plane

$$\frac{\partial^2 p}{\partial t^2} = \nu^2 \left(\frac{\partial^2 p}{\partial x^2} + \frac{\partial^2 p}{\partial z^2} \right). \tag{3.1}$$

where $p(x, z, t)$ is the amplitude of the wave field, representing displacement or pressure, t is time, x and z are horizontal and vertical distances, and ν is the velocity, respectively. For homogeneous media ($\nu = $ constant), the solution of equation (3.1) can be expressed by finite Fourier series, providing the data specifying the initial conditions are band-pass limited and periodic with respect to x and z. Let these conditions be set by the wave field p and its rate of change $\partial p / \partial t$ at $t = 0$. The solution to the equation (3.1) may be written

$$p(x, z, t) = \sum_{k_x} \sum_{k_z} P(k_x, k_z, t = 0) exp[i(k_x x + k_z z + \omega t)], \tag{3.2}$$

where $P(k_x, k_z, t = 0)$ is the finite Fourier transform of the wave field at $t = 0$. Equation (3.2) does not account for evanescent modes. The dispersion relation

$$\omega = \pm\nu(k_x^2 + k_z^2)^{1/2} \tag{3.3}$$

governs the independence between the wavenumbers of spatial frequencies k_x and k_z and the frequency ω. The positive and negative values of ω in equation (3.3) correspond to waves traveling in opposite spatial directions.

From the wave field given at times t and $t - \Delta t$, the value at time $t + \Delta t$ is approximated by the expression

$$p(t + \Delta t) \cong 2p(t) - p(t - \Delta t) + \nu^2 \left(\frac{\partial^2 p(t)}{\partial x^2} + \frac{\partial^2 p(t)}{\partial z^2}\right)\Delta t^2. \qquad (3.4)$$

To simplify the notation, the independent variables x and z within the bracket $p(t)$ etc. are implicit. The space derivative terms in equation (3.4) are computed from differentiation (3.2):

$$\frac{\partial^2 p}{\partial x^2} + \frac{\partial^2 p}{\partial z^2} = \sum_{k_x}\sum_{k_z} -(k_x^2 + k_z^2)P(k_x, k_z, t)\cdot exp[i(k_x x + k_z z)] = -(k_x^2 + k_z^2)p(x, z, t). \qquad (3.5)$$

To examine the numerical stability and accuracy, equation (3.4) can be shown in a matrix form:

$$\begin{bmatrix} p^{n+1} \\ p^n \end{bmatrix} = \begin{bmatrix} (2 - \nu^2(k_x^2 + k_z^2)\Delta t^2) & -1 \\ 1 & 0 \end{bmatrix} \begin{bmatrix} p^n \\ p^{n-1} \end{bmatrix}, \qquad (3.6)$$

where $p^{n+1} = p(t)$ and $p^n = p(t - \Delta t)$. The necessary conditions for stability require that the eigenvalues of the matrix in equation (3.6) are less than or equal to 1.0 in magnitude (Boore, 1972; Smith, 1985). The phase change θ of a Fourier coefficient within Δt time is given by

$$\theta = \nu[k_x^2 + k_z^2]^{1/2}\Delta t. \qquad (3.7)$$

Gazdag (1981) concludes that the solution is stable for all waves when

$$[(1/\Delta x)^2 + (1/\Delta z)^2]^{1/2}\nu\Delta t \leq 1/\pi, \qquad (3.8)$$

and when $\Delta z = \Delta x$ this becomes

$$\nu\Delta t/\Delta x \leq \sqrt{2}/\pi. \qquad (3.9)$$

The differencing error in equation (3.4) is given by

$$\varepsilon(\Delta t) = -2 \sum_{l=4}^{\infty} \frac{\partial^l p(t)}{\partial t^l} \frac{(\Delta t)^l}{l!}; l = 4, 6, 8, ... \qquad (3.10)$$

For most practical purposes the lowest order estimate of the numerical error ε introduced by the discretisation is adequate,

$$\varepsilon(\Delta t) = -\frac{\partial^4 p(t)}{\partial t^4} \frac{(\Delta t)^4}{12}. \qquad (3.11)$$

Another parameter that is examined when we deal with numerical computation is the aliasing effect. Only a finite set of spatial frequencies can be represented on a computational grid without ambiguity. When frequency is higher than the cut-off (Nyquist) frequency of the grid, Fourier coefficients loose their identity when sampled at grid points. It is customary to refer to this effect as aliasing. The numerical solution of the wave equation in inhomogeneous media can lead to aliasing errors, which can also be regarded as truncation errors in the (k_x, k_z) domain, even if the wave initially contains no spatial frequencies greater than the Nyquist frequencies. The reason is that multiplication with the velocity function gives rise to some broadening of the spatial frequency content of the wave during certain time intervals. This is particularly true when the wave encounters regions of strong velocity variations. When the aliasing errors are great, the wave shape deteriorates. The pulse shape is very well preserved in a constant velocity region. However, the reflected and transmitted wave shapes are somewhat distorted, depending upon the pulse width in comparison to the grid size. Wider pulses, having narrower frequency bands, suffer fewer aliasing errors than do shorter pulses. Therefore, the magnitude of aliasing errors depends upon the relationship between the frequency spectrum of the true solution and the highest frequency which can be supported by the computational grid. A qualitative conclusion from Gazdag (1981) is that the pulse width should exceed the grid size by a factor between 2 and 4. This is reasonable, and intuitively obvious, if we consider that the velocity change defined over the grid is limited by the grid size

Δx. We are not dealing with ideal reflecting surfaces, but with models having a smooth velocity function between any two sets of grid points. This suggests that the reflecting surface has a thickness of at least Δx. The pulse width should, therefore, be considerably wider than the grid spacing itself. Generally, the effect of truncation in frequency domain is almost independent of the numerical method used. Therefore, aliasing effects are ignored when the accuracy of the method is considered.

3.3   Constraints in grid spacing related to signal frequency

When planning the modelling, we should follow certain steps to ensure the accuracy of the method. First, from the maximum source frequency and minimum velocity, we find the constraints on the grid spacing (Carcione et al., 2002), namely,

$$dx \leq \frac{\nu_{min}}{2f_{max}}. \tag{3.12}$$

The equal sign implies the maximum allowed spacing to avoid aliasing; that is, two points per wavelength. The actual grid spacing depends on the particular scheme. We examine four different cases of grid sizes, which vary from the ones that are smaller than the wavelength to the ones that are greater than the wavelength. In all four cases the source, receivers and the fractures are situated in an ideal elastic ($V_P = 3300\ ms^{-1}$, $V_S = 1800\ ms^{-1}$, $\rho = 2200\ kgm^{-3}$) full space. The size of the fractures is constant in all the models and are 100 m long. The receiver array at which vertical and horizontal particle displacements are recorded is horizontal and 100 m above the shallower fracture. The source is located at the centre of the modelling area and 100 m above the receiver array. Figure 3.1 shows a schematic representation of the model used. The source type is a vertical force. The source signal is a Ricker wavelet (Ricker, 1977) with a varying peak

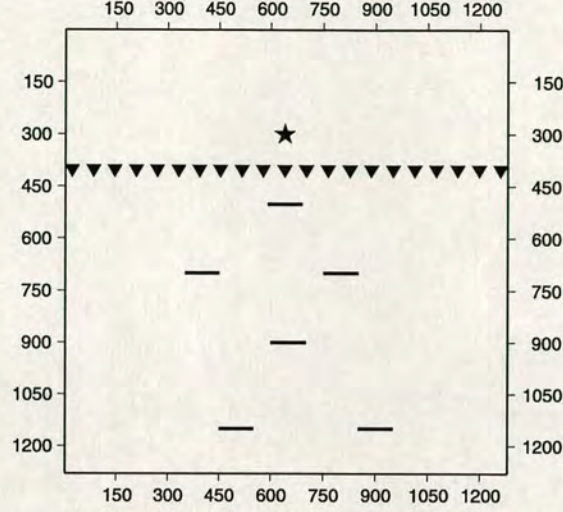frequency for each case and a pulse initial time of 0.1 sec.

Figure 3.1: Schematic representation of the model used for the examination of constrains in grid spacing related to signal frequency. The star indicates the source position, while the triangles indicate the receivers.

In the first case we have a source peak frequency $f = 33\ Hz(\lambda = 100\ m)$ and grid spacing 10 m that remains the same for all models. That means that the relationship between grid size and wavelength will be $\lambda = 10 \times (grid\ spacing)$, so that criterion (3.12) is easily satisfied. We calculate the ratios of equation (3.12) for the P-wave velocity and the S-wave velocity and we find 50 m and 28 m respectively, which are greater than the grid spacing $(dx = dz = 10\ m)$. Figure 3.2 shows the horizontal component of synthetic seismograms recorded at the receiver array. We present the part of the seismogram where the waves reflected from the fractures are shown. That is the reason why time starts from 0,30s in the vertical direction. The validity of equation (3.12) is confirmed by the very clear reflections from the fractures as well as a very clear signal.

In the second case we have a source peak frequency $f = 66\ Hz(\lambda = 50\ m)$. That means that the relationship between grid size and wavelength will be $\lambda = 5 \times (grid\ spacing)$. We calculate the ratio dx of (3.12) for the P-wave velocity and the S-wave velocity and we find $dx = \frac{V_{min}}{2f_{max}} = 25$ m and 14 m respectively, both greater than the grid spacing. Figure 3.3 shows the horizontal
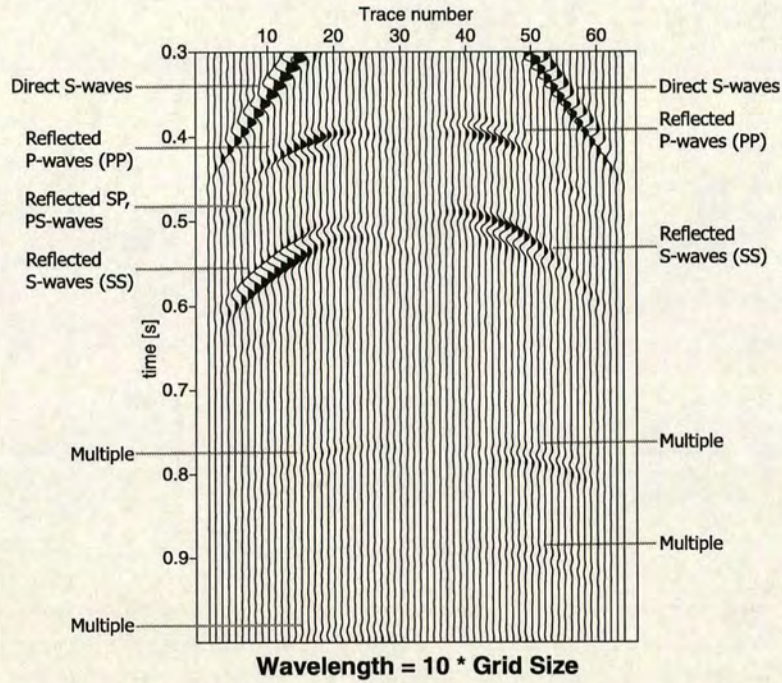
Figure 3.2: Reflected waves from the fractures. We use the same model to examine the limitations of the modelling related to the relationship between grid size and wavelength. The model used to examine the accuracy of the modelling related to the grid size and the wavelength, is the same in all the cases. In this case $\lambda = 10 \times (grid\ spacing)$.

component of synthetic seismograms recorded at the receiver array. In this case equation (3.12) is valid, and that is the reason why we have very clear reflections from the fractures. However, we can see the presence of some noise, compared to Figure 3.2.

In the third case we have a source peak frequency $f = 165\ Hz(\lambda = 20\ m)$. That means that the relationship between grid size and wavelength will be $\lambda = 2 \times (grid\ spacing)$, which is almost on the boundary of criterion (3.12). We calculate the ratio of equation (3.12) for the P-wave velocity and the S-wave velocity and we find 10 m and 5.45 m respectively, which are for the P-wave velocity equal and for the S-wave velocity less than the grid spacing. Figure 3.4 shows the horizontal component of synthetic seismograms recorded at the receiver array. In this case equation (3.12) is valid only for the P-wave. We can see the
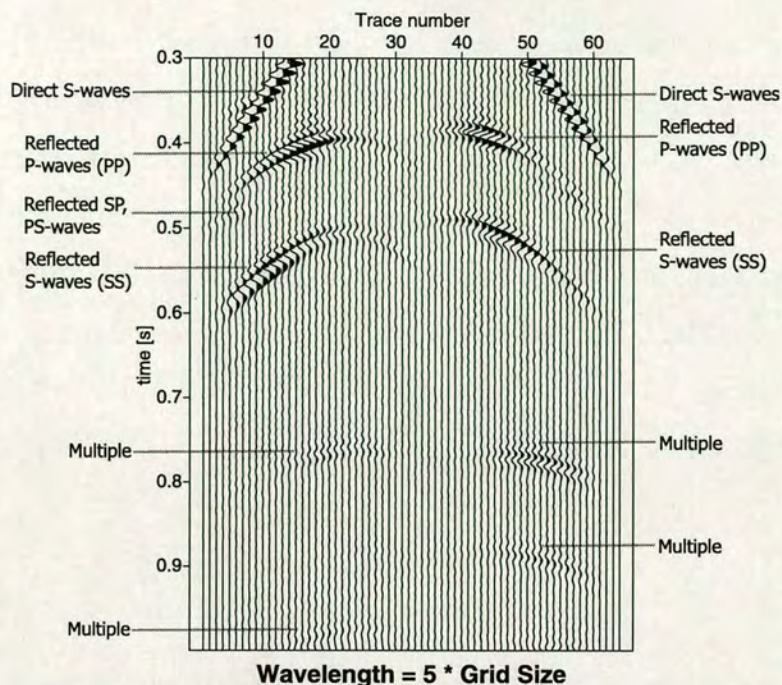
Figure 3.3: Reflected waves from the fractures. In this case $\lambda = 5 \times (grid\ spacing)$.

reflected waves clearly, but in this case the noise in the recording is considerably higher compared to the previous cases.

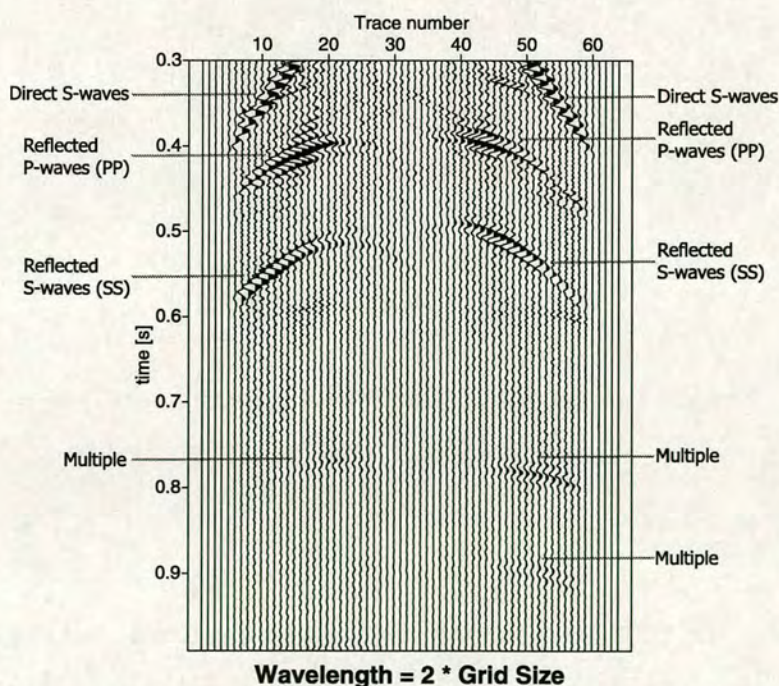**Figure 3.4:** Reflected waves from the fractures. In this case $\lambda = 2 \times (grid\ spacing)$.

Finally, we examine a case where we have a source peak frequency $f = 1650\ Hz(\lambda = 2\ m)$. That means that the relationship between grid size and wavelength will be $\lambda = \frac{1}{5} \times (grid\ spacing)$. We calculate the ratio of equation (3.12) for the P-wave velocity and the S-wave velocity and we find 1 m and 0.55 m respectively, which are for both waves much less than the grid spacing. Figure 3.5 shows the horizontal component of synthetic seismograms recorded at the receiver array. We can see that noise is very strong when criterion (3.12) is not satisfied for either wave.

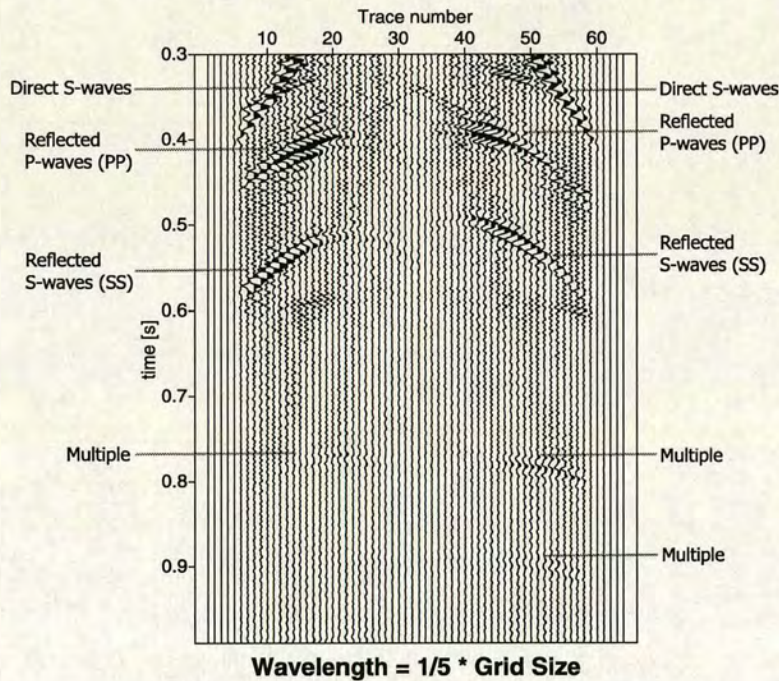**Figure 3.5:** Reflected waves from the fractures. In this case $\lambda = 1/5 \times (grid\ spacing)$.

In conclusion, the grid size should be at least smaller than 1/4 of the wavelength, for a reasonable result. If the wavelength is less than two times the grid size, then the results are not so good.

3.4   Constraints in grid spacing related to the size of the fractures

Another important factor for modelling is the grid spacing compared with the fracture size. We examine different cases in order to test the limit of the grid spacing for which we can model accurately the effect of each individual fracture on the wavefield. The fracture scale is not a function of grid size. We only examine different scales and grid sizes in order to find possible limitations in the modelling technique. In all four examined cases the source, receivers and the fractures are situated in an ideal elastic ($V_P = 3300 \ ms^{-1}$, $V_S = 1800 \ ms^{-1}$, $\rho = 2200 \ kgm^{-3}$) full space. The size of the fractures is constant in all the models and they are $10 \ m$ long. The receiver array at which vertical and horizontal particle displacements are recorded is horizontal and $10 \times (grid \ spacing)$ above the shallower fracture. The source is located at the centre of the modelling area and $10 \times (grid \ spacing)$ above the receiver array. The source type is a vertical force. The source signal is a Ricker wavelet (Ricker, 1977) with a peak frequency of 25 Hz for each case and a pulse initial time of 0.1 sec.

In the first case we use a grid spacing of 100 m ($dx = dz = 100 \ m$). That means that the relationship between grid size and fracture size will be ($grid \ spacing$) $= 10 \times (crack \ length)$. Figure 3.6 shows the horizontal component of synthetic seismograms recorded at the receiver array. We present the part of the seismogram where the reflected waves from the fractures are expected to be recorded. Due to the big size of the grid cell compared to the fracture size, we cannot see reflected waves from the fractures. That is because the cracks are very small compared to the grid size, so they do not affect significantly the compliance c_{ijkl} of the equivalent medium in the grid cell. The strong noise in the synthetics is a result of the small wavelength compared to the grid size. In this case the wavelength is less than two times the grid size, which is the constraint we found

in the previous section. In the following cases the constraint is met, so any noise present in the synthetics is solely a result of limitations in grid spacing.

Grid Size = 10 * Crack Size
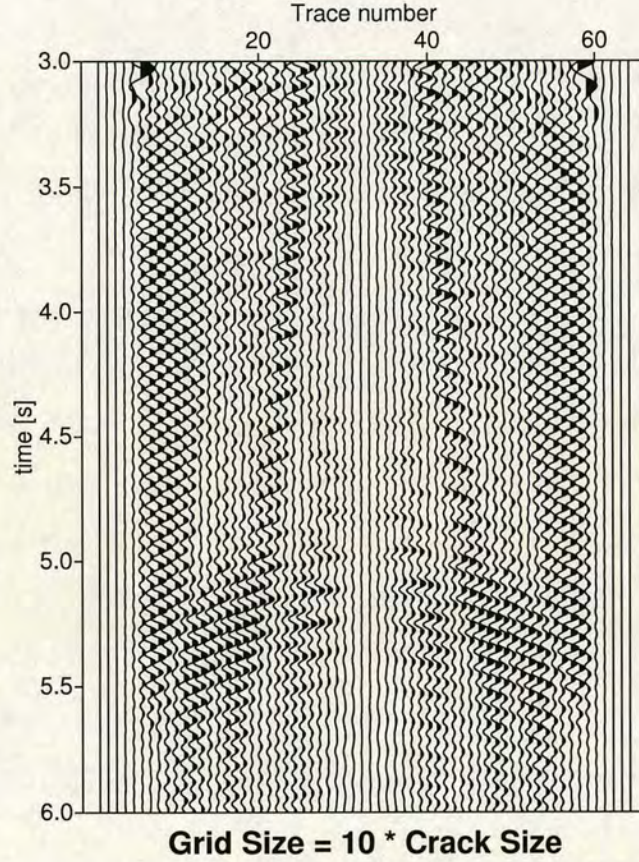
Figure 3.6:   Reflected waves from the fractures. We use the same model to examine the limitations of the modelling related to the relationship between grid size and fracture size. In this case $(grid\ spacing) = 10 \times (crack\ length)$.

In the second case we use grid spacing of 50 m $(dx = dz = 50\ m)$. That means that the relationship between grid size and fracture size will be $(grid\ spacing) = 5 \times (crack\ length)$. Figure 3.7 shows the horizontal component of synthetic seismograms recorded at the receiver array. The size of the grid cell is still big compared to the fracture size, but we can see some reflected waves from the fractures, although not very clear. The reason for that is the same as in the previous case.

Figure 3.7: Reflected waves from the fractures. In this case (*grid spacing*) = 5 × (*crack length*).

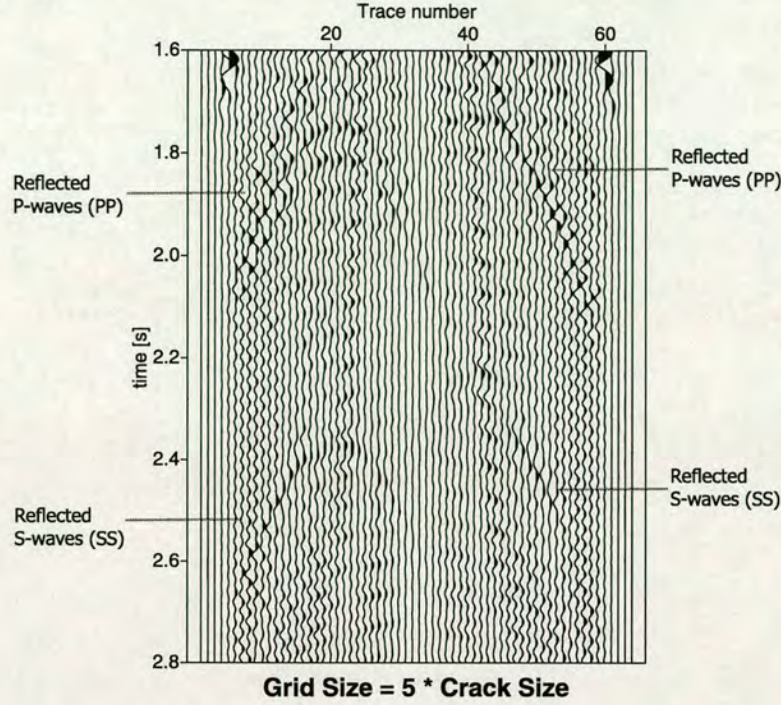In the next case we use grid spacing of 10 m ($dx = dz = 10\ m$). That means that the relationship between grid size and fracture size will be (*grid spacing*) = (*crack length*). Figure 3.8 shows the horizontal component of synthetic seismograms recorded at the receiver array. In this case we have reflections that are clearly outlined in the synthetics and are much more distinguishable compared to the previous cases. That indicates that in order to have clearly distinguishable reflections in the synthetics from seismic modelling, the grid size should have maximum size equal to the size of the fractures in the examined medium.

In the final case we use grid spacing of 1 m ($dx = dz = 1\ m$). That means that the relationship between grid size and fracture size will be (*grid spacing*) = $\frac{1}{10}$ × (*crack length*). Figure 3.9 shows the horizontal component of synthetic seismograms recorded at the receiver array. In this case we also have very distinct reflections. Besides that, the reflected waves have higher amplitude compared to the previous case, which makes reflections between different fractures easier to
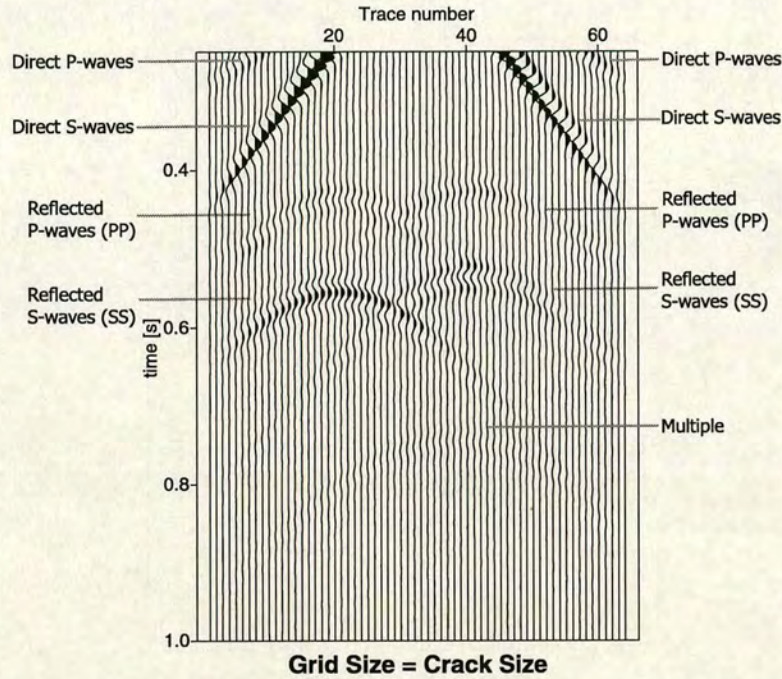
Figure 3.8: Reflected waves from the fractures. In this case (*grid spacing*) = (*crack length*).

distinguish. That happens because each fracture affects greatly the compliance of each grid cell, thus giving very strong reflections. In conclusion, we can say that in order to have reflected waves that are clearly distinguished in the synthetics generated by the seismic modelling, the grid size should have maximum size no bigger than the size of the fractures in the examined medium.

3.4.1   Resolution of the modeling

Resolution refers to the minimum separation between two features such that we can tell that there are two features rather than only one. With respect to seismic waves, we may think of (a) how far apart (in space or time) two interfaces must be to show as separate reflectors (vertical resolution) or (b) how far apart two features involving a single interface must be separated to show as separate features (horizontal resolution). Clearly, the ability to see and distinguish features
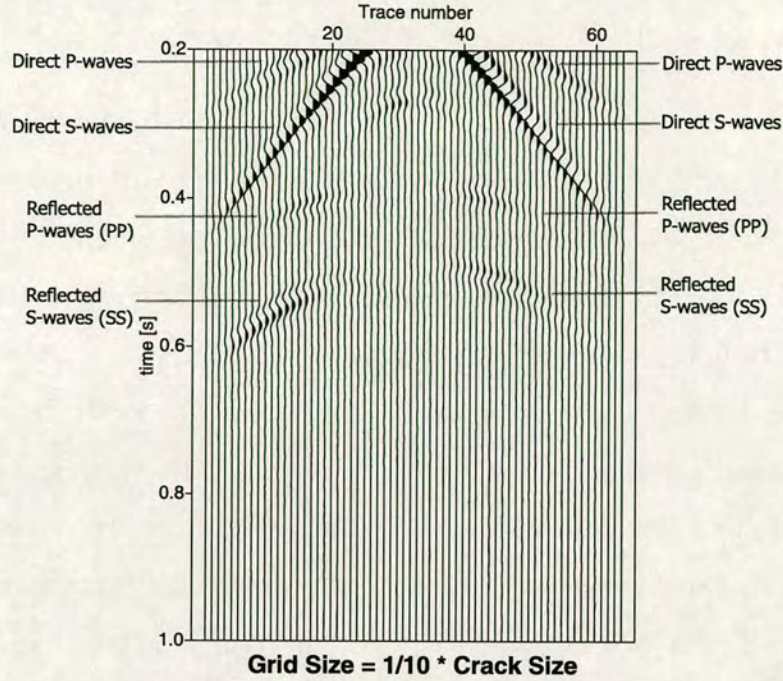
Figure 3.9: Reflected waves from the fractures. In this case $(grid\ spacing) = \frac{1}{10} \times$ $(crack\ length)$.

depends on the signal/noise ratio and the knowledge and experience of the interpreter. Where a correct model is used for interpretation, it is possible to exceed conventional resolution limits, that is, if we know a priori exactly what we are looking for in very good data, then subtle differences can be used to locate and identify it. If seismic wavelets were extremely sharp, resolution would not be a problem. However, real seismic wavelets involve a limited band of frequencies and hence have appreciable breadth.

3.4.1.1   Vertical resolution

Let us first consider resolution in the vertical direction. For two horizontal reflectors a distance Δz apart, the deeper reflection lags behind the shallower by the fraction $2\Delta z/\lambda$ of a wavelength. The limit on how close the two reflections can be, and remain separable is the essence of the problem of vertical resolution. We can tell there are two waves when the arrival of the second wave causes a

perceptible change in the appearance of the first wave.

Rayleigh (Jenkins and White, 1957) defined the reasonable (separable) limit as being when the two events are separated by a half-cycle so interference effects are minimized. For a boxcar frequency spectrum the wavelet shape is that of a sinc function. The Rayleigh criterion is equivalent to a width of approximate $2/3\nu_u$, where ν_u is the upper frequency limit of the boxcar. Thus we must record higher frequencies if we are to achieve higher resolution (Sheriff, 1977). The acceptable threshold for vertical resolution is generally a quarter of the dominant wavelength. This is subjective and depends on the noise level in the data. Sometimes in real dara the quarter-wavelength criterion is too generous, particularly when the reflection coefficient is small and no reflection event is attainable. Sometimes the criterion may be too stringent, particularly when events do exist and their amplitudes can be picked with ease.

We examine two general cases of fracture sizes to see if different sizes affect the resolution criterion. In the first case the fracture length is larger than the wavelength so the fracture acts as an interface, while in the second case the fracture size is smaller than the wavelength so it acts as a single scatterer. First, we examine the case when the fracture acts as an interface. The grid size of the model is 128 x 128 with grid spacing $dx = dz = 30\ m$. The source and receivers are situated in an ideal elastic full space ($V_P = 3300\ ms^{-1}, V_S = 1800\ ms^{-1}$, $\rho = 2200\ kgm^{-3}$). The receiver array at which vertical and horizontal particle displacements are recorded is horizontal and 1020 m above the fracture. The fractures are 1320 m long. The source is located at the centre of the receiver array. The source type is a vertical force. The source signal is a Ricker wavelet with a peak frequency of 25 Hz and a pulse initial time of 0.1 sec. In the medium we have two fractures, both 1320 m long. The wavelenghts are 132 m for P-wave and 72 m for S-wave, which are much smaller than the fracture length. The examination of the resolution we present here is based on the wavelength of the

P-wave. First we show the horizontal component in the case of a single fracture, in order to be able to compare the effect of the existence of the second fracture and the vertical resolution. Figure 3.10 shows clearly the reflected P- and S-waves from the fracture.

Interface - 1 Fracture
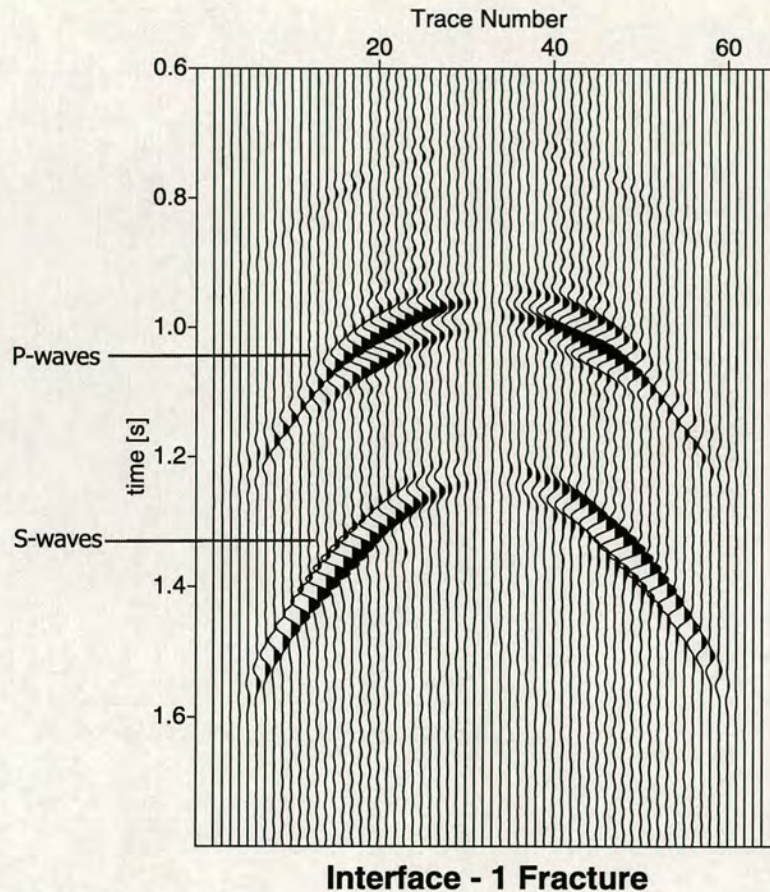
Figure 3.10: Reflected waves from a single fracture. In this case the fracture length is much greater compared to the wavelenght, and the fracture acts as an interface.

In Figure 3.11 we examine the case of two fractures of the same size as in the previous model. The vertical separation of the fractures is 1/4 of a wavelength. By comparison between Figures 3.11 and 3.10 we have on the P-wave arrivals a clear reflection immediately after the reflection from the first fracture. Also on the S-wave arrivals we have another reflection as in the P-waves, immediately after the reflections from the first fracture. Also on the S-waves, we have diffractions

that seem to be from the fracture tips at 1.4 s starting at trace number 24 until trace number 44. That is a feature that is also present in Figure 3.10, but the diffractions are stronger in Figure 3.11.

Interface - Ver. Sep.=Wavelength/4

Figure 3.11: Reflected waves from two fractures that act as an interface. The vertical separation of the fractures is 1/4 of a wavelength.

In the next case the vertical separation is 1/2 of a wavelength. In this case for the P-waves the reflections from the two fractures become more obvious, although they are not yet completely separated. On the other hand the S-wave reflections are clearly separated and we can easily see two distinct arrivals. That is because for the S-waves the distance between the two fractures is almost equal to a wavelength. The reflected waves are shown in Figure 3.12.

When the vertical distance between the two fractures becomes equal to the wavelength (P-wave wavelength), the P-wave reflections from the two fractures become distinct. The difference in the arrival time of the P-waves varies between
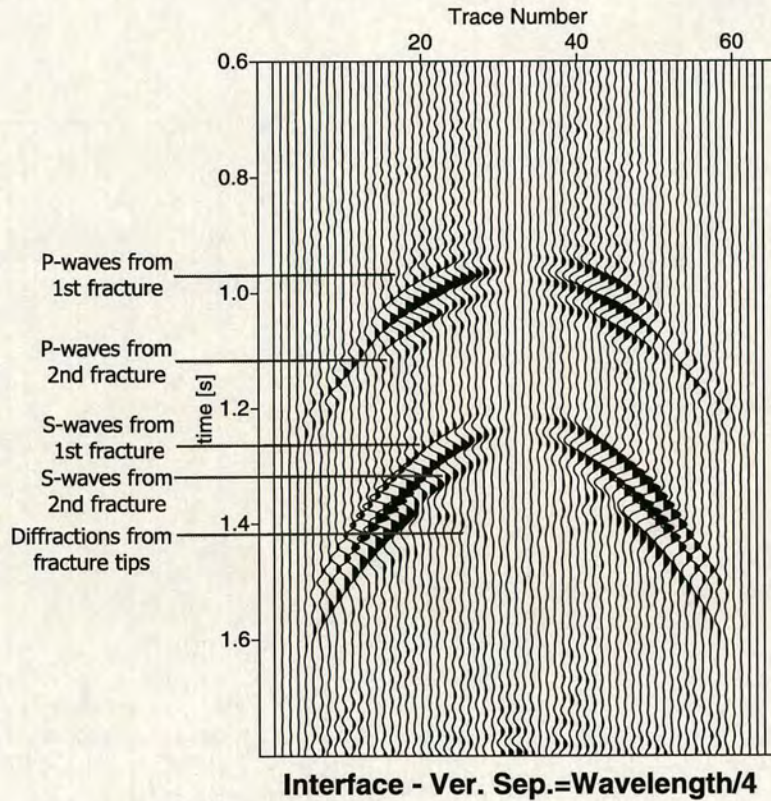
Interface - Ver. Sep.=Wavelength/2

Figure 3.12: Reflected waves from two fractures that act as an interface. The vertical separation of the fractures is 1/2 of a wavelength.

0.15 and 0.3 seconds, as shown in Figure 3.13. In addition, for the S-wave the difference in the arrival time of the S-waves varies between 0.4 s and 0.6 s, for the receivers at large and small distances respectively.

When the vertical distance between the two fractures is large, the reflections from the fractures are clearly distinguished, as expected. However, there may be cases where due to the large distance, reflections from one fracture overlap reflections from the other fracture. That is the case in our model when the vertical distance is twice the wavelength. As is shown in Figure 3.14, the reflected P-wave from the second fracture partly overlaps the reflected S-wave from the first fracture at about 1.3 s.

Based on the definition of the vertical resolution, we can see that in Figure 3.11 the arrival of the wave from the second fracture, both in P- and S-waves, causes
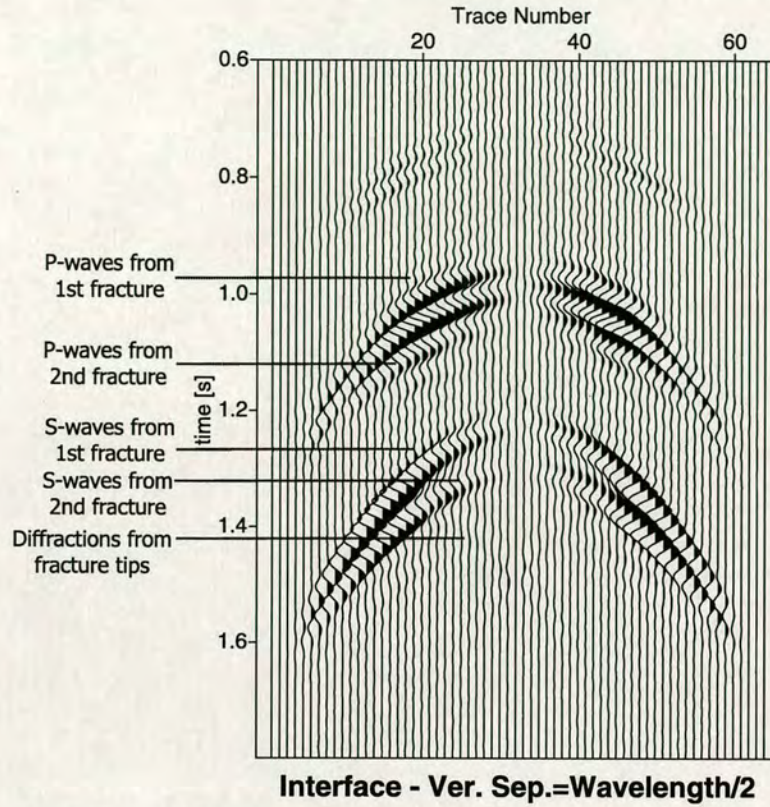
Figure 3.13: Reflected waves from two fractures that act as an interface. The vertical separation of the fractures is equal to a wavelength.

a perceptible change in the appearance of the first wave. So we can say that the two waves are resolved, and when the distance between two fractures is a quarter of a wavelength, the two fractures can be distinguished.

Next, we examine the case when the fracture acts as a single scatterer. The grid size of the model is 128 x 128 with grid spacing $dx = dz = 10\ m$. The source and receivers are situated in an ideal elastic full space ($V_P = 3300\ ms^{-1}, V_S = 1800\ ms^{-1}, \rho = 2200\ kgm^{-3}$). The receiver array at which vertical and horizontal particle displacements are recorded is horizontal and 340 m above the fractures. The fractures are 25 m long. The source is located at the centre of the receiver array. The source is the same as in the previous models. There are two fractures in the medium, both are 25 m long. The wavelength is 132 m for the P-wave and 72 m for the S-wave , which is greater than the fracture length. A vertical
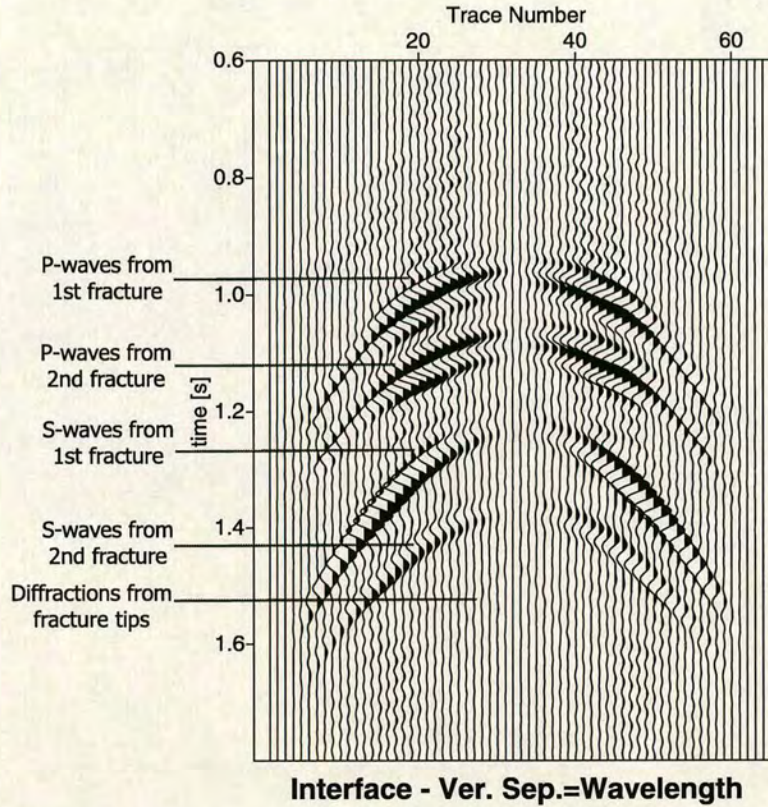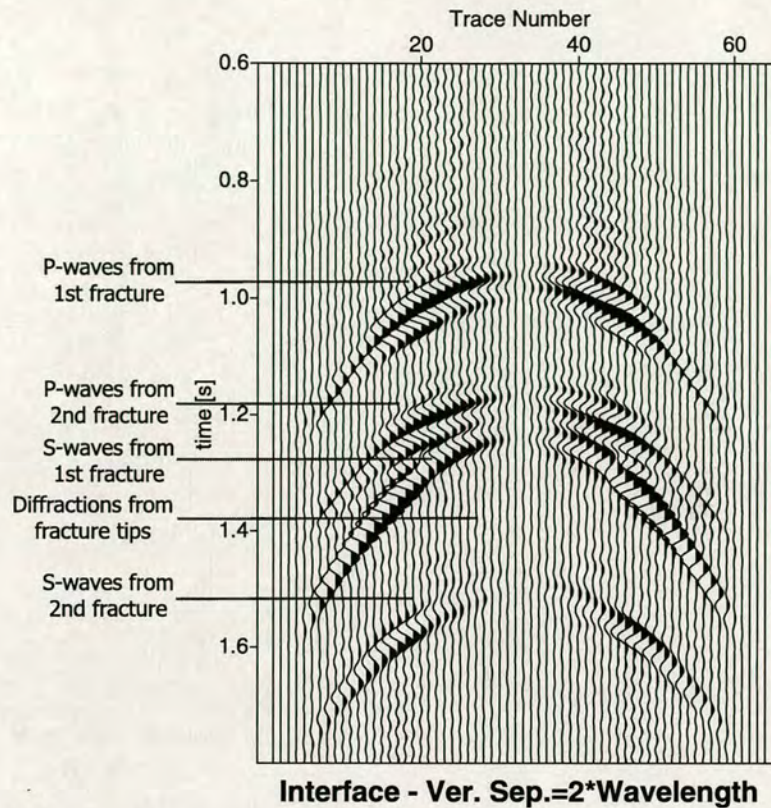
Figure 3.14: Reflected waves from two fractures that act as an interface. The vertical separation of the fractures is twice a wavelength.

distance of a quarter of a wavelength between the two fractures, is sufficient in order to distinguish between the reflections coming from the two fractures. As an example we show the reflections when the two fractures are a wavelength apart. The reflected P- and S-waves are shown in Figure 3.15. We can see clearly the distinct reflections from the two fractures.

3.4.1.2   Lateral resolution

Lateral resolution refers to how close two reflecting points can be situated horizontally, yet be recognized as two separate points rather than one. The Fresnel zone is often taken as limiting horizontal resolution on unmigrated seismic data (Sheriff and Geldart, 1980) although other factors such as signal/noise ratio, trace spacing (sampling), three-dimensional effects, and so on, also affect how far apart

Trace Number

PP reflected
waves

PS, SP reflected
waves

SS reflected
waves

Boundary
reflection

PS, SP reflected
from second fracture

Single Scatter - Crack separation=Wavelength
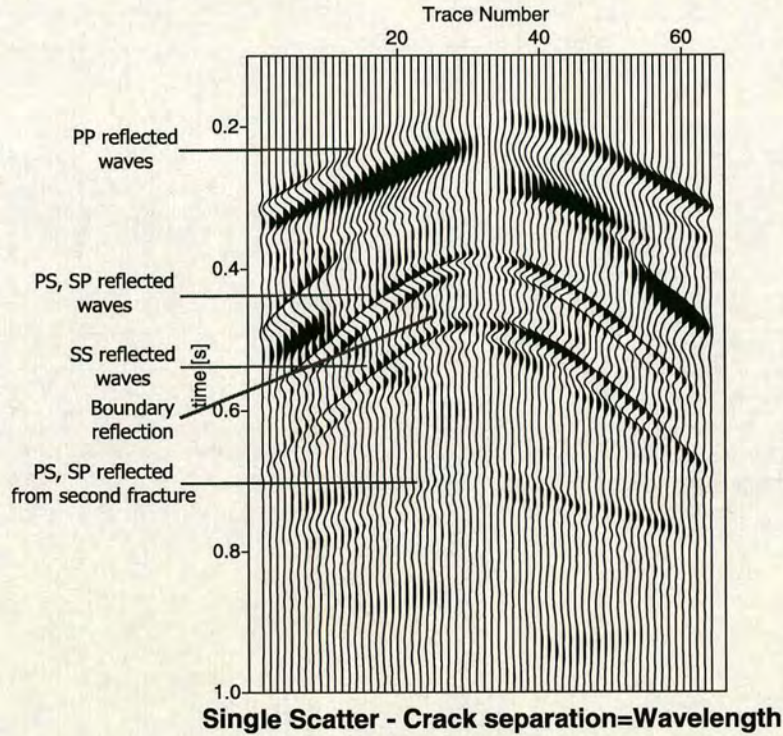
Figure 3.15: Reflected waves from two fractures that act as single scatters. The horizontal separation is twice a wavelength.

fractures have to be to be distinguished as separate features.

Generally, two reflecting points that fall withing the Fresnel zone are considered indistinguishable as observed from the earth's surface. The Fresnel zone depends on wavelength, and it also depends on frequency. For example, if the seismic signal riding along the wavefront is relatively high in frequency, then the Fresnel zone is relatively narrow. The smaller the Fresnel zones, the easier it is to differentiate between two reflecting points. Hence, the Fresnel zone width is a measure of lateral resolution. Besides frequency, lateral resolution also depends on velocity and the depth of the reflecting interface (the radius of the wavefront):

$$r \approx (z\lambda/2)^{1/2} = (v/2)(t/f)^{1/2}, \tag{3.13}$$

where r is the Fresnel zone radius, z is the vertical distance between the fracture we examine and the receivers, λ is the wavelength, $t = 2z/v$ is the travel time of a reflected wave from the fracture for a coincident source and receiver, and v is

the wave speed. Since the Fresnel zone generally increases with depth, as we can see in equation (3.13), spatial resolution also deteriorates with depth.

Horizontal uncertainty always exceeds vertical uncertainty, often by a factor of at least 2. Schneider (1978) gives an example showing that 5 % velocity error smears the position of a discontinuity over a horizontal distance equal to 5 % of the depth; local velocities are usually not known better than this.

As in the case of vertical resolution we examine here two cases, when fractures act as interfaces and when they act as single scatters. The elastic full space and the position of the source and the receivers are the same as in the case of vertical resolution. In both cases (fractures as interfaces and fractures as single scatters), the grid size of the model is 128 x 128 with grid spacing $dx = dz = 10\ m$.

We first start from the case when the fracture length is greater than the wavelength, thus acting as an interface. The wavelength for the P-waves is 66 m and for the S-waves is 36 m, while the fractures are 400 m long. We start by examining the case of a single fracture. The source is located at the center of the medium (x=640m) and at 300m depth (z=300m). The fracture is horizontal and it is located at 640m depth (z=640m). It starts from x=200m and ends at x=600m, that is below the source and on its left side. We will use the resulting wavelet as a basis for comparison, to distinguish the effect of the second fracture. Figure 3.16 shows the PP, PS and SP, and SS reflected waves from a single fracture. We can also see some reflections from the fracture tips.

In the following we examine the lateral resolution when there are two fractures for a variety of horizontal distances between the two fractures. We examine the distances of 1/4 of a wavelength, 1/2 of a wavelength, and equal to a wavelength. That is 16 m, 33 m, and 66 m, respectively for each case. Compared to the fracture length which is 400 m all distances are much smaller than the fractures. The radius of the Fresnel zone from equation (3.13) is 105.9 m for the P-waves
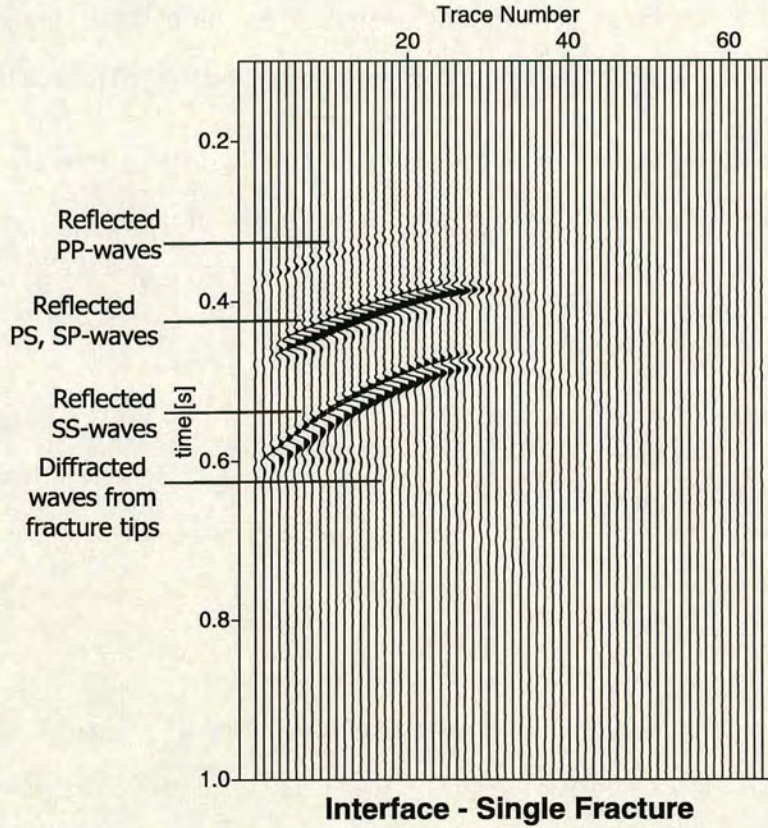
Figure 3.16: Reflected waves from a single fracture that acts as an interface.

and 78.23 m for the S-waves. That means that in all cases the fractures are inside the Fresnel zone, and normally we do not expect to distinguish them. However, as we will show in the synthetics in all the cases there are reflections coming from the two fractures and the arrivals can be identified. We believe that is due to the fact that the features are very long, so a significant part of the fracture is outside the zone. It is due to that part, that we get the reflections from which we can identify the two fractures. Figure 3.17 shows the case when the horizontal distance between the two fractures is 1/4 of a wavelength, that is 16 m, and in Figure 3.18 we show the case when the two fractures are a wavelength apart, that is 66 m. We can see that in both cases, as we have stated earlier, the wavelets do not show significant differences and in both cases the two fractures can be resolved from the reflected waves.

Trace Number

Reflected PP-waves

Reflected PS, SP-waves

Reflected SS-waves

Diffracted waves from fracture tips

time [s]

Interface - Hor. Sep.=Wavelength/4

Figure 3.17: Reflected waves from two fractures that act as an interface. The horizontal distance is 1/4 of a wavelength.

Trace Number

Reflected PP-waves

Reflected PS, SP-waves

Reflected SS-waves

Diffracted waves from fracture tips

time [s]

Interface - Hor. Sep.=Wavelength

Figure 3.18: Reflected waves from two fractures that act as an interface. The horizontal distance is equal to a wavelength.

When fractures are smaller than the wavelength, thus acting as single scatters, the radius of the Fresnel zone is an important factor in the lateral resolution. We

examine the cases when the distance between the two fractures is 1/4, 1/2, equal to, and 2 times a wavelength, that is 33 m, 66 m, 132 m, and 264 m, respectively. The fractures length is 45 m in all cases. The radius of the Fresnel zone, following equation (3.13), is almost 150 m for the P-waves and 111 m for the S-waves. We b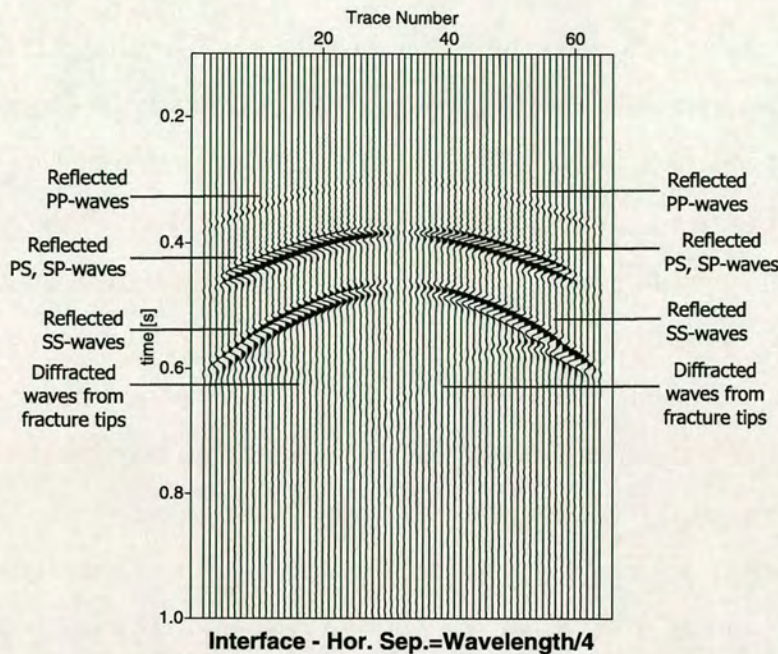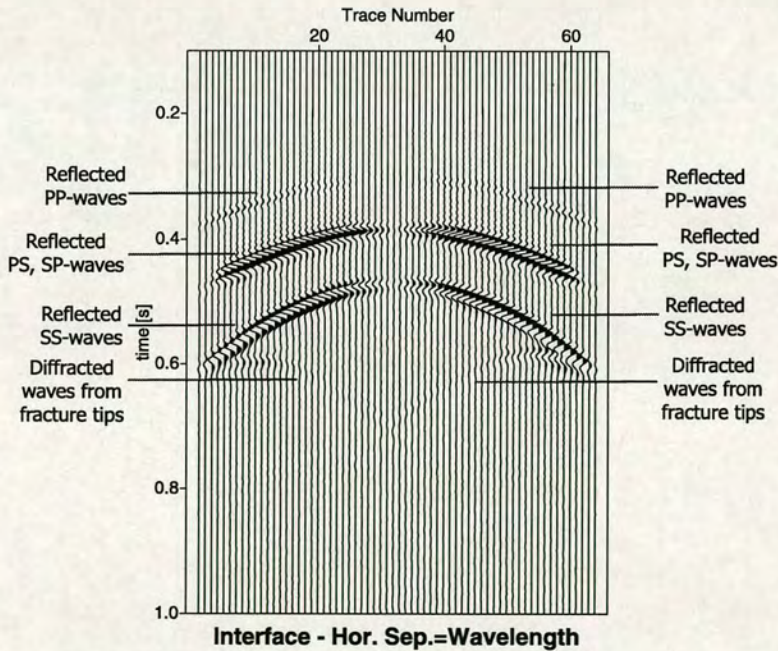egin by showing the synthetic seismograms when we have a single fracture, which will be used as a reference for the evaluation of the lateral resolution. Figure 3.19 shows the horizontal component of the synthetic seismograms, where we can see the first arrivals of the PP waves at 0.2 s, the first arrivals of the PS and SP waves at 0.4 s, and the first arrivals of the SS waves at 0.5 s. The arrivals recorded between the reflected PP waves and the reflected PS and SP waves are diffracted waves from the fracture tips, and they are present on the followin figures too in some of them more clearly than the others.
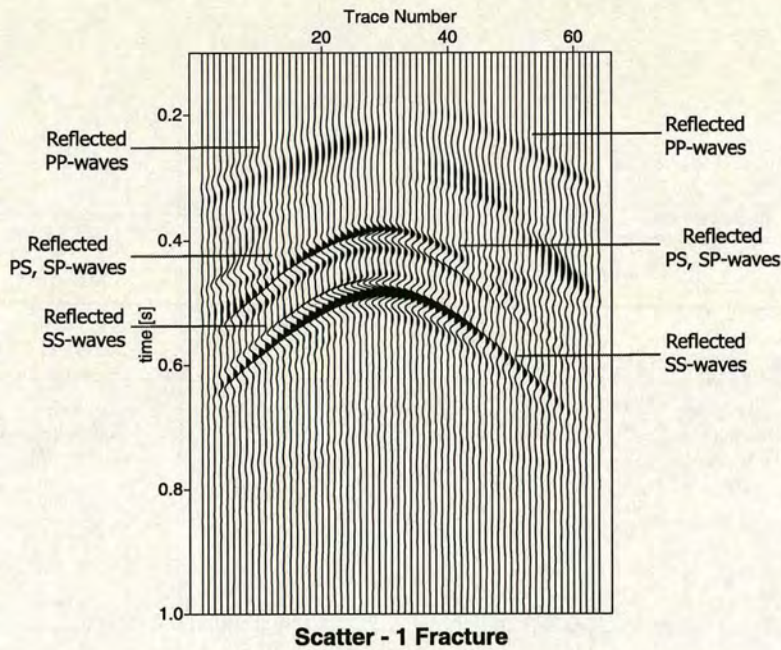

Figure 3.19: Reflected waves from a single fracture that acts as a single scatter.

Figure 3.20 shows the synthetic seismograms when the two fractures are a quarter of a wavelength apart. As we can see on the synthetic seismograms we cannot identify the two fractures. That is because the horizontal distance between the

two fractures is 33 m while the Fresnel zone radius is 150 m and 111 m, for the P- and S-waves respectively. However, there is an indication on the PS and SP waves on the distant receivers from the source (from trace number 1 until trace number 20) that there is a second arrival, but it is not very clear.

Figure 3.20: Reflected waves from two fractures that act as a single scatters. The horizontal separation is 1/4 of a wavelength.

When the distance between the two fractures becomes half a wavelength, the synthetics show more arrivals that indicate two distinct fractures. As shown in Figure 3.21, the wavelets are overlapping and we cannot obtain any reliable information for the characeristics of the fractures, as expected, because the horizontal distance between the fractures is smaller than the radius of the Fresnel zone.

Figure 3.22 shows the synthetic seismogams when the horizontal distance equals a wavelength. In this case the horizontal distance between the fractures is 132 m, which is very close to the radius of the Fresnel zone for the P-waves (150 m) and larger than the radius for the S-wave (111 m). We can identify that on the synthetic seismograms where we see two reflections of PS and SP waves and SS waves that clearly have different characteristics. Although the synthetic seismo-

Figure 3.21: Reflected waves from two fractures that act as a single scatters. The horizontal separation is 1/2 of a wavelength.

grams are not completely resolved, we can surely say that we are dealing with two scatters. Especially for the S-waves that the horizontal distance is greater than the Fresnel zone radius, the two reflections are more distinctly separated.

Finally, when the two fractures are two wavelengths apart, both P- and S-waves are outside the Fresnel zone. As a result both reflections are clearly resolved, and we can identify the reflections coming from each fracture as shown in Figure 3.23. However, we can say that even smaller distances, for example a wavelength, are good enough to be able to identify the existence of two fractures.

3.5   Summary

In this chapter, we examined the accuracy of fracture modelling using the PS method. We presented the truncation error, considering the simple case of the two-dimensional acoustic wave equation. The truncation error is a result of the
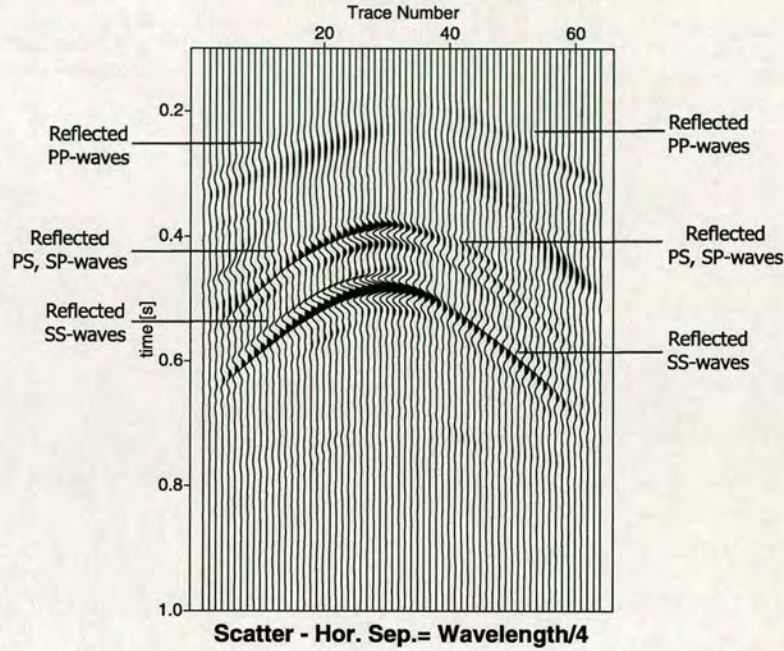
Figure 3.22: Reflected waves from two fractures that act as a single scatters. The horizontal separation is equal to a wavelength.
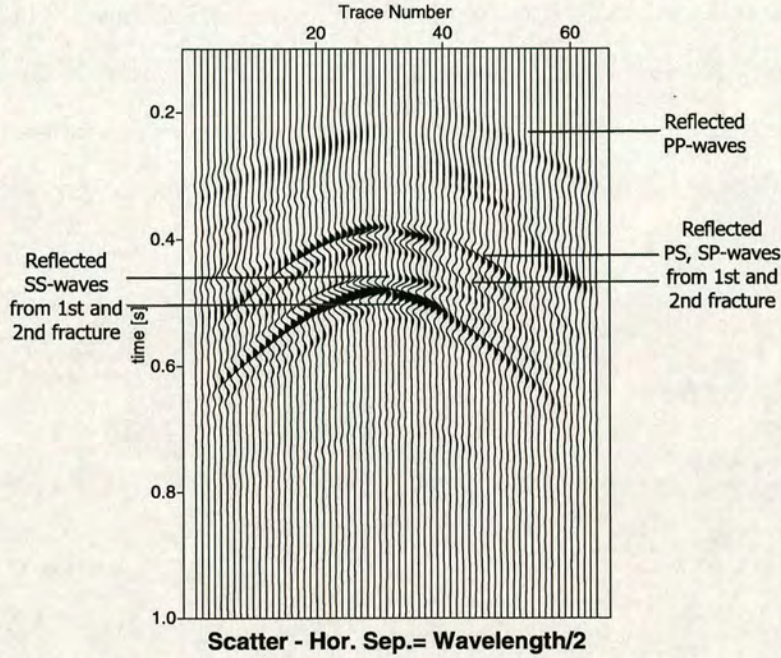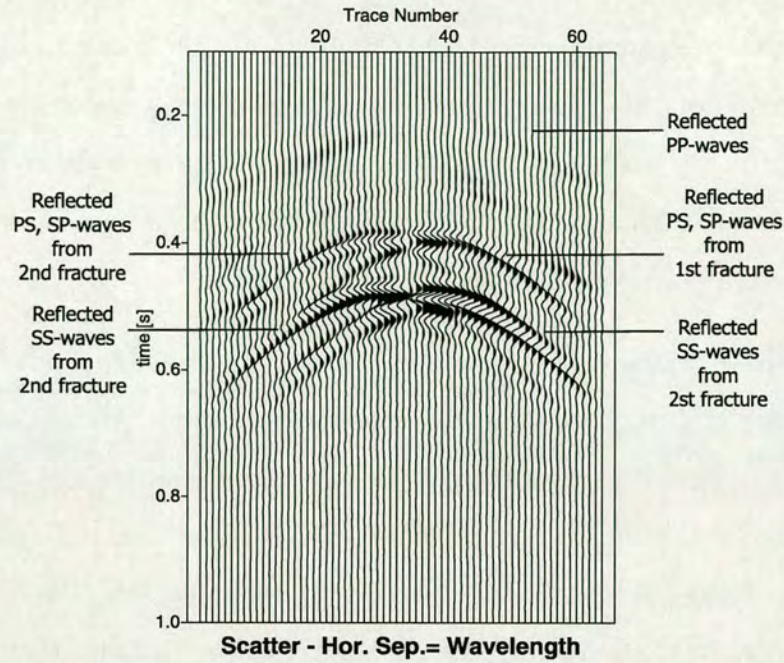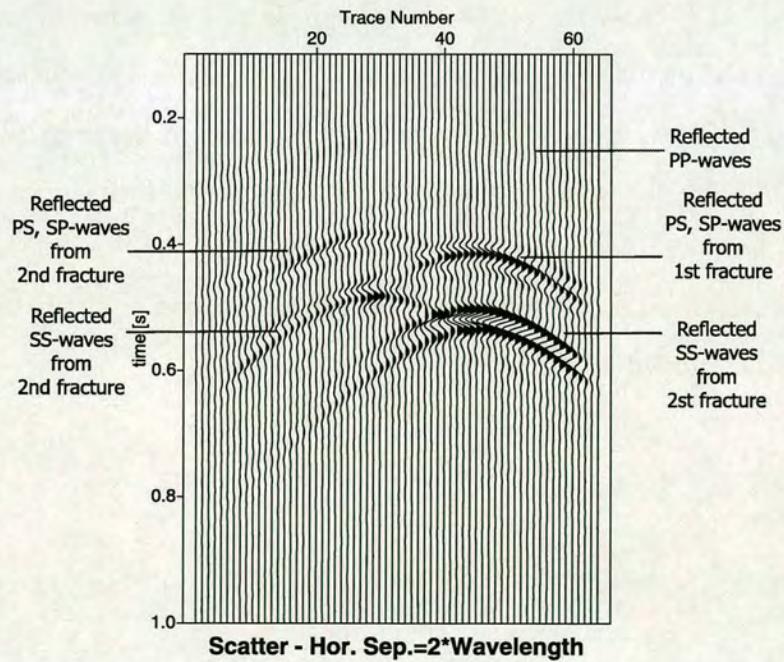

Figure 3.23: Reflected waves from two fractures that act as a single scatters. The horizontal separation is twice a wavelength.

Taylor series type of derivation that is used in the PS method. Another impor-

tant factor that we examined is the aliasing effect. The magnitude of aliasing errors depends upon the relationship between the frequency spectrum of the true solution and the highest frequency which can be supported by the computational grid. In general, aliasing effects are ignored when the accuracy is considered because they are independent of the numerical method.

In order to have clearly distinguished wavelets and reasonable modelling results, there are some limitations in the grid spacing of the finite difference grid. We examined constraints in grid spacing related to signal frequency and related to the size of the fractures. We used a simple model and considered different grid sizes compared to the wavelength and compared to the fracture size. We concluded for the first constraint that the grid size should be at least smaller than 1/4 of the wavelength, and for the second constraint that the grid size should have maximum size no bigger than the size the fractures in the examined medium. Finally, we presented a detailed examination of the resolution of the method. We examined the vertical and the lateral resolution. In the case of vertical resolution, we found that a quarter of a wavelength is the minimum distance between two fractures that is needed to be able to distinguish the two fractures. However, more distance is needed to have distinct arrivals. On the other hand, for the lateral resolution the minimum distance found is half a wavelength. However, distinct arrivals are visible for a distance of a wavelength.

Fracture modelling using the pseudospectral (PS) method

4.1 Introduction

In Chapter 3, we examined the accuracy of fracture modelling using the PS method. We concluded to some limitations in the modelling, which we apply in all the models we present in the rest of the thesis. Besides accuracy, another important aspect of the modelling is the reliability of the results. It is very important besides accurate to have realistic results.

In this chapter, we examine some simple cases of fractured models and we examine the reliability of the generated synthetic seismograms. In the first model we estimate the arrival times using the ray tracing theory and we compare them with the results of the modelling. The rest of the models we present are some basic cases in fracture modelling. The cases we examine are reflections from a single fracture, channel waves trapped between two fractures, and reflections from a fractured layer. We focus on the types of waves that are present in the synthetics, and we attempt to evaluate the ability of the modelling technique to give a reliable seismogram, that exhibits all the resulting types of waves.

4.2   Reliability of synthetic seismograms

The first step is to compare results generated by our modelling method with those obtained by another method. This has been done by Coates and Schoenberg (1995), Nihei and Myer (2000) and Nihei et al. (2000), who compared the synthetic seismograms from the Coates and Schoenberg method described with the exact solutions using boundary element methods. We assess the accuracy by comparing the synthetic seismograms generated by the modelling with the ray theoretical traveltimes.

The model geometry used for accuracy testing is shown in Figure 4.1. The source, receivers and the fracture are situated in an ideal elastic full space ($V_P = 3300\ ms^{-1}, V_S = 1800\ ms^{-1}$, $\rho = 2200\ kgm^{-3}$). The same background medium is used for consistency also in the models presented in the following section, except from the final model. The receiver array at which vertical and horizontal particle displacements are recorded is horizontal and 340 m above the fracture. The fracture is 300 m long.

The source is located at the centre of the receiver array, but not above the center of the fracture. The source type is a force in the z-direction. The source time function is

$$s(t) = \left\{1 - 2\left[\pi f\left(t - t_0\right)\right]^2\right\} e^{-\left[\pi f(t-t_0)\right]^2} \tag{4.1}$$

The source wavelet is a Ricket wavelet with a pulse initial time of 0.1 sec and a frequency of 25 Hz. The same source is used throughout the models in this chapter, except for differences in frequency and wavelengths.

Figure 4.1 also shows the different kinds of waves generated by the source that interact with the fracture. The source generates both P and S waves. When they reach the fracture boundary those waves are reflected and we record PP_r- (shown in blue in Figure 4.1), PS_r- and SP_r- (both shown in red in Figure 4.1), and SS_r- waves (shown in green in Figure 4.1). The subscript r refers to waves that are
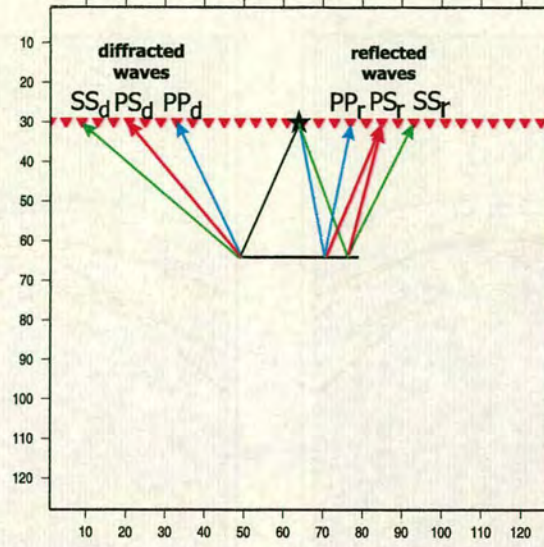
Figure 4.1: Schematic representation of the model used for the testing of the accuracy of the modelling method. The figure also shows the ray paths of the different kind of waves generated by the source that interact with the fracture.

reflected from the fracture, and the subscript d refers to waves that are diffracted from the fracture tips as shown in Figure 4.1. PP_r-waves will be the first to arrive at the receivers. Those are waves that travel both before and after the reflection as P-waves. The next arrivals will be the PS_r- and SP_r-waves. The PS_r-waves travel as P-waves from the source to the fracture, and after the reflection as S-waves from the fracture to the receivers. The case of SP_r-waves is the complete opposite to PS_r-waves. The arrivals of those two different types of waves happen at the same time, because the source-fracture and fracture-receiver distances are equal. As a result, the distance that they travel as P- and as S-waves is exactly the same in both cases, so both of them are labeled as PS_r-waves in Figure 4.1. Finally the SS_r-waves arrive at the receivers, after they travel both legs as S-waves. In addition to the reflected waves, there are waves diffracted from the crack tips. We have P- and S-wave diffractions, and also conversion from P- to S-waves and vice-versa, that are diffracted from the tips of the fracture. Those waves are presented in Figure 4.1 as PP_d- (shown in blue), PS_d- and SP_d (both shown in red) and SS_d-waves (shown in green).
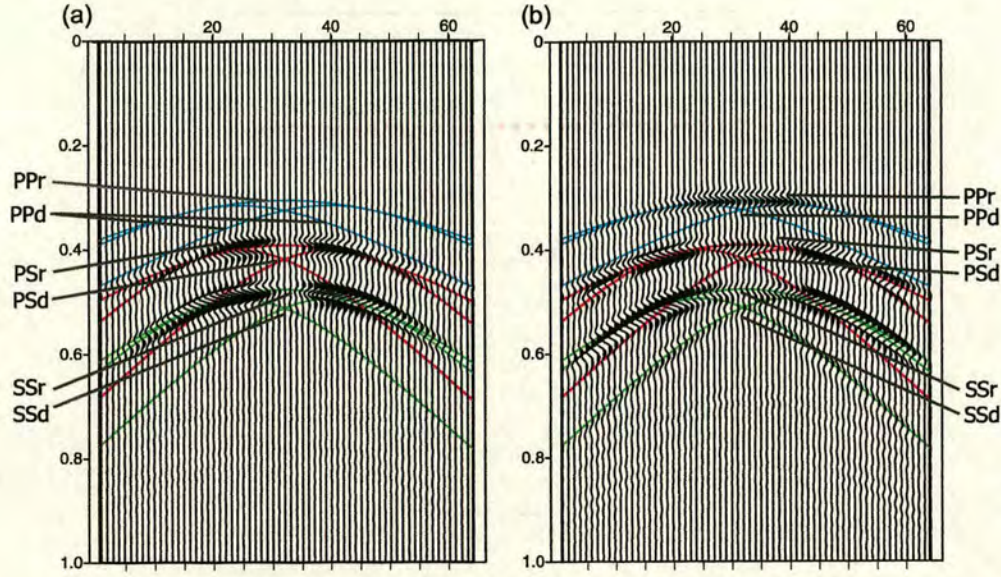
Figure 4.2: Comparison between the theoretical ray traveltimes and the synthetic seismograms generated by the modeling method. We present (a) the horizontal (x) and (b) the vertical (z) components of the seismograms. As we can see from the figure they are in very good agreement with the theoretical traveltimes, thus verifying the accuracy of the method.

We calculate the theoretical ray traveltimes and overlay them on the synthetic seismograms. Figures 4.2(a) and (b) show the horizontal-(x) and the vertical-(z) components respectively of the synthetic seismograms together with the theoretical ray traveltimes. As we can see from Figure 4.2, there is a very good agreement between the theoretical ray traveltimes and the synthetic seismograms. All possible types of waves are accurately reproduced in the synthetic seismograms. Owing to the type of source that we implement, we can see strong arrivals at short offsets on the horizontal component and strong arrivals at long offsets on the vertical component. In addition to that, the diffracted waves from the tips of the fracture and the PP_r- and PP_d-waves are not visible in the horizontal component, but they are clearly present in the vertical component and follow the theoretical traveltimes. That is expected because the source generates vertical displacements, so very close to the source and very far away from it, the horizontal displacement is negligible. Another aspect of the comparison between the theoretical and the synthetic seismograms is that they give us further insight into the waveform

patterns. In general, the comparison shows good agreement between theoretical and synthetic seismograms. The interaction between the incident wavefield and the fracture is exhibited successfully, and the reflected and diffracted waves are presented.

4.3   Numerical examples

In this section we present results from the modelling of some simple cases to examine the reliability of the method for the seismic simulation of fractures. We examine some typical geometries that are common in real earth. The models are simple, because the aim is to exhibit the capability of the method to generate a realistic synthetic seismogram. We begin with the simple case of a single fracture. In this case we examine the implementation of the fracture in the finite difference grid using the equivalent medium theory presented in Chapter 2. We focus on the generated types of waves, and we examine whereas the method can account for all the waveforms present in such cases. The waveforms we examine are the direct, reflected and diffracted P and S waves. In the second case, we examine a model where seismic waves are trapped between two parallel fractures. That is a more complicated case, and it occurs quite frequently in seismic exploration. The seismic waves undergo multiple reflections and we test the ability of the method to present the interaction between upgoing and downgoing waves between the two fractures and the amplitude decay due to the multiple reflections. Finally, we present a high velocity layer of fractures that is situated between two unfractured layers. Such a geological structure is encountered in fractured reservoirs. In this case, we examine the effect of the layering on the reflections of the fractures and the ability of the method to generate realistic synthetic seismograms in such a complicated case.

4.3.1 Model 1: Reflections from a single fracture

The first case we examine is a simple horizontal fracture in an otherwise isotropic medium. The background medium parameters are the same as the ones used in the previous model.
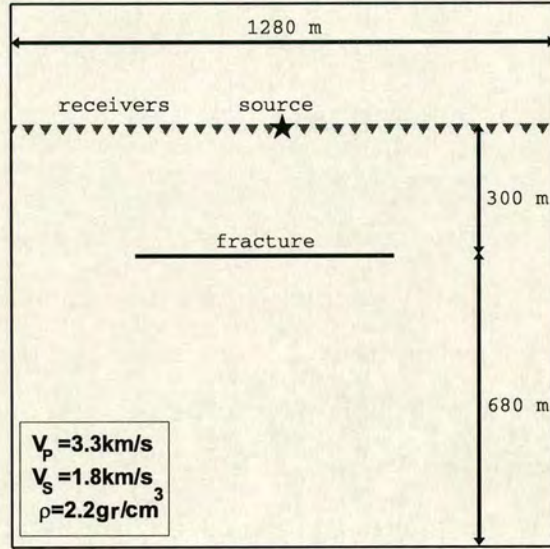
Figure 4.3: The geometry used for the synthetic experiment.Horizontal and vertical particle displacements are recorded at the array 300 m above the fracture. The receiver array has an aperture of 1280 m. The vertical stress source is located at the centre of the receiver array.

Figure 4.3 shows the model geometry. The receiver array at which vertical and horizontal displacements are recorded is horizontal and 300 m above the fracture. The maximum source-to-receiver offset is 640 m. The fracture is 600 m long and the "fracture compliance matrix" becomes zero at each end of the fracture, as it is described in Appendix A. For the cells containing the fracture we take $Z_N = Z_T = 2/\mu$, which generates an extra displacement. The source is located at the centre of the receiver array. We use a grid of 128 x 128 grid cells, in which the spatial-grid step is 10 m and the time step is 0.001 sec.

In this model we examine the simple case of a fracture parallel to the grid, in a homogeneous medium. In Figure 4.4 (a) and (b) we show the horizontal and
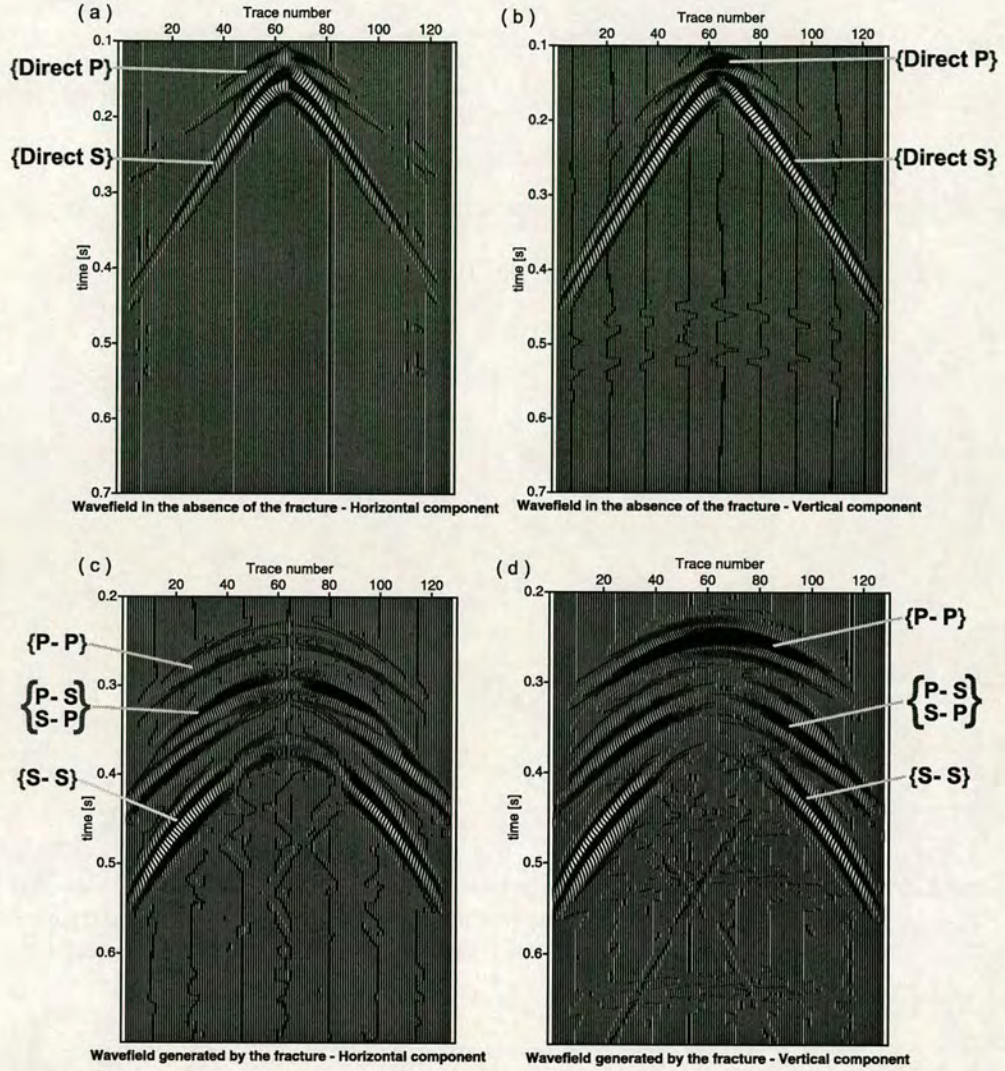
Figure 4.4: (a) The horizontal (parallel to the fracture) and (b) the vertical (normal to the fracture) particle displacements in the absence of the fracture. It is obvious that the medium is isotropic because we don't have shear wave splitting. (c) The horizontal (parallel to the fracture) and (d) the vertical (normal to the fracture) particle displacements due to the reflected wavefield generated by the fracture. The wavefield presented in (c) and (d) is the difference between the wavefield in the presence and in the absence (shown in (a) and (b)) of the fracture. We can see the three different arrivals which are, starting from first to last arrival, the P-P waves, the P-S and S-P waves, and the S-S waves.

vertical components of the particle displacements caused by the source in the absence of the fracture. This might represent a "null hypothesis" for field data. Our source, as we mentioned before, is not a pure P-wave. Figure 4.5 shows the

source radiation. From that source P- and S-waves are going to be generated at the same time. We can see that in the horizontal component (x-direction) we have very strong S-wave and in the vertical component (z-component) we have very strong P-wave. In Figure 4.4 (a) and (b) we can see the direct P-waves only on the receivers near the source and the direct S-waves which propagate along the whole of the horizontal receiver array.
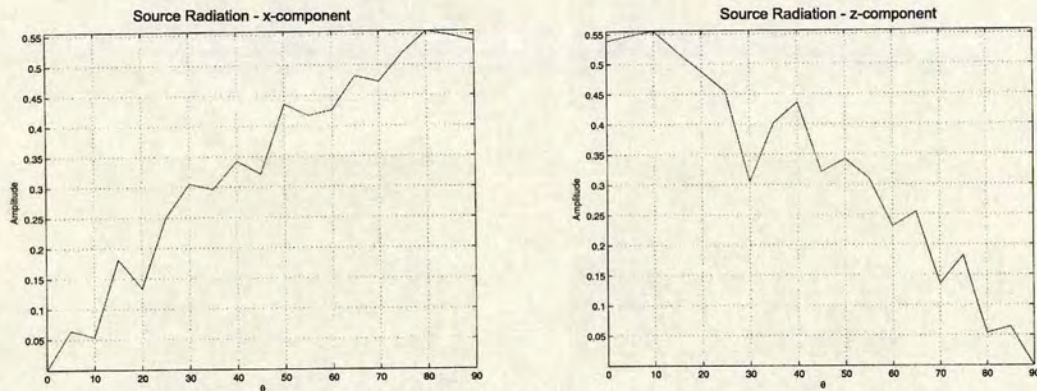
Figure 4.5: Source radiation for the horizontal and the vertical component. We can see that the source creates both a P and an S wave, that have maximum amplitude at the vertical and the horizontal direction, respectively.

In Figure 4.4 (c) and (d) we have the horizontal and vertical components of the particle displacements of the reflected waves from the fracture. The direct waves are much stronger than the reflected waves, so in order to avoid any shadowing of the reflected waves, we remove the direct waves from those figures. These figures show us a clear view of the waves reflected off the fracture. The first arrivals after 0.2 sec are the P-P waves. They are better recorded on the vertical component. At 0.3 sec we have the second arrivals, which are converted waves, either P-S or S-P. That is happening because in our model the source and the receivers are at the same distance from the fracture, so both waves travel half the distance as P-waves and the other half as S-waves. The final arrivals just before 0.4 sec are the S-S waves. Those waves are better recorded by the horizontal components.

4.3.2   Model 2: Channel waves trapped between two fractures

In this case there are two horizontal fractures, parallel to each other and parallel to the grid, with a length of 700 m. The medium we are using is exactly the same isotropic medium as in Model 1.
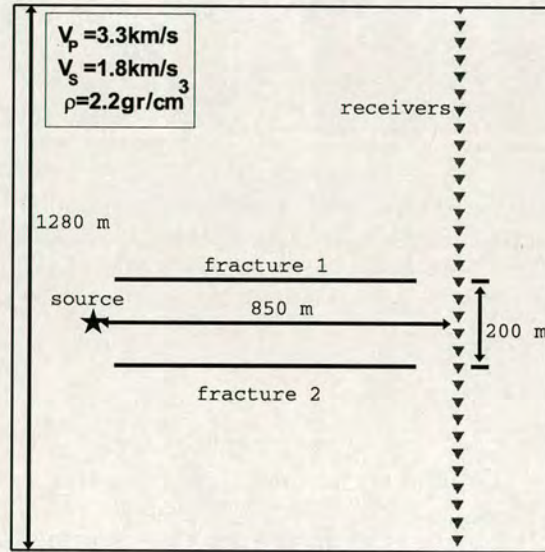
Figure 4.6:   The geometry used for the experiment to produce the synthetic seismograms. Channel waves are caused by the scattering between the two fractures. Immediately after exiting the two-fractures channel, horizontal and vertical particle displacements are recorded at the receiver array. The receiver array has an aperture of 1280 m. The vertical stress source is located 850 m away from the receiver array.

Figure 4.6 shows the experimental geometry. The receiver array is vertical and is located immediately after the end of the fractures, so as to record the multiple reflections of the channel waves. The minimum source-to-receiver offset is 850 m. As in Model 1 the "fracture compliance matrix" becomes zero at each end of the fractures (see Appendix A). Also the values of Z_N and Z_T are the same as in Model 1. The source is located in-between the two fractures, 100 m below the first fracture and 100 m above the second fracture, and is just 50 m away from their starting point. The source type and the grid are the same as in Model 1.
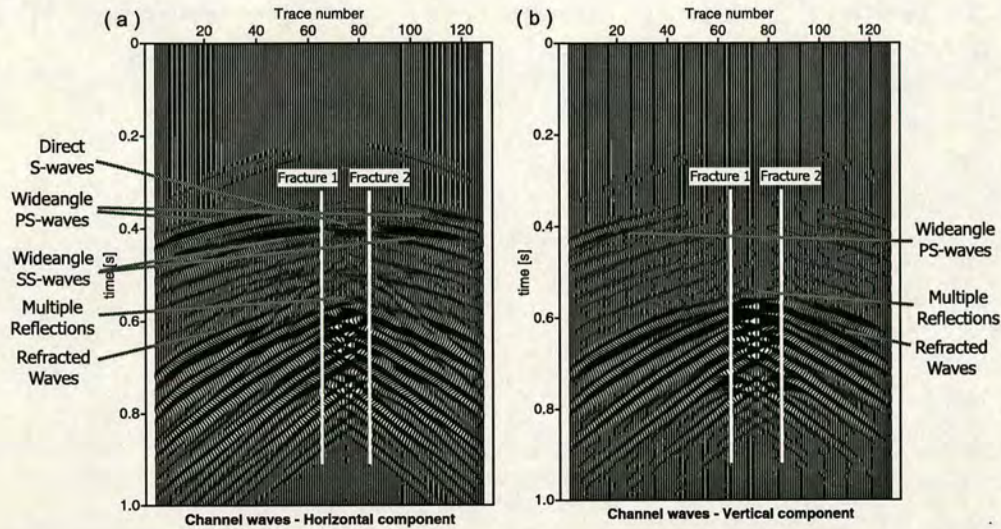
Figure 4.7: (a) The horizontal (parallel to the fracture) and (b) the vertical (normal to the fracture) particle displacements caused by the channel waves. It is obvious from both figures that energy is trapped in between the two fractures and what we see on figures (a) and (b) are the multiple reflections of the trapped waves.

The geometry of the model is such, that the generated waves from the source will be multiply reflected by the two fractures, thus leading to channel waves. As we know, two kinds of boundary conditions can produce channel waves : (a) the impedance contrast is so great that the reflection coefficient is very large (nearly unity); (b) waves within the waveguide are incident on the boundary at an angle greater than the critical angle so that total reflection occurs and little energy leaks through the boundary (Sheriff and Geldart, 1980). For the isotropic medium in our case the existence of the two fractures creates the waveguide phenomenon and we expect waves to bounce back and forth at different angles within the waveguide. For most of the angles, there is destructive interference between the different waves, but for certain angles, there is constructive interference and consequently a strong buildup of energy reflected at these angles. After exiting the waveguide the waves are recorded by the receivers, where we would expect to see clear patterns of multiple reflections. This indeed is the case in Figure 4.7 (a) and (b). Multiple reflections in such cases are also demonstrated by Wu et al.

(2002) and Nihei et al. (2002). That proves the validity of the method employed to do the simulation.

Let us have a more thorough look at Figure 4.7. We have the horizontal and the vertical components of the synthetic seismograms. One major difference between the two components is that direct waves only appear in the horizontal components, which means that we only have direct S-waves. That is more or less expected. We mentioned at the beginning of this section that the source is a force in the z-direction, so the P-waves will propagate in the z-direction and the S-waves in the x-direction. As a result, when the P-waves enter the waveguide they are multiply reflected. On the other hand we do have direct S-waves at 0.45 sec, as we can see on the figure. Also we have some wide angle arrivals at 0.4 sec. Those arrivals are possibly converted P-S waves. The first arrivals of the reflected waves appear at 0.58 sec on the vertical components and at 0.59 sec on the horizontal components.

Figure 4.7 clearly exhibits the multiple reflections of the seismic waves between the two fractures. A great amount of energy is trapped in the waveguide. That is expressed by the high amplitude of the waves observed in the area between the two fractures. However, there is significant energy outside the fractures. That is because the impedance contrast between the background medium and the fracture elastic properties is not strong enough to cause total reflection. Furthermore, after the first reflected waves that arrive at the receivers, the following reflected waves exhibit amplitude decay. That can be attributed to the loss of energy that happens at each reflection. In general, the model represents successfully multiple reflection and scattering phenomena and it also exhibits reliably the amplitude decay expected in such cases.

4.3.3   Model 3: Reflections from a fractured layer

I move now to a more complicated case. That case is a three-layer model with the middle layer fractured. In the first layer the P- and S-wave velocities are respectively, $V_P = 3300ms^{-1}$, $V_S = 2350ms^{-1}$, and the density is $\rho = 1700kgm^{-3}$. In the second layer, which is the fractured one, the P- and S-wave velocities are respectively, $V_P = 4200ms^{-1}$, $V_S = 2490ms^{-1}$, and the density is $\rho = 2700kgm^{-3}$. The third layer, which acts as a halfspace, is a medium equivalent to the first layer, and the values of the P- and S-wave velocities as well as the density are the same as those of the first layer.
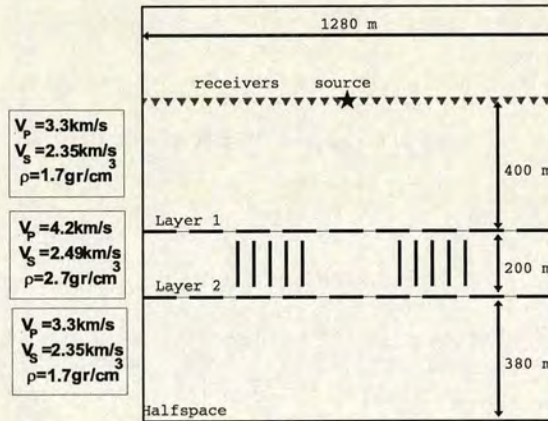
Figure 4.8:   The geometry used for the experiment to produce the synthetic seismograms. The two layers and the halfspace under the second layer are shown. Inside the second layer there are ten vertical, parallel fractures. Horizontal and vertical particle displacements are recorded at the receiver array. The receiver array has an aperture of 1280 m. The vertical stress source is located at the centre of the receiver array. The receiver array is located 400m above the bottom of the first layer.

Figure 4.8 shows the model geometry. The receiver array at which vertical and horizontal particle displacements are recorded is horizontal. It is located 400 m above the top of the second layer. The maximum source-to-receiver offset is 640 m. The first layer starts at the top and has a thickness of 700 m. The second layer has a thickness of 200 m. The halfspace starts at a depth of 900 m until 1280 m. The first layer and the halfspace have the same properties. In the second

layer, we have ten vertical parallel fractures. The fractures form two groups of five fractures each. Each fracture is 140 m high with a spacing of 50 m. The two groups are 300 m apart. Following the previous models the fracture compliance matrix becomes zero at each end of the fractures and for the cells containing the fracture we take $Z_N = Z_T = 2/\mu$. The source is located at the centre of the receiver array and has the same properties as in the two previous models. Also, we use the same grid as in the two previous cases.

Figure 4.9 shows the synthetic seismograms. Figures 4.9 (a) and (b) show the horizontal and the vertical particle displacements assuming that the second layer is not fractured. We have removed from both synthetic seismograms the direct waves, so as to have clear reflections from the interfaces between the different media. The first arrivals are the PP waves at 0.28 sec, which are clearly recorded on the vertical component. Those waves travel as P-waves on the first layer, they are reflected at the interface, and they travel back to the receivers also as P-waves. The next arrivals are the converted PS waves at 0.33 sec, that are clearly recorded on the horizontal component. Those waves are also recorded on the vertical component at wide angles. Those waves travel as P-waves in the first layer and after the reflection they are converted to S-waves. The next arrivals are the PPPP waves at 0.38 sec, that are clearly recorded on the vertical component. They travel as P-waves in both the first and the second layers before and after the reflection on the interface between the second layer and the halfspace. The next recorded waves are the PPSS waves at 0.45 sec which are not clearly visible on the two extremes of the receiver array on either of the components. Those are the waves that travel as P-waves in the first and the second layer and after the reflection on the interface they are converted to S-waves and continue like that to the receivers. The final arrivals are the PSSS waves at 0.5 sec that are clearly recorded on the horizontal component. Those waves are waves that travel as P-waves in the first layer, convert to S-waves at the interface between the first and
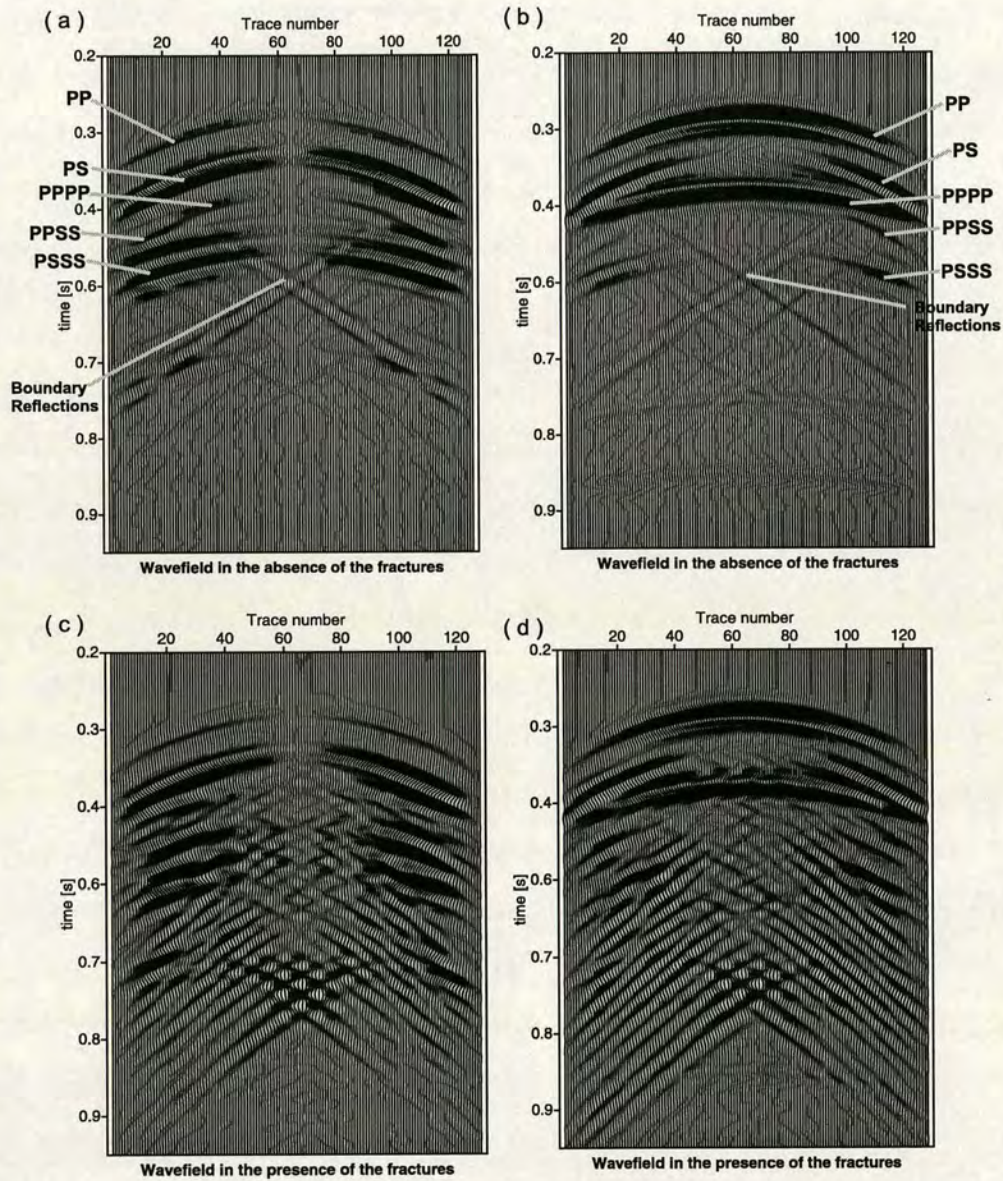
Figure 4.9: (a) The horizontal (normal to the fractures) and (b) the vertical (parallel to the fractures) particle displacements in the absence of the fractures. The only reflections present are from the two interfaces. (c) The horizontal (normal to the fractures) and (d) the vertical (parallel to the fracture) particle displacements in the presence of the fractures. We have reflections both from the interfaces and the fractures. In all four figures the direct waves are removed from the synthetics.

the second layer and stay as S-waves after the reflection at the second interface. Figure 4.10 shows all the waves mentioned above and their paths through the layers.
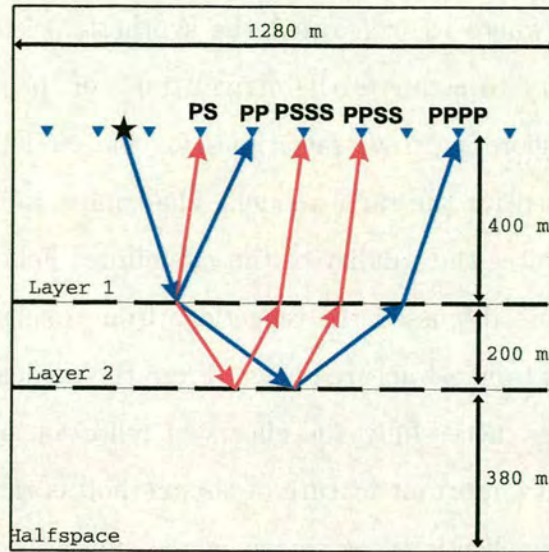
Figure 4.10: Wave paths through the layers

Figures 4.9 (c) and (d) show the horizontal and the vertical particle displacements when we include the fractures in the second layer. In that case we have reflected waves both from the interfaces between the layers and from the fractures. The waves reflected at the first interface (PP and PS waves) are unaffected by the existence of the fractures. On the contrary, PPPP, PPSS and PSSS waves, travel through the fractures before and after the reflection on the second interface. That is the reason why the wavelets of those waves are distorted compared with Figures (a) and (b). Those wavelets also exhibit significant scattering due to the fractures. In general, the synthetic seismograms show the expected features, such as reflections and scattering due to the existence of two interfaces and a fractured layer.

4.4   Summary

In this chapter we presented some example cases of modelling to exhibit the validity of the technique introduced in Chapter 2. We began by a simple case

of a single fracture where we generated the synthetic seismograms. We used the ray tracing theory to estimate the arrival times of the various wave types. We compared the theoretical ray traveltimes for the model with the synthetic seismograms generated for the same model. The comparison showed very good agreement that indicates the validity of the modelling. Following, we presented three models where we discussed the reflections from a single fracture, channel waves and reflections from a fractured layer. From the models we concluded that the method describes successfully the effects of reflection and diffraction from the fracture tips. An important feature of the method is the satisfactory representation of multiple reflections, as shown in the synthetic seismograms. That is significant because multiple reflection is the most common case in fractured reservoirs. Equally important is the reliable presentation of scattering in the synthetic seismograms. As a general conclusion, the modelling results show that the method can generate in a reliable way the effects of the interaction between the seismic wave and the elastic medium.

CHAPTER 5

Effects of sizes and spatial distributions

5.1 Introduction

The problem of the scattering of seismic waves by cracks is a subject of interest for geophysicists because it has many applications concerning the Earth's crust: oil and gas prospecting, the theoretical study of the nucleation process of earthquakes and, more generally, investigation of the propagation of seismic waves in heterogeneous media. Results from deep drilling experiments (Kelner et al., 1999) have shown that the upper 10 km of the continental crust are highly fractured and that most of the reflections registered in the upper crust during reflection experiments come from fracture zones and faults rather than from lithological boundaries (Emmermann and Lauterjung, 1997). In this chapter we study the propagation of seismic waves through media containing fractures with different sizes and spatial distributions by performing numerical simulations using the method presented in Chapter2.

Scaling in fracture systems has become an active field of research in the last 25

The content of this chapter has been published in GJI (Vlastos S., Liu E., Main I.G., and Li X.-Y., Numerical simulation of wave propagation in media with discrete distributions of fractures: effects of fracture sizes and spatial distributions, 152, 649-668, GJI)

95

years motivated by practical applications. In the case of the hydrocarbon industry, scaling laws provide a key to predicting the nature of subseismic fracturing (below the limit of seismic resolution), which can significantly influence reservoir and cap rock quality, from seismically resolved faults. The numerous studies of fracture-system scaling in the literature do indeed suggest that scaling laws exist in nature. They also indicate, however, that such scaling laws must be used with caution and with due regard to the physical influences that govern their validity. In recent years the power law distribution has been increasingly employed to describe the frequency distribution of fracture properties and geometry. However, a power law is not an appropriate model in all cases, and other distributions that have been used include the log normal, gamma, and exponential laws.

The variations in space of fracture characteristics, such as size and orientation, are highly irregular and complicated. Therefore, the study of a fractured reservoir must follow a special pattern, beginning with the examination of local basic characteristics of single fractures, only afterwards continuing with the examination of a multifracture system. Single fracture parameters refer to the intrinsic characteristics, such as opening (width), size and nature of fractures. If the single fracture is associated with the reservoir environment, another essential characteristic, the fracture orientation, will result. The multi-fracture parameters refer to the fracture arrangement (geometry) which further generates the bulk unit, called the matrix block. The number of fractures and their orientation are directly related to fracture distribution and density. When fracture density is related to lithology, another parameter of particular interest, called fracture intensity, is obtained. Fracture intensity is used to associate the fractures with the lithology and the tectonic mechanisms within layers which contributed to the formation of the fractures. This parameter may define the role played by the intrinsic characteristics of each layer (permeability, porosity, cementation, etc.) during the fracturing process, by the thickness of the layer and by its structural

location (top, center, or bottom of the structure).

In this chapter we examine the effect of two fracture characteristics. One is the size of fractures, and the other one is the spatial distribution. We suppose that all the fractures have the same opening displacement, which is very small. We examine the influence of different scalelength distributions and also a variety of spatial distributions, and we are looking for characteristics in the wavefields due to the variations of those characteristics.

5.2   Effect of fracture size

In this part we mainly concentrate on the examination of the effect of the size of fractures relative to the wavelength. To ensure consistency of the results from different models we use the same background medium in all the cases. This guarantees that any variation in the features of the wavefield is due solely to the scalelength (size) or the spatial distribution of the fractures. The matrix parameters are $V_P = 3300ms^{-1}$ and $V_S = 1800ms^{-1}$ for the P- and S-wave velocities, respectively, and the density is $\rho = 2200\ kgm^{-3}$. For demonstration purpose, we assume that the fracture compliances are $Z_T = Z_N = 5.6 \cdot 10^{-10}GPa^{-1}$. Those are the same fracture compliances as the ones used in the models presented in Chapters 3 and 4. The source is located at the centre for all the models. The source wavelet is a Ricker wavelet with a dominant frequency of $25Hz$ and a pulse initial time at $0.1s$. We use a grid size of 256 x 256, with a spatial grid-step of $10m$ and a time-step of $0.001s$. For each of the two spatial distributions we consider two different fracture sizes.

In the first case, we examine fractures that are distributed in space in a nearly regular way. In all cases we have a total number of 60 fractures. The fracture semi-lengths are, $\alpha = 0.1\lambda$ and $\alpha = \lambda$, where λ is the wavelength. Figure 5.1

shows the model where the fracture size is $\alpha = 0.1\lambda$, representing point like scatterers. Figure 5.2 (a), (b) and (c), shows snapshots of the wavefield, calculated by the methods outlined in Chapter 2. The snapshots are taken at consecutive times, 250 ms, 350 ms and 450 ms, respectively, after the initialisation of the source. When the wavelength is larger than the size of the fractures the snapshots show clearly the P- and S-waves propagating through the fractured medium. Each fracture acts as a single scatterer, and each one of them becomes a source of a secondary wavefield, as shown by the wavefronts that are not centered at the source on Figure 5.2. When dealing with such wavelengths, which are long compared with the size of the fractures, the secondary wavefields have a much smaller amplitude than the coherent P and S wavefield. The wavefield then principally reflects the overall properties of the fractured solid.

Figure 5.1: Model geometry when fractures have a nearly normal distribution and the size of the fracture is $\alpha = 0.1\lambda$.

In the following, we examine fractures for which $\alpha = \lambda$. That means that the actual size of fractures (2α) is bigger than the wavelength. Figure 5.3 shows the geometry of the model. When the incident wavelength is shorter than the crack length, we are in the strong scattering regime. Figure 5.4 (a), (b) and (c), shows snapshots of the wavefield taken at consecutive times, 250 ms, 350 ms and

Figure 5.2: Snapshots taken at consecutive times, (a) 250 ms, (b) 350 ms, and (c) 450 ms, after the initialisation of the source for the model shown in Figure 5.1.

450 ms, respectively, after the initialisation of the source. Due to the size of the fractures, each cluster of fractures behaves as a single interface. Compared to Figure 5.2, the wavefront of the reflected waves is not now circular but is instead significantly distorted. That is because the reflection comes from an interface that has size bigger than the wavelength. As a result, in the snapshots, strong coherent

reflected energy from the 'interfaces' can be identified, with strong interference patterns in the wavefront.

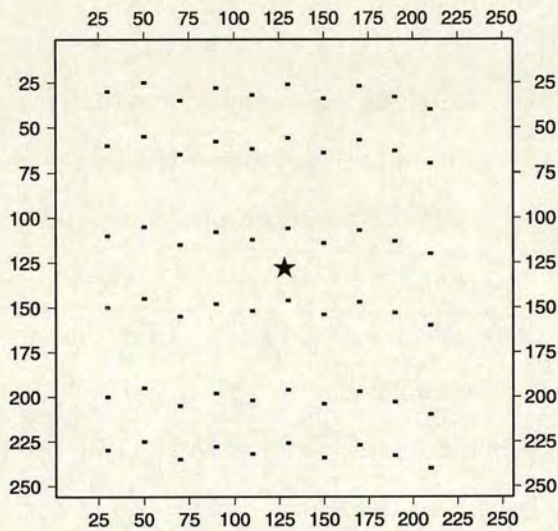**Figure 5.3:** Model geometry when fractures have a nearly normal distribution and the size of the fractures is $\alpha = \lambda$.

In the next case, we examine a completely random distribution of fractures to avoid clustering patterns of fractures. The two models we examine have the same number and the same size of fractures as in the cases when we have near regular distribution. We start by examining once more fractures for which $\alpha = 0.1\lambda$. Figure 5.5 shows the model of the fractures. Figure 5.6 (a), (b) and (c), shows snapshots taken at consecutive times, 250 ms, 350 ms and 450 ms, respectively, after the initialisation of the source. Examination of the snapshots shows similar features of the wavefield with those seen in Figures 5.2 and 5.4. However, it is apparent that the reflected wavefield is strongly attenuated compared to the case of near regular distribution. That is because in the near regular distribution there is more constructive interference between the reflected waves from the fractures.

Finally, we examine the same distribution for fractures with $\alpha = \lambda$. Figure 5.7 shows the model of the fractures. Figure 5.8 (a), (b) and (c), shows snapshots taken at consecutive times, 250 ms, 350 ms and 450 ms, respectively, after the initialisation of the source. The snapshots show similar features with Figure 5.4.
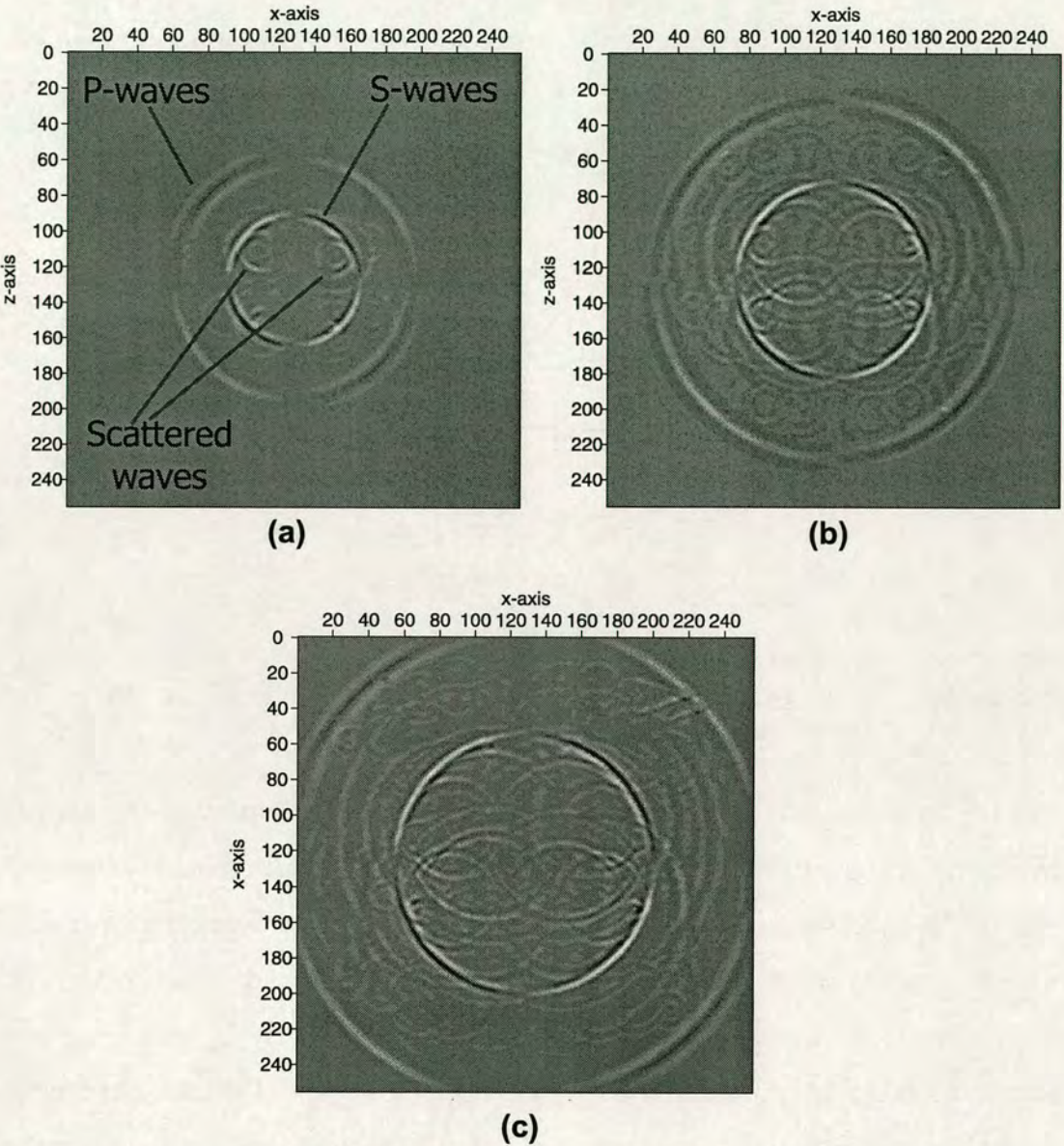
Figure 5.4: Snapshots taken at consecutive times, (a) 250 ms, (b) 350s, and (c) 450 ms, after the initialisation of the source for the model shown in Figure 5.3.

We can see very clear reflections from interfaces as expected from the size of the fractures. However, it is apparent that the reflected wavefield in Figure 5.8 is not as coherent as in Figure 5.4 for the case of the nearly regular distribution. The explanation is that when the fractures are randomly distributed they cannot form large clusters that may be treated as a single reflector, thus acting almost
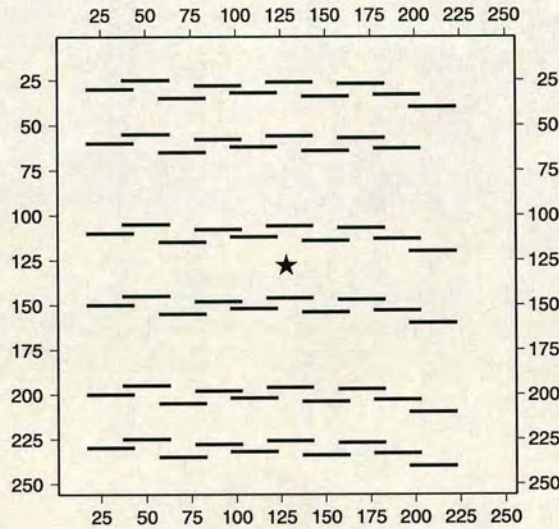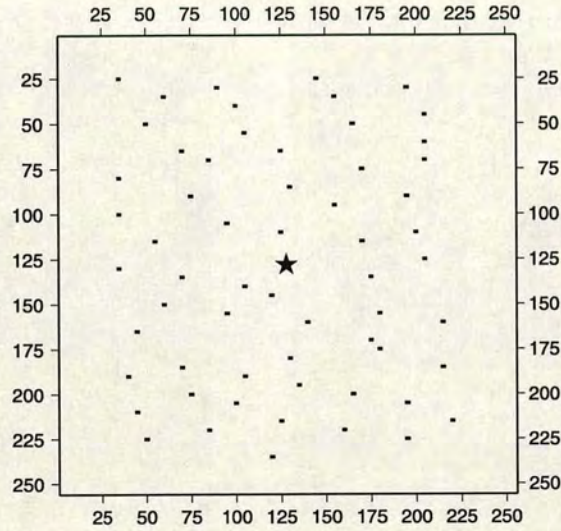
Figure 5.5: Model geometry when fractures have a completely random distribution and the size of the fractures is $\alpha = 0.1\lambda$.

as individual boundaries and the amplitudes of the reflected waves depend on the interference between the various reflections. Comparing the snapshots between the two different distributions we can see that there is strong and coherent energy in areas with high fracture clustering, i.e. in Figures 5.2 and 5.4

5.3   Effect of spatial distributions

We continue by undertaking a more detailed examination of the most common spatial distributions of fractures. We attempt to model four different simulations of distributions of fractures. In each model, there are 100 fractures randomly distributed in a 1280 m × 1280 m area. The geometric model used for the investigation is shown in Figure 5.9.

To create the various random distributions of fractures we use an algorithm that generates four arbitrary distributions, featuring different qualitative characteristics, as shown in the following section. We use parent distributions for the fracture centre spacings that are (a) random uniform, (b) Gaussian, (c) ex-
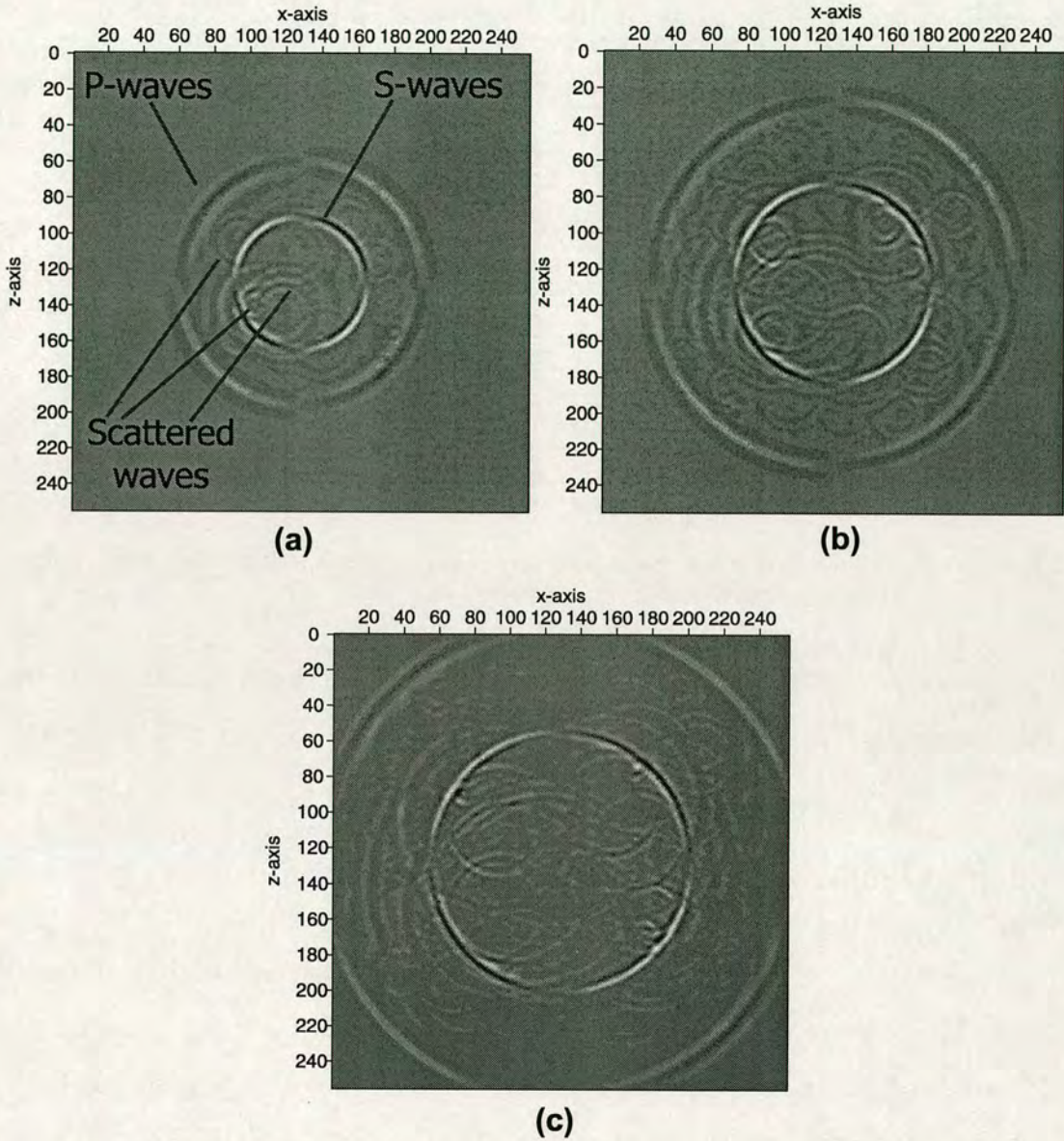
Figure 5.6: Snapshots taken at consecutive times, (a) 250 ms, (b) 350 ms, and (c) 450 ms, after the initialisation of the source for the model shown in Figure 5.5.

ponential, and (d) Gamma. In the cases where we have overlapping of fracture positions, we remove the overlapping fractures and generate new fractures until the desired number of fractures is reached. As a result of this process, the final crack distribution is not necessarily random. Nevertheless, the purpose of this section is to illustrate how different distributions affect multiple scattering.
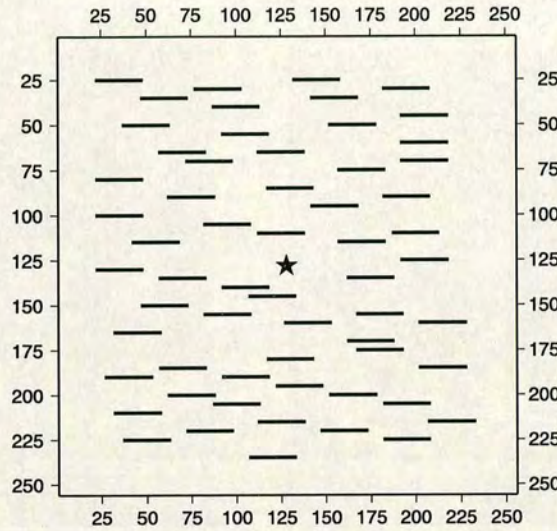
Figure 5.7: Model geometry when fractures have a completely random distribution and the size of the fractures is $\alpha = \lambda$.

The generation of the different fracture distributions is presented in detail in the following section.

5.3.1 Generation of fracture distributions

In this section we will explain how we generate the various distributions of fractures. The fracture distributions presented in the numerical simulations are the following: (a) a random uniform, (b) a Gaussian, (c) an exponential, and (d) a Gamma distribution, as shown in Figure 5.9. The algorithm utilizes a different random number generator (Press et al., 1997), that varies according to the distribution we want to simulate. For each distribution, the generator is applied once to give x-coordinates, and completely independently once more to give z-coordinates. Both x- and z-coordinates are afterwards normalised to the grid size of the model.

Those pairs of x- and z- coordinates are the centres of the distributed fractures. The resulting distribution of fractures, without any alterations, is the parent spatial distribution. The size and orientation of the fractures are given as an input
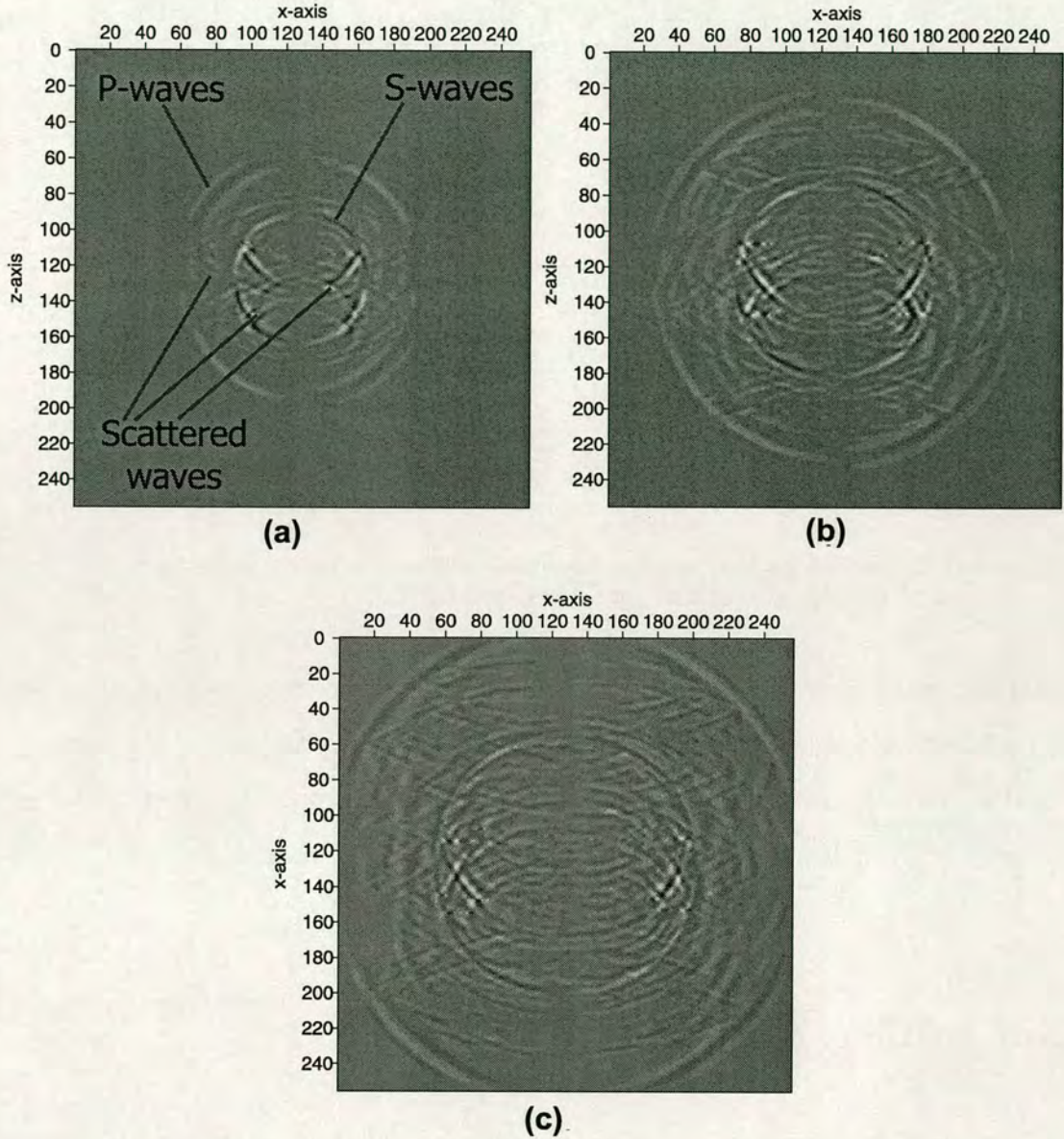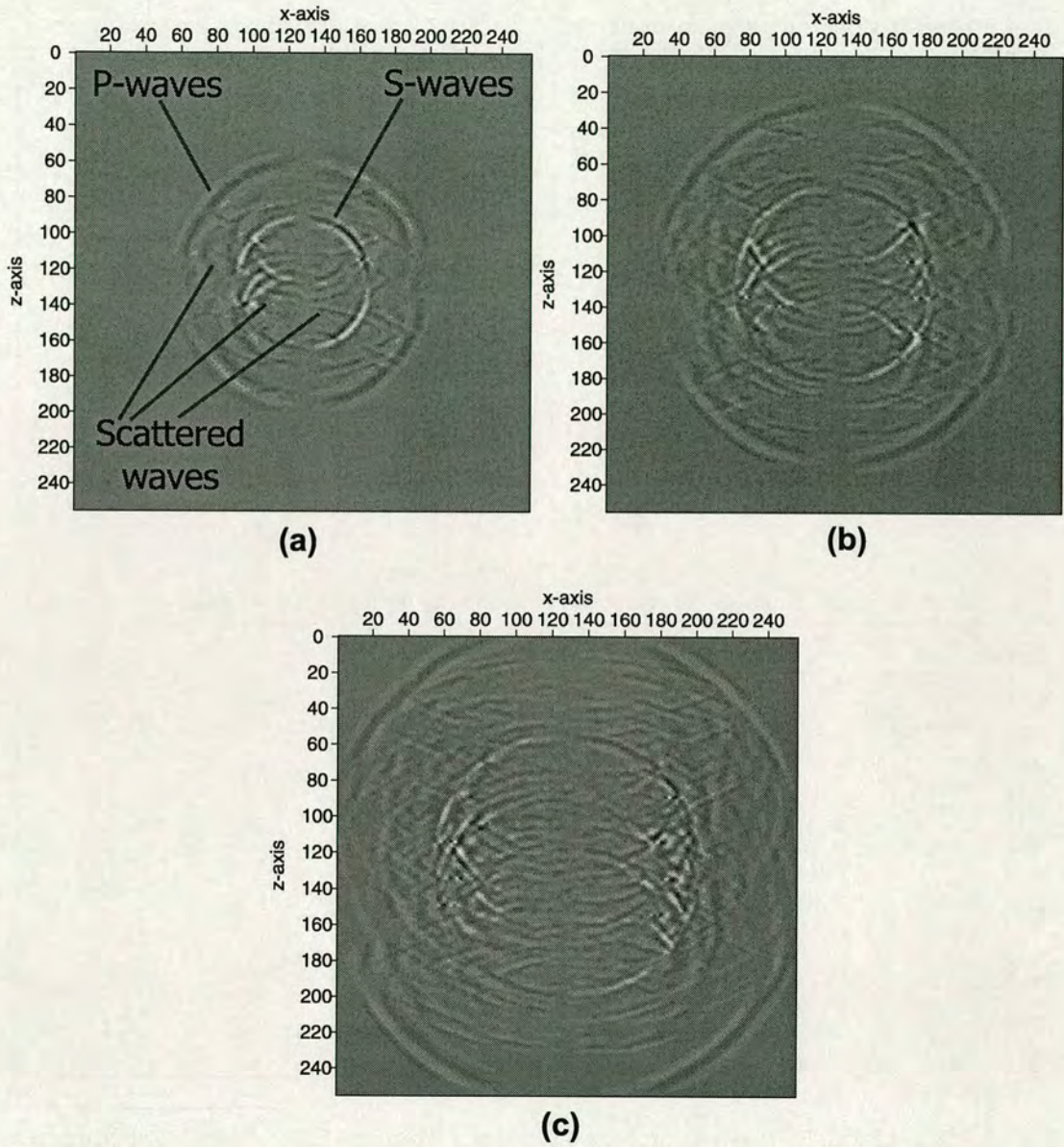
Figure 5.8: Snapshots taken at consecutive times, (a) 250 ms, (b) 350 ms, and (c) 450 ms, after the initialisation of the source for the model shown in Figure 5.7.

to the algorithm. In this paper all the fractures are parallel to the grid. Subsequently, the algorithm examines the fractures for any overlapping cases. We define overlapping as the case where the distance between the centres of two fractures is less than a predefined value. In the current application of the algorithm, we examined only the horizontal distances between pairs of fracture centres hav-
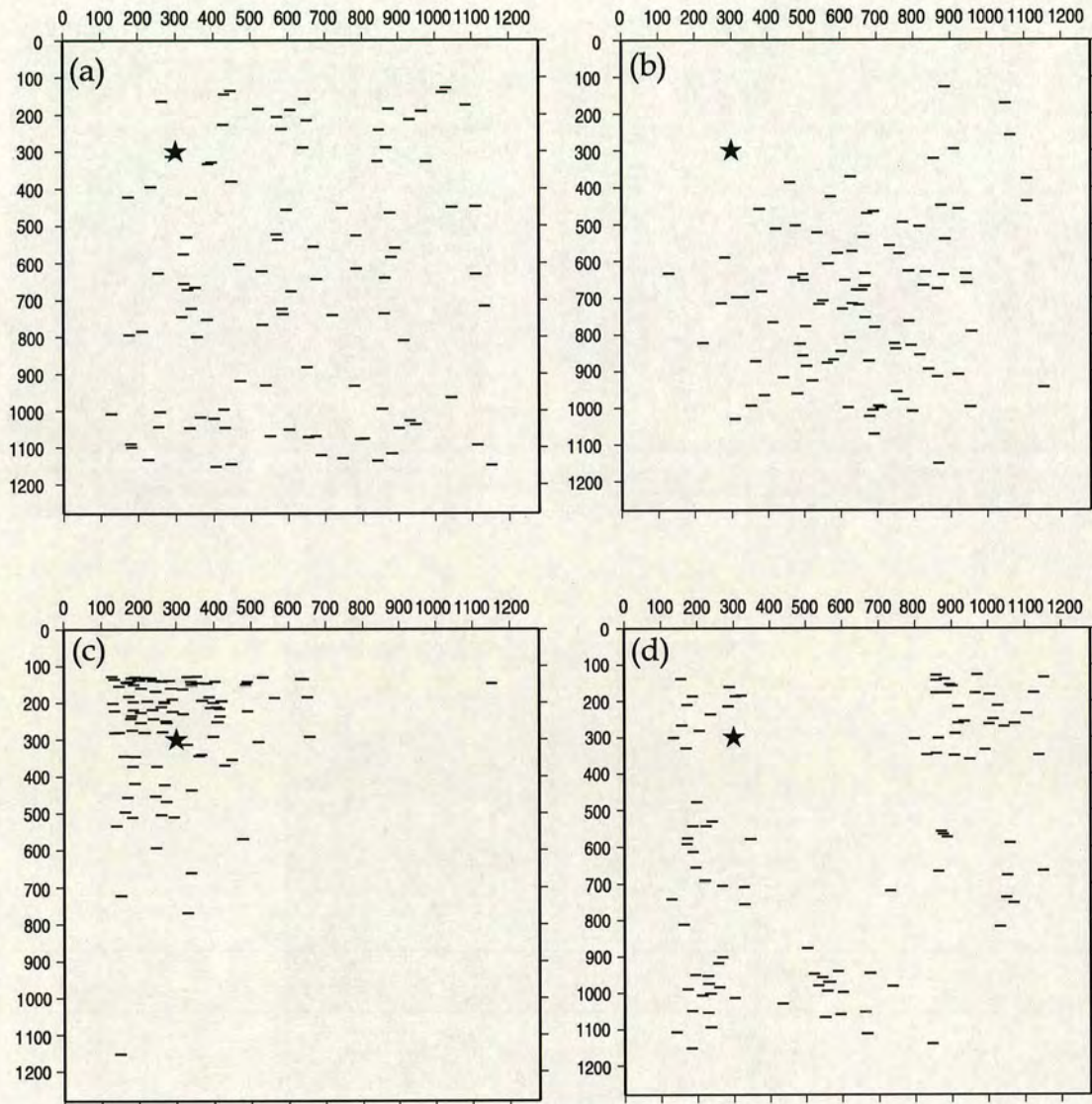
Figure 5.9: Models used to compute snapshots from spatially distributed fractures. The four different models, (a), (b), (c) and (d), illustrate different statistical distributions of fractures. P and S waves are generated at the source (represented by a star) and travel inside the medium.

ing the same z-coordinate. For simplicity in this realisation we deliberately avoid modelling intersected cracks, that is, conjugate fracture sets. However, in theory, such a case can also be modelled with the method we use. In this case, the second overlapping fracture is excluded from the distribution. After testing for overlapping, the remaining number of distributed fractures is counted. If that number is less than desired, the resulting distribution of fractures is rejected. The number

of fractures following the parent spatial distribution is raised by 5. A new group of fractures, spatially distributed according to the parent distribution, is chosen. The new group of fractures follows the same procedure that we described above. This process continues until the desired number of non-overlapping spatially distributed fractures is reached. A flow chart of the filtering algorithm is presented in Figure 5.10.

The final spatial distribution of the fractures is a result of the parent distribution after applying data filtering, so we call this the daughter spatial distribution. The spatial correlation in the daughter population is then determined by the two-point correlation function of the fracture centre locations in two dimensions. Figures 5.11, 5.12, 5.13, and 5.14 show the independent probabilities $P(x)$ and $P(z)$ as a function of the x- and z-coordinates of the centres of the fractures, for the daughter distributions (a), (b), (c), and (d) of Figure 5.9. In the same figures we show the two-point correlation function $C(r)$, for each of the four parent distributions, defined as

$$C(r) = \frac{1}{N^2} N_d(r), \tag{5.1}$$

where N is the total number of points and N_d is the number of pairs of points whose distance is less than r (Hentschel and Proccacia, 1983).

5.3.2   Numerical simulations

In the following simulations, each fracture has the same length, $2\alpha = 30m$, where α is the radius or the half length of the fracture. The surrounding solid (matrix) has P- and S-wave velocities $V_P = 3500 \ ms^{-1}$, $V_S = 2000 \ ms^{-1}$, and density $\rho = 2200 \ kgm^{-3}$. The source is now located at the upper left corner of the model. The source type is a vertical force. A Ricker wavelet with a dominant frequency of 40 Hz is used, so that $k_p\alpha = 1.08$, and $k_s\alpha = 1.88$ (where $k_p = 2\pi f/V_P$ and $k_s = 2\pi f/V_S$ are the P- and S-wavenumbers), or equivalently $\lambda_p/2\alpha = 2.9$
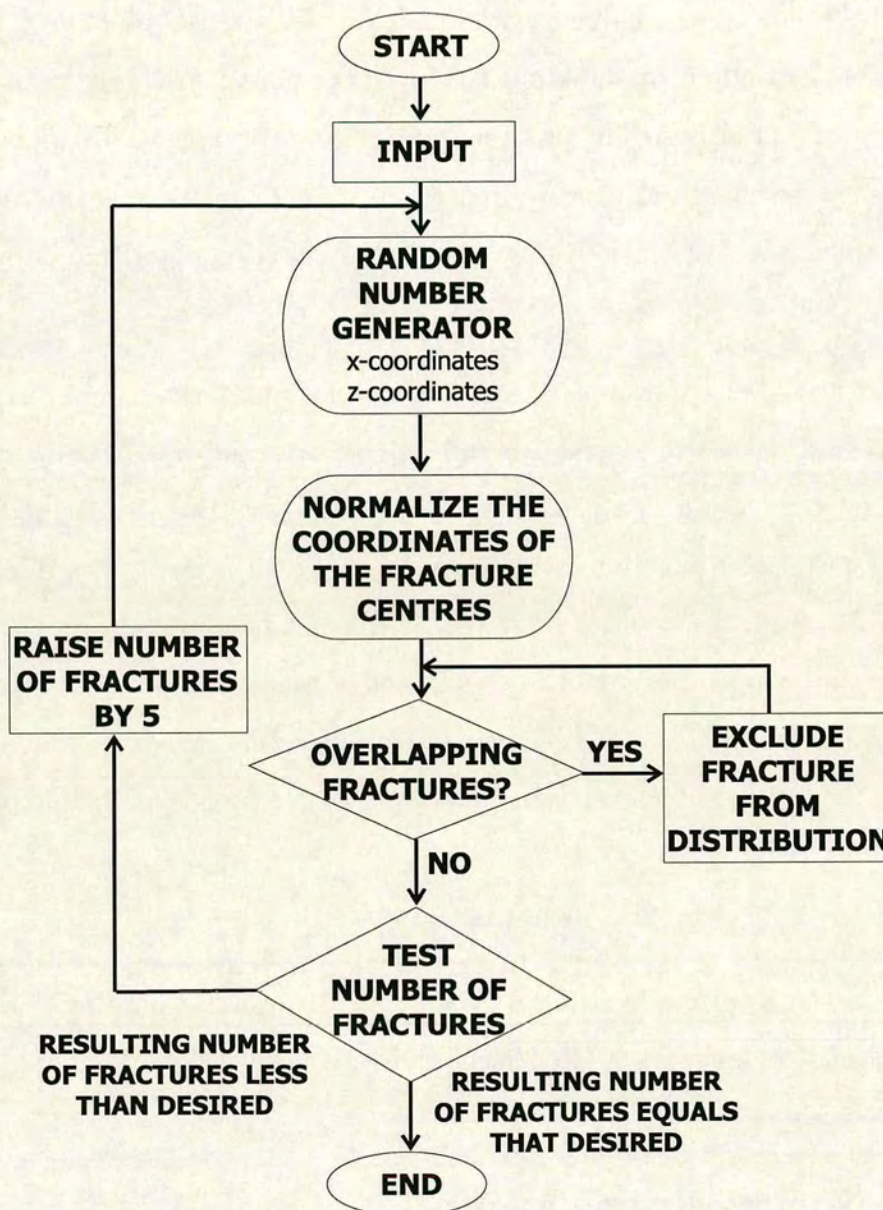
Figure 5.10: Flow chart of the algorithm used to generate the four spatial distributions of fractures shown in Figure 5.9.

and $\lambda_s/2\alpha = 1.67$ (where $\lambda_p = V_P/f$ and $\lambda_s = V_S/f$ are P- and S-wavelengths, respectively). For demonstration purposes, in all models we have used fracture compliance $Z_N = Z_T = 5.6 \cdot 10^{-10} [GPa]^{-1}$ at the elementary scale.

The resulting snapshots taken at t=100 ms, t=200 ms, and at t=300 ms are given at Figure 5.15, Figure 5.16, and Figure 5.17 respectively. As we can see

Figure 5.11: Statistical properties of the random uniform distribution of fractures in Figure 5.9(a). (a) Probability plot of the coordinate of the centre of fractures along the x-direction, (b) Probability plot of the coordinate of the centre of fractures along the z-direction, (c) Two-point correlation function of the parent distribution of fractures.

from Figure 5.9, fractures are more clustered in models (b) and (c), whereas they are more uniformly distributed and more scattered in models (a) and (d). In the extreme case of model (c), where the fractures are exponentially distributed, they are all concentrated in a small area around the source, forming a big cluster. That results in a lot of energy being trapped inside the cluster, between the various fractures. We observe the effect of the high clustering in the snapshots of the wavefield propagation at consecutive times. The wavefronts shown on the snapshots represent the statistical average effect of the fractures encountered
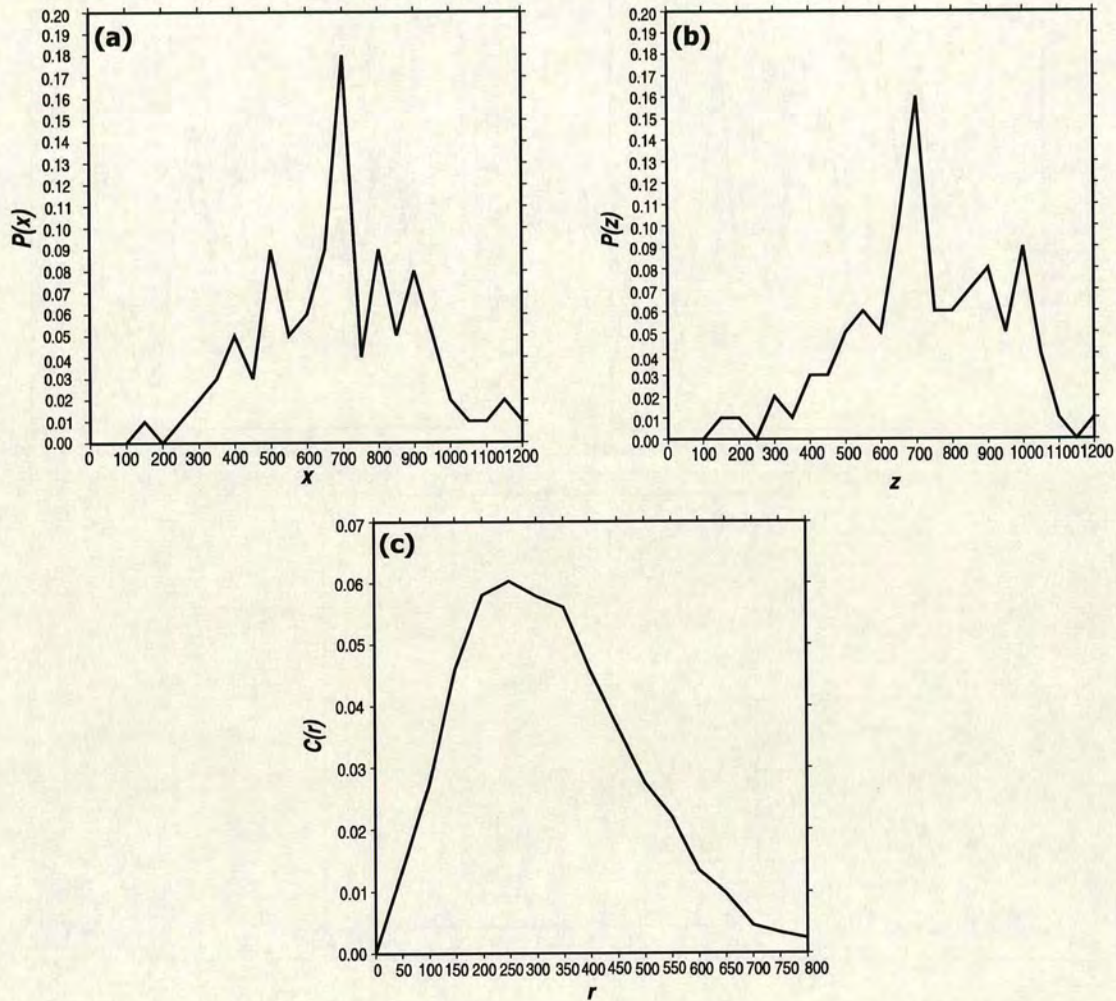
Figure 5.12: Statistical properties of the Gaussian distribution of fractures in Figure 5.9(b). (a) Probability plot of the coordinate of the centre of fractures along the x-direction, (b) Probability plot of the coordinate of the centre of fractures along the z-direction, (c) Two-point correlation function of the parent distribution of fractures.

throughout the wave path, thus resulting in the main expected P and S wavefronts. The energy attenuation becomes clearer at 300 ms, where we see a lot of energy remaining in the area of the fracture cluster, whereas the main wavefront of the S-wave is almost fully attenuated. In model (b) where the fractures follow a Gaussian distribution, the fractures also form a big cluster in the centre of the model, but in this model they occupy more space and the distance between the various fractures is greater. In this case, similar to model (c), we see a significant
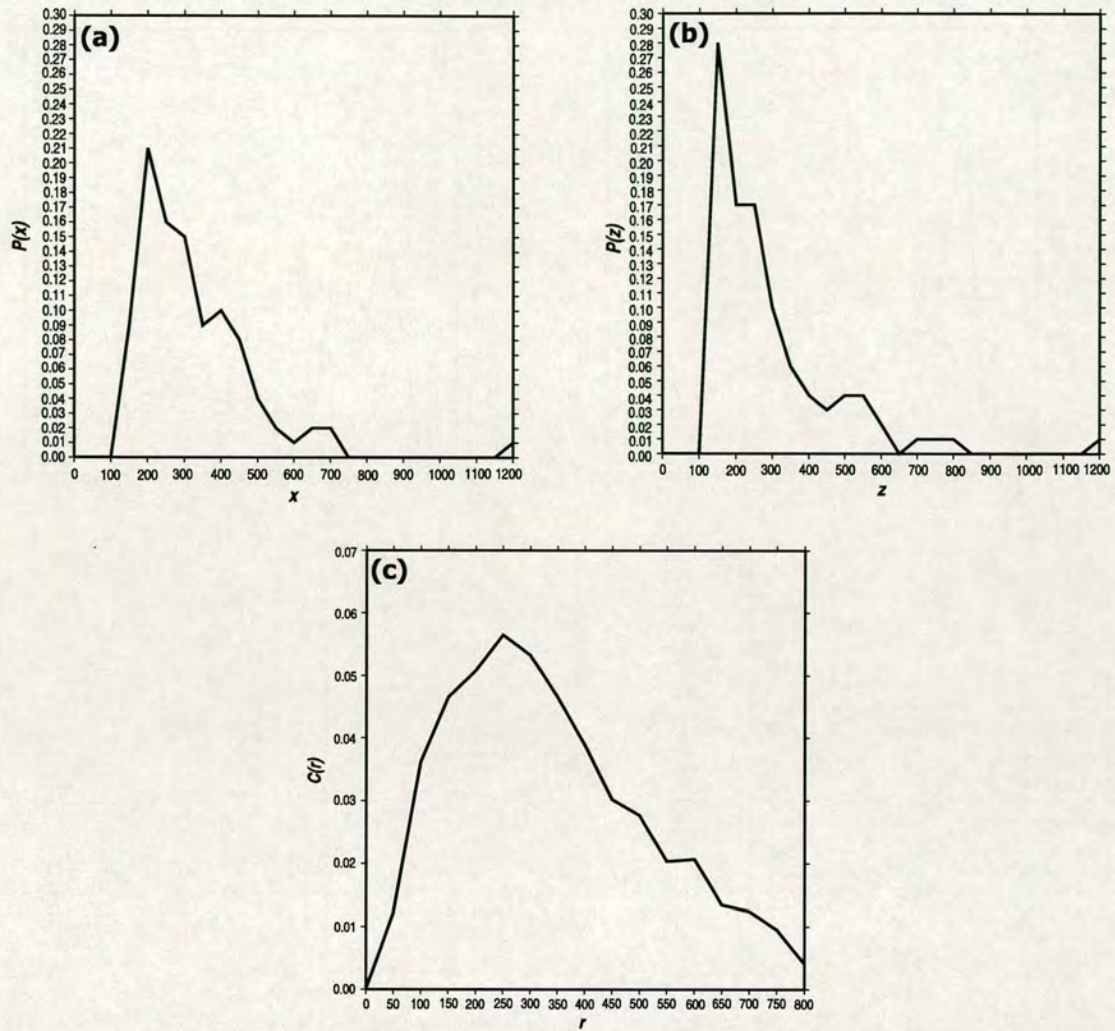
Figure 5.13: Statistical properties of the exponential distribution of fractures in Figure 5.9(c). (a) Probability plot of the coordinate of the centre of fractures along the x-direction, (b) Probability plot of the coordinate of the centre of fractures along the z-direction, (c) Two-point correlation function of the parent distribution of fractures.

amount of energy trapped in the fracture cluster. However, we can observe from the snapshots that there is more energy coming through the cluster. The opposite case of the two previous ones is described in model (d). In this case the fractures follow a Gamma distribution (a power-law with an exponential tail), thus forming a number of small clusters that are significantly distant from each other. It is observed in the snapshots that in this case the main P- and S-wave arrivals are once again clearly observed, and have the highest amplitude compared with the
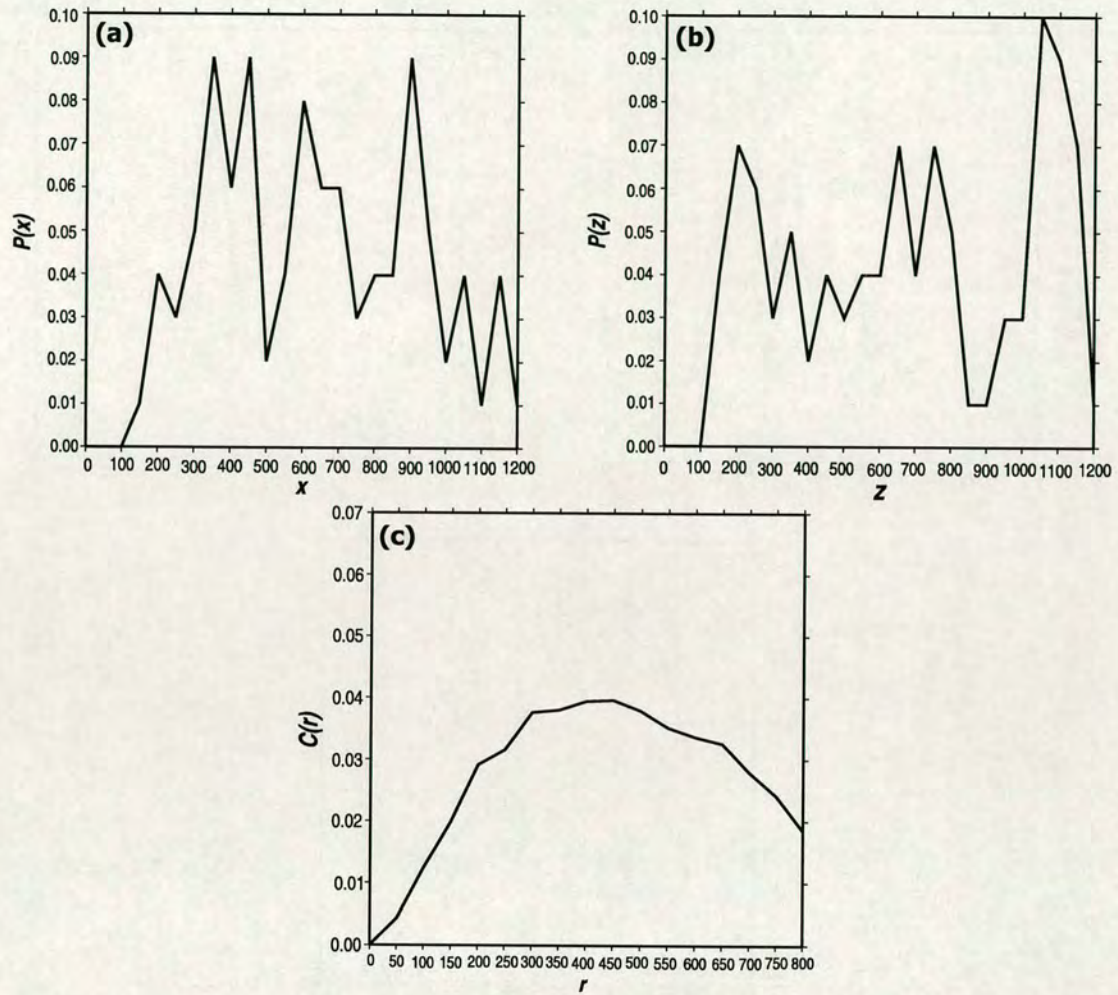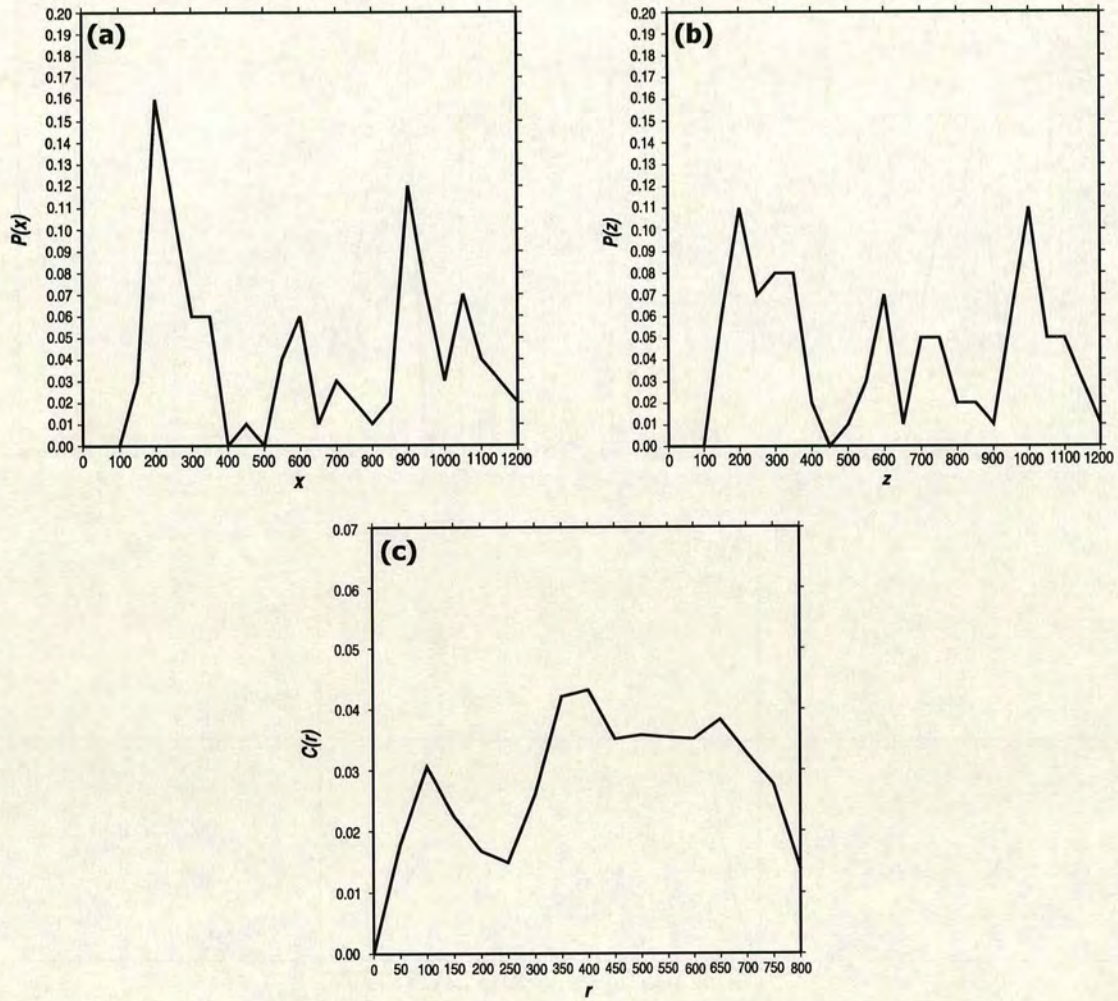
Figure 5.14: Statistical properties of the Gamma distribution of fractures in Figure 5.9(d). (a) Probability plot of the coordinate of the centre of fractures along the x-direction, (b) Probability plot of the coordinate of the centre of fractures along the z-direction, (c) Two-point correlation function of the parent distribution of fractures.

rest of the cases. We believe that the small size of the clusters formed with a Gamma distribution, lets most of the energy propagate through the whole model, because the cluster does not trap a significant amount of energy inside it. Finally, model (a), where fractures are randomly uniform distributed, describes a case where there is no clustering. The fractures are distributed throughout the whole medium. Although the snapshots show some trapped energy between the fractures, the main wavefield propagation is quite clearly observed.
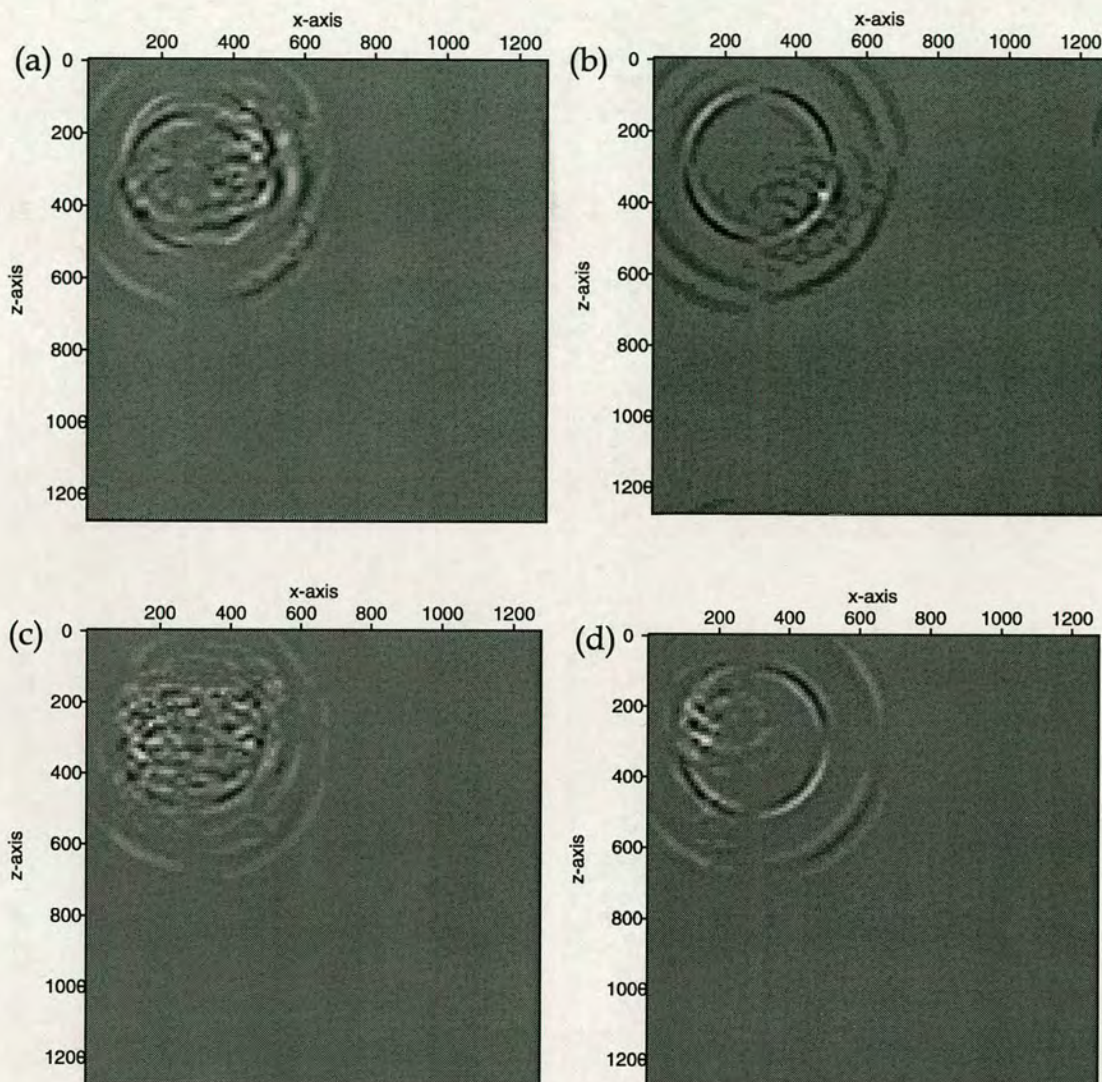
Figure 5.15: Snapshots taken at t=100 ms. (a) to (d) correspond to fracture distributions (a) to (d) in Figure. 5.9. The numbers on the top and on the left side of the snapshots are the model dimensions. We present the x-component of motion.

In summary, we can see that the wavefield propagates with the least energy attenuation when we have the least fracture clustering as shown in model (d), while attenuation increases with the increase of clustering as shown in models (a), (b) and (c).

In the following, we take the models of Figure. 5.9 and calculate the synthetic seismograms. The receivers are positioned along the z-direction and shifted by
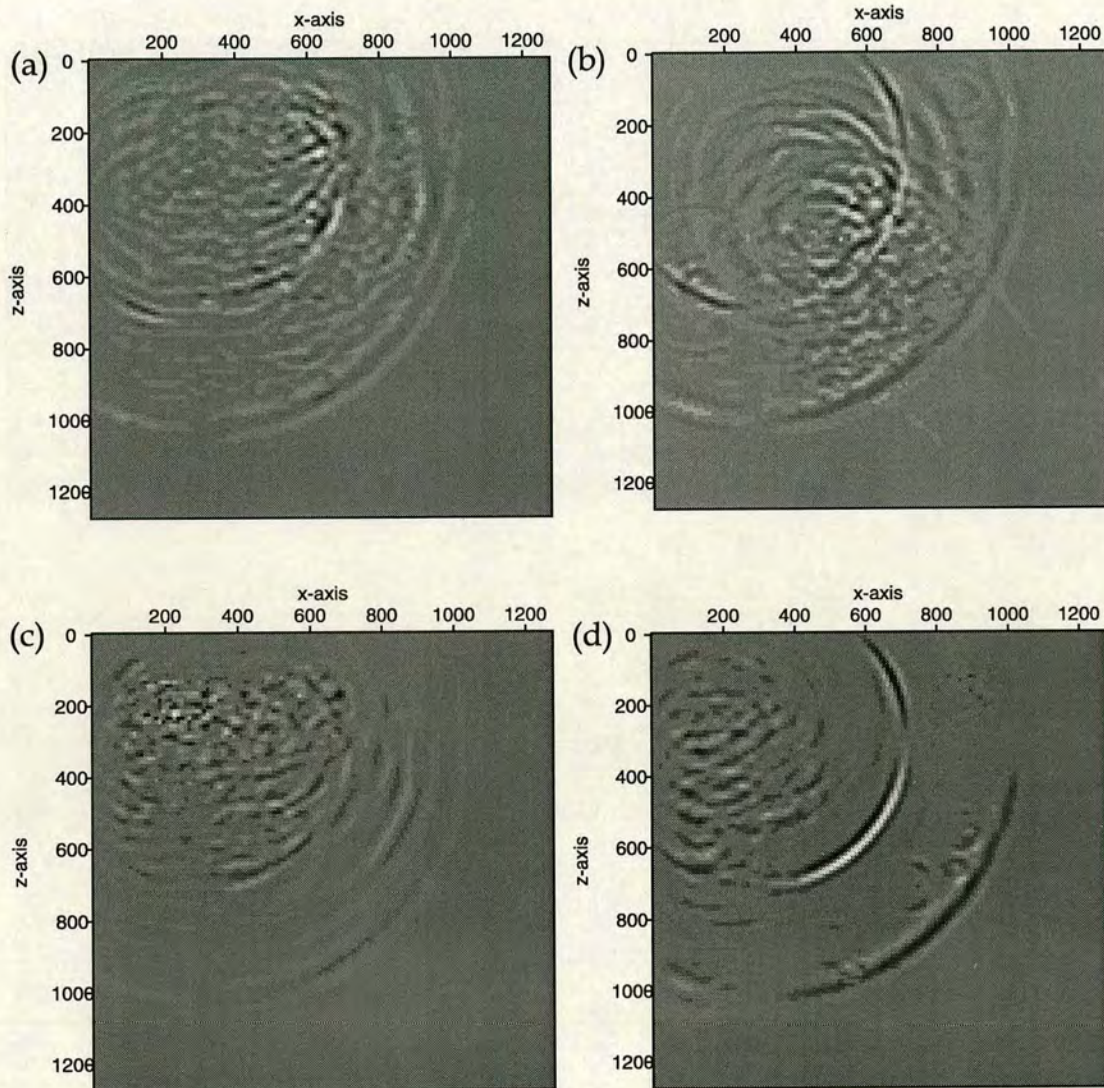
Figure 5.16: Snapshots taken at t=200 ms.

1050 m in the x-direction. We consider five cases, (o) no fractures, (a) random uniform distribution, (b) Gaussian distribution, (c) exponential distribution, and (d) Gamma distribution. Fig. 5.18 shows comparisons of waveforms of the x-components from trace number 100, corresponding to the depth of 1000 m, of each of the models and their corresponding Fourier spectra. In the figure we notice a shift of energy to frequencies higher than the dominant frequency of the initial Ricker wavelet. If we compare the global maxima for all the cases examined, we can see in model (a) the maximum energy is at about 40 Hz, which
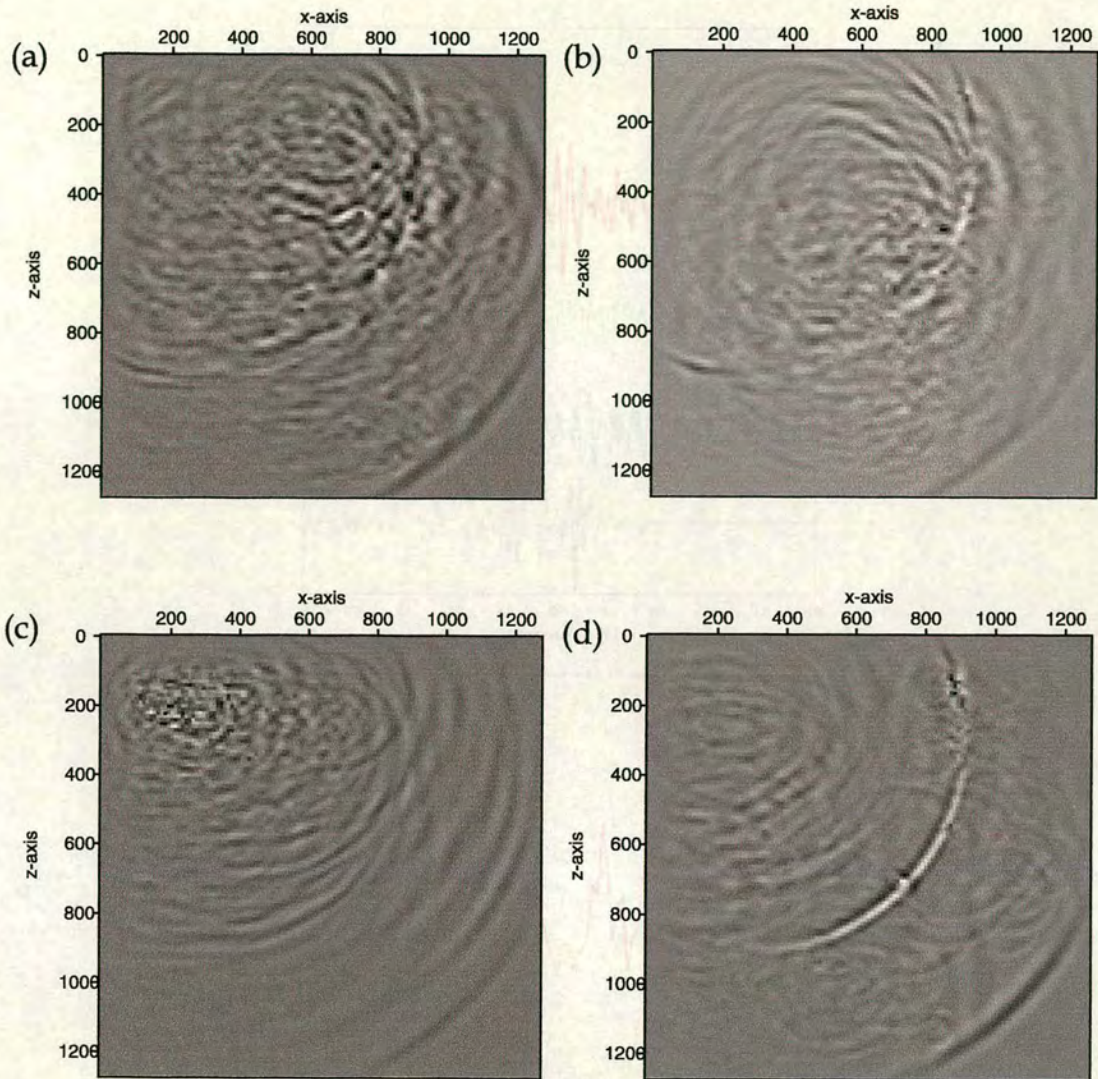
Figure 5.17: Snapshots taken at t=300 ms.

is the source dominant frequency, in model (b) it is at about 49 Hz, in model (c) it goes up to about 67 Hz, and in model (d) it is at 60 Hz. In terms of distance that the wave travels between two consecutive scatterings, in model (a) we have the longest distance and in model (c) the shortest. In model (a) we do not see any frequency shift of the energy, while in model (c) we see the maximum frequency shift indicating that there is a systematic shift of energy to higher frequencies when the multiple scattering dimension becomes shorter.
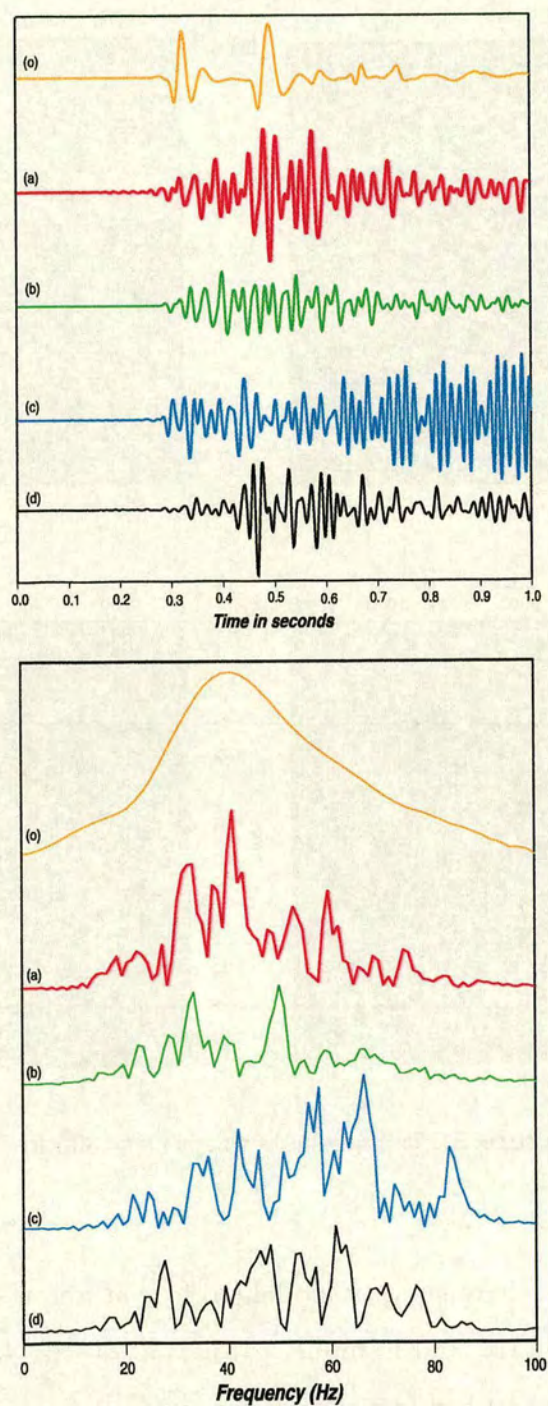
Figure 5.18: Comparison of synthetic seismograms and corresponding spectra from various distributions of fractures : (o) No fractures, and (a), (b), (c), and (d) correspond to the fracture distributions of Figure 5.9 (trace number 100).

Another feature in the spectra is the local minima of the amplitude. The first local minimum is observed at 30 Hz where the length of the fractures is approximately a quarter wavelength. There are also local minima at around 38 Hz, 58 Hz and 70 Hz. Those minima can be a result of the constructive or destructive interference of multiply scattered waves from the fractures. Finally we notice that the amplitude of the wavefield from distribution (b) is much smaller and has relatively low frequency content compared with the other distributions. This is possibly because in this case the local fracture density along the wave path towards the receivers is higher than the other cases. This example demonstrates clearly that different distributions of fractures have a significant influence on multiple scattering.

5.4   Power-law (fractal) distribution of fracture sizes

The final example is used to model wave scattering from discrete fractures with a scalelength distribution. The model we use is given in Figure 5.19(a), where the variation of crack sizes follows a von Kármán correlation function, which gives a power-law distribution (Wu, 1982). We can also use other correlation functions, such as Gaussian or exponential functions. The model shown in Figure 5.19(a) is generated with a correlation length of 40 m. In this model we have 400 fractures randomly distributed in a 2560x2560 m^2 area. The source is a vertical force, it is located in the centre of the model, and is represented by a star in Figure 5.19(a). The longest fracture is 100 m and the shortest 10 m. The mean length of the fractures $< \alpha >$ is 27.5 m, and the fracture density of the medium $\varepsilon = N_f < \alpha >^2 /S$ is 0.046, where N_f is the number of fractures and S is the surface of the medium. For the estimation of fracture density we desided to choose the above definition, instead of $\varepsilon = N_f < \alpha^2 > /S$. (Queen and Rizer, 1990) discuss the two

definitions of fracture density and conclude that the later definition emphasize the contribution of cracks with large sizes. The peak frequency is 40 Hz, which gives $k\alpha$ ranging from 0.36 to 3.6 for P-waves and from 0.63 to 6.3 for S-waves, where k is the wavenumber, the P-wave velocity is 3500 ms^{-1} and the S-wave velocity is 2000 ms^{-1}.
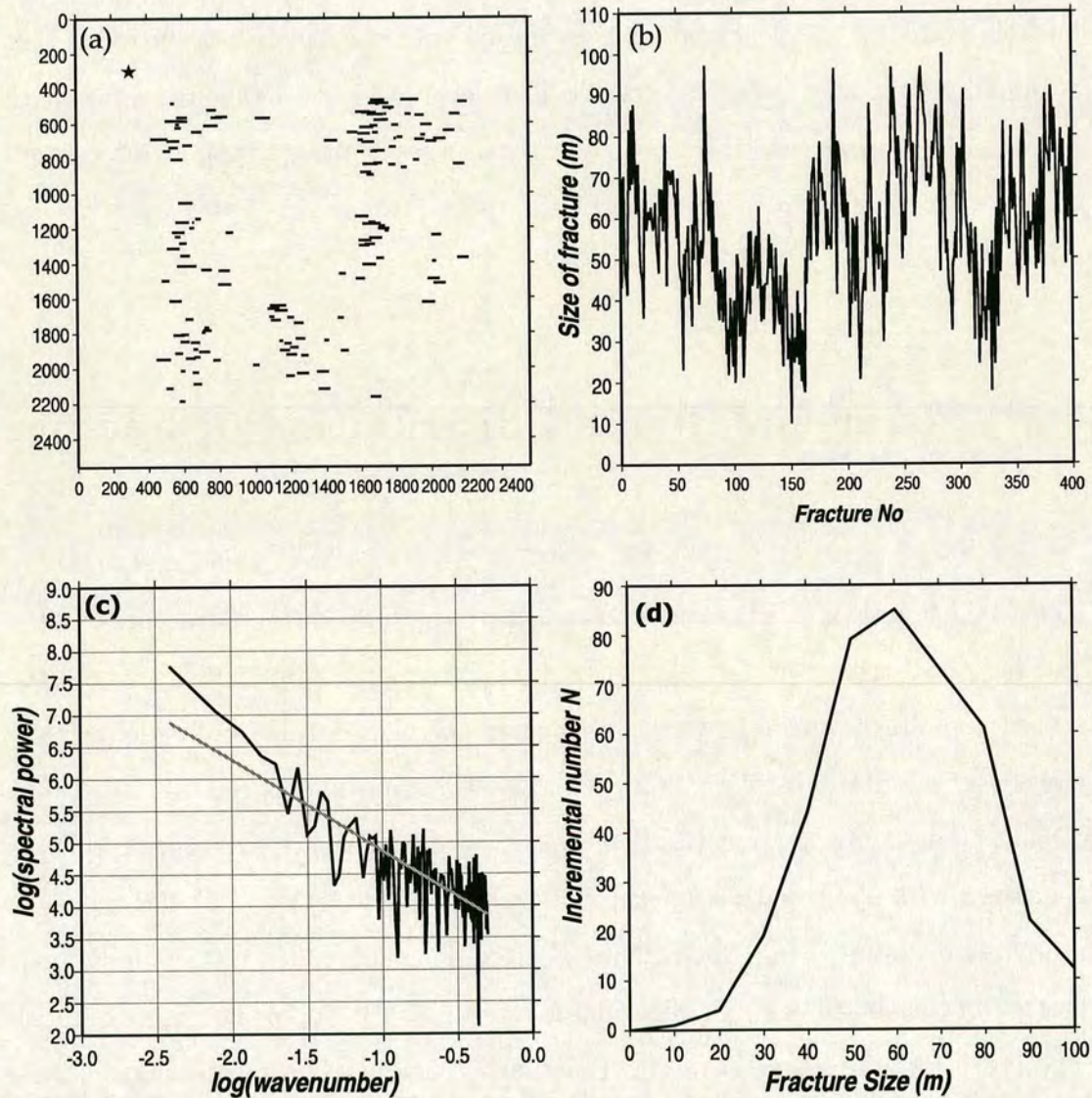
Figure 5.19: (a) Model used to compute synthetic seismograms in a fractured medium with power-law distribution of fracture sizes. (b) Illustration of the sizes of fractures in model (a), that follow a power-law distribution. (c) Power spectra of fracture size distributions shown in (a). (d) Cumulative number of the fractures of model (a) plotted against the fracture size.

Figures 5.19 (b), (c) and (d) illustrate the statistical attributes of the size distribution of the fractures. Figure 5.19(b) shows the different sizes of fractures in the model. Figure 5.19(c) shows the power spectrum of the fracture size distribution (plotted in log-log scale). We see that the variation can be fitted with a straight line. Such a model, that is, with a linear variation of the logarithm of the power spectrum with the logarithm of the spatial wavenumber, is a power-law distribution, often called a fractal (Bonnet et al., 2001). Figure 5.19 (d) shows the variation of the incremental number of fracture population in the corresponding range of fracture sizes. To examine the behaviour of the wavefield due to the fractal distribution of fractures, we take snapshots at consecutive times, t=200 ms, t=250 ms, t=300 ms and t=350 ms. The snapshots are presented in Fig. 5.20. As we can see from the snapshots, the behaviour of the wavefield is very complicated. Clearly, the main P- and S-waves are fading away (heavily attenuated) as they propagate through the medium. This can be attributed solely to the scattering taking place as the wavefield propagates through the high fracture density clusters, since there is no intrinsic anelastic absorption in the model. That is confirmed by the snapshots, where we can see high energy concentrated at the exact positions of the fracture clusters. That is particularly clear in Fig. 5.19(d), where we have high amplitudes in the areas of fracture clusters resulting in strong coda waves, and at the same time low amplitudes of the main P- and S-waves.

5.5 Summary

From the numerical examples we may come to some interesting conclusions. Firstly, we can see the importance of the spatial distribution of fractures in a medium. Our results show that in areas with fracture clustering, there is strong and coherent energy. Also, high clustering results in high local fracture densities, which can cause the energy to be trapped in a certain area. This in turn increases
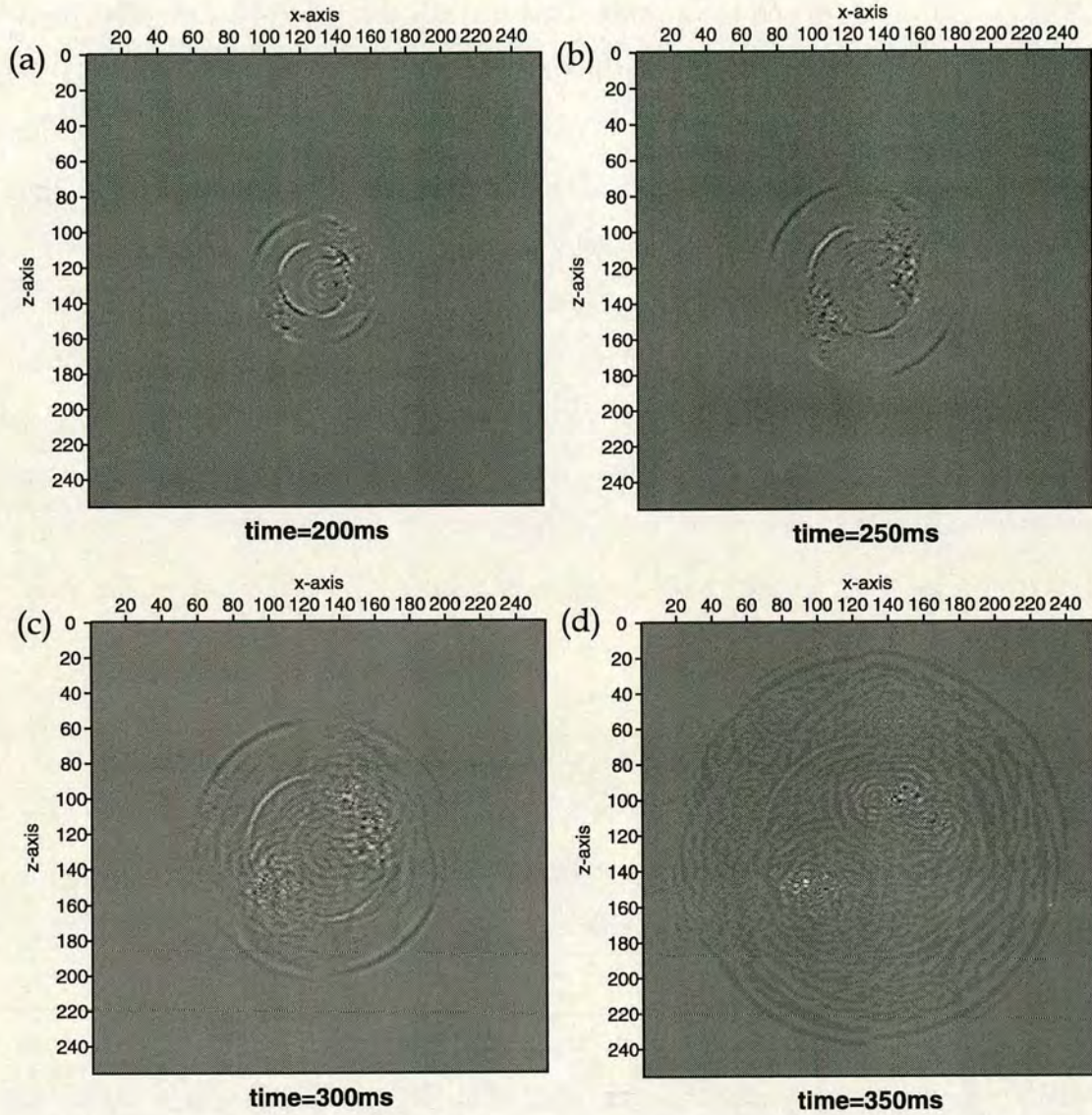
Figure 5.20: Snapshots from model in Fig. 11(a) taken at (a) t=200 ms, (b) t=250 ms, (c) t=300 ms, and (d) t=350 ms.

the complexity of the wavefield and makes individual phases and their identifications very complicated. Also, we observe that different spatial distributions result in different frequency content on the recorded wavefield. The scattering reduces the P and S wave amplitude, in the time domain, and filters or introduces new frequencies in the frequency domain. As we expect frequency-dependent seismic scattering depends on the spatial distribution of fractures (Leary and Abercrombie, 1994). In addition, of great importance is the fracture size relative to the

wavelength, independent of the spatial distribution. It is demonstrated that, when fractures are smaller than the wavelength, they act as point scatterers and generate coherent secondary wavefields according to Huygens' principle, whereas when the size approaches the wavelength they act as individual interfaces and the wavefield is more complicated. To complete our study, we have examined a case of fracture sizes that follow a power-law or fractal distribution. The wavefield generated shows very strong coda waves. This observation confirms the importance of spatial and scalelength distributions in modelling fractured rock.

Numerical modelling techniques, such as the one presented here, can be a useful tool in the understanding of the important role of fractures and their effects on wave propagation. The knowledge gained by such studies may ultimately lead to the extraction of valuable information about the fracture distributions in natural rocks, directly from seismic data. In addition, our method may potentially provide a test of fracture imaging using seismic methods (as demonstrated by Nihei et al., 2000), and purely statistical characterisation of fractured reservoirs based on the concept of seismic scattering. However, the idealised fracture distributions examined here, while providing insight, must be replaced by ones which more closely reflect the physics of fracture growth in any realistic application. This topic is the subject of the next chapter.

CHAPTER 6

Evolution of fracture networks and multiple scattering of seismic waves in fractured rock.

6.1 Introduction

In Chapter 4, we investigated the effects of fracture sizes and spatial distributions on seismic waves. When we examine the properties and the behaviour of a fracture network, it is very important to create a more realistic network that will represent more closely the properties of fractures in natural rocks. Here we use a model of rupture designed to reproduce structural patterns observed in the formation and evolution of a population of strike-slip faults and fractures (Narteau, in press). This model is a multiscale cellular automaton with two states. An active state represents actively slipping fracture segments. A stable state represents 'intact' zones in which the fracturing process is confined to a smaller scale. At the elementary scale, the transition rates from one state to another are determined with respect to the magnitude of the local strain rate and a time

Evolution of fracture networks and multiple scattering of seismic waves in
fractured rock.

124

dependent stochastic process. At increasingly larger scales, healing and fracturing are described according to geometric rules of interaction between active fault segments based on fracture mechanics. A redistribution of the strain rates in the neighbourhood of active faults at all scales ensures long range interactions and non-linear feedback processes are incorporated in the fault growth mechanism. Typical patterns of the development of a population of faults are presented involving nucleation, growth, branching, interaction and coalescence. The material properties are uniform, so the complex behaviours result solely from the random fluctuations and physical interactions. Consequently, the entire process of fault development is an emergent property of the model of fault interaction and does not depend on pre-existing material heterogeneity.

We use the realistic representations of a fracture network to examine scattering attenuation and investigate the effects of this process in the wavefield properties. Seismic attenuation is recognised as a potentially important quantity in reservoir characterisation. Attenuation has been associated with fractures, petrophysical properties, and the general viscous motion of saturating fluid (Leary, 1995a; Leary, 1995b). Attenuation of seismic waves except that caused by geometric spreading is caused by intrinsic absorption (viscous damping) or by scattering. Which of these two mechanisms dominates in any given situation depends on the relative wavelengths of the seismic wave and the acoustic heterogeneities of the fracture system. In the models presented here the results are related only to scattering attenuation. Scattering involves no energy loss, but produces a more extended, lower amplitude wavetrain by the resulting interference.

We model seismic wave propagation in each model that represents the consecutive stages of the evolution of the fracture network. We use the method presented in Chapter 2 for the numerical modelling of the wavefield propagation in the medium. We show snapshots of the wavefield at a certain time step for each stage of the evolution and demonstrate how the changing characteristics of the

fractures affect wave propagation. We examine scattering attenuation of P-waves
for a range of frequencies. We show how variations in the properties of the frac-
tured medium due to the evolution of the fractures are exhibited in the behaviour
of Q^{-1}. We calculate the scattering attenuation as a function of frequency for
each stage and fit the results with a polynomial. We use a statistical method
to pick the best fit and examine the variation of the polynomial. Finally, we
present seismic traces at two source-receiver directions, parallel and perpendicu-
lar to the fracture orientation, to examine the azimuthal dependence of scattering
attenuation. Our results show that there is a significant frequency dependence of
scattering attenuation, and that high values of attenuation observed at certain
frequencies may be linked to characteristic lengthscales of fractures. Also frac-
ture density varies as the network evolves, resulting in significant changes in the
amplitude of attenuation. In addition, our results show that scattering is also
dependent on the angle of the propagation directions, relative to the orientation
of the fractures.

6.2   Generation and evolution of fracture net-work

In this study we use a multi-scale cellular automaton model by Narteau (in press)
to generate the fracture patterns. It is a multi-scale model of rupture of a crustal
shear zone under constant external forcing and reproduces different structural
properties that are observed in the formation and evolution of a population of
strike-slip fractures. In this model a 2-dimensional regular lattice of cells models
a crustal shear zone. At the elementary scale of a fracture segment, a non-
stationary stochastic process controls the formation and the evolution of a pop-
ulation of strike-slip fractures. Geometric rules of fault interactions based on
fracture mechanics and a redistribution mechanism of the strain rates define how

a fracturing state is measured at different scales and the local strain rates evolve from one another.

From a uniform state at $t = 0$, an evolving population of fracture segments creates a heterogeneous spatial distribution of the strain rates. In regions where the strain rates are high, the microfracture density increases, the fracturing process reaches the segment scale and new fault segments may link together in larger faults. In regions where the strain rates are low, the healing process may deactivate fracture segments and reduce the length of active fractures. In response to tectonic loading, this permanent internal process of evolution between the strain rates and a population of fault segments may be described as a 'self-organised' process (Sornette et al., 1994).

The whole system is polarised by the orientation of the tectonic loading and its pre-existing damages. σ_1, σ_2, and σ_3 are the compressive principal stresses. In the model these principal stresses are North-South, vertical and East-West respectively, and, with respect to the Coulomb-Mohr's theory of fault orientations, only vertical strike-slip fracture segment can form. Pre-existing damage favours right-lateral fractures and new segments grow following a main direction, at an angle θ from the maximum compressive stress. θ is taken close to $N30^oW$ implying a conventional coefficient of internal friction $\mu \approx 0.6$. More detailed description of the mechanisms of interaction between fractures, the evolution of the network and the creation of new fracture patterns is given in Appendix B.

In the models of fracture networks presented in this chapter the evolution of the fracture patterns happens under a 'low' tectonic loading. Figure 6.1 shows stages (a)-(l) of a fracture network as it evolves in time as described before. Although there is no clear boundary between them, it is possible to distinguish different phases in the evolution of the fracture patterns.
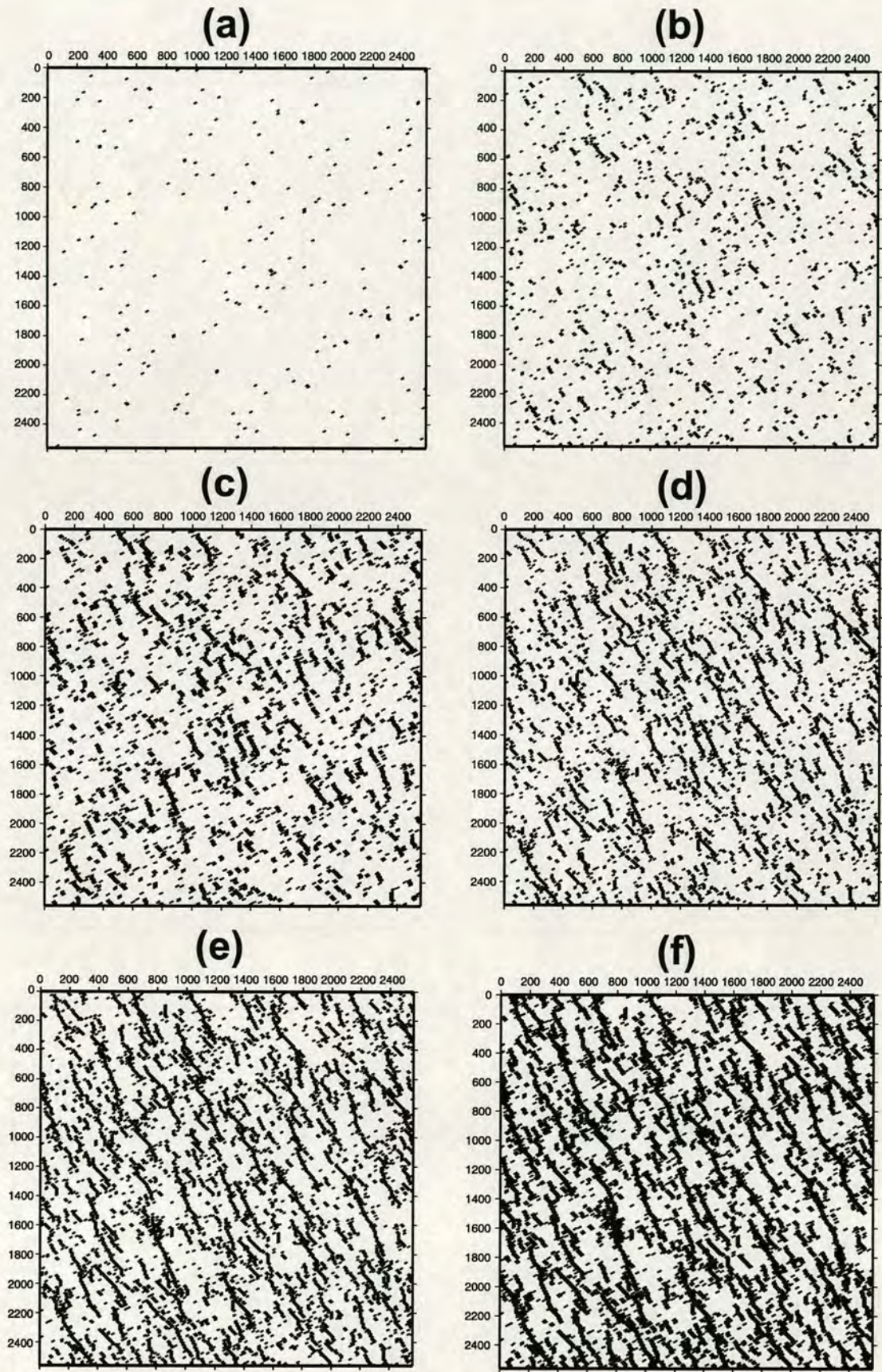
Figure 6.1: Fracture patterns that represent consecutive stages at the evolution of the fracturing. In this figure we present stages (a) - (f). The horizontal direction is the x-direction (metres) and the vertical direction is the y-direction (metres).

(g)

(h)

(i)

(j)

(k)

(l)
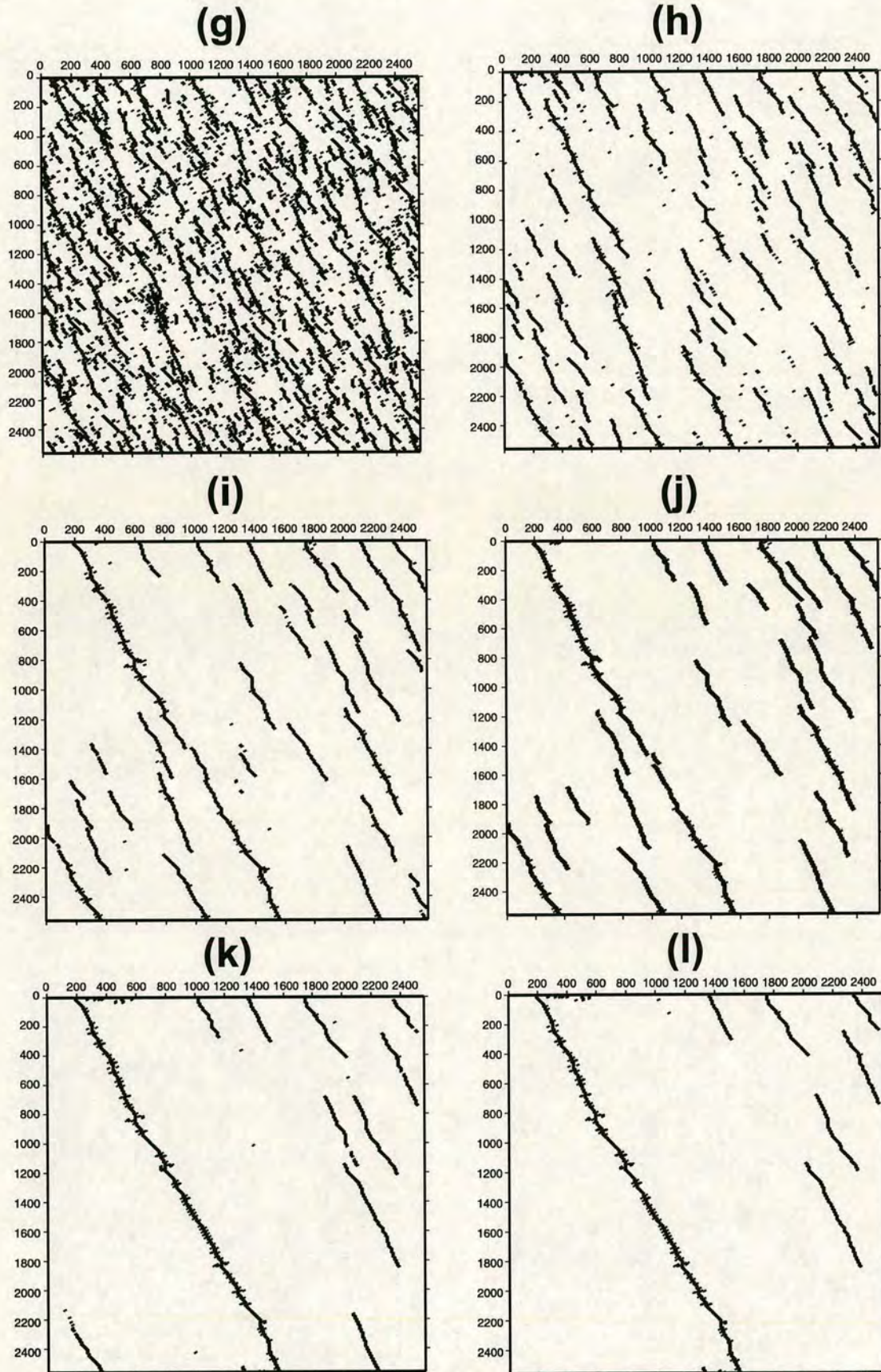
Figure 6.2: Fracture patterns that represent consecutive stages at the evolution of
the fracturing. In this figure we present stages (g) - (l). The horizontal
direction is the x-direction (metres) and the vertical direction is the y-
direction (metres).

Evolution of fracture networks and multiple scattering of seismic waves in fractured rock.

129

Stage (a) is the start of the nucleation stage where we have the first active cells, but no fractures of length two cells or more. At stage (b) we have the formation of the first fractures from the interaction of adjacent active cells. At that stage the growth phase begins and coexists with the nucleation phase. Stages (c) and (d) show the continuation of the nucleation phase together with the growth phase, where we have an increasing number of fractures appearing on the medium. Most of the fractures have an orientation close to the main direction of shear slip. At stage (e) the system reaches the percolation threshold, where a connected fracture network spans the model space. At stage (f) the system has the maximum number of active cells. In stages (g) and (f) there is no characteristic lengthscale of the fractures since the correlation length is infinite. At stage (g) we have the beginning of the interaction phase which continues for stages (h) and (i). At stage (h) the growth phase ends and the system moves towards relaxation. Stage (j) is the initiation of the concentration phase where we have the formation of major fractures from smaller ones. That phase continues for stages (k) and (l), until the system reaches a stable state and only major fractures

6.3 Wave propagation in an evolving fracture network

We conduct forward modelling of wave propagation for each one of the models that represent stages (a)-(l) (Figures 6.1 and 6.2) of the fracture network evolution, to examine the variation in scattering attenuation and its frequency dependence. To ensure consistency between the different models we use the same background medium in all the cases. The background medium parameters are $V_P = 3300 ms^{-1}$, $V_S = 2000 ms^{-1}$, $\rho = 2200 kgm^{-3}$. For the implementation of the fractures we assume that the fracture compliance's are constant having values $Z_T = Z_N = 5.6 \cdot 10^{-10} [GPa]^{-1}$.
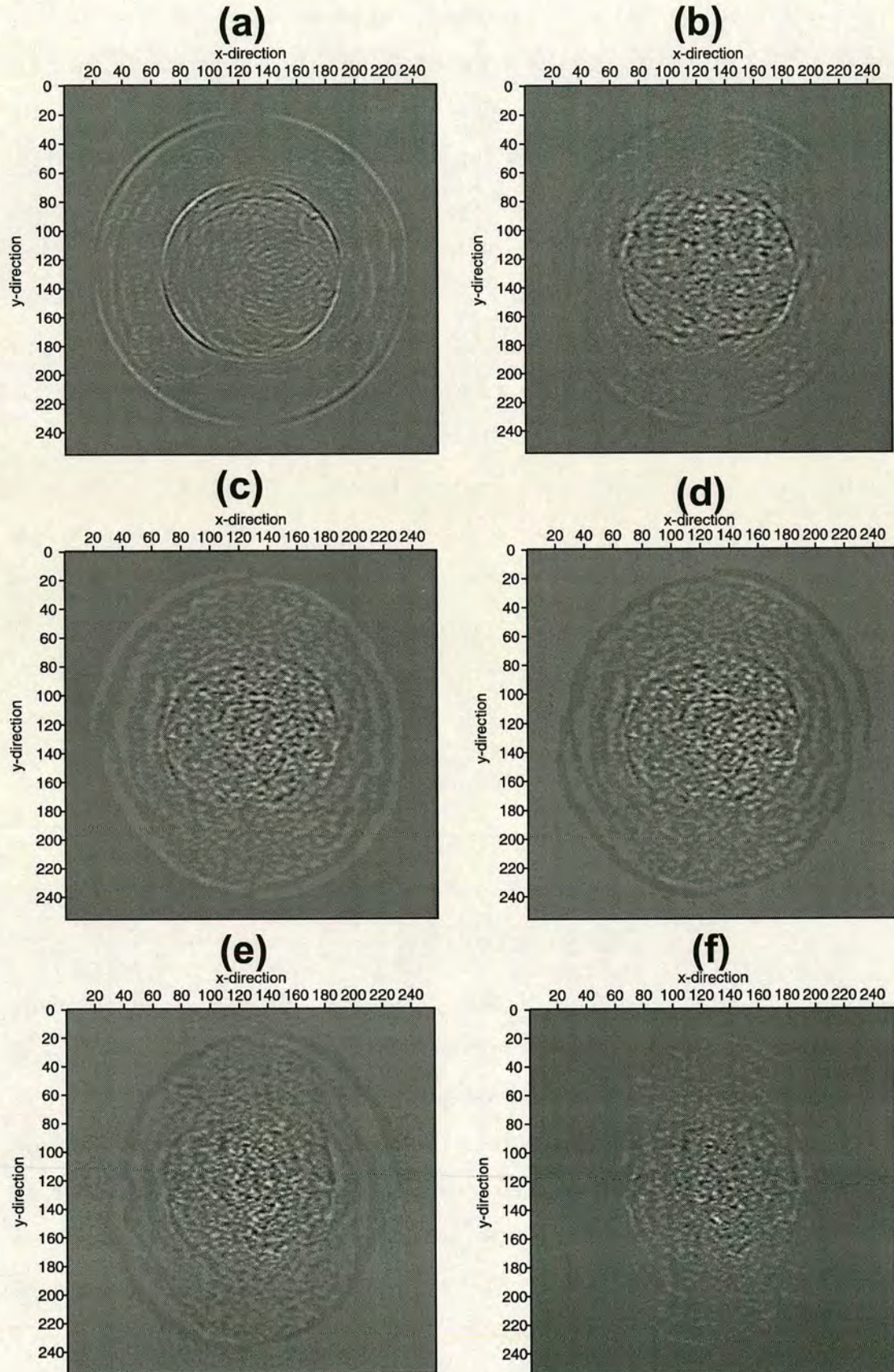
Figure 6.3: Snapshots taken at 350 ms after the initialisation of the source. Figures
(a),(b),(c),(d),(e) and (f), correspond to the respective fault patterns of
Figure 6.1. The horizontal direction is the x-direction (X 10 metres) and
the vertical direction is the y-direction (X 10 metres).

Figure 6.4: Snapshots taken at 350 ms after the initialisation of the source. Figures (g),(h),(i),(j),(k) and (l), correspond to the respective fault patterns of Figure 6.21. The horizontal direction is the x-direction (X 10 metres) and the vertical direction is the y-direction (X 10 metres).

We use a grid of 256×256 elements, with spatial grid-step $10m$ and time-step $0.001sec$. The source wavelet is a Ricker wavelet with a dominant frequency of $30Hz$ and a pulse initial time of $0.1s$. The source is located in the centre of the models ($x = 1280m$, $z = 1280m$). For each model we generate synthetic seismograms, and output snapshots that describe the wave propagation at consecutive time steps. Figures 6.3 and 6.4 shows snapshots of the wavefield taken at $350ms$ after the initialisation of the source, for the consecutive stages of the evolution of the fracture network that are shown on Figures 6.1 and 6.2. The snapshots show a clear variation at the different stages of the fracture evolution. At the beginning of the nucleation [stage (a)] there are only a few active cells, all of which are much smaller than the wavelength. Therefore they act as individual point scatterers and the wave travels undisrupted with a circular wave front. At stages (b)-(d) the first fractures are created and also interaction and formation of large fractures happens. As a result some fractures act as point scatterers and others that are larger than the wavelength act as reflectors. In addition, fracture density increases, and there is strong attenuation and high anisotropy, that makes the wave front elliptical. The long axis of the ellipse usually follows the dominant direction of fracturing. However, that is not in agreement with our results. This inconsistency is a result of the implementation of fractures in the multiscale cellular automaton technique. According to the technique a fracture is not a continuous feature but is made up of a number of fractured cells, each one of which has its own direction of fracturing. So even if as a total the fracture has a certain direction, each fractured cell acts individually and may have a completely different orientation of fracturing. That gives an ellipse with an orientation of the long axis that does not coincide with the orientation of the generated fracture. At stage (e) we are at the percolation threshold, and at stage (f) we have the highest fracture density, while at stage (g) the system begins to relax. All those three cases have high anisotropy due to the high fracture density and high scattering attenuation, with the maximum occurring at stage (f). As a result at

those stages the wavefront in the snapshots is elliptical instead of circular. The remaining stages are the relaxation process, where the number of fractures decreases and very long fractures form. We are now in the short-wavelength limit where reflection off the megafaults dominates and the medium is otherwise homogeneous. As a consequence the scattering attenuation is again low, and the wavefronts become circular again.

6.4   Scattering attenuation

Various results about frequency dependence of attenuation are presented by Main et al. (1990). If the seismic wavelengths λ are much greater than the size α of the scatterers and the number of scatterers is small enough to ignore multiple scattering, then Q is found to be frequency-dependent according to $\tilde{Q}^{-1} \propto \omega^3$, where ω is an angular frequency. This classic behaviour is known as Rayleigh scattering. Hudson (1981) applied the theory of scattering to a sparse fracture system. Hudson (1981) and Hudson (1986) also present theories for seismic velocity in a homogeneous cracked medium, which show that velocity depends on the crack density and aspect ratio, as long as the crack radius remains small compared to the seismic wavelength (long wavelength limit, $k\alpha \ll 1$ where k is the wavenumber). In contrast, Wu (1982) and Wu and Aki (1985) modelled the observed scattering in the earth for the case of $k\alpha \approx 1$. They used smoothly varying heterogeneous distributions of small cracks, and found that the dimension that determines the scattering attenuation is the lengthscale of the heterogeneities in crack density and geometry and not the dimension of an individual crack. Lerche (1985) and Lerche and Petroy (1986) modelled the case of multiple scattering of a dense array of microcracks with a range of sizes. For a Gaussian distribution of microcrack radii they found $\tilde{Q}^{-1} \propto \omega^3$, similar to Rayleigh scattering. However, if the power spectrum of the heterogeneities is a power law, then the frequency

dependence of Q is given by $\tilde{Q}^{-1} \propto (\omega^{\gamma})$ with $\gamma = 3 - \nu$, or $\gamma = m - 1$ (Wu and Aki, 1985), also a power law. Leary (1995a) based on evidence from the Cajon Pass borehole logs and seismic scattering for a power law distribution of fractures in crustal rock, suggested that a power law frequency dependence of $\tilde{Q}^{-1} = f^{-0.57}$ is due to a scale-dependence of fracture density, $C(\nu) = \nu^{-0.4}$. It is possible, as Leary (1995a) indicates, when seismic waves encounter fractures of a given size, energy is scattered and the amount of energy scattered scales as a power of fracture size.

6.4.1   Estimation of scattering attenuation

The dependence of scattering attenuation on frequency may be described by terms that are not linearly related to the first power of frequency. To examine how scattering attenuation depends on frequency and on the different scales of heterogeneities, we use the models presented in Figure 6.1. We estimate Q for each fracture pattern, and examine the effect of the fracture lengthscale and the frequency dependence of Q^{-1}. The estimation of Q^{-1} requires a method that is robust and can handle the rapid spatial changes in the recorded waveforms. We use the spectral method (Aki and Richards, 2002), which calculates Q^{-1} values from the fit of a straight line to the spectral ratio of receiver and source power spectra recorded at different distances. It is assumed that the receivers lie along a common raypath from the source. Another assumption of the method is that the two power spectra can be linearly related by a simple attenuation operator. Deviations from a linear spectral ratio are treated as noise, and averaging the spectra is usually required to give stable estimates of attenuation.

The amplitude spectrum $A(\omega)$ of a wave after travelling a distance L in an attenuating medium is given by Aki and Richards (2002)

$$A(\omega) = A_o exp[-\frac{\omega L}{2\alpha Q(\omega)}], \tag{6.1}$$

where $A_o(\omega)$ is the amplitude spectrum of the source, α is the wave velocity, and $Q(\omega)$ is the attenuation factor of the medium. We replace $Q(\omega)$ by $Q_S(\omega)$, because in the numerical model intrinsic attenuation is not considered. We obtain the scattering attenuation $Q_S^{-1}(\omega)$ as a function of frequency,

$$Q_S^{-1}(\omega) = -\frac{2\alpha}{\omega L} ln(\frac{A(\omega)}{A_o(\omega)}). \tag{6.2}$$

To calculate the amplitude spectrum $A(\omega)$ of the primary pulses, seismograms are windowed around the first P-wave arrival. The seismograms are Fourier transformed and the spectral ratio $A(\omega)/A_o(\omega)$ is computed. This ratio may in some cases yield negative values, corresponding to a magnification of the input signal caused by focusing effects of the heterogeneities. To calculate the scattering attenuation $Q_S^{-1}(\omega)$ we transform equation (6.2) into,

$$ln(\frac{A(\omega)}{A_o(\omega)}) = -\frac{\omega Q_S^{-1}(\omega)}{2\alpha} L. \tag{6.3}$$

We calculate the spectral ratios for the receivers at different distances from the source, and plot them as a function of distances. We fit a straight line to the values and from the slope of the line we calculate the scattering attenuation. That is for one frequency, and to calculate $Q_S^{-1}(\omega)$ for a range of frequencies we follow the same procedure for each frequency. Q_S^{-1} is evaluated in the frequency band of $f = 0Hz$ to $100Hz$.

6.4.2   Sensitivity of scattering attenuation

We now present the attenuation factor Q^{-1} values for the angular frequency range $(\omega = 0 - 628Hz)$ $(\omega = 2\pi f)$ for the fracture patterns presented in Figure 6.1. The results at very low and very high frequencies relative to the Ricker wavelet frequency of 30 Hz may not be accurate due to their low energy content. We also show properties of the evolution of the medium or properties of the heterogeneities in conjunction with the attenuation factor, to have a better idea on how the

evolution of the medium parameters may be linked systematically to changes
in the attenuation factor. Figure 6.5 shows the normalised 'susceptibility' as a
function of deformation for the states (a)-(e) of the fractured medium evolution
as defined in Narteau (in press). Susceptibility K (the probability of fractured
elements to create a connected network) is a good approximation of the correlation
length of the system. If $K = 1$, the correlation length is infinite which indicates
the percolation threshold. Deformation is presented as a percentage of total strain
in the medium. In an evolving medium strain will constantly grow as it evolves, so
in this case deformation is representing a time scale of the evolution. The dotted
lines in Figure 6.5 indicate the stages when the fracture populations (a)-(e) shown
in Figure 6.1 occur. For each stage we show the respective plot of the attenuation
factor as a function of frequency. At each plot the solid lines represent the values
of the attenuation factor, while the two dotted lines show the upper and lower
limits of the error bars. Starting from state (a), susceptibility has a very low
value. At that stage we have only microscopic structures which are active cells
and they are distributed throughout the medium, but there are no fractures. The
attenuation factor has a small fluctuation on its values but on average it has very
low values. That is expected due to the microscopic structures, compared to the
wavelength, that do not cause significant scattering. At stages (b)-(d) fractures of
different and increasing lengthscale, as well as microscopic (one-cell) structures,
begin to appear. Susceptibility rises exponentially from stage (b) to stage (d),
because once the first fractures are created together with the growing procedure
they undergo an interaction procedure which leads to larger fractures.

In all stages the attenuation factor is much higher than in stage (a) because
the size of the fractures is larger and even comparable to the wavelength. At
stage (b) we have a global maximum at $\omega = 208Hz$ and two local maxima at
$\omega = 411Hz$ and $\omega = 454Hz$. Those maxima may be directly linked with the
characteristic lengthscales of the fractures. At stages (c) and (d) fractures have
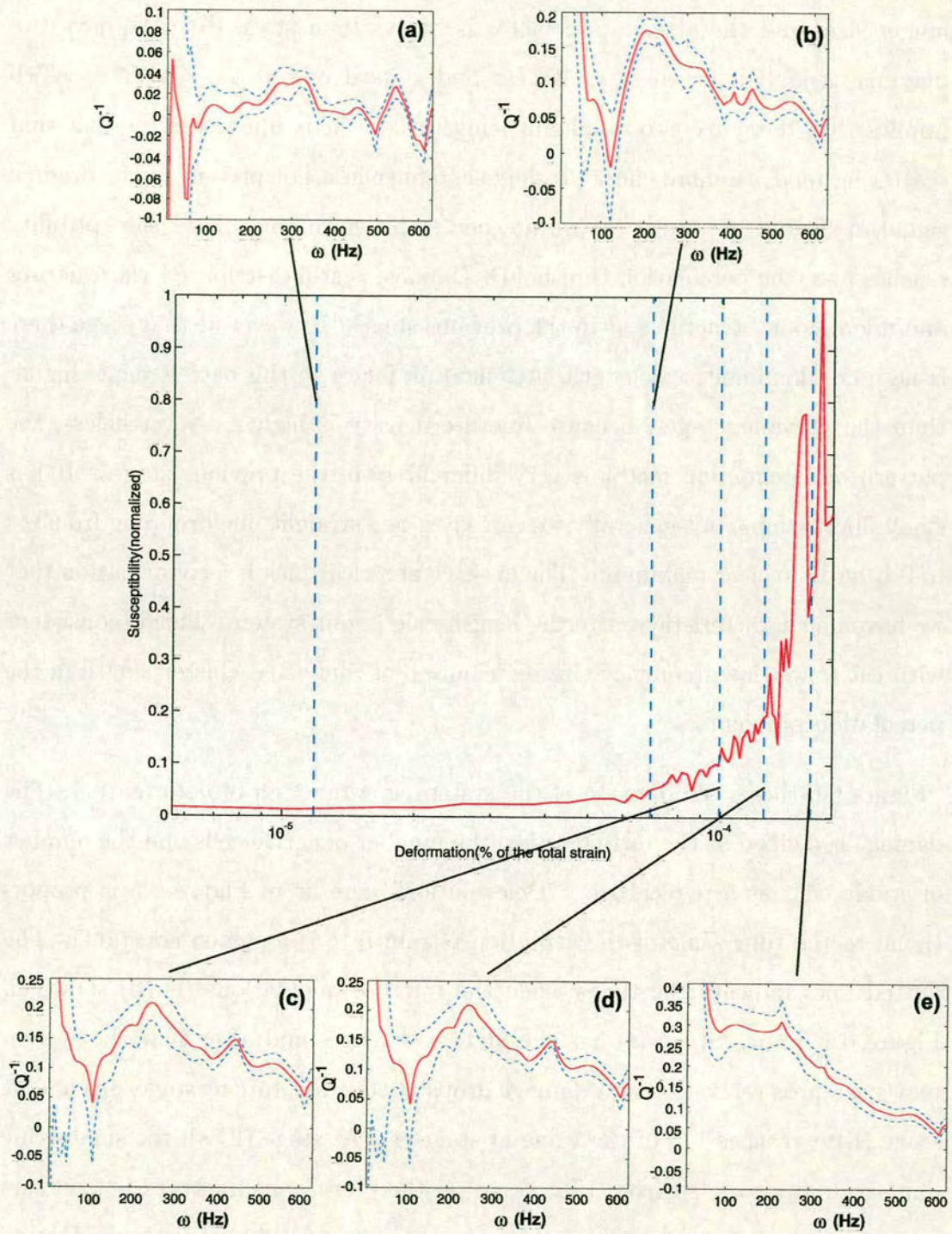
Figure 6.5: Normalised susceptibility as a function of deformation for stages (a)-(e) of the evolution of the fracture network. For each stage (a)-(e), we show the attenuation factor as a function of frequency.

longer sizes and the attenuation factor is higher than stage (b). We have two maxima, a global one at $\omega = 251Hz$ and a local one at $\omega = 447Hz$, which implies that there are two dominant lengthscales. This illustrates the fact that scattering tends to more energy to higher frequencies, not present in the original signal at 30 Hz. At stage (e) we are one step before normalised susceptibility reaches one (the percolation threshold). Damage is still distributed via fractures and microscopic structures as in the previous stages. However at that stage there is no more dominant scalelength. Attenuation factor in this case is much higher than the previous stages, because fracture density is higher. Nevertheless, the pattern of attenuation factor is very different from the previous stages. It has small fluctuations, but generally we can say it is a straight line dropping from 0.4 to 0.1, with no clear maximum. The absence of a clear pick is a confirmation that we have no characteristic scattering lengthscale in our system. This is consistent with the power-law frequency-size distribution of connected cluster length in the percolation problem

Figure 6.6 shows the damage of the system as a function of deformation. The damage is defined as the ratio between the number of active cells and the number of stable cells as a percentage. "Deformation" here as in Figure 6.5 is proportional to the time scale of the evolution (strain rate is assumed constant). The dotted lines indicate the times when the fracture populations (f)-(h) shown in Figure 6.1 occur. Stage (f) has the highest damage, and after that the system moves towards relaxation and damage drops at constant rate at stages (g) and at stage (h) it reaches 1/5 of the value at stage (f). At stage (h) all the small-scale damage disappears, so from that stage on there are only fractures left and no more microscopic structures. In all three stages we are still above the percolation threshold, so there is no characteristic lengthscale.
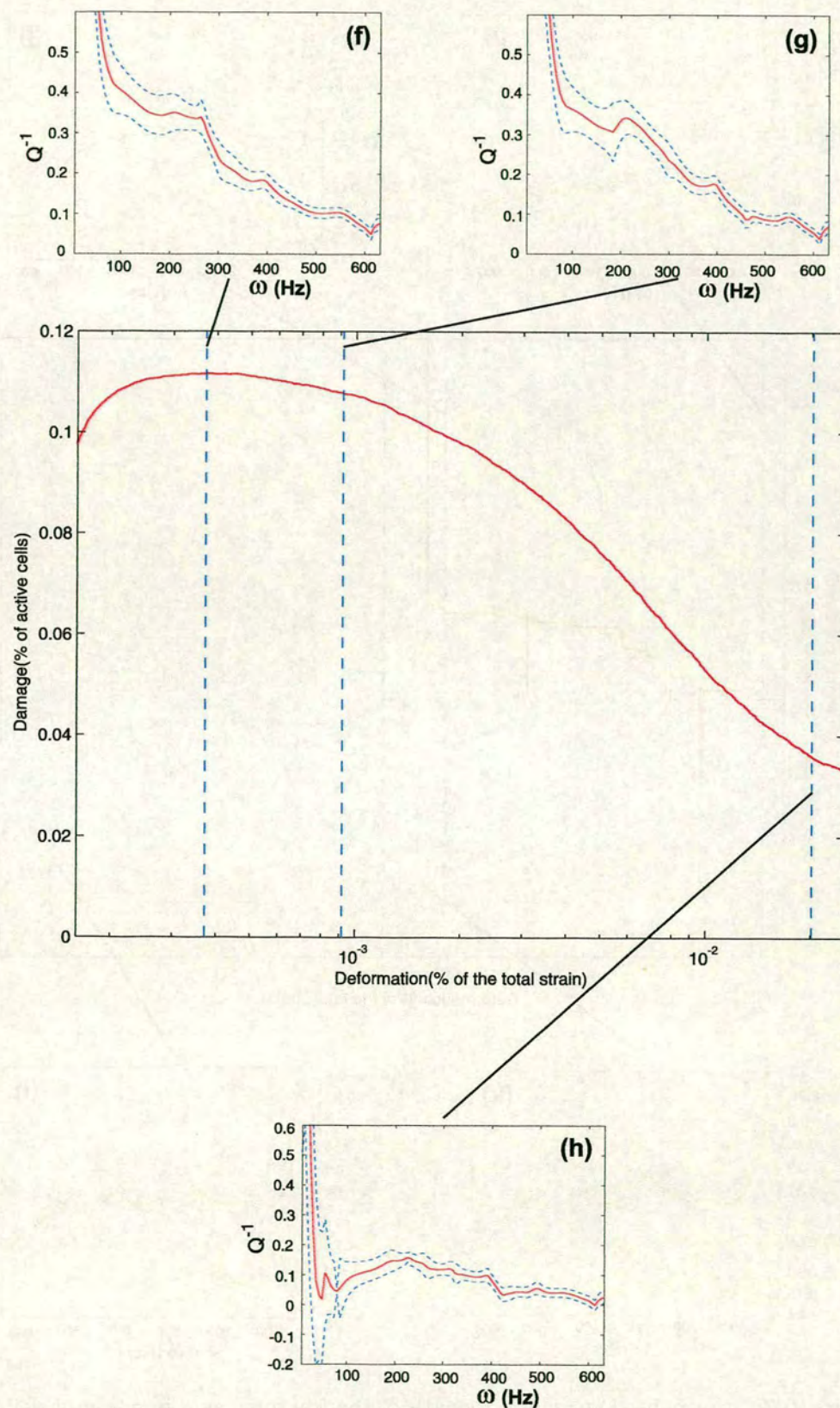
Figure 6.6: Variation of the damage as a function of deformation, for consecutive stages (f)-(h) of the evolution of the fracture network. The attenuation factor is also shown for each one of the stages (f)-(h).

Evolution of fracture networks and multiple scattering of seismic waves in
fractured rock.

140
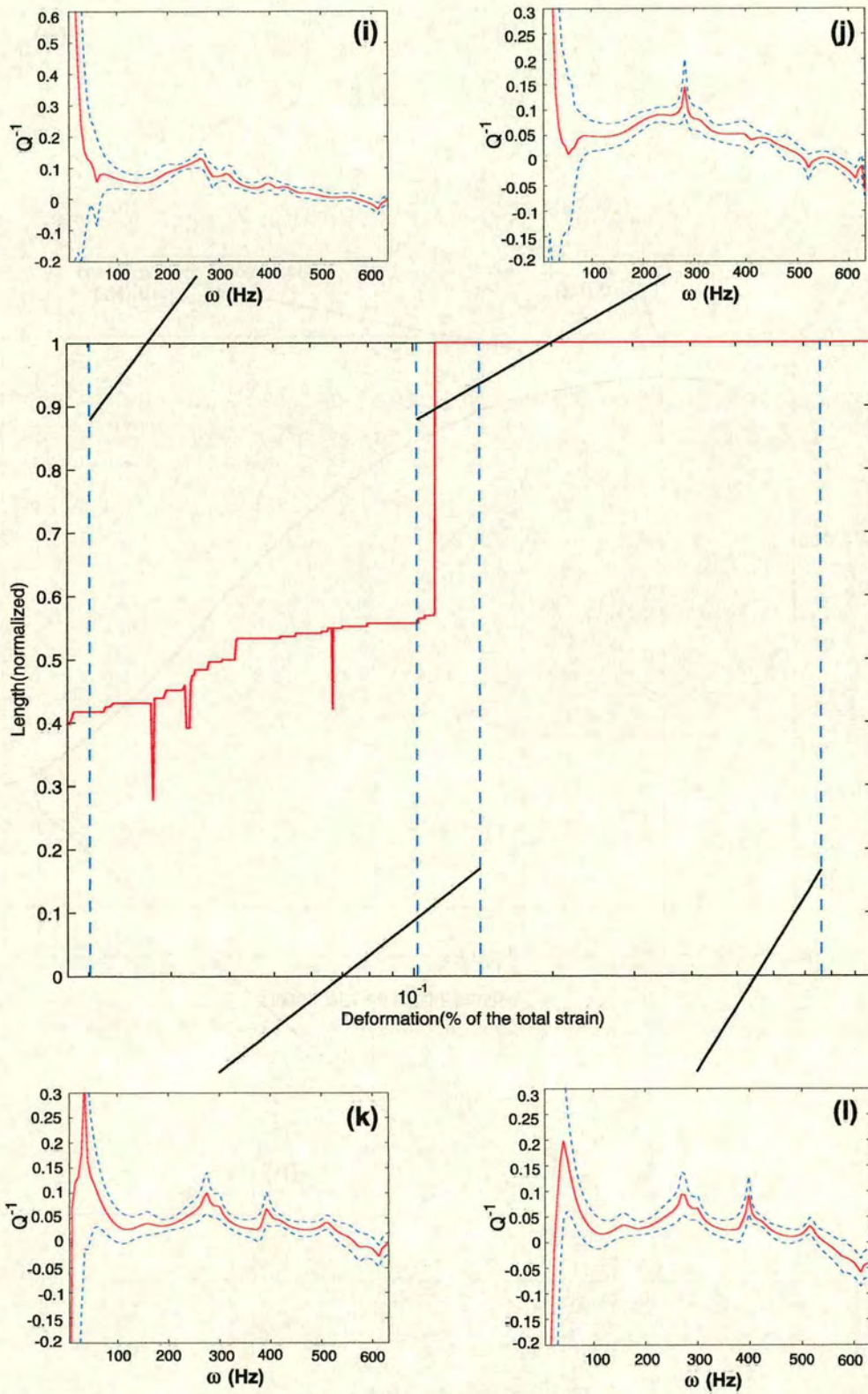
Figure 6.7: Normalised correlation length of the fractures as a function of deformation for stages (i)-(l), accompanied by the attenuation factor as a function of frequency for each stage.

The attenuation factors at stages (f) and (g) have almost the same frequency dependence. The amplitude of attenuation is higher than stage (e) in both cases because fracture density is higher. It follows the same pattern as in stage (e) and declines at an almost constant rate with frequency having small fluctuations in the value. At stage (g) there is a possible local maximum at $\omega = 208Hz$, but it is not very clear. That may imply that after the percolation threshold the system is getting reorganised and a new characteristic lengthscale dominates. At stage (h) the microscopic fractures disappear. As a result the damage has a very low value, which means that the number of active cells is less than the previous stages, even though the fractures that do exist are very large. Therefore, scattering is less, as shown in the attenuation factor that has values around 0.1 compared to average values between 0.3 and 0.4 in stages (f) and (g). Attenuation is almost independent of frequency with only small fluctuations in its values. The change in the pattern of attenuation factor at stage (h), shows that it is a potential way of identifying changes in the properties of heterogeneities, notably the degree of concentration of strain on megafaults.

Figure 6.7 shows the normalised length of the fractures of the medium as a function of cumulative deformation. Cumulative deformation is proportional to the time scale of the evolution, and the dotted lines indicate the stages when the fracture populations (i)-(l) shown in Figure 6.1 occur. At the final stages of the evolution of the system which are shown here, there is no more nucleation of new fractures. However, existing fractures interact and form big fractures that span along the whole medium. That is demonstrated in Figure 6.7, where we see that the normalised length rises steeply, although it has some fluctuations, until it reaches a maximum and it becomes constant at the two final stages. At stage (i) the attenuation factor has a very similar pattern and values to that of stage (h). It is almost constant for all frequencies, although it slightly decreases at high frequencies. However, in that stage the local maximum that was not

clearly seen at stage (h) is stronger here at $\omega = 263Hz$. The seismic wave probably "recognises" a characteristic lengthscale as it travels in the medium. At stage (j) the first major fracture appears (Figure 6.1j), which is a result of fracture interaction. That important change in the properties of the medium is clearly shown in the scattering attenuation (Figure 6.7j). At that stage we have even lower fracture density so attenuation factor has lower values. It starts from a low value at small frequencies and it rises until it reaches a maximum at $\omega = 282Hz$ and then drops constantly. We expect that this maximum in attenuation factor is linked with the lengthscale of the major fracture. At stage (k) normalised length reaches its maximum values and the system is almost at the end of the evolution. The major fracture is already formed and here we have the formation of smaller secondary fractures that have almost the same size. The attenuation factor shows almost the same pattern as in stage (j), but in this case there is a global maximum at $\omega = 276Hz$, a local maximum at $\omega = 392Hz$ and possibly another local maximum at $\omega = 509Hz$ (Figure 6.7k). So the global maximum is slightly shifted to a lower frequency compared with stage (j), which may indicate a small change in size, and we also have a clear local minimum and another one which is not obvious. The two local minima may be linked with the fact that at that stage the medium has other heterogeneities that on average they have two distinct dominant lengthscales. The final stage (l) when the system reaches stability has similar attenuation factor pattern to stage (k), with one global and two local maxima. However, the global maximum is shifted to a slightly smaller frequency and the two local maxima are shifted to slightly higher frequencies (Figure 6.7l). That can be interpreted as small changes in the dominant lengthscales.

6.4.3   Attenuation analysis

In this section we continue the examination of attenuation and concentrate on its behaviour with frequency, and the effect of the continuous changes of the properties of the heterogeneities. We examine the parameter $ln(A/A_o)$ for each stage of evolution for a number of receivers with $ln(\omega)$ for the same frequency range as in the previous section. Figures 6.8 and 6.9 show $ln(A/A_o)$ as a function of $ln(\omega)$ for the stages of evolution (a)-(l) and for a number of receivers. In general, the behaviour of attenuation can be divided into two distinct areas. In the small to middle frequency range, it declines almost linearly with frequency until it reaches a minimum for a value of $ln(\omega)$ between 4 and 5, which is between $\omega = 54Hz$ and $\omega = 150Hz$. In the middle to high frequency range attenuation rises following an almost quadratic variation. When analysing the results we note that the results for very low and very high frequencies may not be very accurate.

However, there are stages that the general conclusions do not apply, for example stages (k) and (l). Also, for the same evolution stage there is different behaviour of attenuation for different receivers. That is expected because seismic waves follow different paths to arrive at different receivers, thus encountering different fractures that affect in a different way the amplitude of seismic waves. To have a consistent analysis, for each stage we average the values at each frequency for receivers at different distances. By doing so, we obtain the net effect of the various fractures affecting the wave propagation. For a better understanding we fit a polynomial to the data which can accurately describe the attenuation variations with frequency. We examine polynomials with degree from 1 to 8, in order to achieve a good fit. We use a statistical information criterion to determine the optimal polynomial degree and examine each state. The most commonly used statistical criteria are the Schwarz Information Criterion proposed by Leonard and Hsu (1999), Akaike's (1978) Information Criterion and the Bayesian Information Criterion.
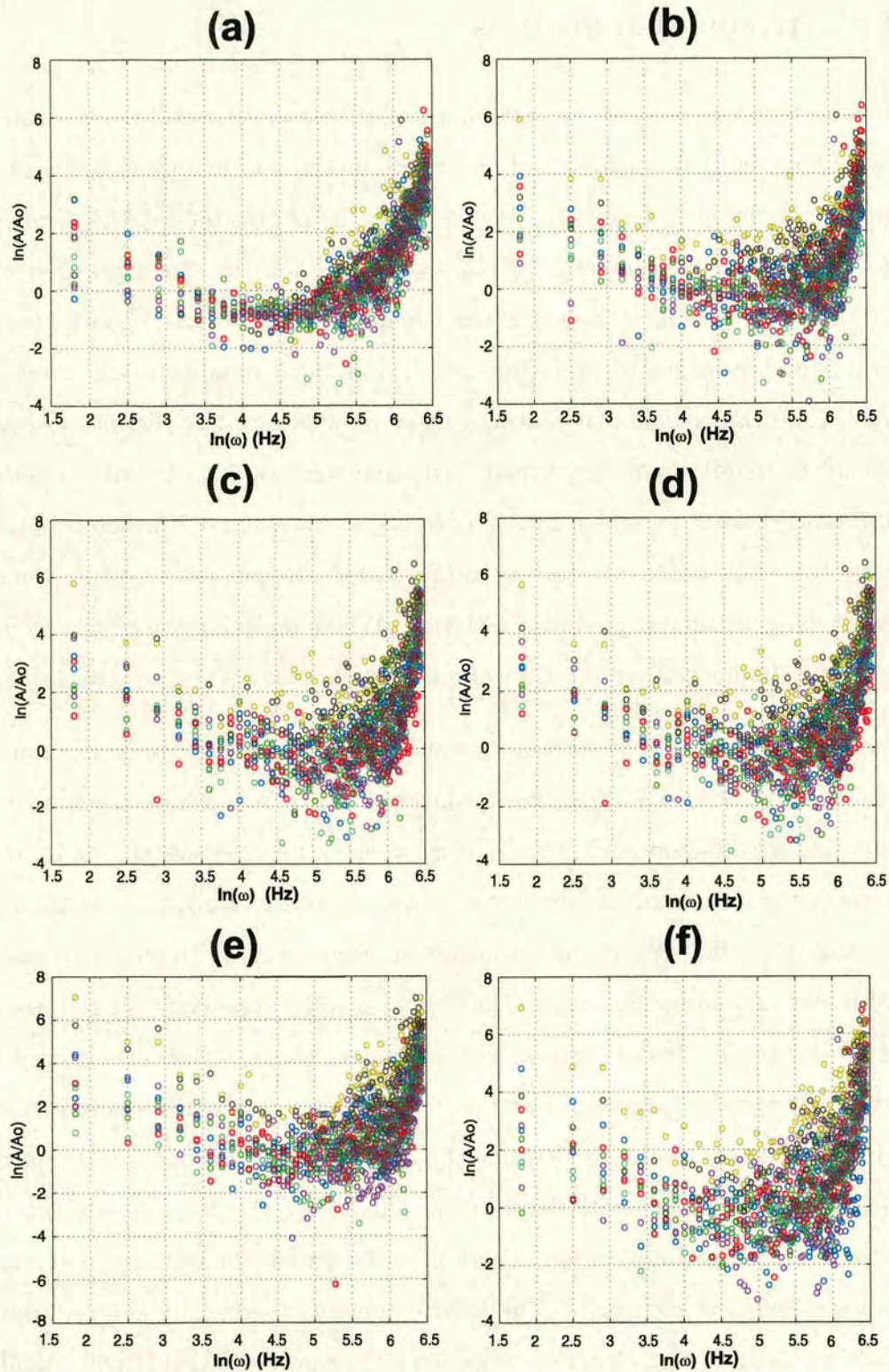
Figure 6.8: Attenuation $ln(A/A_o)$ as a function of frequency for stages (a)-(f) of the evolution of the fracture network. Notice that for each frequency we have more than one data points. That is because we have measurements taken at receivers at various distances from the source, so absorption varies with distance.
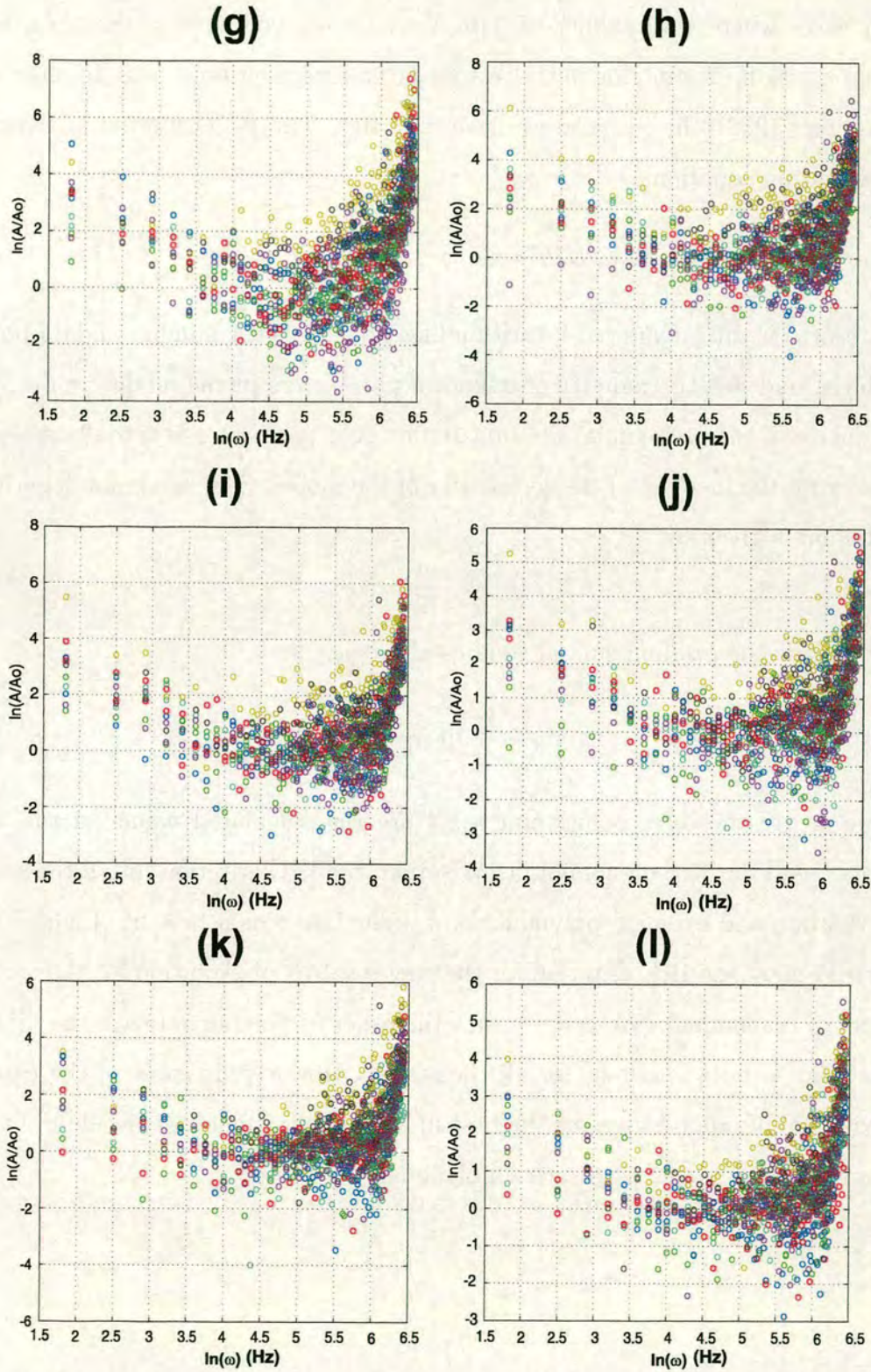
Figure 6.9: Attenuation $ln(A/A_o)$ as a function of frequency for stages (g)-(l) of the evolution of the fracture network. Notice that for each frequency we have more than one data points. That is because we have measurements taken at receivers at various distances from the source, so absorption varies with distance.

For cases where the number of data are $n > 46$, computer simulations have shown that BIC is superior to the rest of the statistical criteria (e.g. Koehler and Murphree, 1988). In our case we have $n = 103$. The BIC criterion is given by the following equation,

$$BIC = L(y) - \frac{1}{2}pln(\frac{n}{2\pi}), \qquad (6.4)$$

where $L(y)$ is the maximised logarithm likelihood, n is the number of data points we have, and p is the number of unknown parameters in the model, in our case the degree of the polynomial we want to fit. That parameter is actually an extra penalty for the increase of the complexity of the model. The maximum logarithm likelihood is given by,

$$L(y) = -\frac{n}{2}ln(S_R^2), \qquad (6.5)$$

where S_R^2 is the residual sum of squares and it is,

$$S_R^2 = \sum_{i=1}^{n}[y_i - \gamma(x_i)]^2, \qquad (6.6)$$

where y_i are the data points and $\gamma(x_i)$ are the calculated values of the data points based on the polynomial fit. We apply the BIC criterion for all the stages of evolution and examine polynomials of order 1 to 8 as a best fit. Figures 6.10 and 6.11 show the BIC criterion for the stages (a)-(l) of evolution for the various orders of polynomial. We can see that the order of polynomial with the highest BIC value is not consistent for all the stages. However, in most of the cases a polynomial of order 5 gives us the best fit, so for consistency we decide to fit the data for all the stages with such a polynomial.
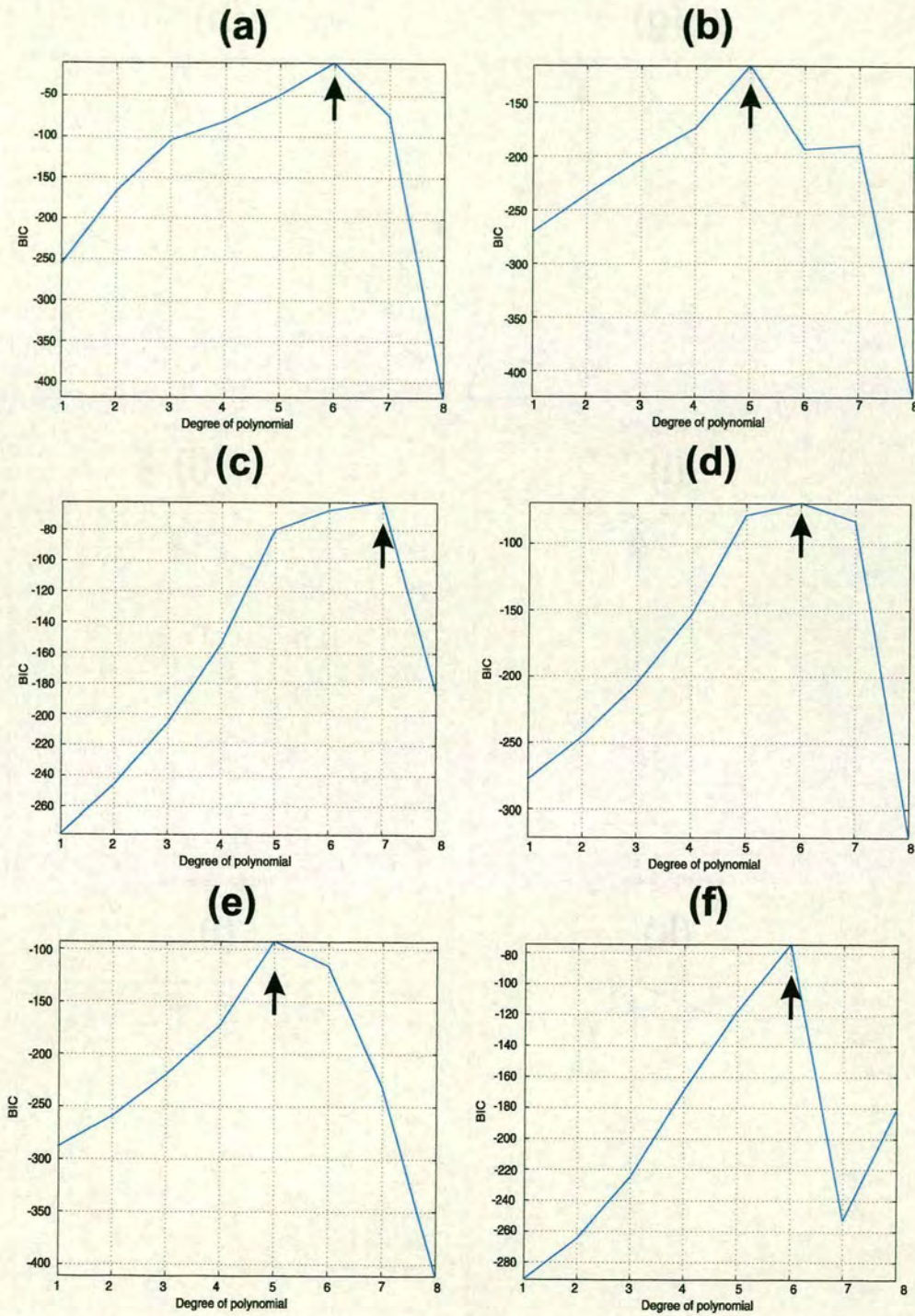
Figure 6.10: Plot of the BIC criterion, as defined in equation (6.4), as a function of
the degree of the polynomial that we fit to the data. The degree of the
polynomial that gives the best fit is the one with the highest value of
BIC. An arrow points to the degree of the polynomial that gives the
best fit for each one of the states (a)-(f). For most of the states the
best fit is given by a polynomial of degree 5.
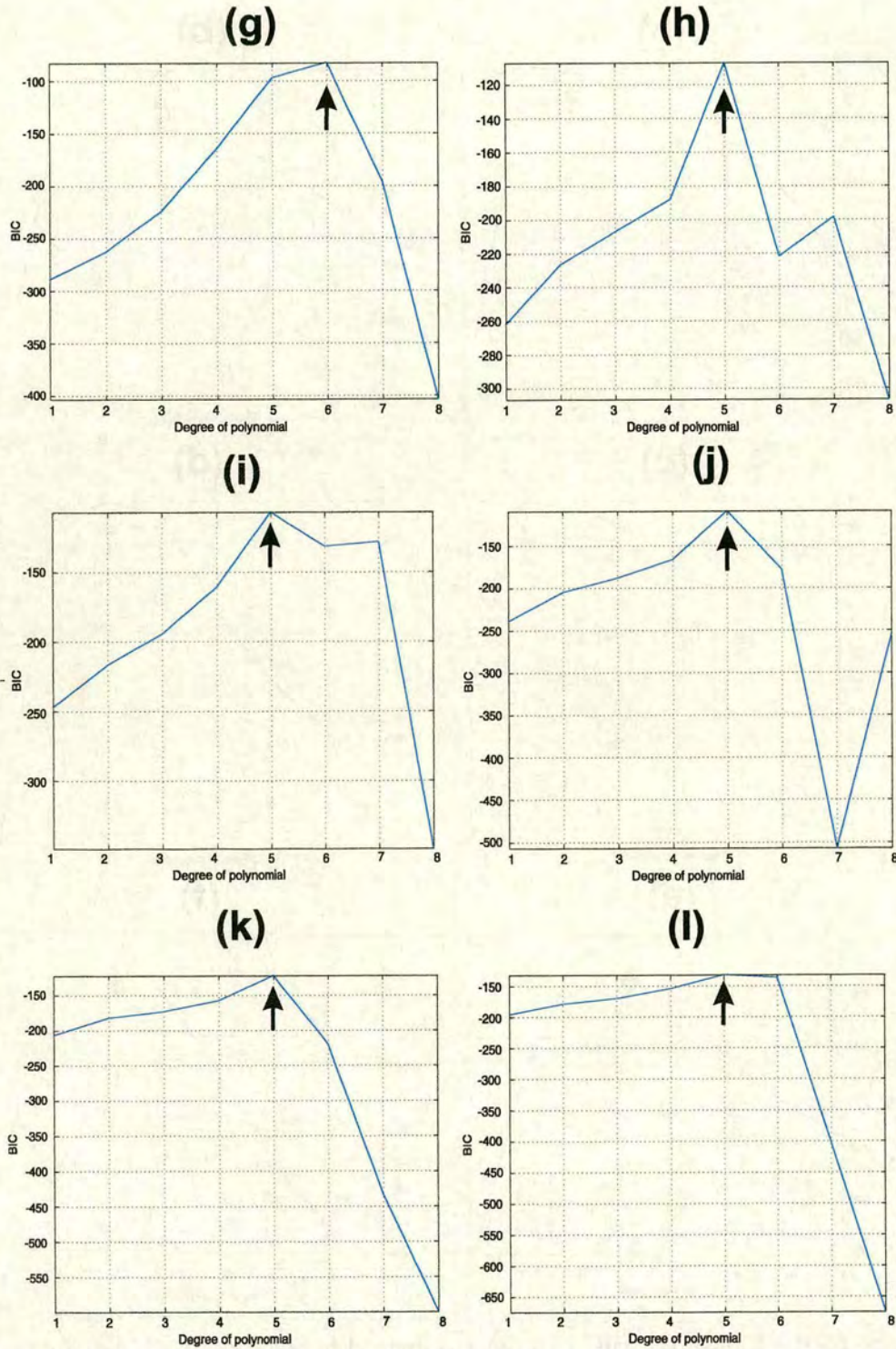
Figure 6.11: Plot of the BIC criterion, as defined in equation (6.4), as a function of
the degree of the polynomial that we fit to the data. The degree of the
polynomial that gives the best fit is the one with the highest value of
BIC. An arrow points to the degree of the polynomial that gives the
best fit for each one of the states (g)-(l). For most of the states the best
fit is given by a polynomial of degree 5.

Evolution of fracture networks and multiple scattering of seismic waves in fractured rock.

149

Figures 6.12 and 6.13 shows the averaged data of $ln(A/A_o)$ with $ln(\omega)$ for all the stages of evolution together with the polynomial fit to the data. We can see that the fit to the data in most of the cases is very good. In general we can see the same behaviour as in the attenuation factor. Stage (a) can be divided in two areas, the small to middle frequency range which is linear until a minimum at a value of $ln(\omega)$ slightly higher than 4, and the middle to high frequency which is quadratic and rises until a very high maximum. That behaviour changes at stage (b) until stage (d). Here we have a steep almost linear dip for most of the frequency range until a minimum at $ln(\omega)$ slightly greater than 5.5. However, at that linear part we see significant fluctuation from the linear behaviour between 4.5 and 5.5. The remaining part is characterised by a very steep quadratic increase. At stage (e) until stage (g) the linear dip is much more prominent with almost no fluctuations and the minimum value is the lowest among all the stages. Also the remaining data show a clear linear behaviour until the global maximum. At stage (h) until stage (j) we have a different behaviour. At those stages we can divide the data in three discrete areas. In the low to middle frequency range we see again a linear decrease until a local minimum this time around $ln(\omega) = 4$. In the middle to high frequency range $ln(A/A_o)$ starts from the local minimum, then it moves towards higher values and drops to a global minimum around $ln(\omega) = 5.5$. Finally, there is the high frequency area where we see a rapid linear increase. In the last stages (k) and (l) we have the same distinction in three areas although the behaviour is different. The small frequency range is a linear decrease until a global minimum. The middle to high frequency part is on average a straight line around $ln(A/A_o) = 0$, which means that at the stages of relaxation and when the system is stable $A \approx A_o$. It is also important to note that at those stages we have the final formation of a major fracture that is up to 5 times longer than the wavelength, so the seismic wave is not significantly attenuated by those features. The final part of the data is steeply increasing following a linear trend.
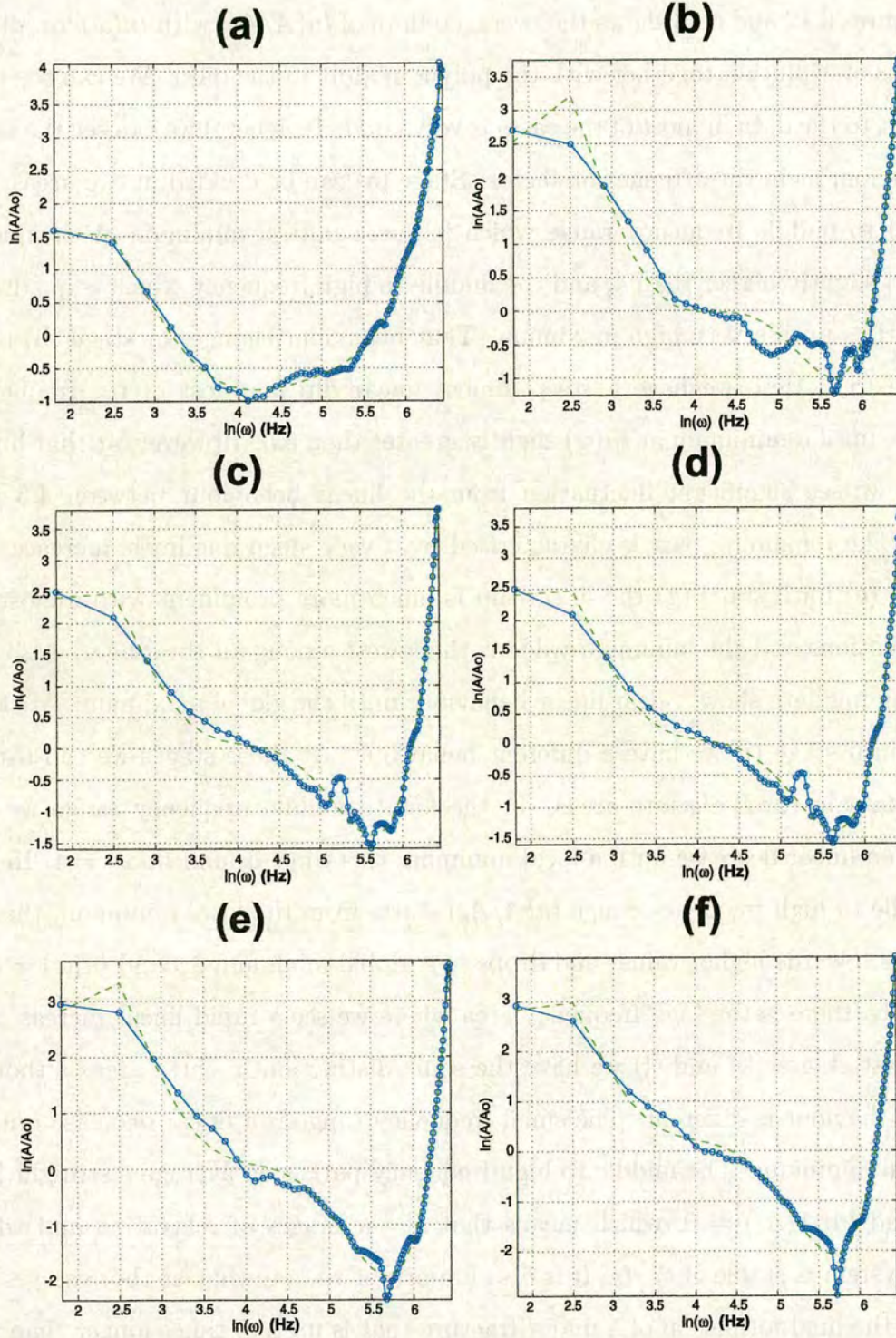
Figure 6.12: Plot of attenuation with frequency averaged over the values for different
receivers for all the frequencies (straight line). We also show the fit to
the data by the polynomial of degree 5 (dotted line). By comparing
the two plots we can see that the polynomial gives a very good fit. The
plots are for states (a)-(f) of the fracture evolution.
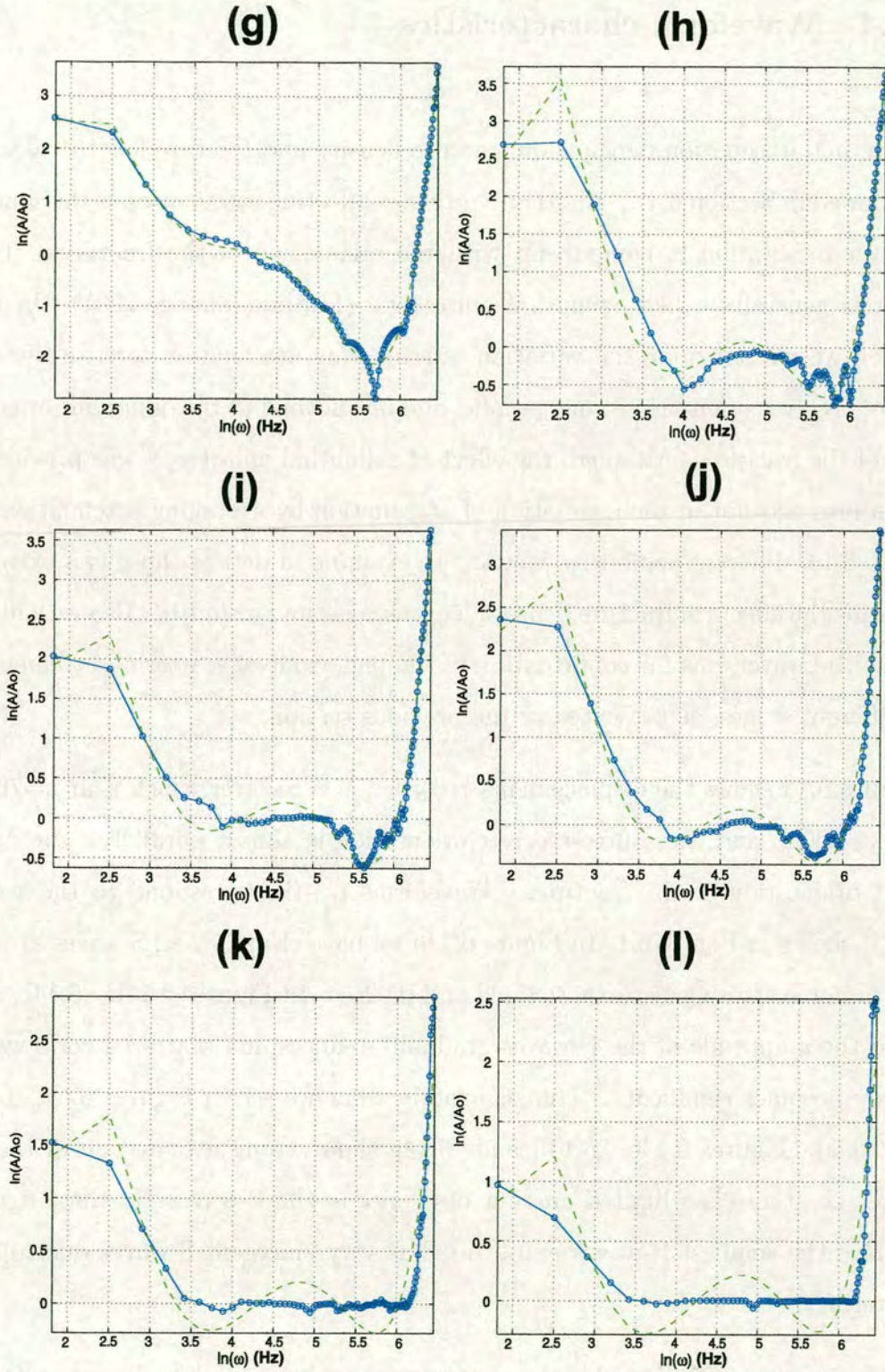
Figure 6.13: Plot of attenuation with frequency averaged over the values for different receivers for all the frequencies (straight line). We also show the fit to the data by the polynomial of degree 5 (dotted line). By comparing the two plots we can see that the polynomial gives a very good fit. The plots are for states (g)-(l) of the fracture evolution.

6.4.4   Waveform characteristics

Scattering attenuation depends on fracture density and fracture lengthscales, as
we showed in Section 6.4.2. Another parameter affecting attenuation is the source-
receiver orientation in comparison with the orientation of the fractures. That
effect is generally called azimuthal anisotropy (Liu and Zhang, 2001). In this
section we will examine the variation of scattering attenuation for two distinct
source-receiver orientations, one parallel and one normal to the dominant orienta-
tion of the fractures. Although the effect of azimuthal anisotropy was previously
taken into account in the estimation of attenuation by averaging attenuation es-
timated for different azimuths, we want to examine in details those two extreme
cases for the effects of fracture density, lengthscales, and azimuth. Also we will ex-
amine the waveforms for confirmation of the behaviour of scattering attenuation
at different stages, as presented in the previous section.

Figure 6.14 shows the displacements recorded at a receiver which is at x=700m
and y=300m, and the source-receiver orientation is almost parallel to the dom-
inant orientation of the fractures. Waveforms (a)-(l) correspond to the states
(a)-(l) shown in Figure 6.1. In Figure 6.14a we have clear P- and S-waves arrival,
and minor scattering between 0.45sec and 0.62sec. In Figures 6.14b, 6.14c, and
6.14d the amplitude of the P-waves gradually reduces and scattered coda waves
energy becomes significant. That is exactly what we see in Figures 6.5b, 6.5c,
and 6.5d. Figures 6.14e, 6.14f, and 6.14g show strong attenuation of the P-
waves, i.e. there is a limited amount of energy in the P-waves. In these figures
we have the smallest P-waves amplitude but very emergent S-waves due to S-P
scattering.

The energy is redistributed in the coda-waves that have much higher energy than
in the previous cases. Also the coda-waves shows a variety of frequency contents.
Figures 6.14h and 6.14i show a change in the properties of the waveform. Once

Evolution of fracture networks and multiple scattering of seismic waves in fractured rock.

153
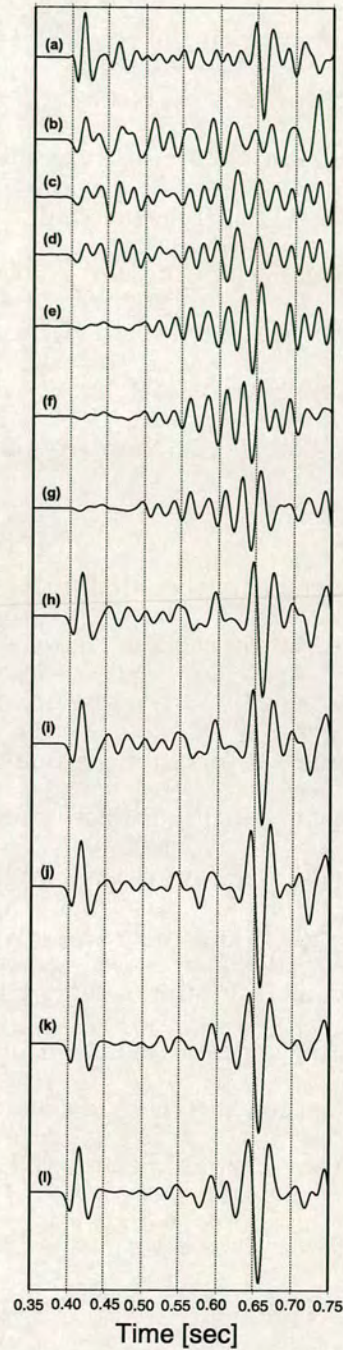
Figure 6.14: Displacement recorded at a receiver situated at x=700m and y=300m for each one of the states (a) - (l) shown in Figure 6.1. The source-receiver direction is parallel to the dominant direction of fracturing.

more there is high energy in the P-waves and S-waves and some scattering that distributes energy in the coda-waves, although scattering is significantly lower

than before. That is in agreement with the results in Figures. 6.6h and 6.7i. An
interesting feature of the waveforms here is that the amplitudes of the S-waves
are higher than the amplitudes in Figure 6.14a, which result from constructive
interference between reflected waves. It seems that the P-waves are not affected
and there may be a simple explanation for that. When the source-receiver direc-
tion is parallel to the dominant direction of fracturing, P-waves are polarised in
the propagation direction while S-waves are polarised normal to that direction.
Finally, Figures 6.14j, 6.14k, and 6.14l, show even less scattered energy on the
coda waves and strong P- and S-waves.

Figure 6.15 shows the displacements recorded at a receiver that is at x=2250m
and y=720m. The source-receiver direction in that case is normal to the dominant
direction of fracturing. Waveforms (a) - (l) correspond to states (a) - (l) shown in
Figure 6.1. By comparing Figures 6.14 and 6.15, one clear observation is that the
displacements due to the P-waves in Figure 6.15 are lower than in Figure 6.14,
while the displacements due to the S-waves are higher in Figure 6.15 than in
Figure 6.14. That is because in Figure 6.15, P-waves propagate normal to the
orientation of the fractures while in Figure 6.14 they travel along the direction of
the fractures, therefore suffering more attenuation in Figure 6.15. The opposite
happens with S-waves because their direction of polarisation is normal to the one
of P-waves, and as a result they are less attenuated. (The other reason for the
difference in displacement is the source radiation).

We now present scattering attenuation for the dominant frequency of the source,
for each one of the states in Figure 6.16. The circles represent states (a) - (l) and
the x-axis is the deformation as in Figures 6.6, 6.7, and 6.8. State (a) has the
lowest attenuation, then we see a steep rise until state (b) which is the initialisa-
tion of growth. Attenuation continues to increase more gradually at states (c) and
(d), followed by a steep rise in attenuation between (d) and (e), which continues
between (e) and (f) where the maximum attenuation occurs. In Figures. 6.14f
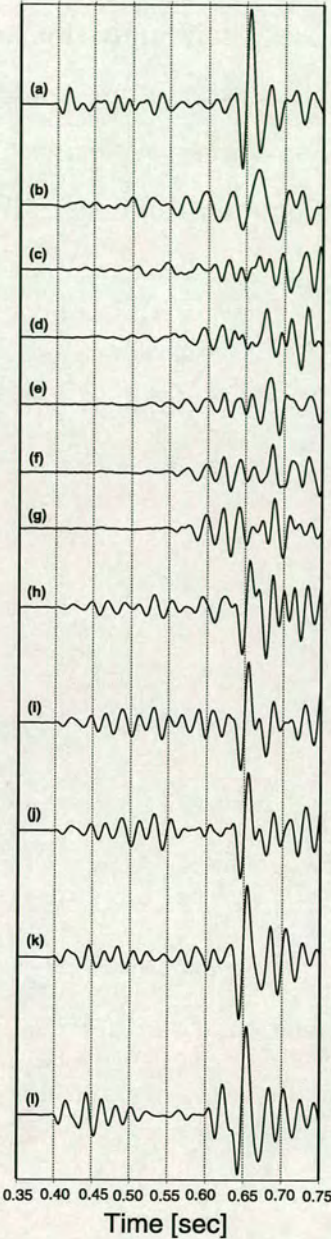
Figure 6.15: Displacement recorded at a receiver situated at x=2250m and y=720m for each one of the states (a) - (l) shown in Figure 6.1. The source-receiver direction is normal to the dominant direction of fracturing.

and 6.15f, the waveforms show the maximum attenuation. This coincides with the state of evolution were there is the maximum fracture density and fractures of all the different lengthscales. Afterwards the localisation of the deformation along major fractures occurs and thus at stages (h) and (i) fracture density decreases.

As a result, attenuation decreases significantly. Finally there is a dominant major fracture with some intermediate sized fractures, which makes reflection dominate and scattering attenuation even lower. We can see the continuous decrease in Figure 6.16, until it reaches the minimum at state (l).
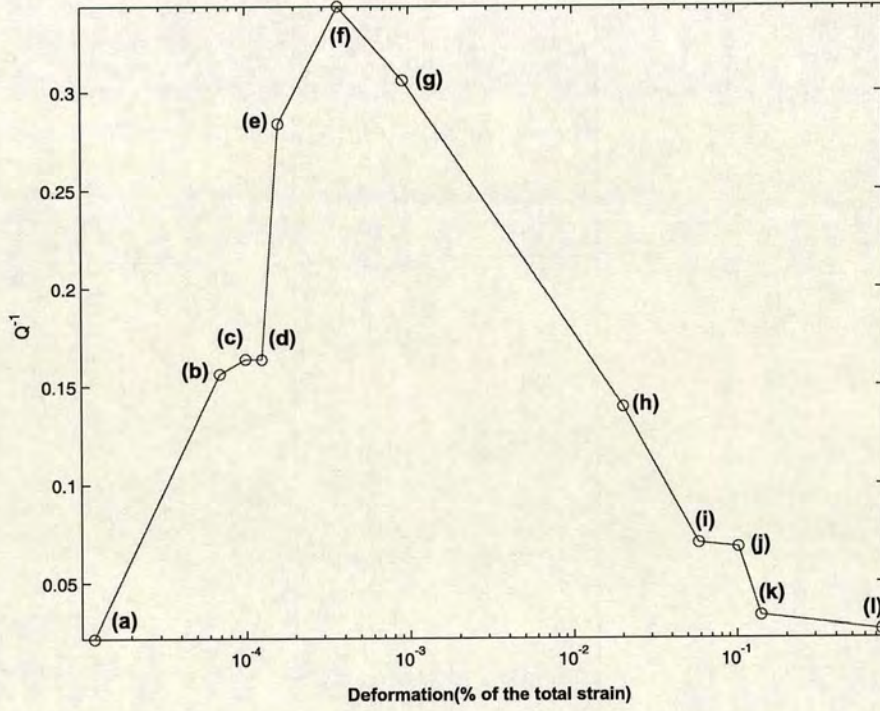
Figure 6.16: Scattering attenuation at the dominant source frequency ($f = 30Hz$), for each one of the stages (a)-(l) of the evolution. The circles on the graph represent the values at the consecutive stages of evolution.

6.5   Summary

We have calculated and examined the snapshots of the wavefield for the various fracture models provided by C.Narteau. The results demonstrate the influence of the changing fracture density and lengthscale of the fracture on the wavefield propagation. We can see that on the initial stages, when fracture density is low and the fracture size is less than the wavelength, anisotropy and absorption are low and the fractures act as individual point scatterers. At the percolation thresh-

old, fracture density becomes high and therefore high absorption and scattering
is visible in the snapshots and we also have high anisotropy that makes the wave-
front elliptical. At later stages when we have the concentration of fractures to a
small number of major fractures, fracture density is lower, so the wavefront be-
comes circular once more, but the size of fractures is bigger than the wavelength
and they act as interfaces which give very strong reflections.

In all the states the amplitude of the scattering attenuation factor shows max-
imum and minimum values at certain frequencies which we believe can be at-
tributed to the statistical properties of the medium at the certain stage, ie. char-
acteristic lengthscale of fractures. That indication becomes stronger by the lack
of such features when the medium is in a stage that no characteristic lengthscale
exists, which is at or above the percolation threshold. Also there is a very clear
change in the properties of the attenuation factor when the properties of the
medium change significantly, such as in the case when we have the creation of the
first fractures or the percolation threshold or the creation of a major fracture. In
such cases we have important alterations in the value of the attenuation factor
and also to the behaviour with frequency.

Similar changes are observed in the frequency dependence of Q^{-1}. The seismic
waveforms validate the scattering attenuation results. They show a link between
changes in fracture density and lengthscale of heterogeneities and variations in
scattering attenuation. They also exhibit the importance of azimuth in the effects
of scattering attenuation on P- and S-waves. The results in this study give a very
clear picture about the potentials of using scattering attenuation as a means of
describing the properties of a medium and identifying dominant lengthscales of
fractures. Although in the real data it is not easy to discriminate between scatter-
ing attenuation and intrinsic attenuation, as it is using a numerical technique, we
believe that attenuation measurements can be used successfully towards an accu-
rate characterisation of a fractured reservoir. In real data fractures are commonly

vertical. In such cases the most commonly used method for fracture imaging is vertical seismic profiling (VSP). Acquisition of VSP data involves a surface source that is located either close to the well head (zero-offset case) or away from the well head (offset VSP) and a geophone in the well bore. Several traces are recorded at the same geophone depth, then edited and summed. A VSP generally gives better data than surface seismic methods because the energy does not have to travel as far and therefore undergoes less attenuation. Consequently, the resolution of a VSP is usually appreciably better than that of surface seismic data. There are different types of VSP's from which the one used for vertical fractures is the walkaway VSP. A walkaway VSP is a repeated VSP survey along several walkaway lines having different azimuths. That allows the seismic interpreter to estimate azimuthal anisotropy around the well, that may indicate aligned vertical fractures and anisotropic horizontal stresses. When integrated with other types of anisotropy measurements, walkaway VSP data can contribute significantly to an improved image of the subsurface.

Estimation of scattering attenuation from the mean wavefield

7.1 Introduction

In the last chapter I presented numerical simulations of the effect of crack distribution and crack lengthscale on the dispersion and attenuation of elastic waves for a single realisation. With a number of such results it is also possible to predict *average* wavefield quantities for averages over a statistical ensemble of medium realizations. In this chapter, we use the ensemble-averaged wavefield to examine scattering attenuation and the attenuation coefficient Q^{-1} for a range of different crack sizes. The aim is to theoretically investigate the dependence of the attenuation of elastic waves due to crack scattering on the property of crack distributions.

Wave propagation in a continuous random medium can often be described by a stochastic linear differential equation. A stochastic equation is a family of equations depending upon a parameter α which ranges over a space in which a probability density $p(\alpha)$ is defined. The probability density $p(\alpha)$ determines the probability of a given value of α and therefore of the corresponding equation of the family. The coefficients in such an equation characterize the propagation

medium. They may include its refractive index $n(x)$, its density $\rho(x)$, its dielectric constant, etc. A random medium is a family of media, each is defined by one value of α, and each with its own index $n(x, \alpha)$, density $\rho(x, \alpha)$, etc. The variable $p(\alpha)$ gives the probability of each member of the family. The inhomogeneous term represents the source of the waves, which may either be random or deterministic (i.e., not random). A random medium may also consist of a random distribution of discrete scattering objects distributed throughout some fixed medium within which waves can propagate. This description is appropriate when matter is viewed on a molecular scale, so we are interested at the distribution of the molecules but not at the properies of the medium they are inside. Propagation in such a medium can be analysed in terms of stochastic equations.

The practical reason for studying stochastic equations is the belief that their solutions represent physical phenomena which could not be satisfactorily investigated in any other way. Let us consider, for example, the propagation of an electromagnetic wave through air. Because the wave travels so fast, it is adequate to assume that the air molecules do not move during the passage of the wave. If the locations of all the molecules were known, one could in principle determine how they scatter the wave. However, the full details of the scattered wave would be too complex to be useful. Furthermore it is out of the question to determine the locations of all the molecules. In view of these two difficulties, it is hoped that the observable features of the wave scattering will be determined by the gross features of the molecular distribution. Therefore the actual distribution of molecular positions is replaced by a random medium, i.e., a collection of molecular distributions with a probability associated with each. The mean particle density and some other statistics of the random medium are adjusted to equal the corresponding properties of the actual particle distribution. Then the mean scattered waves and other statistics of the random waves are presumed to equal the corresponding properties of the actual wave.

7.2   Mean wavefield

In this section we will describe the basic ideas that form the mean wavefield theory. Theories on wave propagation in random media predict average wavefield quantities for averages over a statistical ensemble of medium realizations. When we relate the theoretical results on scattering attenuation with real data we make two basic assumptions. Firstly, in practice we are interested in the properties of a specific geological medium and we have to replace ensemble averaging by spatial averaging of a single realization that requires the medium to be ergodic. We assume that this condition is satisfied. Secondly, different functions of the recorded wavefield differently take into account the wavefield fluctuations caused by scattering. Therefore, different attenuation estimates are obtained dependent on what wavefield function is being averaged (Sato, 1982; Wu, 1982).

The ensemble-averaged wavefield is describe by the meanfield theory (Keller, 1964). The mean wavefield was applied to examine the effect of randomly distributed cracks by Yamashita (1990). Following Yamashita (1990), we assume N cracks, and N is assumed to be very large. The density of crack distribution is, however, assumed to be low. The crack distribution is assumed to be homogeneous to simplify mathematical analysis. All the cracks are assumed to be stationary during the scattering process. The crack surfaces are assumed to be stress-free (cavity). The relative displacement is assumed to occur across the crack surface no matter how small a disturbance is incident on the crack. In other words, no criterion is assumed for the occurrence of relative displacement across the crack.

Let us denote by u_o the incident displacement wave in the absence of any crack. The total displacement field is then the sum of incident wave u_o and the contri-

bution u_s^j from the j-th crack:

$$u = u_o + \sum_{j=1}^{N} u_s^j. \qquad (7.1)$$

The wave u_s^j scattered from the j-th crack can be expressed as

$$u_s^j = \Psi_s^j(u^j), \qquad (7.2)$$

where u^j is the external displacement field acting upon the j-th crack and the operator Ψ_s^j determines the scattering property of the j-th crack. The stochastic property of the crack is assumed to be described by the location of the centre of the crack, the crack length and the crack orientation. The stochastic property of each crack is assumed to be independent of that of the other cracks. The configurational average of u from Equations(7.1) and (7.2) is

$$<u> = u_o + \frac{n}{N} \sum_{j=1}^{N} \int \Psi_s^j(<u^j>_j)p(\theta_j)p(\alpha_j)dr_j d\theta_j d\alpha_j, \qquad (7.3)$$

where p is the probability density function, r_j is the location of the centre of the j-th crack, θ_j is the angle to denote the orientation of the j-th crack, α_j is the half length of the j-th crack, and n is the number density of the crack distribution. The quantity $<u^j>_j$ represents the external displacement field acting on the j-th crack averaged over all possible configurations of all the other scatterers. Foldy (1945) introduced the following approximation in Equation 7.3:

$$<u^j>_j \cong <u>. \qquad (7.4)$$

That approximation reduces Equation(7.3) to the form of an integral equation

$$<u> = u_o + \frac{n}{N} \sum_{j=1}^{N} \int \Psi_s^j(<u>)p(\theta_j)p(\alpha_j)dr_j d\theta_j d\alpha_j. \qquad (7.5)$$

Foldy's approximation (Equation 7.4) is thought to be valid as $N \to \infty$.

A result of the meanfield theory is that when we examine scattering attenuation, the resultant attenuation is mainly a statistical effect (Sato, 1982; Wu, 1982)

caused by averaging different realizations of the wavefield having individual phase fluctuations. The real scattering attenuation of seismic wavefields is smaller than that of the meanfield. In the following section, we present in details the theoretical background and the estimation of scattering attenuation from the meanfield and the theoretical background.

7.3   Estimation of scattering attenuation using the meanfield theory

Attenuation of seismic waves is caused by scattering and absorption (intrinsic attenuation). Attenuation by scattering depends on how fast rock parameters vary in space and how large these variations are. Scattering attenuation and absorption are important parameters for rock characterization. Both can have the same order or one can be stronger than the other dependent on the geology. Attenuation due to scattering can dominate in heterogeneous media.

Theoretical (analytic) and numerical studies demonstrate that scattering produces apparent attenuation with distance in a manner similar, in some respects, to intrinsic loss mechanisms (Wu, 1982; Richards and Menke, 1983; Frankel and Clayton, 1984; Malin and Phinney, 1985). Scattering also causes variations in waveforms and amplitudes across seismic arrays (Ringdal and Husebye, 1982). Numerical techniques have several advantages over analytic treatment of scattering. We can produce synthetic seismograms for any point on the grid. It includes all multiply scattered waves, converted waves (P to S, S to P), diffractions, and caustics. Most theoretical studies of seismic scattering assume the first Born approximation, which states that only single scattering occurs and that scattering losses from the primary wave can be neglected (Pekeris, 1947; Chernov, 1960). This approximation is valid only for weakly scattering media and appears inap-

propriate for many portions of the crust (Hudson and Heritage, 1981; Richards and Menke, 1983). Unlike some approaches to scattering which assume the ray approximation, the numerical methods are not restricted to certain ratios of wavelength to scatterer size and can be used for media with velocity fluctuations over a wide range of lengthscales. Amongst other things both Born and ray approximations violate the principle of energy conservation because they do not include multi-scattering energy.

Scattering attenuation is quantified by the parameter Q_S^{-1} in analogy to Q_i^{-1} which is a measure for anelastic or intrinsic attenuation. In addition to the attenuation of the direct wave, scattering causes the excitation of the seismic coda. Within the framework of single scattering theory the coda following the direct wave arrival is composed of single scattered wavelets, which are generated at the random heterogeneities of the medium. According to Aki (1980) coda Q (Q_C) has to be identified with the total transmission Q, i.e. $Q_C^{-1} = Q_S^{-1} + Q_i^{-1}$. The coda decay with time is controlled by a geometrical spreading term and by Q_C. To find an estimate of the scattering attenuation, we take a volume of material that is cycled in stress at a frequency ω, then a dimensionless measure of the internal friction (or the anelasticity) is given by

$$\frac{1}{Q(\omega)} = -\frac{\Delta E}{2\pi E},$$
(7.6)

where E is the peak strain energy stored in the volume and $-\Delta E$ is the energy lost in each cycle because of imperfections in the elasticity of the material. The definition is rarely of direct use, since only in special experiments it is possible to drive a material element with stress waves of unchanging amplitude and period. More commonly, one observes either (i) the temporal decay of amplitude in a standing wave at fixed wavenumber or (ii) the spatial decay of amplitude in a propagating wave at fixed frequency. Both cases give a solution to Equation (7.6) in the limit $\Delta E \to dE \to 0$. They describe an exponential decay with distance or time. The most common situation involves attenuation of a signal composed

of a range of frequencies, and we make the strong assumption that attenuation is a linear phenomenon, in the sense that a wave may be resolved into its Fourier components, each of which can be studied in terms of (i) or (ii), and that subsequent Fourier synthesis gives the correct effect of attenuation on actual seismic signals. In the case of either (i) or (ii), for a medium with linear stress-strain relation, wave amplitude A is proportional to $E^{1/2}$. (For example, A may represent a maximum particle velocity, or a stress component in the wave. We assume also that $Q \gg 1$, so that successive peaks have almost the same strain energy). Hence,

$$\frac{1}{Q(\omega)} = -\frac{1}{\pi}\frac{\Delta A}{A},\tag{7.7}$$

from which we can obtain the amplitude fluctuations due to attenuation. In this chapter we will concentrate on case (ii). In order to derive a form $A = A(x)$ for distance x, a particular wave peak can be followed along a distance dx, and the gradual spatial decay of A can be observed. (We assume here that the direction of maximum attenuation is along the x-axis, which is also the direction of propagation). Then $\Delta A = (dA/dx)\lambda$, where λ is the wavelength given in terms of ω and phase velocity c by $\lambda = 2\pi c/\omega$. Equation (7.6) becomes $\int_{A_o}^{A}\frac{dA}{A} = \int_{o}^{x}\frac{-\omega}{2cQ}dx$, with the exponentially decaying solution

$$A(x) = A_o(x)exp[-\frac{\omega x}{2cQ}].\tag{7.8}$$

From observations of exponentially decaying values of $A(x)$, we use Equation (7.8) to define the value of a spatial Q. In the case of a plane wave, the amplitude spectrum $A(\omega)$ after passing an attenuating medium with thickness z_o is given by applying Equation (7.8) by Aki and Richards (2002) for a variety of frequencies. Equation (7.8) becomes

$$A(\omega) = A_o(\omega)exp[-\frac{\omega z_o}{2\alpha_o Q(\omega)}],\tag{7.9}$$

where $A_o(\omega)$ is the amplitude spectrum of the initial signal at $z_o = 0$, α_o is the wave velocity and $Q(\omega)$ is the quality factor of the medium. We replace $Q(\omega)$ by

$Q_s(\omega)$, because in the numerical models intrinsic attenuation is absent and the energy loss of the direct wave is caused by scattering only. We obtain

$$Q_S^{-1}(\omega) = -\frac{2\alpha_o}{\omega z_o} ln[A(\omega)/A_o(\omega)]. \tag{7.10}$$

To calculate the amplitude spectrum $A(\omega)$ of the transmitted wave, the seismograms at the receiver line are either used in their original form or we use a window to remove the coda waves. We will refer to this in details in the following section. The seismograms are Fourier transformed and the spectral ratio $A(\omega)/A_o(\omega)$ is computed. This ratio may in some cases yield negative apparent values of $Q_S^{-1}(\omega)$, corresponding to a magnification of the input signal caused by focusing effects of the heterogeneities, or by amplification of noise in $A_o(\omega)$.

7.4   Numerical results

In this section we present the models used to examine scattering attenuation as well as the synthetic seismograms created for the different cases. We theoretically study, the attenuation of acoustic waves due to crack scattering by employing the idea of mean wave formalism. We examine a model of fractures distributed in a uniform way. Scattering attenuation depends strongly on the size of fractures compared to the wavelength. It has been shown by Yomogida and Benites (2002) that when the size of scatterers is compared with the wavelength scattering attenuation is similar to the cavity case. When the crack length is much smaller than the wavelength then scattering attenuation becomes considerably smaller. That happens because only the volume of heterogeneities and not the detailed shape is an essential factor in scattering. Another important factor is the angle between the orientation of the cracks and the direction of propagation of the incident wave. As cracks are aligned more obliquely to the incident wave, attenuation becomes smaller, particularly when the wavelength becomes much shorter than the representative size of heterogeneities. Also, Yamashita (1990) stated

that the attenuation coefficient Q^{-1} decays in proportion to k^{-1} in the high frequency range (wavelength much shorter than the crack length) and its growth is proportional to k^2 in the low frequency range (wavelength much longer than the crack length), where k is the wavenumber.

We begin by generating the medium. We use the random uniform distribution of fractures presented in Chapter 5 (Figure 5.9a). We create 10 different models by slightly changing the positions of the centre of the fractures by 1.5 or 2.5 metres from the original model, in a random way. We use the numerical technique presented in Chapter 2 to model seismic wave propagation through each of the different fracture models. The model examined consists of 100 fractures. The speed of acoustic waves is $2000ms^{-1}$. To obtain the meanfield we can use four different techniques (Shapiro and Kneib, 1993). The mean wavefield can be obtained by : (a) stacking individual records without any traveltime corrections, (b) stacking the wavefield after traveltime corrections, (c) by stacking amplitude spectra of individual records, and (d) by averaging the logarithms of amplitude spectra. Those methods give different scattering-attenuation estimates dependent on what wavefield function we are averaging. The two first procedures differ by the inclusion or exclusion of the traveltime correction. The two last procedures differ only by what is made first: averaging (stacking) or taking the logarithm. Usually it is assumed that both the dependence of the logarithm of the averaged amplitude spectrum $ln < A >$ and the average of logarithms of amplitude spectra $< lnA >$ on distance can be fitted by a straight line. The underlying assumption here is that the corresponding attenuation estimates which are determined from the slope of the fitted line are independent on travel distance. In this work we use technique (a), so we stack individual records taken at the same receiver for each one of the 10 different models. We use records taken at the same receiver so we do not need to make any traveltime correction. The technique is illustrated in Figure 7.1.
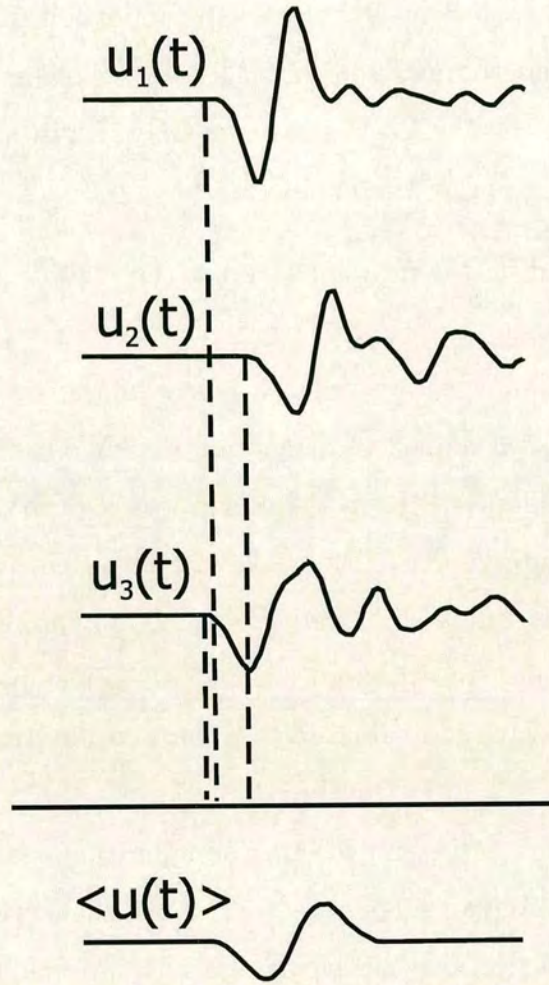
Figure 7.1: Sketch of the averaging procedure. The meanfield results from averaging records without phase corrections and without traveltime corrections (Shapiro and Kneib, 1993) .

We use a Ricker wavelet with dominant frequency is 40 Hz, thus having a wavelength of 50 m, given that the velocity of the acoustic waves is $2000 ms^{-1}$. All the fractures have the same size in each model. We examine different sizes of fractures and each model contains 100 fractures. The fractures have half size of 5 m, 15 m, 25 m and 50 m, respectively. The density of the background medium is $\rho = 2200 kgm^{-3}$, and it is the same as in the models presented in previous chapters. The model used in the following simulations contains 128x128 grid points with a grid interval of 10m. The source is situated in the centre of the model and the receiver line is horizontal at 300 m depth. We put one receiver at

each grid point, so the distance between adjacent receivers is 10m. We record the synthetics for each of the 10 different models and then stack the records taken at each receiver to get the mean wave. We keep the source wavelength constant at a frequency of $f = 40Hz$, thus having a wavelength $\lambda = 50m$ and wavenumber $k = 0.126$.
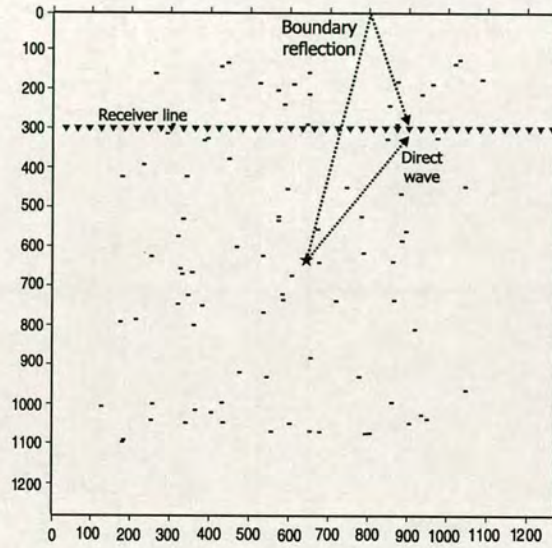
Figure 7.2: Geometry of the model used to examine scattering attenuation of the mean wavefield

Figure 7.2 shows the geometry of the model where we show the direct waves recorded at the receiver 90 as well as the boundary reflections. Figure 7.3 shows the waveforms recorded at receiver 90 for models 1 to 8 and Figure 7.4 shows the waveforms recorded at the same receiver for models 9 and 10, the mean wave corresponding to the average of models 1-10 and the source waveform that is recoded when we have no fractures in the medium. The case examined in this model is when fractures have half-size α of 5 m. The product of wavenumber k and half-size α is $k\alpha = 0.63$, or $ka \approx 1$, which is why there is a significant coda in the individual models.

We estimate the arrival time of the direct wave and the boundary reflections based on the geometry of the model for receiver 90. The estimated arrival time of
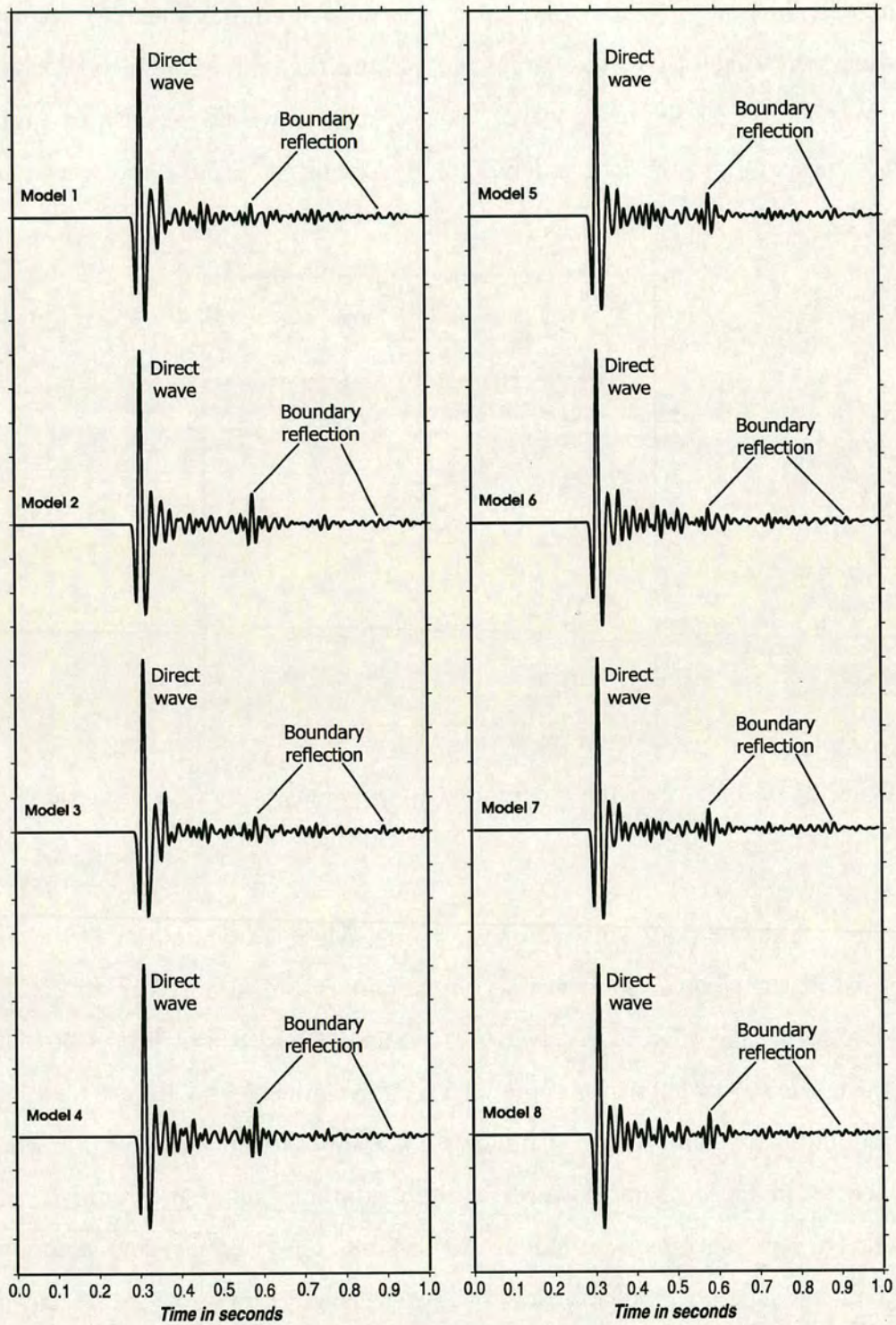
Figure 7.3: Waveforms recorded at receiver 90 for models 1 to 8 in the case of $k\alpha = 0.63$. In each model we change the position of the fractures in a random way
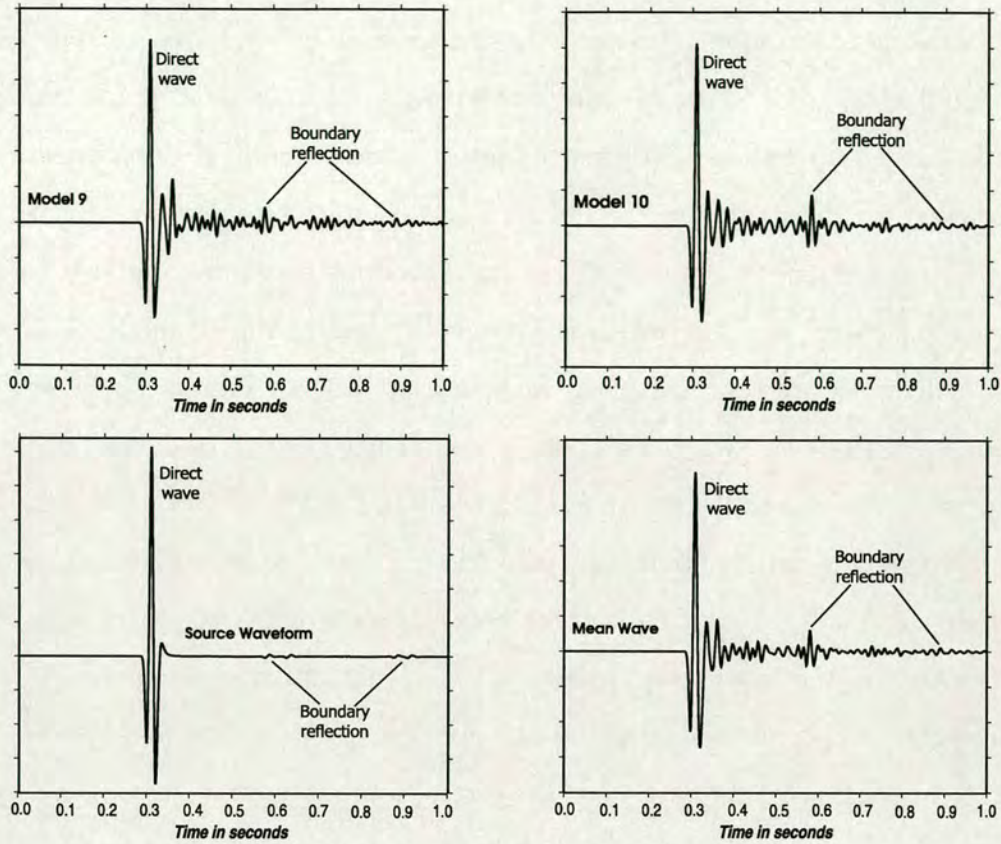
Figure 7.4: Waveforms recorded at receiver 90 for model 9 and 10 in the case of $k\alpha = 0.63$. We also show the mean wave recorded at the same receiver and the source waveform for a model without fractures. The mean wave is the mean value of the signal recorded for each one of the model

the direct wave is 0.298s which is in good agreement with the synthetic seismograms presented in Figures 7.3 and 7.4. Also we have boundary reflections that have estimated arrival times between 0.58s and 0.65s from the upper boundaries and between 0.85s and 0.95s from the distant boundaries. We confirm those findings from Figure 7.4 where we show the waveform for a model with no fractures and clearly shows the direct wave and the boundary reflections. The waveforms in Figures 7.3 and 7.4 for each model show the direct waves near 0.3s and a strong reflection near 0.6s. That reflection as we explained is a boundary reflection. There is also another boundary reflection near 0.9s, which is not as strong as the one at 0.6s. In each model we see reflections from fractures that are recorded at different times. For instance, there is a reflection in model 1 near 0.45s while the

same reflection is in model 4 near 0.43s and in model 8 we have two relfections between 0.4 and 0.43s. That is expected because in each model fractures are situated at different positions, so the wave finds a different number of fractures while it propagates towards the receiver for each model. In the mean wave we have the boundary relfections at 0.6s and 0.9s, two reflections between 0.4 and 0.5s, and another reflection at 0.72s, which is present in most of the 10 models. All the other reflections are canceled when we stack the traces. Figure 7.5 shows four snapshots of the mean wavefield taken at consecutive times. It shows the strong mean wavefield propagating through the medium and secondary waves that are generated by the fractures. In this case the fracture size is much less than the wavelength ($\alpha = \lambda/5$), so each fracture becomes a source of secondary wave. We can see that in the last two snapshots, where significant scattering occurs. This implies that longer path lengths have a more complex mean wavefield. That is expected because at long paths we have strong scattering, that gives strong coda waves which make the wavefield complicated.

Figure 7.6 shows the waveforms recorded at receiver 90 for models 1 to 8 and Figure 7.7 shows the waveforms recorded at the same receiver for models 9 and 10, the mean wave and the source waveform for a model without fractures, when fractures have half-size α of 15 m. The product of wavenumber k and half-size α is $k\alpha = 1.89$.

As in the previous case, the direct waves arrive at the receiver at about 0.3s after the initialisation of the source. Also we can see in the wavelets from all the models that the boundary reflection at 0.6s is present, however it seems that the amplitude of the reflection is smaller. There is a clear reflection near 0.44s which is present in all the models. There is also a number of minor arrivals, that are different for each model due to the different positions of the fractures. Compared to the previous case, the amplitude of the direct wave is smaller and also there are stronger coda waves, compared to the cases in Figures 7.3 and 7.4.
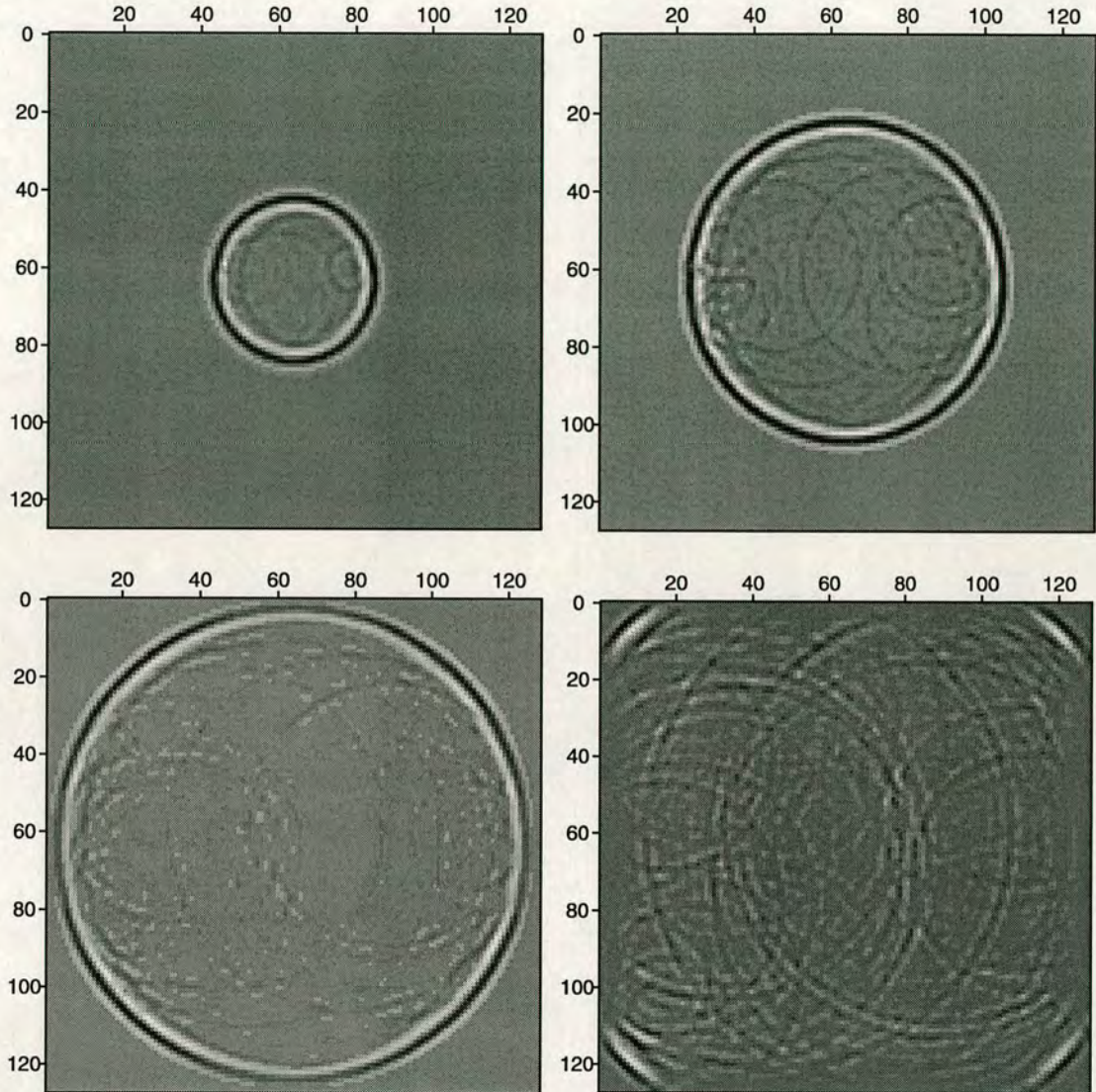
Figure 7.5: Snapshots of the mean wave taken at consecutive times in the case of $k\alpha = 0.63$

That is because in this case, the fractures are larger than in the previous case ($\alpha = \lambda/3$). As a result, we see stronger scattering attenuation, so more energy is redistributed to the coda waves. We would expect in the mean wave, the arrivals from the randomly positioned fractures to be canceled after the averaging procedure. However, we see clearly the boundary reflection near 0.6s and at 0.9s. That happens because the boundaries are the same in all models and they give the same arrivals in all models, so they are not affected by averaging. Also the arrival

Figure 7.6: Waveforms recorded at receiver 90 for models 1 to 8 in the case of $k\alpha = 1.89$

Figure 7.7: Waveforms recorded at receiver 90 for model 9 and 10 in the case of $k\alpha = 1.89$. We also show the mean wave recorded at the same receiver and the source waveform for a model without fractures

at 0.44s is present in the mean wave. That is an effect of multiple reflections from the fractures, and the existence of such an arrival in the mean wave indicates the non-perfect averaging. The larger size of fractures leads to higher scattering and the application of the concept of the mean wave is limited. Figure 7.8 shows four snapshots of the mean wavefield taken at consecutive times. The snapshots show the mean wavefield and some secondary waves. The secondary waves are more strongly attenuated as shown in the waveforms too.

Figure 7.9 shows the wavelets recorded at receiver 90 for models 1 to 8 and Figure 7.10 shows the wavelets recorded at the same receiver for models 9 and 10, the mean wave and the source waveform for a model without fractures, when fractures have half-size α of 25 m. The product of wavenumber k and half-size α
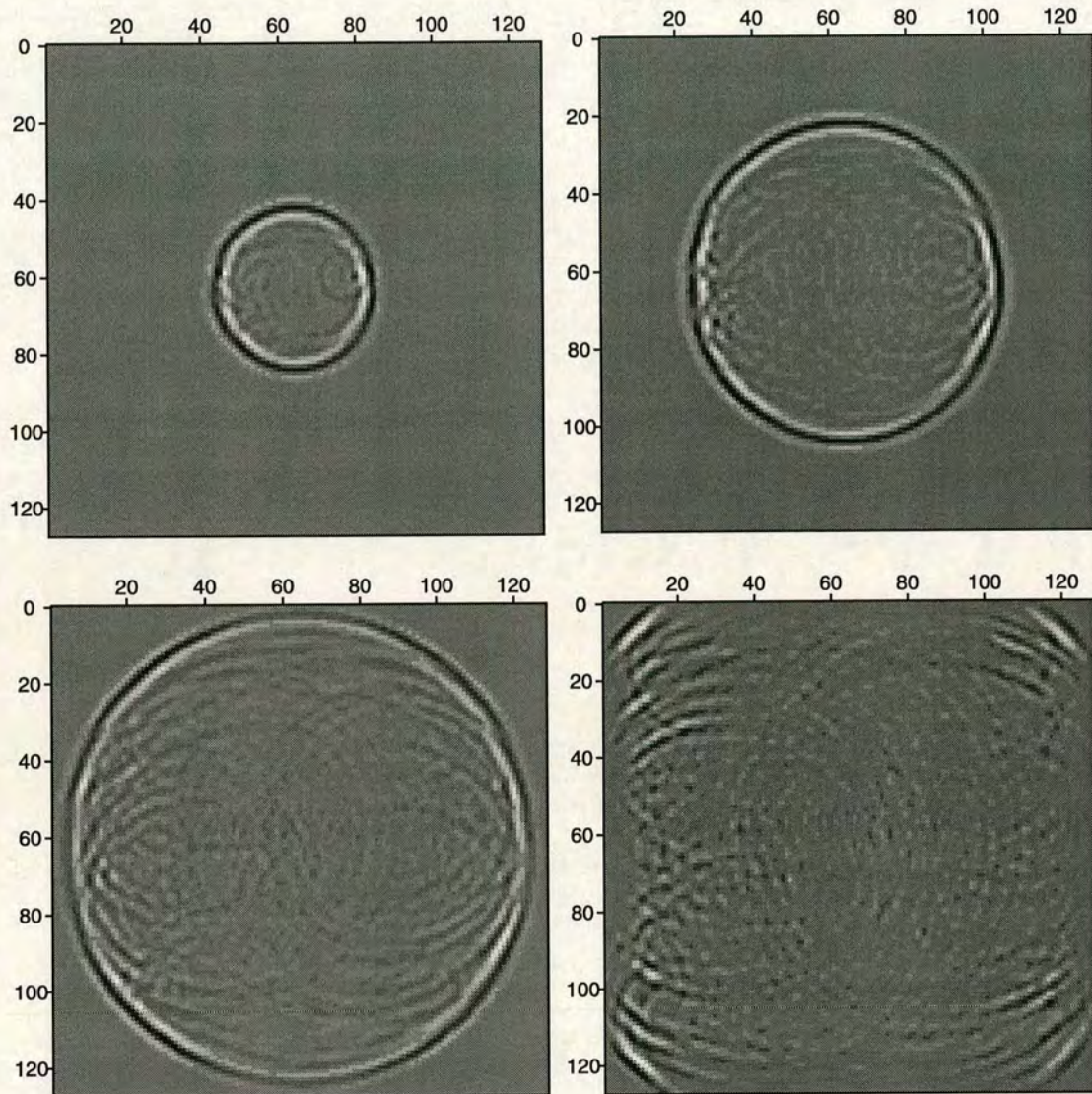
Figure 7.8: Snapshots of the mean wave taken at consecutive times in the case of $k\alpha = 1.89$

is $k\alpha = 3.15$.

In this case the boundary reflections are not clearly distinguishable as in the previous cases, however we can identify the arrivals from the waveforms at 0.6s and 0.9s. Here we have large fractures and the wave is strongly attenuated before it reaches the boundary, so the reflections are not as strong as previously. A common characteristic in all models is that there are not distinct reflections. Once
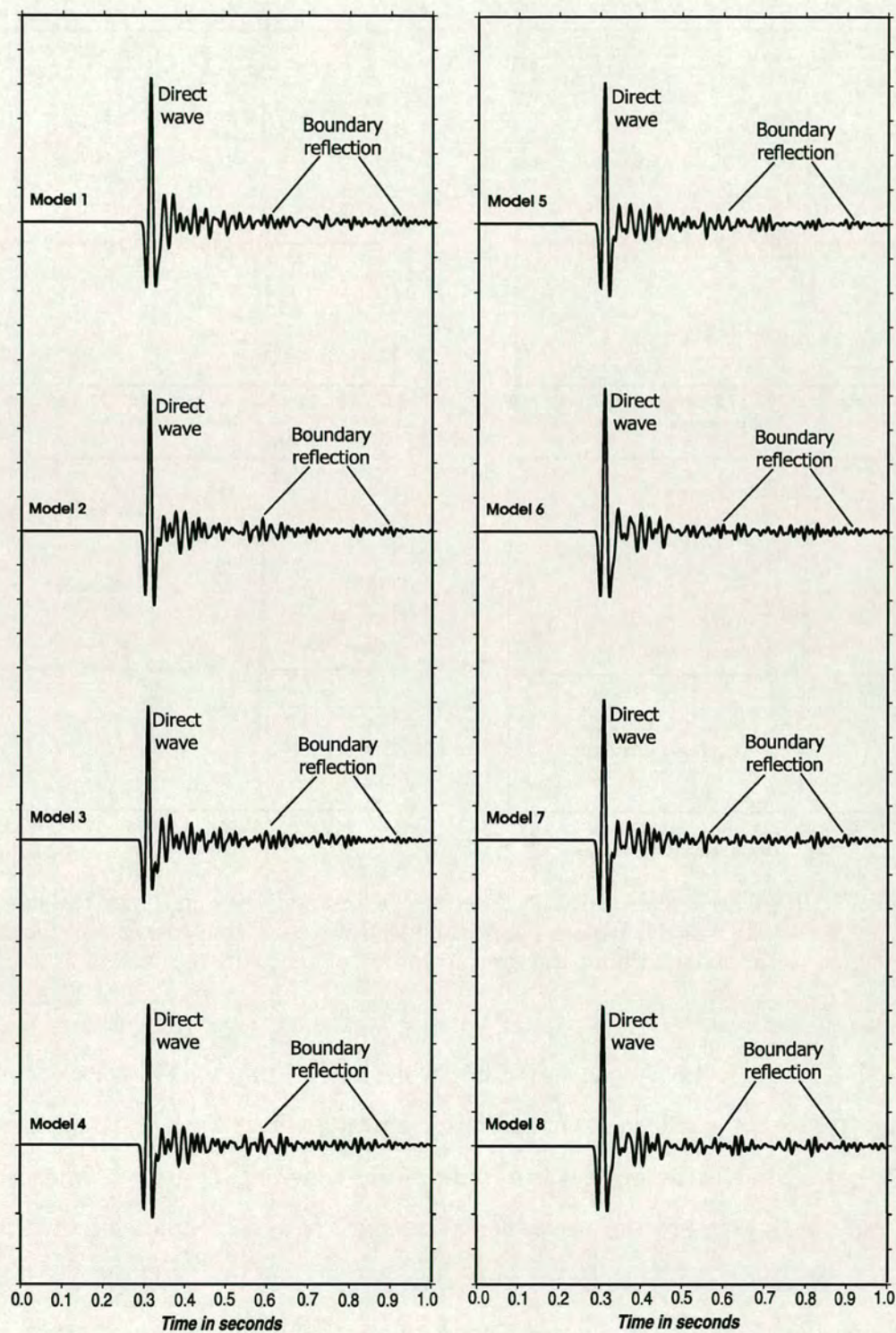
Figure 7.9: Wavelets recorded at receiver 90 for models 1 to 8 in the case of $k\alpha = 3.15$
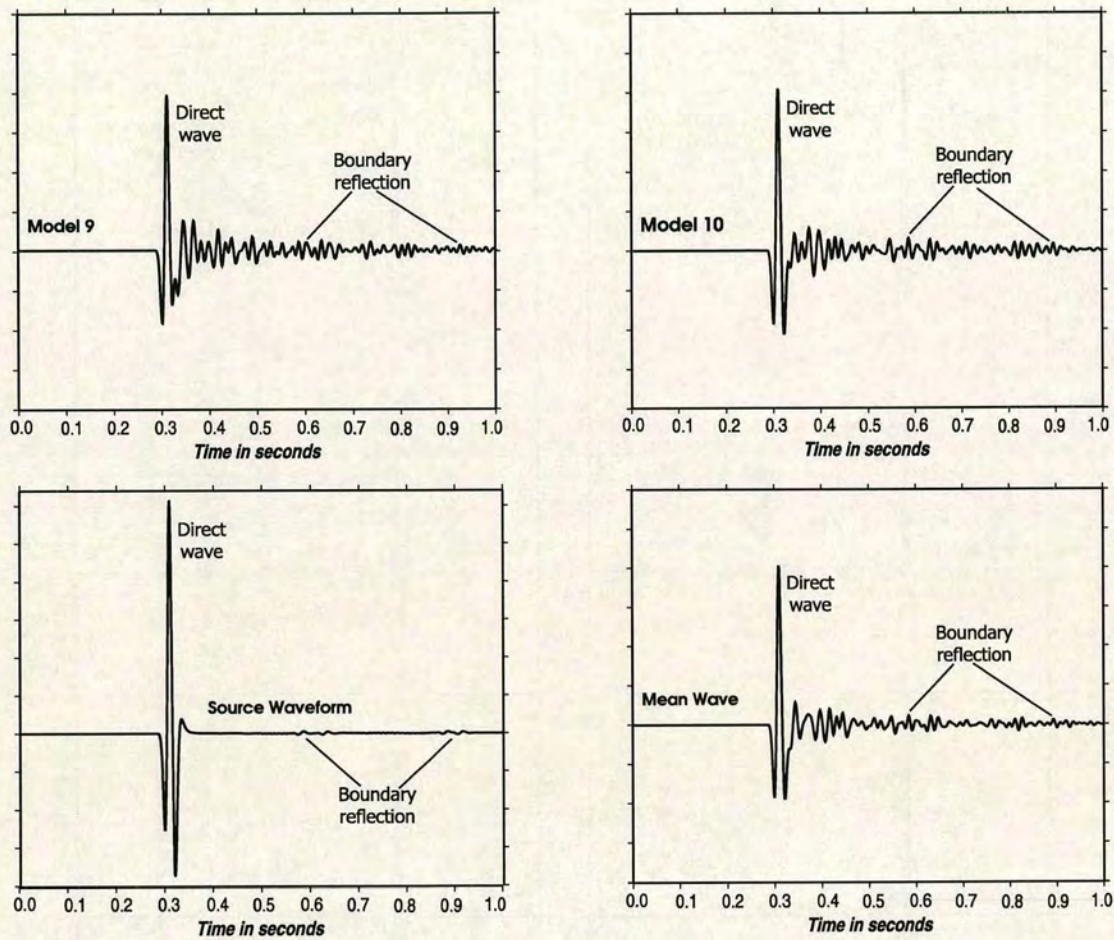
Figure 7.10: Wavelets recorded at receiver 90 for model 9 and 10 in the case of $k\alpha = 3.15$. We also show the mean wave and the source waveform for a model without fractures, recorded at the same receiver

more that is an effect of strong scattering, while at the same time we see clear coda waves. We see some reflections immediately after the direct wave at 0.32, 0.35 and 0.37s, but after 0.5s the wavelet is a result of less coherent scattering. The size of the fractures is equal to the size of the wavelength ($\alpha = \lambda/2$), therefore fractures act as interfaces, that give strong scattering and attenuation. Figure 7.11 shows four snapshots. Although the wavelet is more attenuated than in the previous case, we cannot see significant differences from the previous case.

Finally, Figure 7.12 shows the wavelets recorded at receiver 90 for models 1 to 8 and Figure 7.13 shows the wavelets recorded at the same receiver for models 9 and
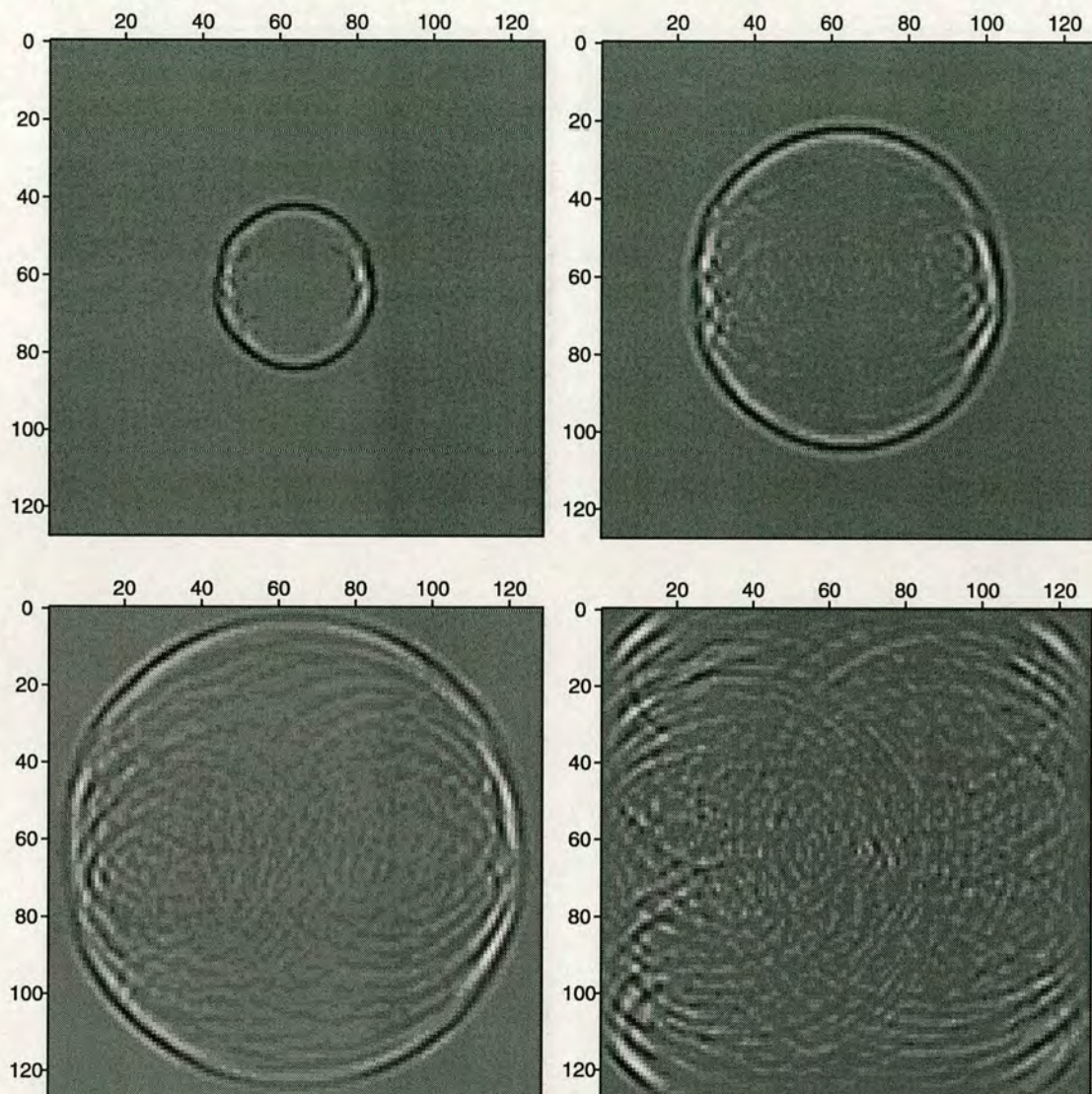
Figure 7.11: Snapshots of the mean wave taken at consecutive times in the case of $k\alpha = 3.15$

10, the mean wave and the source waveform for a model without fractures, when fractures have half-size $\alpha = 50m$. The product of wavenumber k and half-size α is $k\alpha = 6.3$.

In the models studied here the fracture size is larger than the wavelength. We have very strong attenuation. We can see strong reflections at 0.32, 0.34 and 0.4s. The most dominant feature of the waveforms for all the models are the
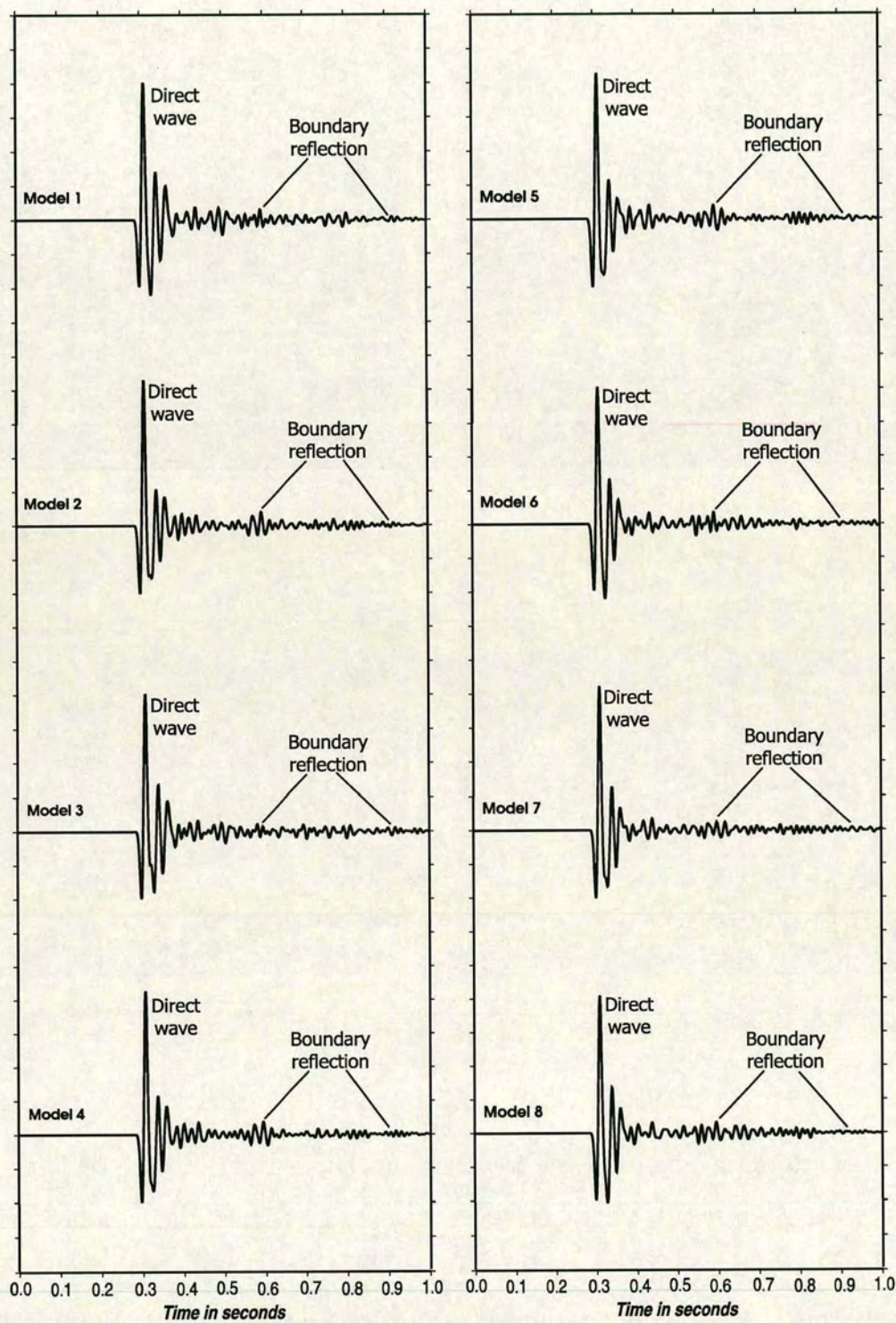
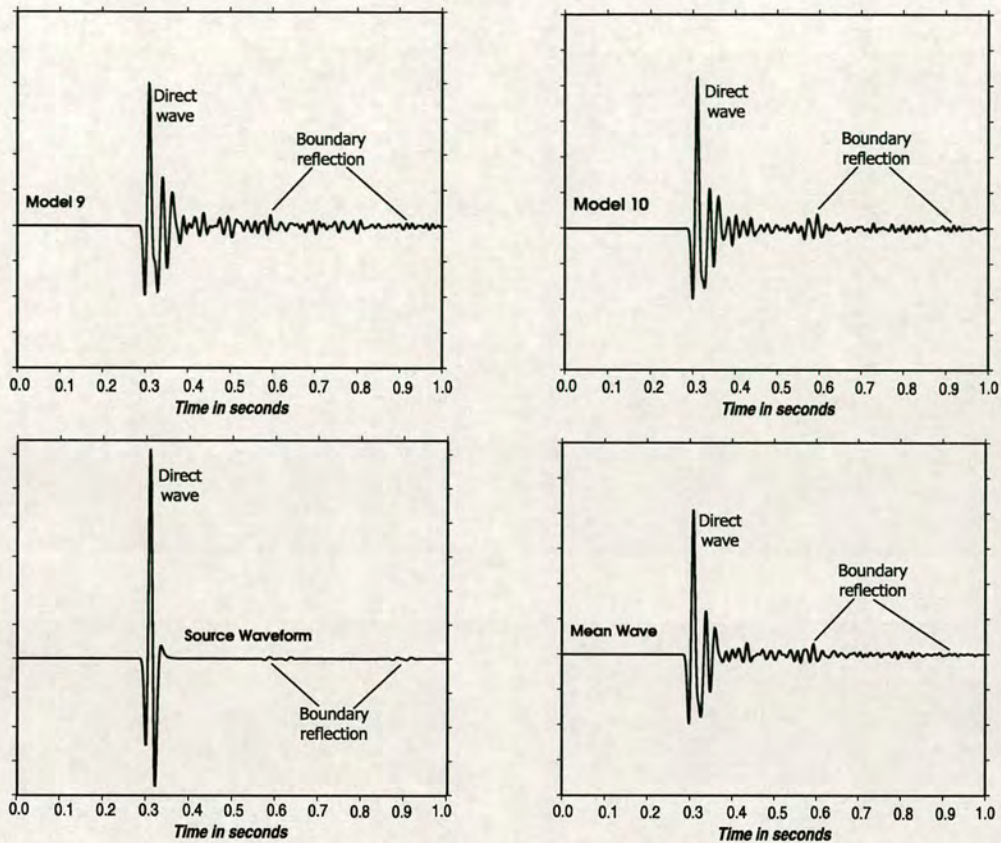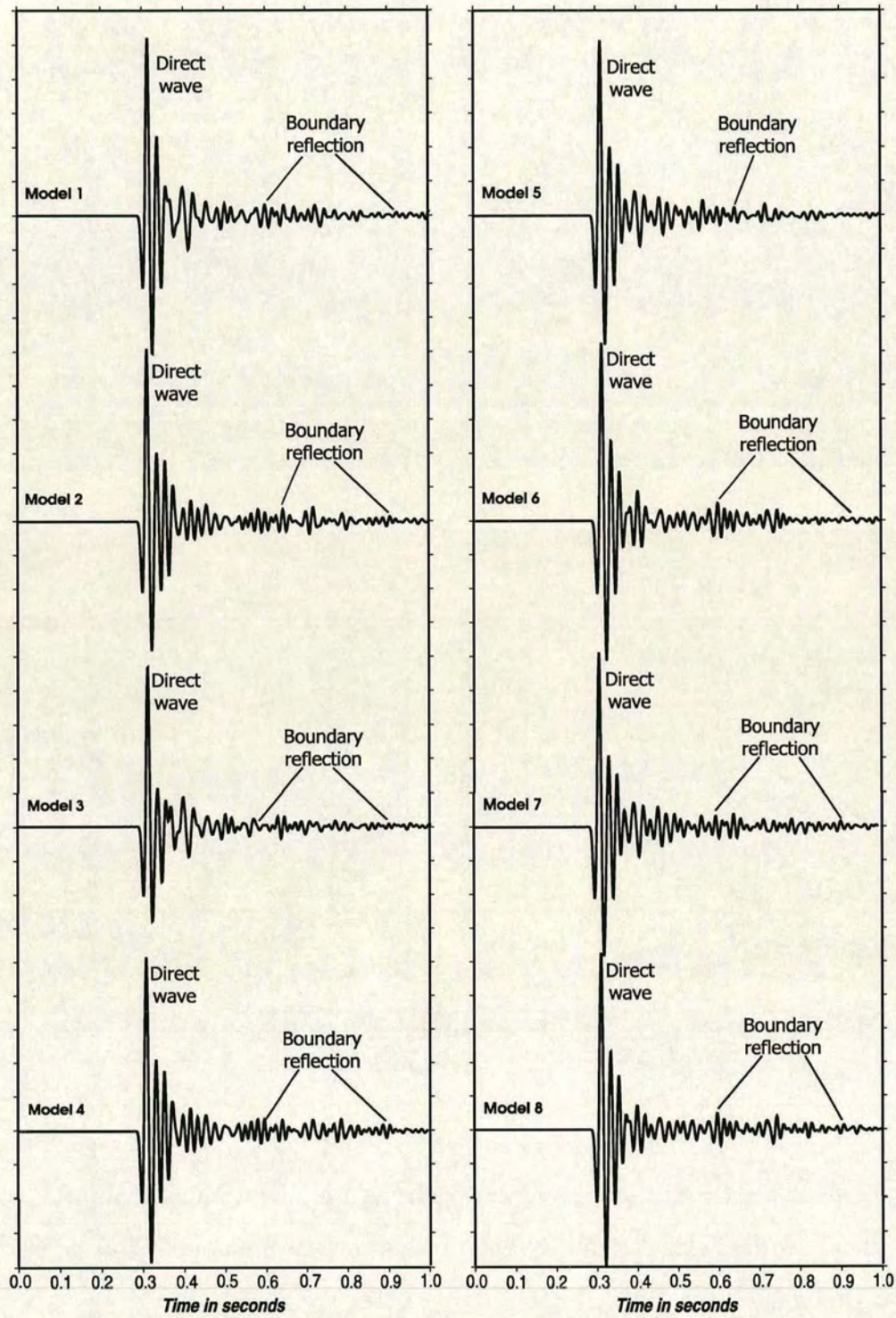**Figure 7.12:**   Wavelets recorded at receiver 90 for models 1 to 8 in the case of $k\alpha = 6.3$
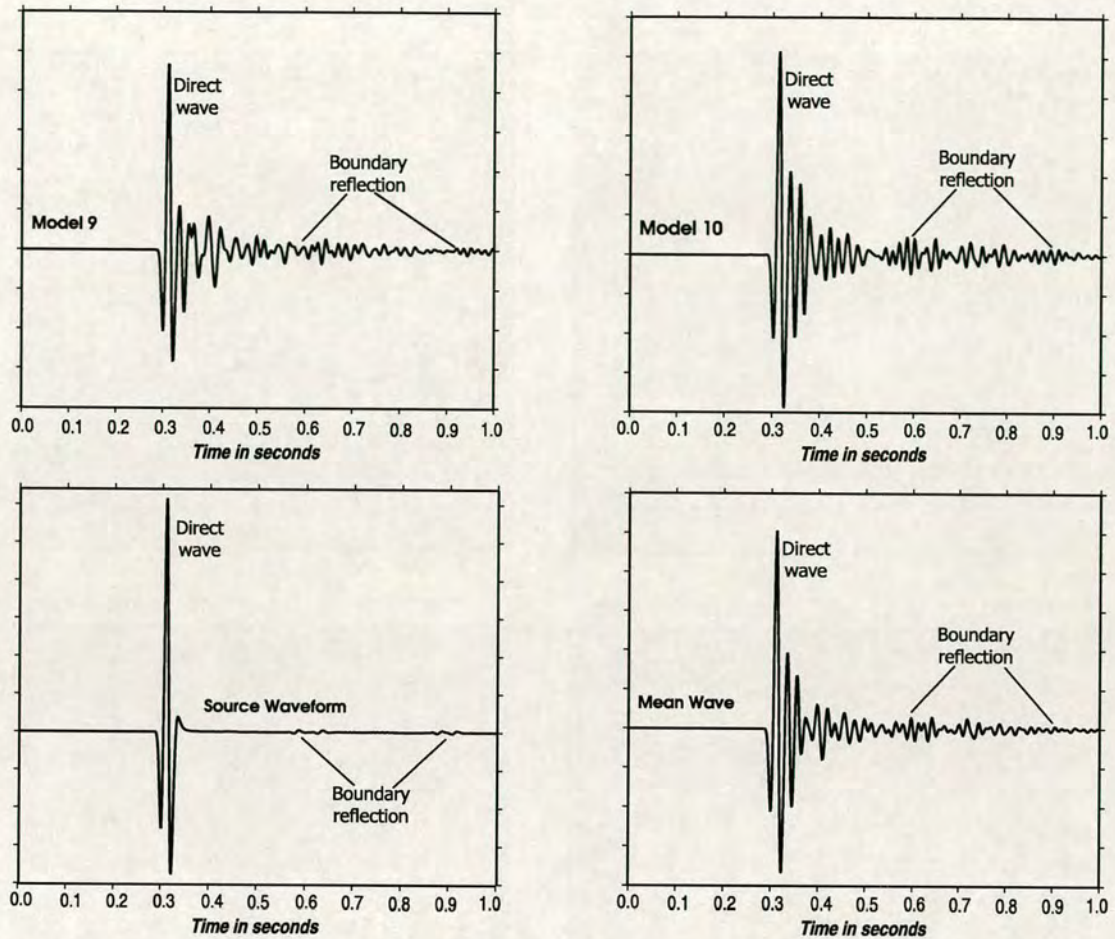
Figure 7.13: Wavelets recorded at receiver 90 for model 9 and 10 in the case of $k\alpha = 6.3$. We also show the mean wave and the source waveform for a model without fractures, recorded at the same receiver

strongly scattered waves, which makes identification of individual reflections very difficult. That is expected due to the size of the fractures that are larger than the wavelength. Another effect of the long fractures is the strong reflections that give direct waves with high amplitude. That is because fractures act as individual interfaces. The same features are visible in the mean wave, where we can see a clear reflection near 0.41s, and some other features which we cannot say if they are reflections or the result of scattering. The same results are more obvious in the snapshots shown in Figure 7.14. In the final snapshot we can see the strong scattering. The scattering is so strong that it distorts the circular shape of the propagating mean wave.
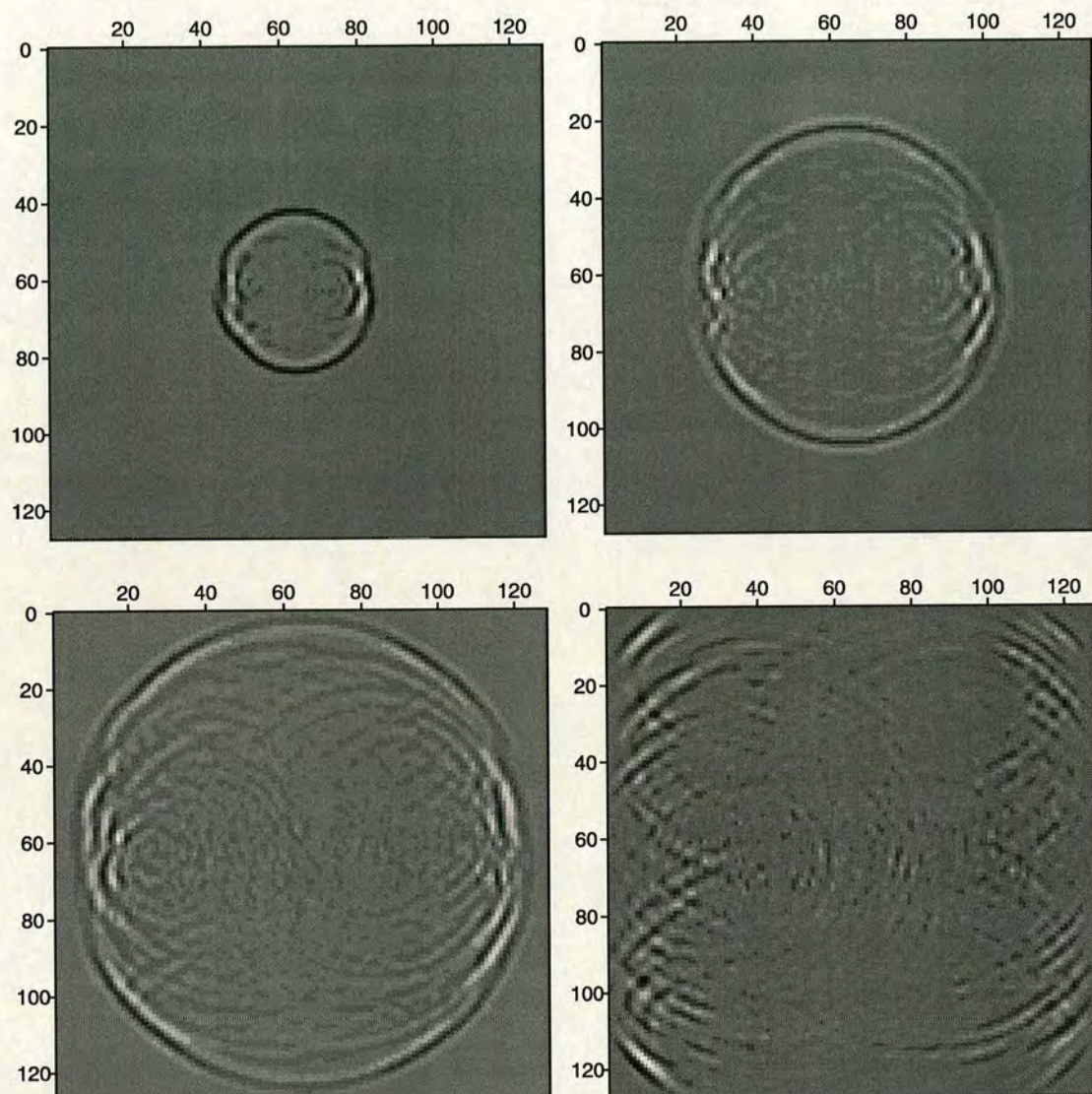
Figure 7.14: Snapshots of the mean wave taken at consecutive times in the case of $k\alpha = 6.3$

We use the results of the numerical modelling and follow the method we presented in the previous section (Section 6.4.1) to estimate scattering attenuation. Figure 7.15 shows scattering attenuation Q^{-1} as a function of angular frequency ω. In this figure, we also include the case of $k\alpha = 4.41$. We take as accurate only the results for frequencies from $\omega = 50Hz$ up to $\omega = 500Hz$. We can see a general shift of the maximum attenuation that is relevant to the normalised wavenumber $k\alpha$. However, due to the strong coda waves the amplitudes are not very smooth

and it is not possible to obtain very clear results for scattering attenuation.
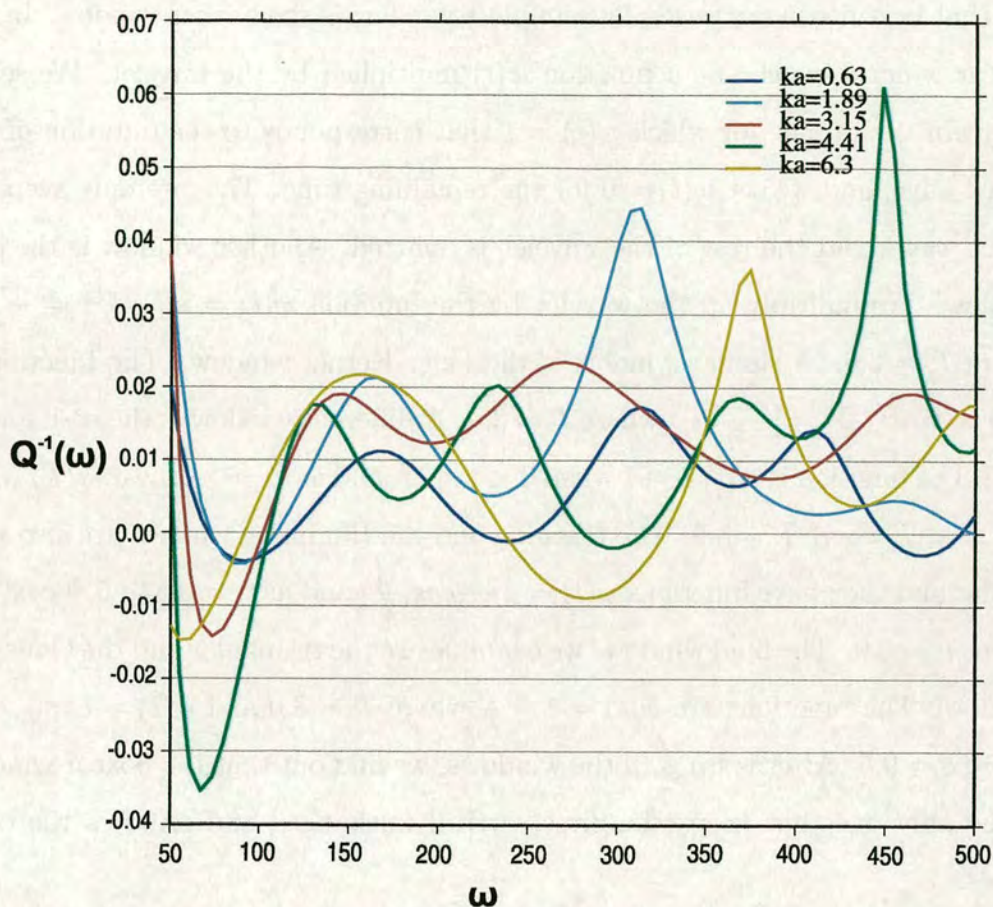
Figure 7.15: Estimation of scattering attenuation Q^{-1} as a function of frequency ω for the mean wave. We examine the cases of $k\alpha = 0.63$, 1.89, 3.15, 4.4 and 6.3

7.5   Estimation of scattering attenuation

The existence of coda waves immediately after the direct arrivals, especially in the cases of fractures that are long compared to the wavelength, introduced significant complications to the extraction of accurate results about attenuation of the mean waves for different cases of fracture sizes. For the estimation of scattering attenuation, we concentrate on the direct arrivals. To obtain the amplitude spectra $A(\omega)$ of the primary pulses, seismograms are windowed around the direct

arrivals. We examine different kinds of windowing techniques in order to find the one that best fits in our case. The simplest window is the boxcar window. In the boxcar window we choose a function $w(t)$ multiplied by the wavelet. We select a certain time range for which $w(t) = 1$ that corresponds to the duration of the direct wave, and we set $w(t) = 0$ for the remaining time. Thus we only keep the direct waves and the rest of the wavelet is omitted. Another window is the sinc window. We multiply all the wavelet by the function $w(t) = sinc(\frac{\pi t}{T}) = \frac{sin(\frac{\pi t}{T})}{\frac{\pi t}{T}}$ where $T = 3.0$. A similar window is the Fejer Kernel window. The function is $w(t) = sinc^2(\frac{\pi t}{T}) = [\frac{sin(\frac{\pi t}{T})}{\frac{\pi t}{T}}]^2$ where $T = 3.0$. A different window is the cosine window. The function is $w(t) = +1$ when $0 < t < \frac{4T}{5}$ and $w(t) = \frac{1}{2} + \frac{1}{2}cos(5\pi tT)$ when $\frac{4T}{5} < t < T$ where $T = 3.0$. The Hanning and the Hamming window are also very similar and they have functions $w(t) = \frac{1}{2} + \frac{1}{2}cos(\frac{\pi t}{T})$ and $w(t) = 0.54 + 0.46cos(\frac{\pi t}{T})$, where $T = 3.0$. The final windows we examine are the triangular and the Gaussian window. The functions are $w(t) = 1 - \frac{t}{T}$ where $T = 3.0$ and $w(t) = exp(-\alpha t^2)$ where $a = 0.5$. After testing all the windows, we find out that the boxcar window is the only one that keeps the direct arrival unchanged and removes the coda waves.

7.5.1   Effect of travel distance

We use the boxcar window while analysing the power spectra for the previous models. We add a new model to the above models for which $\alpha = 35m$, therefore for this model $\alpha = \frac{\lambda}{1.5}$ and $k\alpha = 4.41$. The position of the fractures and the layout of the model is the same as in the other models. The only difference is the size of the fractures. To estimate scattering attenuation we follow the process we explained in a previous section (Section 6.4.1). We take the waveforms of the mean wavefield that are recorded in receiver 90 for each one of the models. We window the waveforms around the first-arrival. We use the waveforms that are recorded at the same receiver, so the waves travel through the same distance, thus we do not

need to make any travel-distance corrections. The waveforms are Fourier transformed to obtain the amplitude spectra $A(\omega)$ of the primary pulses. Figure 7.16 shows the amplitude spectra as a function of the normalised wavenumber for five different cases of $k\alpha$. The figure also includes the source amplitude spectra for comparison. The amplitude spectra of the windowed meanfield shows the same decay and shift of the dominant frequency. Now the spectra is smooth because random fluctuations caused by non-perfect averaging are largely left outside the window. We can see that when the fractures are smaller than the wavelength, which corresponds to normalised wavenumber $k\alpha \leq 3.15$, there is a shift of the peak frequency towards lower values and the corresponding amplitude is less than the initial source amplitude. On the other hand, when fractures become larger than the wavelength ($k\alpha = 4.4$ and 6.3), the behaviour is completely opposite and there is a shift of the peak frequency towards higher values and at the same time the amplitude is significantly higher compared to the initial source amplitude at the high frequencies. This indicates that as the size of the fracture becomes larger, scattering attenuation becomes higher and the energy is redistributed to the coda waves. We can see that for $k\alpha = 4.4$ the redistribution procedure of the energy from lower towards higher frequencies starts and it is complete for $k\alpha = 6.3$, when most of the energy is at high frequencies. That is the effect of the strong reflections due to the large size of the fractures.

We calculate the slope of the curve $ln\frac{A(\omega)}{A_o(\omega)}$ over travel-distance. From Equation (7.8) we get, $ln\frac{A(\omega)}{A_o(\omega)} = -(\frac{\omega}{2\beta}Q^{-1})r$, where $A(\omega)$ is the amplitude of the waveform recorded at a receiver at a distance r from the source, $A_o(\omega)$ is the amplitude of the waveform recorded at the source, and β is the acoustic-wave speed. We fit a least-square line to the data for each model and from the slope of the line we calculate scattering attenuation Q^{-1}. Figure 7.17 shows the values $ln\frac{A(\omega)}{A_o(\omega)}$ for the different models and the least-square line for the dominant frequency of 40Hz. In Figure 7.17,(a) to (e) correspond to the normalised wavenumber
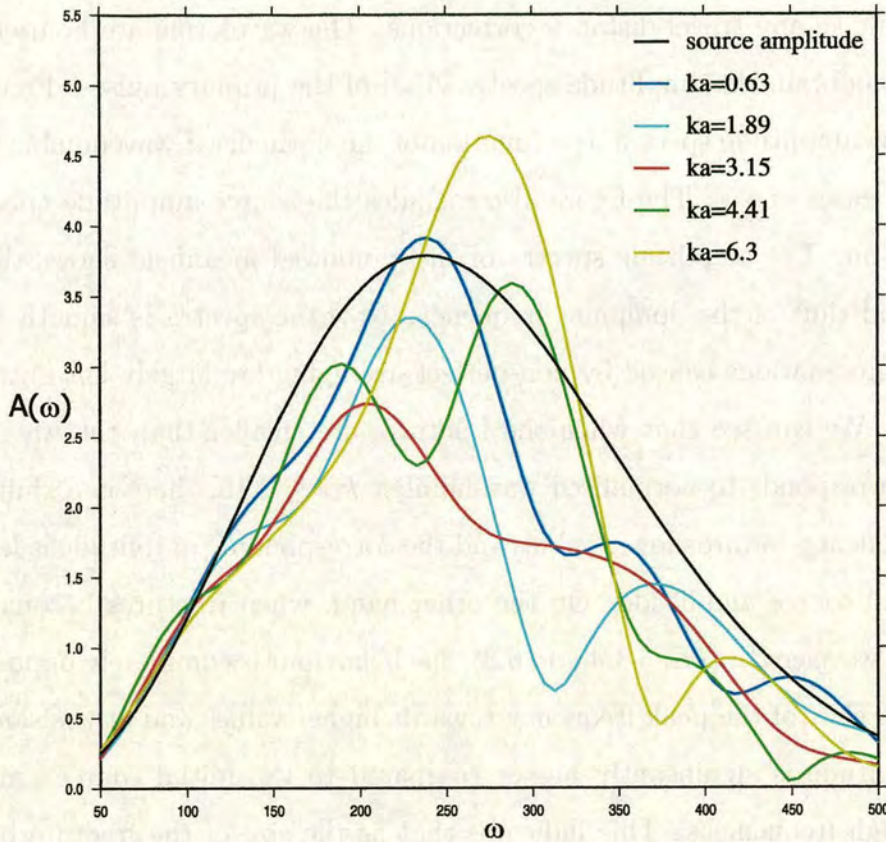
Figure 7.16: Amplitude spectra as a function of the normalised wavenumber ($k\alpha$) for the various models we examined. We also show the source amplitude spectra for comparison

$k\alpha = 0.63, 1.89, 3.15, 4.41$, and 6.3, respectively. The fluctuations of the values of $ln\frac{A(\omega)}{A_o(\omega)}$ indicate that scattering attenuation depends significantly on the distance. That may be an effect of the different paths that the wave travels to reach the receiver and especially on the different fractures that the wave interacts with. The scattering of the log values away from the least-square fit line is because the spatial averaging does not suppress incoherent energy sufficiently, due to the high fracture density in our models. This indicates that the mean wavefield theory may not be valid in cases of high fracture density. Another possibility is that the fluctuations from the linear fit is an effect of the window we applied. As the travel distance becomes larger the wavefield fluctuates stronger and there is a larger portion of energy transferred to the coda. In the region of strong fluctuations,

which is when the fracture size becomes equal or larger than the wavelength, it is very hard to determine for a certain trace where the first arrival ends and where the coda begins.

Generally, we can conclude that travel distance affects scattering attenuation estimates. At short travel-distances meanfield attenuates mainly because of arrival-time fluctuations of individual records. With increasing travel-distance, amplitude fluctuations play an increasing role in meanfield attenuation. In Figure 7.17 the variation of the slope of the least-square fit line, indicates that the dependence becomes stronger as fractures become longer compared to the wavelength. From the slope of the least-square fit for different values of $k\alpha$ we obtain an estimate of scattering attenuation for each case. Figure 7.18 shows scattering attenuation Q^{-1} as a function of the normalised wavenumber $k\alpha$. We see that scattering attenuation becomes higher as the normalised wavenumber increases until $k\alpha = 4.4$. After $k\alpha = 4.4$ scattering attenuation decreases, which is in agreement with the results of previous works (Frankel and Clayton, 1986, Frenje and Juhlin, 2000).

7.5.2   Effect of azimuth from crack normal

Another important factor that affects scattering attenuation is the angle from crack normal. We examine scattering attenuation for the same models of the previous section. We investigate scattering attenuation as a function of the angle from the fracture normal. In all the models we put the source at the position with coordinates x=630m and y=630m. We take 11 receiver lines each one of which has a number of receivers at different distances from the source. Each receiver line is at a different angle from the fracture normal. The angles are 0°, 10°, 20°, 30°, 45°, 60°, 70°, 80°, and 90°. We examine the cases of $k\alpha = 0.63$ and $k\alpha = 1.89$. For each direction we use a maximum number of 30 receivers. We get the least-square fit line for each angle. Figures 7.19 and 7.20 show the values $ln\frac{A(\omega)}{A_o(\omega)}$ as
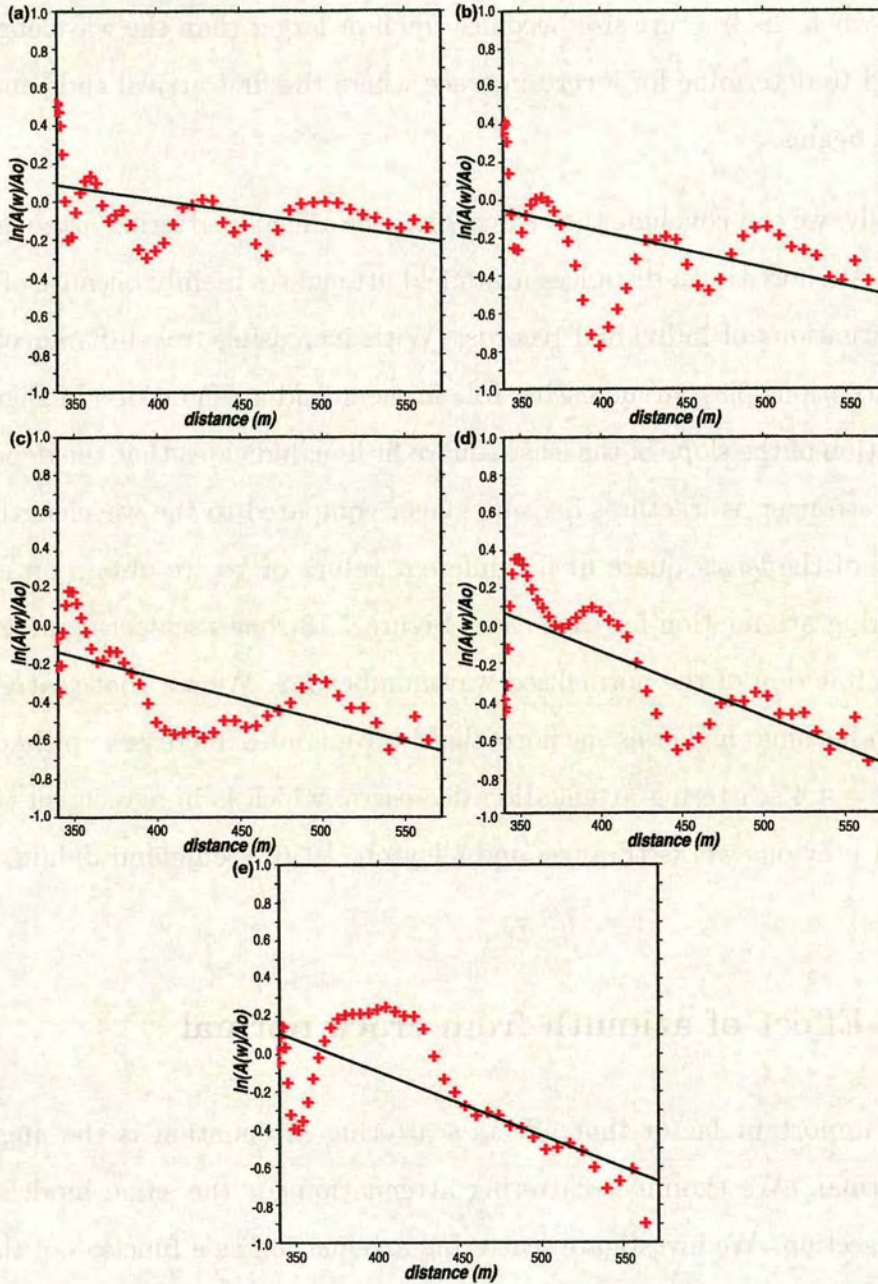
Figure 7.17: Variation of $ln \frac{A(\omega)}{A_o(\omega)}$ as a function of the travel distance for the dominant frequency of 40Hz. Figures (a) to (e) correspond to the normalised wavenumbers $k\alpha = 0.63$, 1.89, 3.15, 4.41, *and* 6.3, respectively. Each cross refers to a measured value at each receiver, and the solid line is the least-square fit

a function of the different angles from the fracture normal for the normalised wavenumber $k\alpha = 0.63$. In Figure 7.19, figures (a) to (f) correspond to 0º, 10º,
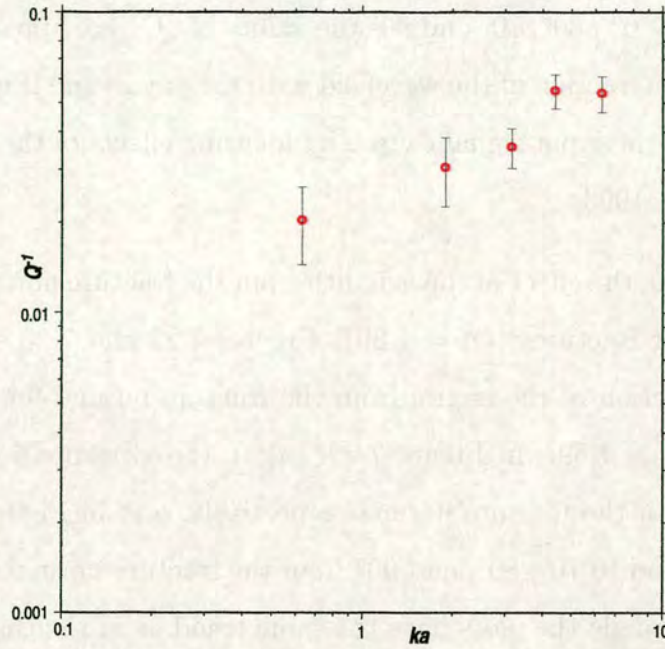
Figure 7.18: Scattering attenuation Q^{-1} as a function of normalised wavenumber $k\alpha$ with error bars representing standard deviation

20°, 30°, 45°, 60° from the fracture normal respectively, and in Figure 7.20, (a), (b) and (c) correspond to 70°, 80°, and 90° from the fracture normal respectively. As in the previous section there is a strong fluctuation of the values around the least square-fit line. The fluctuation becomes even stronger for angles of 30°, 45°, and 60°. Figure 7.21 shows the resulting scattering attenuation Q^{-1} as a function of the angle from the crack normal of the fracture. We can see that as the angle becomes higher the error bars become more significant. If we fit a line to the values of each angle, we find that scattering attenuation Q^{-1} increases with respect to increasing angle from the fracture normal. That means that the lowest value of Q^{-1} is obtained when the wave propagates normal to the fracture and the highest when the wavelet propagates parallel to the fracture. The general trend does not apply for the angles of 20° and 60°. That may be just an effect of the path that the waves travel for certain angles. Moreover, there does not seem to be any reason why those two angles should have this kind of different behavior, except from statistical fluctuations from the general trend. Another interesting

feature is that for 0° , 30°, 70° and 90° the values of Q^{-1} are apparently negative, an effect of the interaction of the wavefield with the cracks and it corresponds to a magnification of the input signal caused by focusing effects of the heterogeneities (Roth and Korn, 1993).

We also examine the effect of the azimuth from the fracture normal for the same models for larger fractures ($k\alpha = 1.89$). Figures 7.22 and 7.23 show the values $ln\frac{A(\omega)}{A_o(\omega)}$ as a function of the angles from the fracture normal for the normalised wavenumber $k\alpha = 1.89$. In Figure 7.22, (a) to (f) correspond to 0°, 10°, 20°, 30°, 45°, 60° from the fracture normal respectively, and in Figure 7.23, (a), (b) and (c) correspond to 70°, 80°, and 90° from the fracture normal respectively. In general for each angle the plots have the same trend as in the case of $k\alpha = 0.63$. However, it is obvious that the absolute values of $ln\frac{A(\omega)}{A_o(\omega)}$ are significantly higher than the case of $k\alpha = 0.63$ presented in Figures 7.19 and 7.20. That is an effect of the large sizes of fractures resulting in high attenuation. Figure 7.24 shows the resulting scattering attenuation Q^{-1} as a function of the angle from the fracture normal.

7.6   Summary

In this chapter we have applied the mean wavefield theory to study scattering attenuation variation with the size of the fractures and the angle of incidence. To generate the mean wavefield we use ten models where the positioning of the fractures is slightly different and we average the wavefield recorded at each receiver for all models. We calculate $ln\frac{A(\omega)}{A_o(\omega)}$, where $A(\omega)$ is the amplitude of the averaged recorded wavefield and $A_o(\omega)$ is the amplitude of the source wavefield. We assume that the dependence of the logarithm of the averaged amplitude spectrum on distance can be fitted by a straight line. The underlying assumption here is that the corresponding attenuation estimates which are determined from
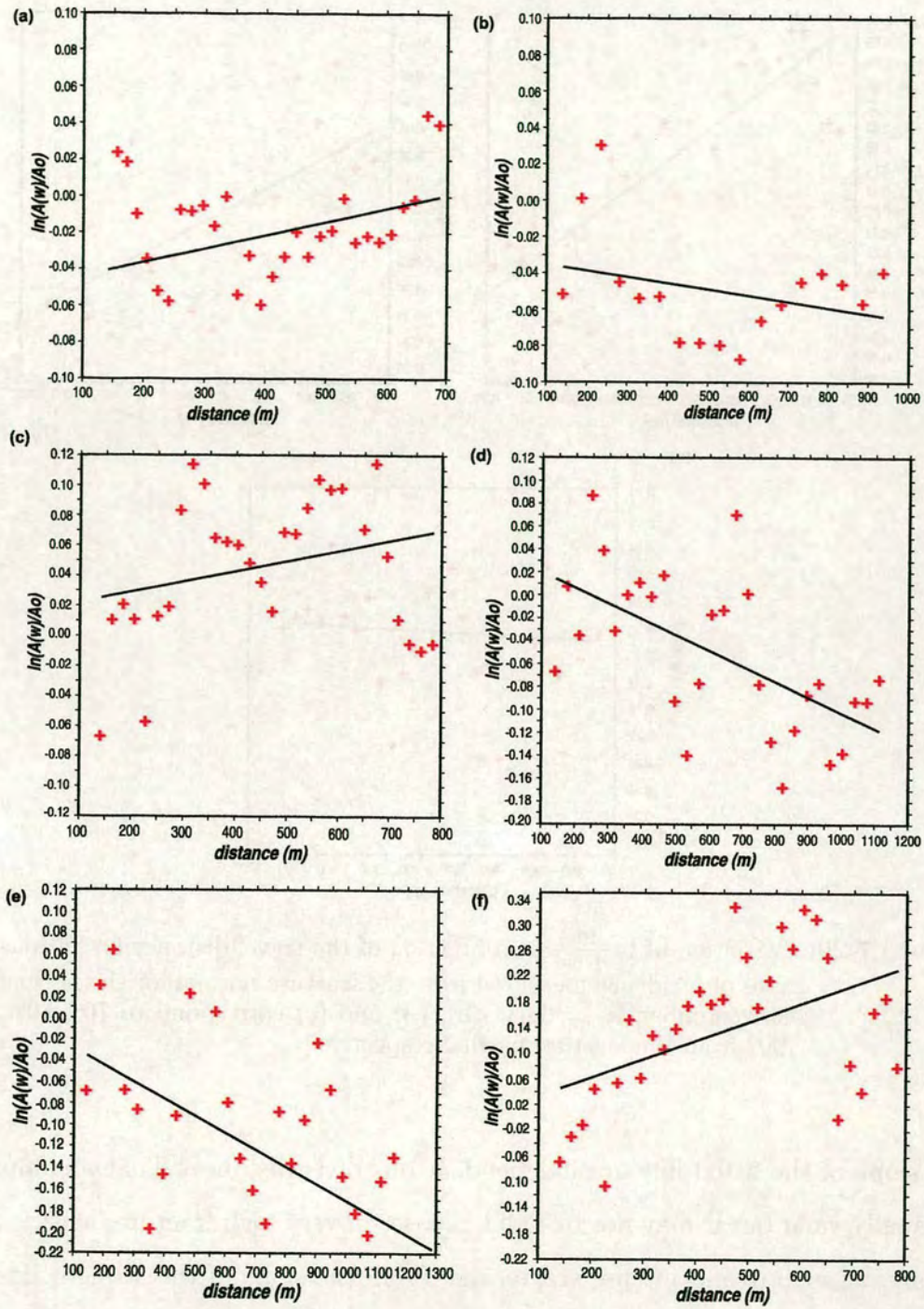
Figure 7.19: Variation of $ln\frac{A(\omega)}{A_o(\omega)}$ as a function of the travel distance for various angles of incidence measured from the fracture normal for the normalised wavenumber $k\alpha = 0.63$. (a) to (f) correspond to 0°, 10°, 20°, 30°, 45°, 60° from the fracture normal respectively
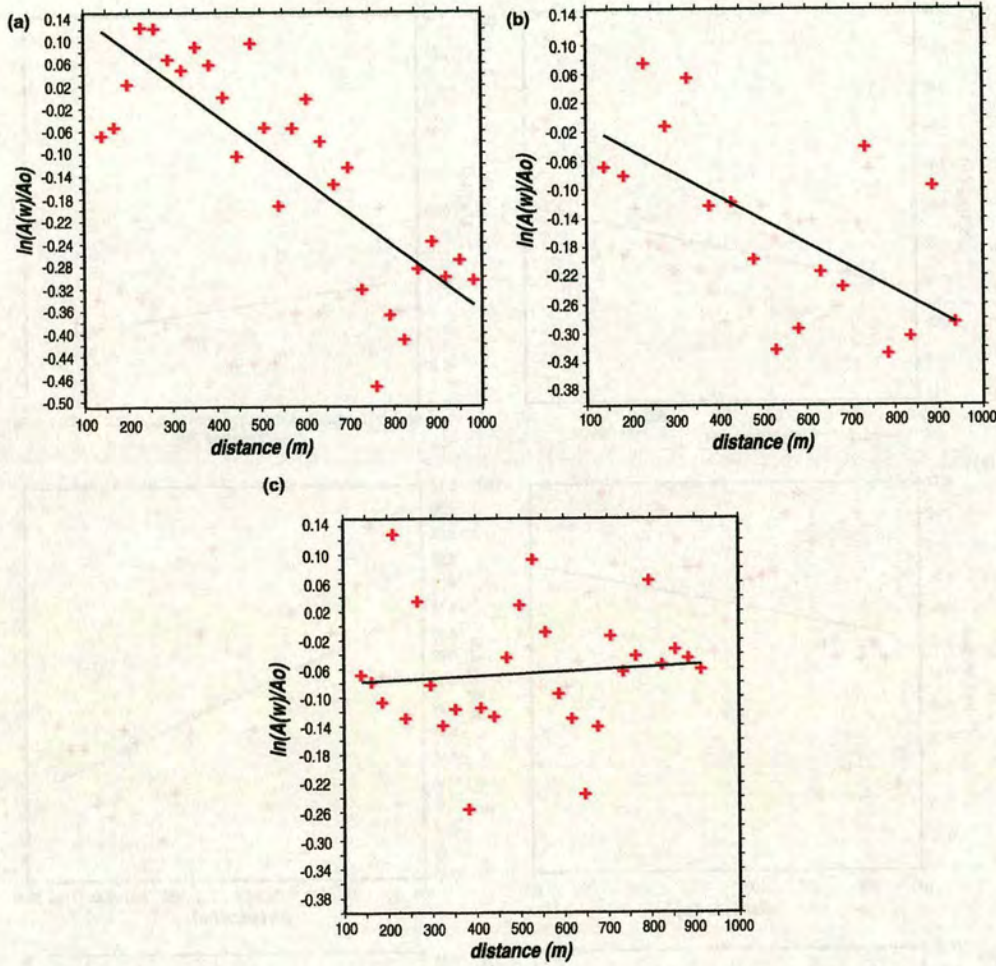
Figure 7.20: Variation of $ln\frac{A(\omega)}{A_o(\omega)}$ as a function of the travel distance for various angles of incidence measured from the fracture normal for the normalised wavenumber $k\alpha = 0.63$. (a), (b) and (c) correspond to 70°, 80°, and 90° from the fracture normal respectively

the slope of the fitted line are independent on travel distance. That assumption is usually valid but it may not be valid in cases of very high fracture density with strong anisotropy and intense scattering. From the slope of the straight line we calculate scattering attenuation Q^{-1}. Although the results show some distinct features of the variation of scattering attenuation Q^{-1} with $k\alpha$, the strong coda waves in some cases can lead to misinterpretation of the results. There is also an effect of the travel distance. When we fit a straight line to the results of $ln\frac{A(\omega)}{A_o(\omega)}$, those results come from receivers at different distances from the source.
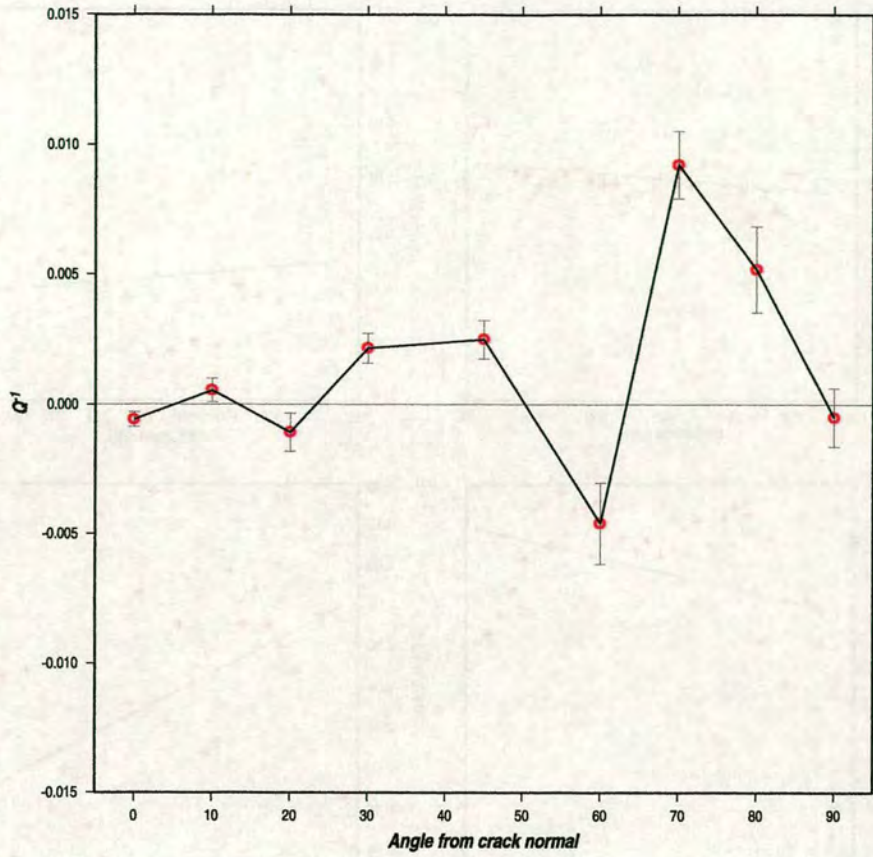
Figure 7.21: Scattering attenuation Q^{-1} as a function of the angle from the crack normal. Error bars represent standard deviations. The figure is for the normalised wavenumber $k\alpha = 0.63$

Shapiro and Kneib (1993) found that the shorter the travel distance, the better the spatial averaging suppresses fluctuations. Non-perfect averaging leads to a meanfield "tail" at large distances. If we decide to limit our study only to receivers at small distances we will not obtain a reliable estimate of scattering attenuation. Therefore, we decide to use a window around the direct arrivals. It is clear that the estimations of the scattering attenuation obtained from logarithms of amplitude spectra will depend on the length and type of window to extract the direct arrivals. The second aspect of windowing is the window shape. The choice of a window shape always has to compromise between the amount of variance and bias introduced. The choice of a window function is less important because averaging smooths and bias, partly averages away. We have decided to
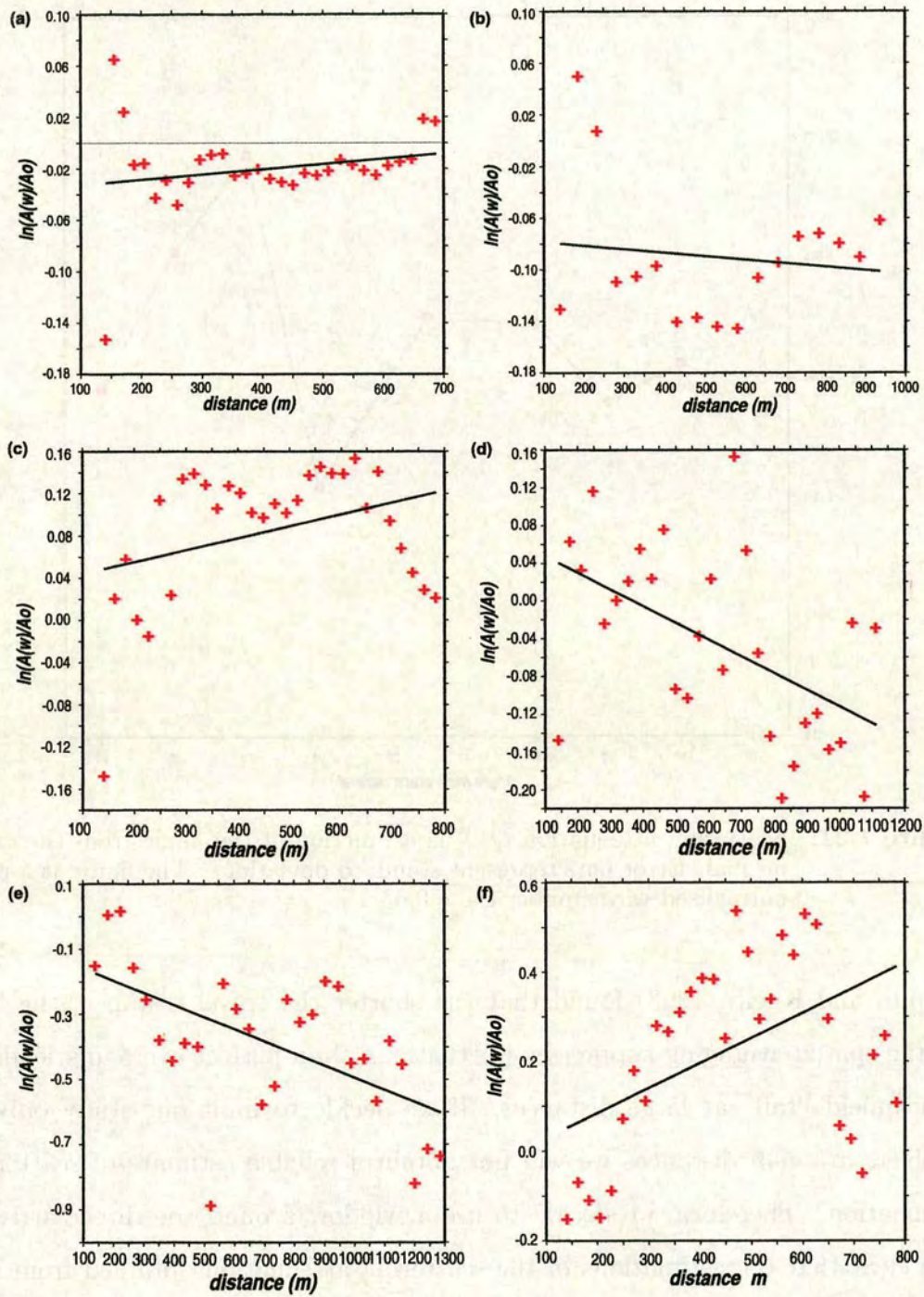
Figure 7.22: Variation of $ln\frac{A(\omega)}{A_o(\omega)}$ as a function of the travel distance for various angles of incidence measured from the fracture normal for the normalised wavenumber $k\alpha = 1.89$. (a) to (f) correspond to 0°, 10°, 20°, 30°, 45°, 60° from the fracture normal respectively
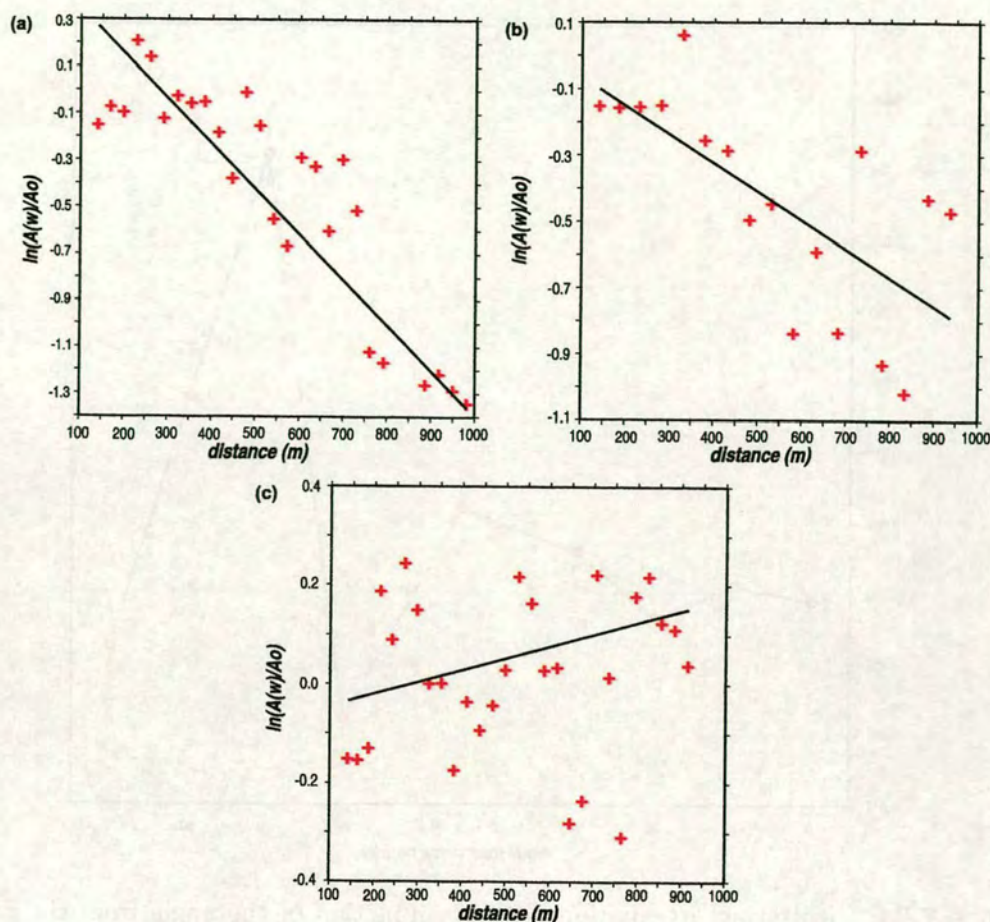
Figure 7.23: Variation of $ln\frac{A(\omega)}{A_o(\omega)}$ as a function of the travel distance for various angles of incidence measured from the fracture normal for the normalised wavenumber $k\alpha = 1.89$. (a), (b) and (c) correspond to 70°, 80°, and 90° from the fracture normal respectively

use a boxcar window, which has different length and limits depending on each individual waveform in order to use only the direct arrival. All the results from the slopes of the linear fit for each $k\alpha$ are gathered to study scattering attenuation Q^{-1} as a function of normalised wavenumber $k\alpha$. We see that Q^{-1} becomes high as the normalised wavenumber $k\alpha$ increases until it reaches $k\alpha = 4.41$, and at this point the fracture size becomes larger than the wavelength. After that point scattering attenuation declines (i.e. $k\alpha = 6.3$)

For high frequencies each fracture excites scattered waves of significant amplitude, with the largest corresponding to wavelengths comparable to the fracture
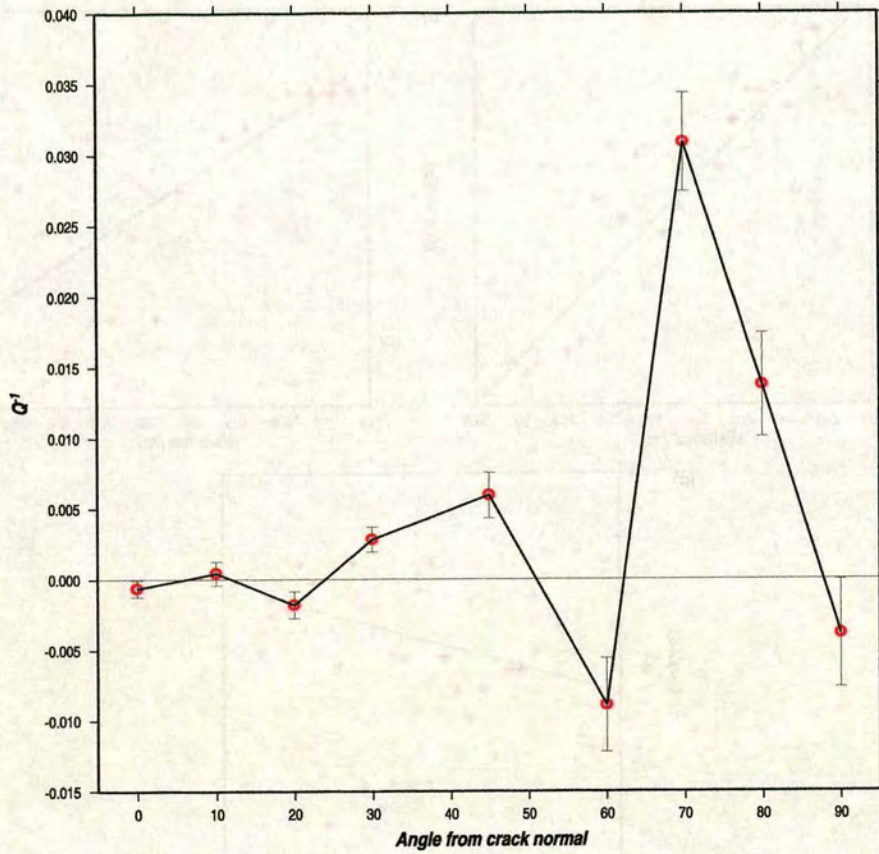
Figure 7.24: Scattering attenuation Q^{-1} as a function of the angle from the crack normal. The figure is for the normalised wavenumber $k\alpha = 1.89$

size. For low frequencies, wavelengths much larger than the size of the fractures, the waves excited by each fracture are negligible but the fractured medium excites a reflected wave as if it was one heterogeneous medium of some effective thickness. Those effects on the overall scattered wavefield by a fracture distribution are depicted in Figure 7.25.

Finally, we examine the effect of the angle of incidence on the wavelet from the fracture normal on scattering attenuation Q^{-1}. We calculate the logarithms of amplitude spectra for different angles starting from 0° up to 90°, and then fit a straight line to the data for each angle. From the slope scattering attenuation Q^{-1} can be estimated. Scattering attenuation Q^{-1} increases constantly from 0° to 90°. However, there are some exceptions in that trend with negative values in
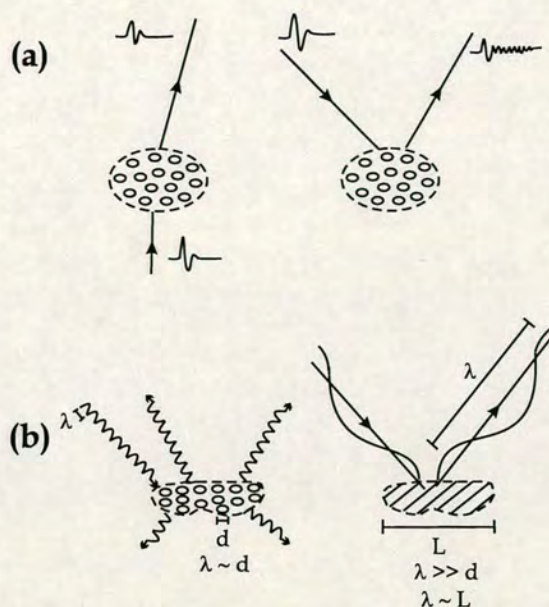
Figure 7.25: (a) Schematic view of distortion of the primary wave by the cluster of cavities in both forward and backward scattering cases. In the forward case, the primary wave is attenuated with little distortion of its waveform, and producing weak late arrivals. This is not true in the backward case, which produces many late arrival phases of significant amplitude. (b) Schematic view of how a cluster of cavities produces scattered waves in different frequencies or wavelength ranges. For high frequencies, waves scattered by each cavity are strong. In low frequencies (wavelength much larger than the size of each cavity), the entire cluster produces scattered waves as if it were a single large heterogeneous body. Figure taken from Yomogida et al. (1997)

some cases. This is almost certainly an effect of the magnification of the input signal caused by focusing effects of the heterogeneities. It is interesting to note that the highest value of Q^{-1} is for 70° and not for 90°. In general, the highest value of Q^{-1} is when the wave travels parallel to the fracture and the lowest value when the wave travels normal to the fracture.

CHAPTER 8

Single-phase flow in porous media: Theory and numerical modelling

8.1 Introduction

Until this point we have examined seismic wave propagation in a fractured network, and presented the basic theory of wave propagation and the available techniques of analytical and numerical solutions to the wave equation. A new technique has been introduced to describe the wave propagation through a fractured medium and to study the effects of fracture properties on the wave attributes. However, we assume that the fractures are filled with gas, which is not always realistic. In this chapter we introduce the existence of fluid in the fractures.

Fracture networks often form the only significant paths for fluid flow in impermeable rocks, such as carbonates. In permeable rocks, such as sandstones, fracture can often dominate the conductivity by providing quick routes for fluid movement and the matrix provides storage for fluid. Networks of fractures also control many crustal processes, such as deformation. There is a very practical side to the study of fractures and associated fluids, as reviewed by Pollard and Aydin (1988): "They influence mineral deposition by guiding oreforming fluids, and they provide fracture permeability for water, magma, geothermal fluids, oil and gas.

Because joints may significantly affect rock deformability and fluid transport, they are considered by engineering geologists in the design of large structures". During the design and construction of many major engineering projects, the effects of fractures on deformation and permeability have been considered as one of the most important factors. Also in large near surface excavations, changes in fluid pressure within a fracture network may play a key role in controlling the stability of a structure.

The upper crust is complicated in terms of its components and structure; under most circumstances it may be described as a system of rock-blocks separated by fractures that may be filled with fluids. Such systems exhibit complex, discontinuous behaviour and generally are anisotropic and spatially heterogeneous. The rock-block system may be subject to a complex loading history due to superposed tectonic events at various scales and to human activities. Fluid flow may not be uniformly distributed within such rock-block systems and it is the aperture of a fracture that determines its transmissivity. Many field experiments and borehole data have revealed that the movement of ground water in fractured rock masses is dominantly controlled by a small proportion of fractures (e.g.Neretnieks, 1985; Bourke et al., 1985; Nolte et al., 1989; Michie, 1996; Barton et al., 1985; Jones et al., 1999).

In general, the response of a sub-surface flow system to a hydraulic perturbation is governed by the geometric attributes of the system and the properties of fluids. Deformation can affect fluid migration due to changes in fracture network, including the closure and opening of hydraulic conduits, as well as the creation of new ones. The converse is also true, fluid pressure can change the effective stress within the rock and, thus, the shear stress required to cause slip and dilation along discontinuities. Under most circumstances a rock-block system may be treated as a deformable discrete medium, within which the geometry and mechanical properties of discontinuities, the deformability of the rock-blocks and

the stress state (including fluid pressure distribution) control the deformation and flow, often producing large finite strains and non-linear behaviour.

In this chapter we present the fundamentals of single phase fluid flow. We go through the derivation and meaning of the macroscopic transport equations for single phase flow in porous media and discuss how they are solved. We start by showing some basic concepts relating to porous media and to single phase flow. In the following we refer to the material balance and Darcy's law approach to flow in porous media and show the equation for single phase compressible flow in porous media. Based on those theoretical ideas, we introduce a numerical technique that simulates fluid flow in a fractured network. We describe in detail the fundamental assumptions for the simulation and the physical mechanisms that are involved.

8.2   Flow models

In terms of mathematical models, simulations of fluid flow through a rock-block system fall into one of two models: (1) equivalent continuum, and (2) discrete network.

The equivalent continuum assumption or homogenisation principle can be used to apply continuum-based numerical methods to problems in discontinua. Such an assumption is valid only when a characteristic volume considered in a problem is not less than its Representative Element Volume (REV). The REV is a critical volume that should be larger than the volume of the process domain if all equivalent constitutive properties become constant (Odling, 1997; Jing and Stephansson, 1997). Based on continuum methods, numerical models for underground fluid transport require descriptions of the hydro-geological properties of all the materials, and can be constructed with different levels of details. Sometimes, however, these parameters may be difficult or impossible to measure at an

appropriate scale. In these cases, numerical modelling can still be used to help develop a conceptual understanding to some degree. Due to its simplicity and ease of implementation, continuum modelling is commonly used.

On the other hand, discrete network models assume that the hydraulic behaviour can be represented by the conductivity of individual discontinuities. Discrete fracture networks can be generated if the hydraulic properties of each fracture, such as fracture size, orientation, connectivity, transmissivity and storability, can be determined. Otherwise, simulated fracture networks may need to be generated with properties from the same statistical distributions as the real system. The outcome of such models can be evaluated in terms of the overall hydraulic behaviour at various length scales and the models tested by comparing with measured data.

In general, discrete network models can be used in three ways to study the deformation and fluid flow of a rock-block system (Long, 1996): (1) As a tool for conceptual evaluation or model-based process investigations (e.g. Smith and Schwartz, 1984; Long and Witherspoon, 1985; Zhang and Sanderson, 1995; Zhang and Sanderson, 1998). In this case, the requirements for characterization of a rock-block system as an equivalent continuum is examined. (2) As a practical tool for site-specific simulations (e.g. Zhang and Sanderson, 1996; Zhang and Sanderson, 2001; Zhang et al., 1999b). In these cases, an equivalent continuum may not be defined, and discrete network modelling is an alternative. (3) As a tool to build continuum approximations, as in the estimation of large-scale permeability by averaging local-scale measurements. Several equations have been developed to estimate the permeability tensor by combining hydraulic and geometric data of fractures (Oda, 1986; Oda et al., 1987; Lee et al., 1995). The idea of estimating continuum properties from discrete network models has been extended by others (Hudson and La Pointe, 1980; Long and Witherspoon, 1982; Hsieh et al., 1985; Cacas et al., 1990). The 2-D permeability tensor of a rock-block system has been evaluated by Zhang et al. (1996) based on the distinct element

method for discrete networks, and the effects of network geometry examined.

Recently, percolation models have been applied to examine geometric properties and transport phenomena observed in porous and fractured rocks (e.g. Englman et al., 1983; Charlaix et al., 1987; Gueguen and Dienes, 1989; Balberg et al., 1991; Berkowitz and Balberg, 1992; Zhang and Sanderson, 1994; Zhang and Sanderson, 1998). For fracture networks near the percolation threshold, a fractal structure develops. Attempts have been made to model and characterize such structures and to compare their hydraulic properties with the fractal properties of well tests predicted by Barker (1988) (e.g. Stauffer, 1985; Sahimi, 1987; Zhang and Sanderson, 1998; Sanderson and Zhang, 1999). There are also discrete fracture networks models for the transport of groundwater. However, unlike distinct element methods, such models have no coupling of deformation and fluid flow, and only allow examinations of the effects of the geometric attributes of fractures on flow.

8.3 Fluid flow in fractured systems

It is believed that in tight rocks fluid flow happens mainly through systems of fractures and such reservoirs are only accessible via fracture porosity. It is very important to know the concepts related with such a system and which affect the flow through such a system. We begin by introducing the meaning of a fractured system. In this context, we imply systems (such as in many carbonate reservoirs) where small scale conductive fractures occur but most of the oil is in the rock matrix. In certain non-porous fractured rock reservoirs (e.g. fractured volcanics), it is possible to have all the oil in the fractures but these are less common. Typically, in porous fractured systems fracture porosity is $\phi_f \approx 0.1 - 1\%$ (Sorbie and McDougall, 1998) of bulk volume. The main geometric features of fractures which are thought to affect fluid flow are the fracture orientation, width, aperture, conductivity, connectivity and spacing.

Special cases of fluid flow occur in stylolites and vugs. Stylolites are frequently found in limestones. They are laterally extensive features formed by grain-to-grain saturated contacts caused by the phenomenon of pressure solution. These features may significantly reduce vertical permeability thus causing systems containing them to have very low (k_v/k_h) ratios (at certain scales). Vugs are dissolution "holes" in a carbonate rock caused by diagenetic reactions.

The most widely used simulation models for modelling flow in fractured systems are the dual porosity models. They have separate conservation/flow equations for the matrix and the fractures and matrix-fracture flow is represented by transfer functions. They are most frequently used to model multiphase flow in fractured carbonates. Variants of this model allow for; (i) flow only in fractures and (ii) flow in both fractures and matrix. In the following sections we limit our examination to single phase fluid flow, and we present only the corresponding features and theoretical equations of multi phase fluid flow in Appendix C.

8.3.1   Single phase rock properties

The main properties of the rock that affect single phase flow are the permeability (k), porosity ϕ, k/ϕ correlations, and the permeability anisotropy. By permeability (k) we refer to the conducting capacity of a rock. The unit of permeability is Darcy (D) and milliDarcy (mD). Typical permeabilities for reservoir rocks are between $1 - 10D$ (very high), $0.1 - 1D$ (high), $30 - 100mD$ (medium low), $1 - 30mD$ (low), $< 1mD$ (very low). Permeability can be anisotropic and is a second-order tensor.

Porosity is the fraction of a rock that is pore space, and it varies from ϕ=0.25 for a fairly permeable rock down to ϕ=0.1 for a very low permeability rock. There may be an approximate correlation between k and ϕ. Fluid travels in a rock through pores and pore throats. Pores are the tiny connected passages that exist

in permeable rocks; typically of size 1 μm to 200 μm. The narrower constrictions between pore bodies are referred to as pore throats. It is the narrower throats that control the capillary entry pressure in a drainage process.

It has been found in many systems that there is a relationship between permeability, k, and porosity, ϕ. Broadly, higher permeability rocks have a higher porosity. Since permeability can be directional, it is possible to have $k_x \neq k_y \neq k_z$ in a given system. This is often seen in practice when comparing the horizontal permeability, (k_h), with the vertical permeability, (k_v). Often, it is found that $(k_v/k_h < 1)$, i.e. there is more resistance to vertical flow than horizontal flow.

8.3.2 Reservoir fluid properties

Fluid in a reservoir has some characteristic properties. We will briefly describe the phase, the viscosity and the compressibility, in order to have a general understanding. A basic property of the fluid is its phase, which is a chemically homogeneous region of fluid separated from another phase by an interface. We assume here that phases are immiscible.

The viscosity of a fluid is one of the main properties describing a fluid in Darcy's law. It is a measure of the (frictional) energy dissipated when it is in motion resisting an applied shearing force. Units are $Pa \cdot s$ (SI) or poise (metric). The most common unit in oilfield applications is centiPoise (cP). Typical examples are water viscosity at standard conditions, $\eta_w \sim 1$cP; typical light North Sea oils have $\eta_o \sim 0.3$-0.6cP at reservoir conditions (T 200°F; P 4000-6000psi); at reservoir conditions, medium viscosity oils have $\eta_o \sim 1$-6cP; moderate viscous oils have $\eta_o \sim 50$-1000cP and tars may have $\eta \sim$ up to 10000cP.

Finally, compressibility (c) of oil or gas can be defined in terms of the volume (V) change or density (ρ) change with pressure: $c = -(1/V)(\partial V/\partial P) =$

$(1/\rho)(\partial\rho/\partial P)$. This quantity is normally expressed in units of psi^{-1}. Typical ranges of compressibilities in units of $10^{-6}psi^{-1}$ are: (a) for formation rock 3-10, (b) for water 2-4, (c) for undersaturated oil 5-100, (d) for gas at 1000psi 900-1300, and (e) for gas at 5000psi 50-200.

8.4   Differential equations for fluid flow in reservoirs

The processes occurring in petroleum reservoirs are basically fluid flow and mass transfer. Up to three immiscible phases (water, oil, and gas) flow simultaneously, while mass transfer may take place between the phases (chiefly between the gas and oil phases). Gravity, capillary, and viscous forces all play a role in the fluid flow process.

The model equations must account for all these forces, and should also take into account an arbitrary reservoir description with respect to heterogeneity and geometry. The differential equations are obtained by combining Darcy's law for each phase with a simple differential material balance for each phase. In this section, we derive the simple differential equation that describes single-phase flow.

8.4.1   Darcy's law

It was established experimentally by Darcy (1956) that the fluid flow rate is linearly related to the pressure gradient in a fluid saturated porous medium. Darcy's law for single-phase flow states that in a horizontal system the volumetric flow rate, $\hat{Q}$, through a sample of porous material of length L and a cross-sectional

area A, is given by:

$$\hat{Q} = \frac{KA}{\eta}\frac{\Delta P}{L}, \tag{8.1}$$

where ΔP is the applied pressure drop across the sample, η is the viscosity of the fluid, and K is the absolute permeability of the medium. In the general form we can write Darcy's law in the following form:

$$V = \frac{\hat{Q}}{A} = -\frac{K}{\eta}\frac{\partial P}{\partial x}, \tag{8.2}$$

where $V = \hat{Q}/A$ is the vector fluid velocity field, $\partial P/\partial x$ is the fluid pressure gradient, and K is the permeability tensor. Note that the negative sign in Equation (8.2) indicates that the pressure declines in the direction of flow.

The differential form of Darcy's law may be generalized to three dimensions as follows:

$$V_x = -\frac{K_x}{\eta}\frac{\partial P}{\partial x}. \tag{8.3}$$

$$V_y = -\frac{K_y}{\eta}\frac{\partial P}{\partial y}. \tag{8.4}$$

$$V_z = -\frac{K_z}{\eta}\frac{\partial P}{\partial z}. \tag{8.5}$$

where V_x, V_y, and V_z are the x-, y-, and z-components of the fluid flow rate vector, $\vec{V}$, oriented in some arbitrary direction in three-dimensional space.

Equations (8.3), (8.4), and (8.5) do not take gravity into account, and must be modified to include gravity terms. The gravity term becomes larger with depth. The deeper the fluid is in earth the larger the gravity factor will be. In simple words that means that a fluid that is deep in the earth will need a higher pore pressure gradient in order to have the same velocity as another fluid situated in a shallower area. For generality, we shall take the depth, D, to be an arbitrary function of the coordinates, (x, y, z). Then the differential form of Darcy's law becomes:

$$V_x = -\frac{K_x}{\eta}\left(\frac{\partial P}{\partial x} - \rho g\frac{\partial D}{\partial x}\right). \tag{8.6}$$

$$V_y = -\frac{K_y}{\eta}\left(\frac{\partial P}{\partial y} - \rho g \frac{\partial D}{\partial y}\right). \qquad (8.7)$$

$$V_z = -\frac{K_z}{\eta}\left(\frac{\partial P}{\partial z} - \rho g \frac{\partial D}{\partial z}\right). \qquad (8.8)$$

where ρ is the density of the fluid and g is the acceleration due to gravity.

In order to apply Darcy's law we have the following limitations (Mavko et al., 1998): (a) Darcy's law applies to representative elementary volume much larger than the grain or pore scale; (b) Darcy's law is applicable when inertial forces are negligible in comparison to pressure gradient and viscous forces, and the Reynolds number is small ($Re \approx 1$ to 10). The Reynolds number for porous media is given by $Re = \frac{\rho v l}{\eta}$, where ρ is fluid density, η is the fluid viscosity, v is the fluid velocity, and l is a characteristic length of fluid flow determined by pore dimensions. At high Re, inertial forces can no longer be neglected in comparison with viscous forces, and Darcy's law breaks down; (c) some authors mention a minimum threshold pressure gradient below which there is very little flow (*Bear*, 1972), and (d) when the mean free path of gas molecules is comparable to or larger than the dimensions of the pore space, the continuum description of gas flow becomes invalid. In these cases, measured permeability to gas is larger than the permeability to liquid. This is sometimes thought of as the increase in apparent gas permeability caused by slip at the gas-mineral interface. This is known as the Klinkenberg effect (Bear, 1972).

8.4.2   General equation for single-phase flow

We examine the simplest case of one-dimensional, single-phase, compressible flow, in order to show the basic considerations in deriving a differential equation for fluid flow. We will make this equation more general to include the cases of two and three dimensions. In deriving the equation for one dimension, the possibilities that the cross-sectional area for flow A, as well as the depth D, are functions

of the single space variable x are included. Also a term for injection of fluid is added by using a variable, q, equal to the mass rate of injection per unit volume of reservoir (a negative q implies extraction). That term incorporates the case of fluid injection, which is a common method used during oil production, or fluid extraction. Finally, we take into account that the density of the fluid will be changing with time. (Frequently, the porosity of the medium, ϕ, can also change with time.)

Let us consider a mass balance about the box in Figure (8.1). The box has length Δx; the left face has area $A(x)$, the right face has area $A(x + \Delta x)$. The rate at which fluid mass enters the box at the left face is given by:

$$\rho(x) \cdot V_x(x) \cdot A(x) = (A\rho V_x)_x. \tag{8.9}$$

The rate at which fluid leaves at the right face is:

$$\rho(x + \Delta x) \cdot V_x(x + \Delta x) \cdot A(x + \Delta x) = (A\rho V_x)_{x+\Delta x}. \tag{8.10}$$

The volume of the box is $\bar{A}\Delta x$. Here $\bar{A}$ indicates the average value of A between x and $x + \Delta x$. Then the rate at which fluid mass is injected into the box is $\bar{q}\bar{A}\Delta x$.

The mass contained in the box is $\bar{\phi}\bar{\rho}\bar{A}\Delta x$. Then the rate of accumulation of mass in the box is $\frac{\partial(\bar{\phi}r\bar{h}o)}{\partial t}\bar{A}\Delta x$. Since mass must be conserved, we have:

$$[rate\ in] - [rate\ out] + [rate\ injected] = [rate\ of\ accumulation]. \tag{8.11}$$

Thus

$$(A\rho V_x)_x - (A\rho V_x)_{x+\Delta x} + \bar{q}\bar{A}\Delta x = \bar{A}\frac{\partial(\bar{\phi}\bar{\rho})}{\partial t}\Delta x. \tag{8.12}$$

Dividing by Δx gives:

$$-\frac{(A\rho V_x)_{x+\Delta x} - (A\rho V_x)_x}{\Delta x} + \bar{A}\bar{q} = \bar{A}\frac{\partial(\bar{\phi}\bar{\rho})}{\partial t}. \tag{8.13}$$

Taking the limit as $\Delta x \to 0$ and that $\bar{A} \to A(x)$, $\bar{\rho} \to \rho(x)$, etc., we obtain:

$$-\frac{\partial(A\rho V_x)}{\partial x} + Aq = A\frac{\partial(\phi\rho)}{\partial t}. \tag{8.14}$$
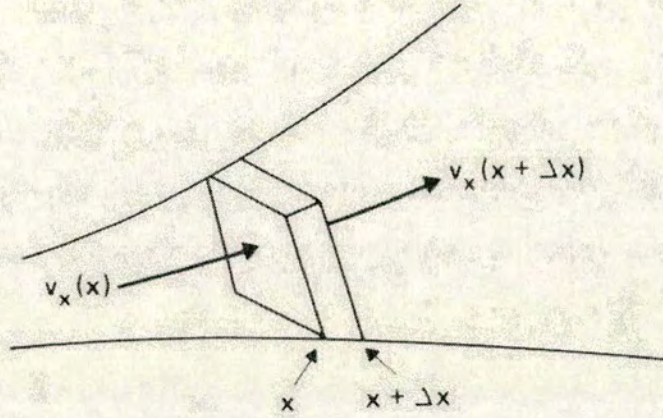
Figure 8.1: Differential elements of volume for one-dimensional flow

.

We can continue the above equation as follows:

$$-A\frac{\partial(\rho V_x)}{\partial x} + Aq = A\frac{\partial(\phi\rho)}{\partial t} = -\frac{\partial(\rho V_x)}{\partial x} + q = \frac{\partial(\phi\rho)}{\partial t}. \qquad (8.15)$$

The x-component of the velocity vector V_x is given by equation (8.6):

$$V_x = -\frac{K_x}{\eta}\frac{\partial P}{\partial x}. \qquad (8.16)$$

By Equations (8.15) and (8.16) we take:

$$-\frac{\partial}{\partial x}(-\rho\frac{K_x}{\eta}\frac{\partial P}{\partial x}) + q = \frac{\partial(\phi\rho)}{\partial t} \Rightarrow \frac{\partial}{\partial x}[(\frac{\rho K_x}{\eta})(\frac{\partial P}{\partial x})] + q = (\frac{\partial(\phi\rho)}{\partial P})(\frac{\partial P}{\partial t}). \quad (8.17)$$

8.5   The theoretical model for fluid flow modelling

When we examine fluid flow in a fractured network, two phases take part in the process, the solid phase - that is the rock - and the fluid phase. In this section, we

present the theoretical models that we use describe the two phases. During the process of fluid flow, the two phases interact. We also present the algorithm that describes the coupling between the two phases (Maillot et al., 1999). We start by the solid phase and describe the equation of motion, the constitutive relations describing the mechanical response of the medium to stresses, and Hooke's law. For the fluid phase we describe the diffusion equation with a source term proportional to volume variations of the medium. Finally, we describe the coupling between the two phases, the slip condition and the friction law for the brittle behaviour.

8.5.1   The solid phase

In the framework of the infinitesimal deformation theory, the displacement accelerations are related to the stress tensor by Cauchy's equation of motion:

$$\rho\frac{\partial^2 u_i}{\partial t^2} = \nabla_j \sigma_{ij}, \tag{8.18}$$

which relates the stresses σ_{ij} in the medium to the displacement field u and the rock density ρ, in the absence of external forces. This is the equation we intend to solve by a finite difference approximation. In order to solve this equation, we need a constitutive relationship between the stress and the strain $\epsilon_{ij}(x,t)$ and hence the displacements.

8.5.2   The constitutive relations

Before presenting the constitutive relations, we separate the total stress in the medium $\sigma_{ij}(x,t)$ into: (i) a pre-stress component $\sigma_{ij}^P(t)$, due to, for example, the lithostatic pressure, and to tectonic loading stresses; and (ii) a component $\sigma_{ij}^B(x,t)$ due to the fractures in the medium:

$$\sigma_{ij}(x,t) = \sigma_{ij}^P(t) + \sigma_{ij}^B(x,t), \tag{8.19}$$

where the pre-stress

$$\sigma_{ij}^{P}(t) = \sigma_{ij}^{P}(0) + tf(i,j)c_{ijkl}\dot{\epsilon}_{kl}, \tag{8.20}$$

is a sum of the initial pre-stress $\sigma_{ij}^{P}(0)$ and of stresses due to the strain rates $\dot{\epsilon}_{ij}$ applied during t. The strain rates $\dot{\epsilon}_{ij}$ are constant in space and time. They represent strains due to a uniform tectonic loading of the medium. c_{ijkl} are the elastic stiffnesses, and $f(i,j)$ is a Boolean function with values 1 or 0 specifying whether the component $\dot{\epsilon}_{ij}$ of the loading strain rates is applied or not.

During tectonic straining and at any point in the medium not undergoing failure, stresses and strains are linearly related through Hooke's law

$$\sigma_{ij}(x,t) = c_{ijkl}(x)\epsilon_{kl}(x,t). \tag{8.21}$$

8.5.3   The fluid phase

Macroscopically, we may consider fluid flow in porous rocks as well as in fracture zones as a process of fluid pressure diffusion, with anisotropic diffusivities varying spatially and temporally by several orders of magnitude, and pore pressures also presenting high local variations. When fluids are injected into a porous rock mass at a sufficiently high pressure we can have two possible types of fracture processes. Depending on the fluid and rock properties and on the local stress field, hydraulic fracturing or induced seismicity may occur. However, any changes in the fracture network will almost certainly complicate the identification of pore pressure changes in seismic signatures, so we keep the fracture network unchanged. Such models are called 'static' in terms of the stress field, and the fracture network is used only to account for the porosity and permeability. A major simplification of the model is that the fluid is assumed to have the same bulk modulus K_f as the solid K_s (Maillot and Main, 1996). We also assume that both fluid and solid phases are chemically inert and at constant temperatures, that the implicit void spaces are fully connected, and the porosity ϕ is uniform and constant. Only a

single phase of fluid is considered. We combine mass conservation, Darcy's law and a linear equation of state $[\rho_f = \rho_{f_0}(1 + p/K_S)]$, to obtain the time evolution of the fluid pressure p:

$$\frac{\partial P}{\partial t} = \frac{\partial}{\partial x_i}(D_{ij}\frac{\partial P}{\partial x_j}) - \frac{1}{3}\frac{\partial \sigma_{ii}}{\partial t}, \qquad (8.22)$$

where

$$D_{ij}(x,t) = \frac{K_S}{\phi\eta}\kappa_{ij}(x,t) \qquad (8.23)$$

is the diffusion tensor, with η and $\kappa_{ij}(x,t)$ respectively the viscosity of the fluid and the permeability of the matrix. We add the last term of Equation (8.22), which acts as a pore pressure source or sink, to include the effect of solid matrix isotropic stress variations (the stress is taken as positive in tension). This term encompasses the transient stresses of the seismic radiations (in fact only of the P-waves, since the S-waves do not make volume changes) as well as those of the static stress, as Equation (8.22) is integrated over time. That is the first coupling between the solid and the fluid phases in this model.

We use a lattice Boltzmann method to solve Equation (8.22), which is valid in the most general media with anisotropic, heterogeneous and time-dependent diffusivity [Equation (8.23)] (see Maillot and Main, 1996). The lattice Boltzmann model is an approach for the solution of the pore pressure diffusion equation. It is based on the construction of a simplified microscopic discrete model which macroscopically obeys the partial differential equation to be modelled. It provides unconditionally stable, easily implemented, and efficient numerical algorithms. It consists of the streaming and relaxation of particle densities along the axes and at the nodes of a regular lattice.

Bhatnagar-Gross-Krook (BGK) models, that are described in the next section, were introduced by Quian et al. (1992) who gave a simple and clear description of this relaxation method "if $N(t)$ is a quantity at time t and N_p is its predicted

value, then $N(t+1)$ is given by

$$N(t+1) = (1 - \lambda)N(t) + \lambda N_p, \tag{8.24}$$

where λ is the relaxation parameter, which must be between 0 and 2 to ensure numerical stability. In our model, we let the relaxation parameters be space, time, and direction dependent, and add a static term, to obtain a diffusion BGK model which supports anisotropy, spatial and temporal gradients of the diffusivity, and gravity effects, which are all necessary features of a realistic model of pore fluid diffusion in the earth.

8.5.4   The lattice BGK model

The physical space is discretised by a regular lattice with nodes denoted x, while the discrete times are denoted t, with a space step γ and a time step τ. Each node x has b nearest neighbours $x + \gamma e_\alpha$, (α=1,...b), where e_α are the lattice vectors. The basic variable of the model is the pore fluid pressure $P_\alpha(x, t)$ going in the direction of e_α. It relates to the total pore fluid pressure $P(x, t)$ through

$$P(x, t) = \sum_{\alpha=1}^{b} P_\alpha(x, t), \tag{8.25}$$

and its evolution is described by the following lattice Boltzmann equation

$$P_\alpha(x + \gamma e_\alpha, t + \tau) = (1 - \lambda_\alpha)P_\alpha + \lambda_\alpha P_\alpha^{eq} + \Omega_\alpha, \tag{8.26}$$

$$\Omega_\alpha = t_\alpha \sum_{\beta=1}^{b} \lambda_\beta (P_\beta - P_\beta^{eq}) + t_\alpha h_i e_{\alpha i}, \tag{8.27}$$

and all terms on the right hand side of Equation (8.26) are evaluated at (x, t). Since the relaxation parameters $\lambda_\alpha(x, t)$ in Equation (8.26) have been made space, time, and direction dependent, they will lead to a diffusion tensor $D_{i,j}$ (Equation 8.23) in the macroscopic diffusion equation. The local equilibrium pressure

$P_\alpha^{eq}(x,t)$ plays the role of the predicted value in Equation (8.26) and is defined as

$$P_\alpha^{eq}(x,t) = t_\alpha P(x,t). \qquad (8.28)$$

The velocity of the fluid does not appear explicitly here because we aim at modelling the diffusion equation. By adding a velocity term to the equilibrium distribution of Equation (8.28), the convection-diffusion equation can in principle be easily obtained by the same method, but this is beyond the scope of this thesis. In this case the velocities can be calculated once the local pressure gradients are known. Various partial differential equations can be obtained depending on the choice of the equilibrium distribution. The first term in Equation (8.27) only ensures that the total pressure $P(x,t)$ is conserved by the relaxation step, and the second term in Equation (8.27) accounts for gravity effects. $h_i(x,t)$ is a function of the body force due to gravity and of the relaxation parameters $\lambda_\alpha(x,t)$.

In the above equation we adopt the summation convention of repeated indices only on Latin indices. We will also make use of the parity symmetry of the lattice which implies $e_\alpha = -e_{\alpha+b/2}$ and $t_\alpha = t_{\alpha+b/2}$. To keep this symmetry, we further assume that $\lambda_\alpha = \lambda_{\alpha+b/2}$. The lattice Boltzmann in Equation (8.26) can be understood to be a two step process: (i) a streaming step which moves the P_α to neighbouring nodes, and (ii) a relaxation step which decreases the difference $P_\alpha - P_\alpha^{eq}$ in each direction.

8.5.5 Brittle behaviour

We assume that cohesion C and an internal friction coefficient n fully specify conditions for failure for the rock mass. We apply the standard Mohr-Coulomb criterion to the effective stress σ_{ij}^{eff} to determine where and when failure occurs [Figure (8.2)]. Although the criterion determines in which mode and in which direction a fracture occurs and grows, we will, however, not make use of the infor-

mation about the orientation of the fracture because it is implicitly determined by the stress distribution computed from the equation of motion. In other words, the criterion is used simply to determine whether or not a node reaches failure. This is applied to a given point in space, not to a given plane. We therefore look for any plane at that point such that

$$|\tau| - n\sigma^{eff} \geq C, \tag{8.29}$$

where τ is the friction of the plane, and σ^{eff} is the effective mean normal stress calculated from the effective stress

$$\sigma_{ij}^{eff} = \sigma_{ij} - \alpha\delta_{ij}P. \tag{8.30}$$

This equation is the second (and last) coupling between the solid and the fluid phases in our model. The Terzaghi coefficient α ($0 \leq \alpha \leq 1$) may be defined through macroscopic or microscopic considerations (e.g. Nur and Byerlee, 1971), but is usually close to 1 when dealing with fracture processes (Scholz, 1990, p.30). We assume $\alpha = 1$ in this study. When and where rupture occurs, the stress is divided into the deviatoric and isotropic components. Failure does not change the isotropic part, σ_{kk}, which still follows Hookes law (Equation (8.21)). The deviatoric part follows the simple friction law

$$\tilde{\sigma}_{ij}(x,t) = \tilde{\sigma}_{ij}(x,t_0)(\zeta + (1-\zeta)f(t-t_0)) \qquad (for \quad t \geq t_0), \tag{8.31}$$

where ζ ($0 \leq \zeta \leq 1$) is the proportion of deviatoric stress still present after rupture, which is a measure of the seismic efficiency ($\zeta = \tau_d/\tau_s$ in Figure (8.2)). Seismic efficiency is the proportion of potential energy available for radiation during dynamic failure. For an elastic medium with constant stiffness it is the ratio of the radiated energy to the total energy. t_0 is the time of onset of rupture, and f a sine shape function which goes from 1 to 0 during relaxation time, t_r, defined through the timescale

$$t_r^* = \frac{t_r}{(\Delta x/C_s)}. \tag{8.32}$$

t_r^* is the ratio between the time, t_r, taken by the rupture and the time taken by a shear wave (of velocity C_s) to travel by one lattice step Δx. The length Δx may be interpreted as the thickness of the fracture gouge (Nielsen and Tarantola, 1992). The dimensionless timescale t_r^* controls the duration of rupture, and hence the spectrum of the seismic radiation. If it is very large (in the order of a few hundred), there is essentially no seismic radiation and failure occurs quasi-statically. In this case the seismic efficiency is low. If it is very small, high frequencies are emitted, and the seismic efficiency is high. Numerically, however, if $t_r^* < 1$, strong numerical dispersion occurs and the calculated seismic radiation is not accurate. However, as seismic radiations are not allowed to trigger ruptures, the actual choice of t_r^* should have no bearing on the birth and growth of fractures. Also in the implementation of the theoretical model in this thesis, the choice of t_r does not influence the behaviour of the medium. However, the dynamic value τ_d, combined with the distribution of cohesions C, has a drastic influence on the medium. The dynamic value τ_d is a proportion of the static value τ_s.
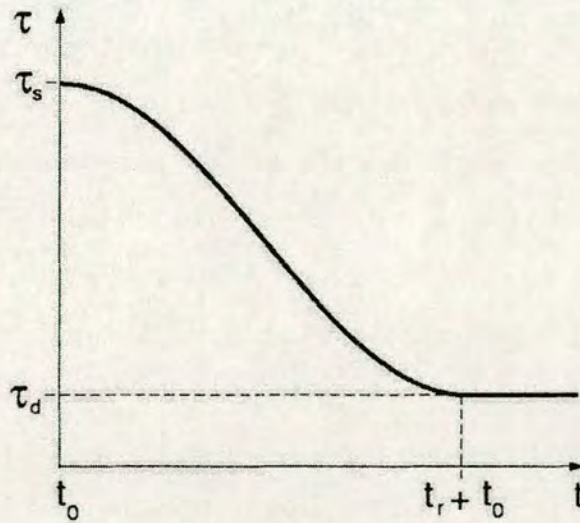
Figure 8.2: Friction as a function of time during dynamic failure used in our model (Equation (8.31). τ represents any component of the deviatoric stress tensor. τ_s: static friction (before failure); τ_d: dynamic friction (after failure); t_0: time of onset of rupture; t_r: relaxation time (Maillot et al., 1999).

With the friction law [Equation (8.31)], the characteristic length of slip as defined by Boore (1981) is replaced by a characteristic time of decay of the friction from its static to its dynamic value, regardless of the slip velocity. A phenomenon of spreading of the rupture front follows, over a distance $V_r t_r$ (V_r is the velocity of propagation of the rupture, close to C_s), that is similar to that induced by a characteristic length of slip. This friction law [Equation (8.31)], although rather simple, thus retains an important feature of dynamic rupture (Nielsen et al., 1995).

8.6   Numerical implementation

The numerical model for fluid flow was inherited from Dr. Maillot, who originally created the algorithm. The algorithm is written in High Performance Fortran and runs in a parallel machine. Some changes were made to the algorithm on the visualisation of the resulting pore fluid pressure maps, as well as on the implementation of the pre-existing fracture network. The overall algorithm for the simulation of fluid flow and the evolution of the fracture network due to changes in pore pressure, may be described as follows. The pore pressure diffuses according to Equation (8.22) and to specified values at injection points. During the diffusion regime, the occurrence of failures is constantly checked with Equation (8.29) and Equation (8.30). The last term of Equation (8.22) is null because, in the first-order model, pore pressures do not perturb the stress field. When failure occurs, the pressure diffusion is stopped and we enter the elastic regime: stresses are updated according to the equation of motion (Equation 8.18), Hooke's law (in the forms of Equations (8.19), (8.20), and (8.21), and the friction law at broken points (Equation 8.31). Seismic radiation is generated at the broken points, pore pressures are updated according to the last term of Equation (8.22) only, and again, new failures are checked with Equation (8.29) and Equation (8.30). When

no further failures are triggered, the kinematic energy in the medium is absorbed by adding a small force proportional and opposite to the gradient of the stress in order to converge to the static state (this simulates the natural process of seismic attenuation). A static state is reached when the maximum displacement velocity has been reduced by a factor of 10^4. The elastic regime is then finished. The prescribed dynamic values of friction at broken points are relaxed (that is, when the elastic regime is entered again, stresses at previously broken points will be updated according to Equation (8.18) rather than Equation (8.31). Diffusivities may be updated at broken points according to desired values in fractures. The new static state of stress serves as a starting point to resume the pore pressure diffusion regime.

In order to define the initial state of the medium in a way that when and how fractures will start can be controlled, there are three dimensionless numbers that are defined:

$$\gamma = \frac{\sigma_1 - \sigma_2}{C}, \tag{8.33}$$

$$\chi = \frac{\sigma_1 + \sigma_2}{2p}, \tag{8.34}$$

$$\psi = \frac{\sigma_1^e - \sigma_{1r}^e}{\sigma_{1r}^e - \sigma_{2r}^e}, \tag{8.35}$$

where σ_1 and σ_2 are the principal components of the stress σ_{ij}, σ_1^e and σ_2^e, those of the effective stress, and σ_{1r}^e and σ_{2r}^e, those required to trigger rupture (Figure (8.3)). All stresses and the pore pressure are uniform at the beginning of a simulation.

γ is the ratio between the differential stress and the cohesion, which controls the opening mode of the fractures. In the case of a heterogeneous cohesion C, its minimum value within the medium is taken in Equation (8.33). If $\gamma < 1$, fractures would occur mainly in mode I (that is when displacements are perpendicular to the fracture surface). In the model used in the thesis we examine only induced fracturing, rather than hydrofracturing, so we always specify $\gamma > 1$ (i.e we only
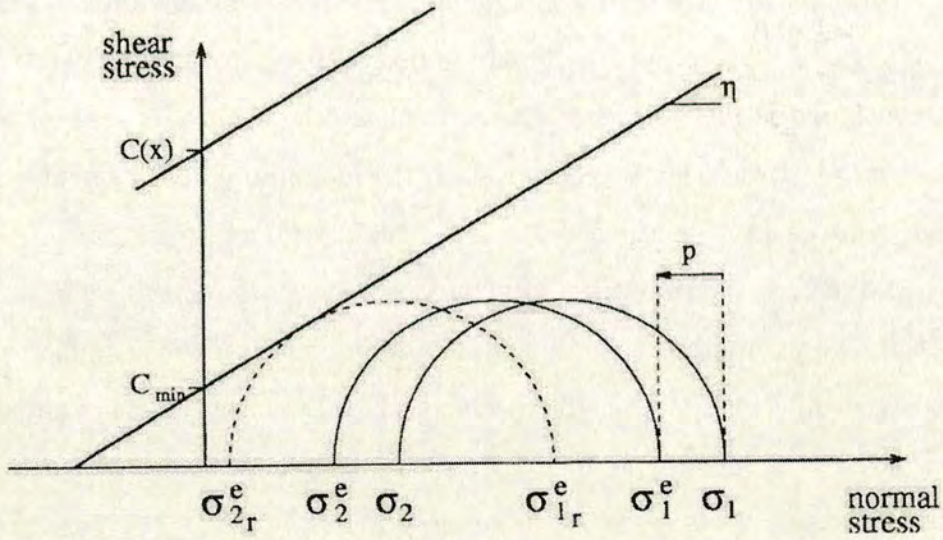
Figure 8.3: Diagram of the Mohr-Coulomb failure criterion at the initial state of the simulation. The internal friction n and the cohesion $C(x)$ are medium properties that define the failure envelopes (diagonal lines). (σ_1, σ_2) are the principal components of the stress tensor; (σ_1^e, σ_2^e), of the effective stress; and $(\sigma_{1r}^e, \sigma_{2r}^e)$ represent the effective stress required for rupture. P is the pore pressure, which triggers the first failure. Further failures may be triggered either by the same mechanism or by a local increase of $\sigma_1 - \sigma_2$ due to elastic redistributions of stresses around a failed element (Maillot et al., 1999).

consider mode II fractures). χ is the ratio between the isotropic stress and the pore fluid pressure. ψ determines how far the medium is from rupture at the beginning of the simulation. The lower ψ, the closer the medium is to rupture. The choice of these three parameters determines completely the initial stress state of the medium. The model can be applied in both the cases of injection or extraction, providing we make the corresponding choice of parameters.

8.6.1   Assumptions

In this section we will make some remarks regarding both the theoretical and numerical parts of the model. We compare our implementation with the general case of arbitrary bulk moduli of the solid and the fluid phases. We compare Equa-

tions (8.18)-(8.23) with the ones developed by Rice and Cleary (1976). The pore pressure diffusion equation (Equation 8.22) is equivalent to the relevant equation of Rice and Cleary (1976) in the framework of our assumptions (equal bulk moduli of fluids and solids, full connection of pores, etc.), with the differences that we replaced the permeability κ by a tensor in order to account for the anisotropic fracture permeabilities, and that the porosity ϕ appears explicitly in our equation. However, Rice and Cleary (1976) considered one of the governing equations of a porous medium strain by adding strain compatibility conditions. We have not included these conditions here, thus strain compatibility is not guaranteed in our model. This can be interpreted as a "one-way" coupling by comparing our pore pressure evolution [Equation (8.22)] and Hooke's law [Equations (8.19), (8.20), and (8.21)]. As a result, in our model only stresses influence the pore pressure, and not vice versa. The simplification was first suggested by Bell and Nur (1978). A simple solution to this problem (Rice and Cleary, 1976), at least in the static state, is to replace the stress by the effective stress [Equation (8.30)] in Hooke's law [Equations (8.19), (8.20), and (8.21)] and in the equilibrium equation [Equation (8.18)], which then becomes $\nabla_j \sigma_{ij}^{eff} = \alpha \nabla_i P$. That means that "reverse" coupling is a result of the local pore pressure gradients that act formally as body forces in the equilibrium of effective stresses. However, the "reverse" coupling is not applied in this study because it is computationally too intense. Stress equilibrium would have to be calculated at each diffusion time step. Such calculations involve either a full time integration of elastic stresses across the computation grids, or an inversion procedure. The possibility of applying another approach has been examined, but is not in the scope of this thesis. Therefore, we have finally retained only two fluid-rock couplings, the "one-way" coupling presented above, and the use of the effective stress in the failure criterion.

Thus, coupling between solid and fluid phases essentially occurs around new or growing fractures. There are, however, more coupling processes. Those are

the influence of the stress perturbations away from faults on the permeability and the porosity, which are not taken into account. The resulting variations of permeability could in principle be included in the model if a particular rock is to be modelled for which an experimental relationship between applied stress and permeability variations is available.

Concerning timescales, that of the fluid diffusion is much greater than those of the sliding on a fault and of the seismic radiations. It is therefore reasonable to stop the fluid diffusion each time a failure starts, and to restart it when the stress has again reached a static state. The pore pressure, however, does play a role in the first timescale because it is instantaneously perturbed by compressions/dilatations of the rock matrix due to the passage of seismic P-waves, and this in turn perturbs the effective stress.

Mode I (tension) fractures are at this implementation not allowed in the model. Only mode II (shear) fractures can occur. There is therefore no fracture-induced dilatancy, and the pore pressure on the fault is not modified by the rupture process. It may only be modified by the injection of fluid, or by stress changes in the volume around the fracture rather than along it.

8.7   Summary

In this chapter we presented a mathematical model that simulates single phase fluid flow. We introduced the two basic mathematical models, the equivalent continuum and the discrete network model. We also discussed the basic properties of the rock and the reservoir fluid, that affect single phase flow. For the mathematical model of fluid flow we used continuous mechanics. We described the pore fluid pressure variations by a diffusion equation and the solid matrix is described by the dynamic equation of motion. The model includes the generation

of new fractures due to changes in pore pressure, but this is not examined here because it is not in the scope of the thesis.

In the model we included two major simplifications. The first one is that the fluid and solid phase bulk moduli are equal, which limits the model to constant compressibilities. The second simplification is that the model does not include strain compatibility conditions, which amounts to neglecting elastic stress variations due to local pore pressure gradients. The model includes the interaction between the solid and the fluid phase by two features. Firstly, the influence of the pore fluid pressure on rupture via effective stress, and secondly, the influence of the volumetric deformation on the pore fluid pressure. For the solution of the diffusion equation we use a lattice BGK model based on a macroscopic approach of lattice gases. The model can handle anisotropy, heterogeneity and time dependence of the diffusivity.

In general, this chapter presents the theoretical background of the mathematical model that we use to model single phase fluid flow. The implementation of the model and the numerical modelling results are discussed in the following chapter.

Dual simulation of fluid flow and seismic wave propagation in a fractured network: Effects of pore pressure

9.1   Introduction

In the previous chapter, we have presented the basic concepts of single phase fluid flow simulation. We introduced a numerical simulation technique to describe fluid flow in a fractured network. Using such a simulation, we will be able to examine the direct effects of fluid flow in seismograms. That will initially give us an indication of which properties are mostly affected, and provides the possibilities of inferring the variations of fluid properties directly from seismic data.

The idea that seismic waves can be used to identify the presence of fluids and the transport properties of rocks takes its root from theoretical studies that go back at

The content of this chapter has been submitted in GJI (Vlastos S., Schoenberg M., Maillot B., Liu E., Main I.G, and Li X.-Y., 2004, Dual simulation of fluid flow and seismic wave propagation in a fractured network: Effects of changes in pore pressure on seismic signature, submitted in May 2004 in GJI)

least 50 years. More recently, many examples in time-lapse or 4D seismic surveys have demonstrated that seismic waves can be used to monitor changes in oil or gas reservoirs as a function of time. Probably the earliest 4D project was that conducted by Arco in 1982/83 on the Holt reservoir in north Texas, documented by Greaves and Fulp (1987). This was a fireflood, in which air was pumped down into the reservoir sand and ignited as an enhanced oil recovery mechanism. A small 3D survey was recorded prior to the fireflood. It was repeated during the flood, and again at the end. The seismic pictures were quite dramatic and demonstrated the effects of the flood very well. This work was ahead of its time. Gradually, a number of repeat surveys was acquired. This allowed time-lapse analyses to be conducted, and some of these early studies have been published, for example Gawith and Gutteridge (1996), and Johnson et al. (1998). An early application of the 4D method was to track steam injection for heavy oil extraction projects, and this has seen commercial use in places as far apart as Canada and Indonesia. Good example are published by Jenkins et al. (1997) and Waite and Sigit (1997), especially since this case history involves visible pressure effects as well as those due to temperature. In 4D seismic commonly, several 3D seismic surveys of the same reservoir made at different times are compared (e.g. Hirsche et al., 1990; Johnston, 1997). A common practice in such cases is that differences in reflection amplitude or impedance are interpreted in terms of reservoir changes (e.g. Johnston, 1997; Sonneland et al., 1997).

In this chapter we explain how pore pressure changes affect fracture compliance, thus leading to variations in seismic signatures. During production from a reservoir, the movement of fluids is accompanied by substantial change in the pore pressure field. As fluid drains, pore pressure in general decreases, increasing the effective pressure on fractures, grain boundaries and microcracks. Higher static load on such surfaces decreases their compliance non-linearly and decreases fracture opening and/or pore throat size, thus increasing the stiffness of the

rock (increasing compressional and shear velocities) and decreasing permeability (Schoenberg, 2002). Conversely, pore pressure buildup leads to a decrease in effective pressure and an increase in rock compliance. If we can establish a relation, that links pore pressure changes with rock compliance variations, we may be able to predict static effective stress from the knowledge of the dynamic properties (wavespeed and their associated polarisations), and in particular, to probe the pore pressure field changes induced by fluid movements.

We present a theoretical formula that directly links pore pressure changes with fracture compliance variations. We implement the formula on the numerical simulation and apply the technique in an initial model. In this thesis we concentrate on seismic attributes that respond directly to the presence of fluids, and in particular on static fluid effects on the compliances of porous and fractured rocks.

9.2   Effects of pore pressure

Fracture surfaces, grain boundaries, microcracks and joint faces are much more compliant and therefore more sensitive to stress than the intact rock. Following this assertion the properties of the fractured rock are analysed based on changes in fracture compliance and fracture anisotropy as the traction on the fractures varies due to pore pressure changes, while properties of the intact background rock are assumed to be constant. During fluid injection pore pressure generally increases, resulting in a decrease in the effective pressure on fractures, grain boundaries and microcracks. Lower static load on such surfaces increases the compliance in a non-linear way and increases fracture opening and/or pore throat size, thus decreasing the stiffness of the rock (decreasing compressional and shear velocities) and increasing permeability (Schoenberg, 2002). In this section we will explain the implementation of the effects of pore pressure changes in the elastic properties of the rock. As we mentioned in Section 8.6, coupling between the two

phases happens around the fractures. Therefore, we are interested in the effect of pore pressure changes in the area of the fractures, not in the intact rock. That is based on the assumption that fluid flows mainly through the fractures. We concentrate mainly in the fracture compliance, and present a theoretical formula that directly links pore pressure changes with fracture compliance variations. We also examine the local variation of effective stress and present the case of fractures under anisotropic stress.

9.2.1 Estimation of fracture compliance

The corresponding theory that describes the estimation of effective compliance for a fractured medium is presented in details in Chapter 2, in the fracture implementation section. For a volume V assumed to be homogeneous except for the presence of compliant surfaces across which displacement discontinuity can occur (Schoenberg and Sayers, 1995),

$$\epsilon_{ij} = [s_{ijkl_b} + s_{ijkl_f}]\sigma_{kl} = s_{ijkl_b}\sigma_{kl} + \frac{1}{2V}\sum_q \int_{S_q} ([u_i]n_j + [u_j]n_i)dS. \qquad (9.1)$$

Strain tensor ϵ_{ij} and stress tensor σ_{kl} are the dynamic strain and stress due to the passing of a seismic wave whose wavelength is taken to be much larger than the linear extent of the volume V; s_{ijkl_b} is the elastic compliance tensor of the background medium, s_{ijkl_f} is the excess compliance tensor due to the presence of fractures or other surfaces across which displacement discontinuity occurs; S_q is the surface area of the qth displacement discontinuity; $[u_i]$ is the local displacement discontinuity across the surface; and n_i is the local normal to the fracture surface.

For a set of aligned compliant surfaces, or fractures, with orientation defined by unit normal n_i, it is assumed in 'linear slip deformation' theory that there exists a linear relation between the integral of the displacement discontinuity $[u_i]$ due

to the passage of a wave across all the fractures and the dynamic traction $\sigma_{jk}n_k$ on a plane parallel to the fractures; i.e.

$$\frac{1}{V}\sum_q \int_{S_q} [u_i]dS = Z_{ij}\sigma_{jk}n_k, \tag{9.2}$$

where Z_{ij} is the symmetric non-negative definite "fracture compliance tensor" (of dimension stress^{-1}) of this set of aligned fractures in the 1,2,3 coordinate system. Substituting Equation (9.2) into Equation (9.1), we have,

$$s_{ijkl} = s_{ijkl_b} + s_{ijkl_f} = s_{ijkl_b} + \frac{1}{4}(Z_{ik}n_ln_j + Z_{jk}n_ln_i + Z_{il}n_kn_j + Z_{jl}n_kn_i). \tag{9.3}$$

Those expressions for s_{ijkl_f} satisfy the symmetry conditions of the 4th rank compliance tensor, $s_{ijkl} = s_{ijlk}$, $s_{ijkl} = s_{jikl}$, $s_{ijkl} = s_{klij}$. For a vertical fracture set with a horizontal unit normal given by

$$n_i = \delta_{i1}cos\theta + \delta_{i2}sin\theta, \tag{9.4}$$

the excess fracture compliances are found by substituting Equation (9.4) into Equation (9.3), where θ is measured from fracture normal.

9.2.2 Estimation of effective static stress traction on aligned fractures

In the subsurface, first let static stress be of opposite sign than the usual convention so that compression is positive. Then, in a porous medium, the relationship between effective static stress σ_{eff} and the applied external static stress σ_{ext} is given by

$$\sigma_{eff} = \sigma_{ext} - P\alpha I, \tag{9.5}$$

where $P > 0$ is pore pressure and α is a scalar empirical factor (usually $\alpha \leq 1$). In some cases of anisotropy, αI should be most likely replaced by an anisotropic tensor. For isotropy, though, the usual practice is to assume $\alpha = 1$. As pore pressure is isotropic, symmetry considerations dictate that on any surface, changes

in pore pressure can only change the normal component of traction; tangential components of traction are invariant to pore pressure changes. One may think of a pore pressure drop as allowing the grains and other parts of the rock mass to "settle" into one another. Such compaction generally decreases the acoustic compliance of the compliant surfaces and the permeability of the fracture network. A pore pressure rise generally does the opposite. The assumption that Z depends on the static effective stress traction on the fracture faces contains a far reaching implication - that effective stress changes influence the fracture parameters but does not cause a great number of new fractures to open suddenly, which would undermine the assumption of a more or less deterministic functional relationship between static stress and fracture parameters.

We assume an anisotropic state of external static stress with one of the principal directions of the stress tensor being the vertical with principle stress σ_3, and let the horizontal 1- and 2-directions be the other principle directions with principle stresses σ_1 and σ_2, respectively. Consider the set of compliant surfaces at a particular orientation with a normal unit vector specified in polar coordinates by

$$
\begin{bmatrix}
sin\phi cos\theta \\
sin\phi sin\theta \\
cos\phi
\end{bmatrix} , \tag{9.6}
$$

where ϕ is the polar angle and θ is the azimuthal angle. The effective stress traction, a vector acting on that fracture plane, is,

$$
\begin{bmatrix}
\sigma_1 - P & 0 & 0 \\
0 & \sigma_2 - P & 0 \\
0 & 0 & \sigma_3 - P
\end{bmatrix}
\begin{bmatrix}
sin\phi cos\theta \\
sin\phi sin\theta \\
cos\phi
\end{bmatrix}
=
\begin{bmatrix}
(\sigma_1 - P)sin\phi cos\theta \\
(\sigma_2 - P)sin\phi sin\theta \\
(\sigma_3 - P)cos\phi
\end{bmatrix} , \tag{9.7}
$$

The normal component of this traction, denoted by $\tau_\perp$, is

$$\tau_\perp = \begin{bmatrix} sin\phi cos\theta, & sin\phi sin\theta, & cos\phi \end{bmatrix} \begin{bmatrix} (\sigma_1 - P)sin\phi cos\theta \\ (\sigma_2 - P)sin\phi sin\theta \\ (\sigma_3 - P)cos\phi \end{bmatrix}$$

$$= -P + \frac{\sigma_1 + \sigma_2}{4} + \frac{\sigma_3}{2} + \frac{\sigma_1 - \sigma_2}{4}cos2\theta - \left[\frac{\sigma_1 + \sigma_2}{4} - \frac{\sigma_3}{2} + \frac{\sigma1 - \sigma2}{4} \right] cos2\phi.$$

$$(9.8)$$

For vertical fractures, the normal is horizontal, $\phi = \pi/2$ and $cos2\phi = -1$. Then , from Equation (9.8), the normal component of traction becomes

$$\tau_\perp = -P + \frac{\sigma_1 + \sigma_2}{2} + \frac{\sigma_1 - \sigma2}{2}cos2\theta.$$

$$(9.9)$$

At any orientation, the tangential components of traction are independent of P.

9.2.3 The case of vertical fractures under anisotropic stress

For a medium with a continuous distribution (over orientation) of fracture sets, a fracture compliance density tensor $Z_{ij}(n_k)$ can be defined over a unit hemisphere (u.h.s.). From Equation (9.3), the excess compliance due to the fracturing may be written as an integral over the solid angle Ω,

$$s_{ijkl_f} = \frac{1}{4} \int_{u.h.s.} [Z_{ik}(n_q)n_l n_j + Z_{jk}(n_q)n_l n_i + Z_{il}(n_q)n_k n_j + Z_{jl}(n_q)n_k n_i] \, d\Omega.$$

$$(9.10)$$

Under anisotropic static stress, slip interfaces will be subjected to different traction as a function of orientation, and the traction will have a tangential component except on fractures normal to a principal stress direction. For simplicity, we assume that the fracture sets, or sets of compliant surfaces, at all orientations are rotationally symmetric, i.e. they remain rotationally symmetric. Rotational symmetry of the fracture set implies that the fracture compliance matrix in the

coordinate system convenient to the fractures depends on two compliances: a normal compliance Z_N and a tangential compliance Z_T. Following that the fracture compliance tensor Z_{ij} becomes

$$Z_{ij} = (\delta_{ij} - n_i n_j) Z_T + n_i n_j Z_N = Z_T \delta_{ij} + (Z_N - Z_T) n_i n_j. \qquad (9.11)$$

In the model that we present here we only consider vertical fractures. In this medium, the fracture normals lie in the (1,2)-plane and an arbitrary fracture normal is given in initial notation by Equation (9.4). The integral over the unit hemisphere reduces to an integral over the unit semi-circle, in particular, let $-\pi/2 < \theta < \pi/2$. For rotationally symmetric fractures, Z_{ij} is given by Equation (9.11), and substitution of Equations (9.11) and (9.4) into Equation (9.10) gives

$$
\begin{aligned}
s_{ijkl_f} = & \int_{-\pi/2}^{\pi/2} \frac{Z_T(\theta)}{4} \left[\delta_{ik}(\delta_{l1}cos\theta + \delta_{l2}sin\theta)(\delta_{j1}cos\theta + \delta_{j2}sin\theta) + \right. \\
& \delta_{jk}(\delta_{l1}cos\theta + \delta_{l2}sin\theta)(\delta_{i1}cos\theta + \delta_{i2}sin\theta) + \\
& \delta_{il}(\delta_{k1}cos\theta + \delta_{k2}sin\theta)(\delta_{j1}cos\theta + \delta_{j2}sin\theta) + \\
& \delta_{jl}(\delta_{k1}cos\theta + \delta_{k2}sin\theta)(\delta_{i1}cos\theta + \delta_{i2}sin\theta) d\theta \\
& + \int_{-\pi/2}^{\pi/2} [Z_N(\theta) - Z_T(\theta)] (\delta_{i1}cos\theta + \delta_{i2}sin\theta)(\delta_{j1}cos\theta + \delta_{j2}sin\theta) \\
& (\delta_{k1}cos\theta + \delta_{k2}sin\theta)(\delta_{l1}cos\theta + \delta_{l2}sin\theta) d\theta.
\end{aligned}
\qquad (9.12)
$$

For $n_3 = 0$ we have $s_{ij33_f} \equiv 0$ for arbitrary vertical fractures. For rotationally symmetric fractures, we see from Equation (9.12) that

$$s_{ijk3_f} \equiv 0, i, j, k = 1, 2. \qquad (9.13)$$

This results in a compliance matrix in 6X6 condensed notation of the form:

$$
\begin{bmatrix}
S_{11_f} & S_{12_f} & 0 & 0 & 0 & S_{16_f} \\
S_{12_f} & S_{22_f} & 0 & 0 & 0 & S_{26_f} \\
0 & 0 & 0 & 0 & 0 & 0 \\
0 & 0 & 0 & S_{44_f} & S_{45_f} & 0 \\
0 & 0 & 0 & S_{45_f} & S_{55_f} & 0 \\
S_{16_f} & S_{26_f} & 0 & 0 & 0 & S_{66_f}
\end{bmatrix},
$$

which is the form of a monoclinic medium with up-down symmetry (the 1,2-plane is the mirror plane of symmetry).

Let us consider the case of a vertically fractured medium (with rotationally symmetric fractures) subject to an anisotropic external stress field with principal external stresses σ_1, σ_2 and σ_3 in the 1-, 2-, and 3-directions, respectively. As a preliminary simplifying assumption let the fracture compliances at any angle be independent of the tangential component of effective stress traction on the fracture faces and depend on just the normal component, $\tau_\perp(\theta)$, given by Equation (9.9).

A reasonable approach is to assume very compliant fractures at low normal stress with fractures approaching low values asymptotically as normal stress becomes large. Approximating such dependence by exponential decay functions, we may write,

$$
Z_N(\theta) = Z_{N_\infty}(\theta) + [Z_{N_o}(\theta) - Z_{N_\infty}(\theta)]\, e^{-\tau_\perp(\theta)/\tau_N(\theta)}, \tag{9.14}
$$

$$
Z_T(\theta) = Z_{T_\infty}(\theta) + [Z_{T_o}(\theta) - Z_{T_\infty}(\theta)]\, e^{-\tau_\perp(\theta)/\tau_T(\theta)}.
$$

This is the general case where the parameters governing the exponential decay functions are themselves functions of θ. However, in the model examined here we assume that Z_{N_∞}, Z_{N_o}, τ_N, Z_{T_∞}, Z_{T_o}, τ_T are independent of θ and Equation (9.15)

becomes

$$Z_N(\theta) = Z_{N_\infty} + [Z_{N_o} - Z_{N_\infty}] e^{-\tau_\perp(\theta)/\tau_N}, \qquad (9.15)$$

$$Z_T(\theta) = Z_{T_\infty} + [Z_{T_o} - Z_{T_\infty}] e^{-\tau_\perp(\theta)/\tau_T}.$$

The θ-dependence is just through the $cos2\theta$ dependence of $\tau_\perp$. Note that as $\tau_\perp$ is an even function of θ, Z_N and Z_T are also even functions of θ. Now integrating over all values of θ from $-\pi/2$ to $\pi/2$ will give the excess compliance tensor for this stressed medium as a function of σ_1, σ_2 and pore pressure P. Immediately it may be seen that $S_{16_f} = S_{26_f} = S_{45_f} = 0$ as these involve integrating an odd function times an even function from $-\pi/2$ to $\pi/2$. Thus a consequence of these assumptions and simplifications is that if the background medium is of orthorombic or higher symmetry, the long wavelength equivalent medium is orthorombic. So the 6X6 compliance matrix becomes

$$S_f = \begin{bmatrix} S_{11_f} & S_{12_f} & 0 & 0 & 0 & 0 \\ S_{12_f} & S_{22_f} & 0 & 0 & 0 & 0 \\ 0 & 0 & 0 & 0 & 0 & 0 \\ 0 & 0 & 0 & S_{44_f} & 0 & 0 \\ 0 & 0 & 0 & 0 & S_{55_f} & 0 \\ 0 & 0 & 0 & 0 & 0 & S_{66_f} \end{bmatrix}. \qquad (9.16)$$

In the simulations presented in this chapter, the coefficients τ_T and τ_N are empirically set to $1.35 MPa$. Also the compliances at zero stress have been set to $Z_{T_o} = 5.681 \cdot 10^{-9} GPa^{-1}$, $Z_{N_o} = 2.8409 \cdot 10^{-10} GPa^{-1}$, and the compliances at infinite stress are $Z_{T_\infty} = Z_{T_o}/5$ and $Z_{N_\infty} = Z_{N_o}/2$.

9.3 Numerical simulation of wave propagation during the fluid injection

In the examples presented in this section, we have implemented the fluid flow model in 2D using a 256 X 256 'd2q9' lattice for the BGK diffusion model. Following the terminology of Quian et al. (1992), a 'd2q9' lattice is a 2D square lattice where each node is connected to eight neighbours: four horizontally and vertically, four at 45°, and itself. The boundary conditions are periodic, that is, the top side of the grid links to the bottom side, and the left side to the right side. The plane of computation is taken to be horizontal, justifying the absence of a gravity term in Equation (8.22) and an injection well is inserted in the centre. The dimension of the model is characterised by the length scale L representing the overall extent of the model, and the timescale T being the duration of the fluid injection at the well. The spatial discretisation is $\Delta x = 10m$, and therefore the dimension of the model is 2560m X 2560m. The errors expected in the diffusion model are of the order $O(\epsilon^2)$, with $\epsilon = \Delta x/L = (\Delta t_d/T)^{1/2}$ (Maillot and Main, 1996). Δt_d is the required time step for the diffusion process. The diffusivity D, must satisfy $D\Delta t_d/\Delta x^2 \leq 1$. The time step is $\Delta t_d = 1s$.

The diffusivity in the model was set as follows: in the unfractured (background) rock, it is isotropic and is equal to $D = 10^{-3}m^2s^{-1}$. In the fractures, the principal components are D_1 along the local direction of the fractures and D_2 normal to the fractures, with $D_1 = 10^4 D$ and $D_2 = 10^2 D$. For the solid state we assume an isotropic background medium, so anisotropy is caused only by the presence of fractures. The background medium parameters are $V_P = 3300m/s$, $V_S = 2000m/s$, that are the P- and S-wave velocities. The rock density is set to $\rho = 2200kgm^{-3}$ and the internal friction is also constant and set to 0.6.

We examine the case of a pre-existing fractured network, which is hydraulically conducting. The fracture patterns are generated by a stochastic multiscale

cellular automaton model (Narteau, in press) and provided to the author by
Dr.Narteau. The matrix is considered to be isotropic, and the fractures are
aligned. The map of cohesions $C(x)$ was constructed based on the fracture net-
work. The cohesion is on average 10 times higher in the unfractured areas than
in the fracture positions. As we mentioned above, the initial conditions are very
important because they define the state of the medium at the initialisation of the
simulation. We will not refer to the initial conditions at this stage, because we do
not include the generation of new fractures in the following results. That is be-
cause in the current study we want to concentrate on the effects of fluid flow and
the evolution of the fracture network will complicate the results, thus not giving
us the ability to be certain that the features are due to the pore pressure changes.
Therefore in the following simulations the fracture network remains unchanged.

In the fractured medium fluid is injected in the centre of the model and present
a pore-pressure map at four consecutive time steps. Figure 9.1 shows the pore-
pressure maps at 10, 40, 70, and 100 hours after the initialisation of the injection.
The area shown in this figure is a small area around the injection point, and not
the whole modelled area. The black lines represent the pre-existing fractures.
The values of the pore pressure are presented by a colour code explained on the
right side of each map. The emergence of an elliptical pore pressure contour can
be seen at 100 hours, aligned with its semi-major axis parallel to the fracture
orientation.

To model the seismic wave propagation accurately in a complicated network
of fractures, we use a the finite-difference technique introduced in Chapter 2 of
this thesis. For each cell of the finite-difference grid the properties of the elastic
material is given by an equivalent medium based on the theory described in
Chapter 2. By applying a dense grid we have very high resolution and accuracy in
the representation of the rock properties. When the fluid injection starts the pore
pressure changes affect greatly rock properties. As shown in the previous section

Dual simulation of fluid flow and seismic wave propagation in a fractured
network: Effects of pore pressure
237
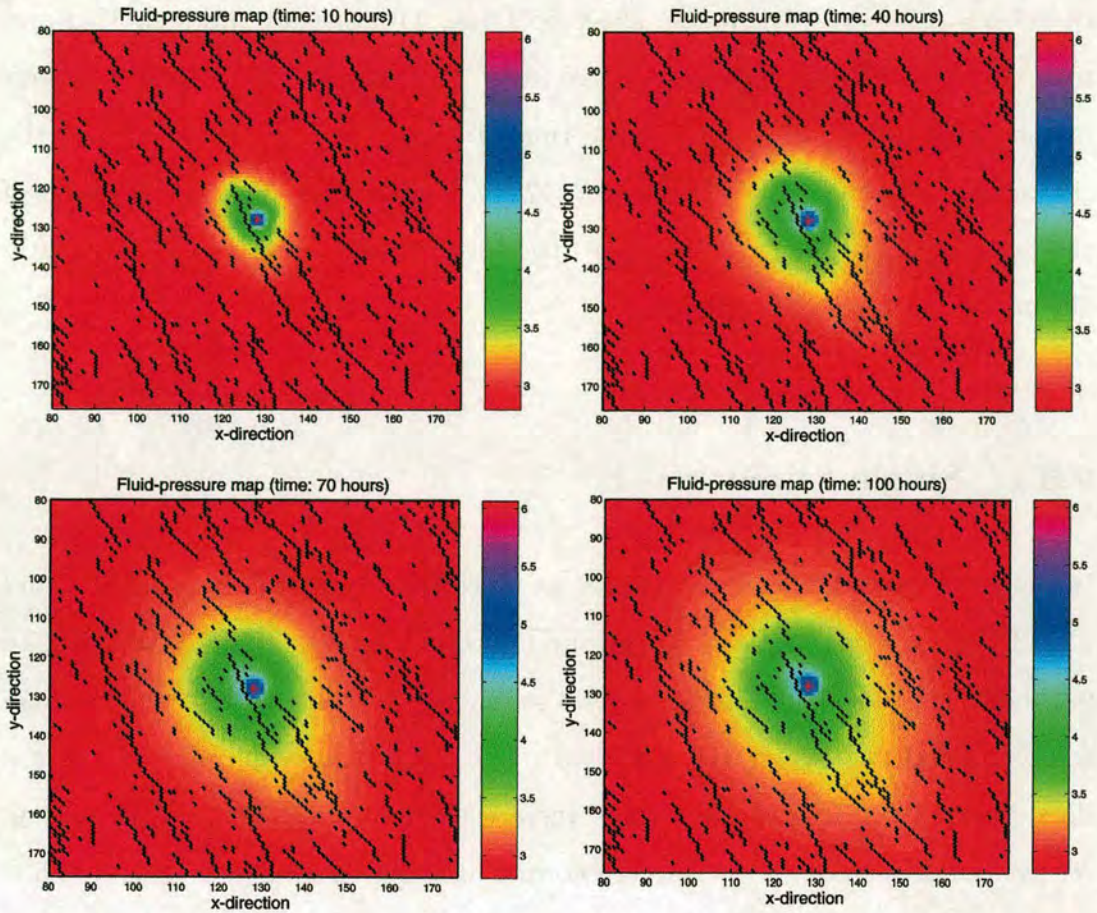
Figure 9.1: Pore pressure map in a small area around the injection point
(1000X1000m). The figures show the pore pressure at four consecutive
times, 10, 40, 70, and 100 hours, after the initialisation of the injection
of the fluid. The black lines are the pre-existing fractures of the medium.

fracture compliances change with the variation of pore pressure. At each time
step of the fluid flow simulation, we calculate the corresponding dynamic effective
elastic properties of the rock based on the formulas we presented. Therefore, we
have a continuous feedback from the changing elastic properties due to the pore
pressure changes into the seismic simulation. In that manner we can produce
consecutive time-lapse data and examine the potential of extracting information
about the pore pressure changes directly from seismic waves.

For the seismic simulation the background medium parameters are $V_P =
3300 ms^{-1}$ and $V_S = 2000 ms^{-1}$ for the P- and S-wave velocities, and the den-

sity is $\rho = 2200 kgm^{-3}$. We use 256X256 grids, with spatial grid-step $10m$ and time-step of $0.001sec$. The source wavelet is a Ricker wavelet with a dominant frequency of $40Hz$ and a pulse initial time of $0.1s$. The source is located at the centre of the model ($x = 1280m$, $y = 1280m$), exactly at the same position of the fluid injection point, so the waves travelling to the receivers will be greatly affected by pore pressure changes.

9.3.1   Single azimuth

Initially, we record the seismic waves at a receiver located at $x = 1000m$ and $y = 300m$, at consecutive stages of the injection numerical simulation. Figure 9.2 shows the model configuration used for the seismic simulations. The source-receiver direction is at a 16° angle with the y-direction, while on average the direction of the fractures is at a 30° angle with the y-direction. So the source-receiver angle relative to the fracture normal direction in average is 104° (red line on Figure 9.2). We examine the variation for different azimuths (remaining lines in Figure 9.2) in the next section.

Figure 9.3 shows the x-component of the wavelets recorded at the receiver. The black trace is recorded at the pre-injection stage when pore pressure is equal throughout the model and is used as a reference. Then we start the fluid injection and we get feedback from the pore pressure changes at 10, 40, 70, and 100 hours after the initialisation of the injection as shown in Figure 9.1. We simulate the wave propagation for the medium at the four consecutive time steps of the fluid injection. The red, green, blue, and orange traces are recorded at the receiver at a stage 10, 40, 70, and 100 hours after the injection initialisation, respectively. There are clear variations on the characteristics of the waveforms as pore pressure changes. The direct P-waves recorded at 0.37 sec, do not seem to be affected by the pore pressure changes and seem to maintain the same amplitudes. In
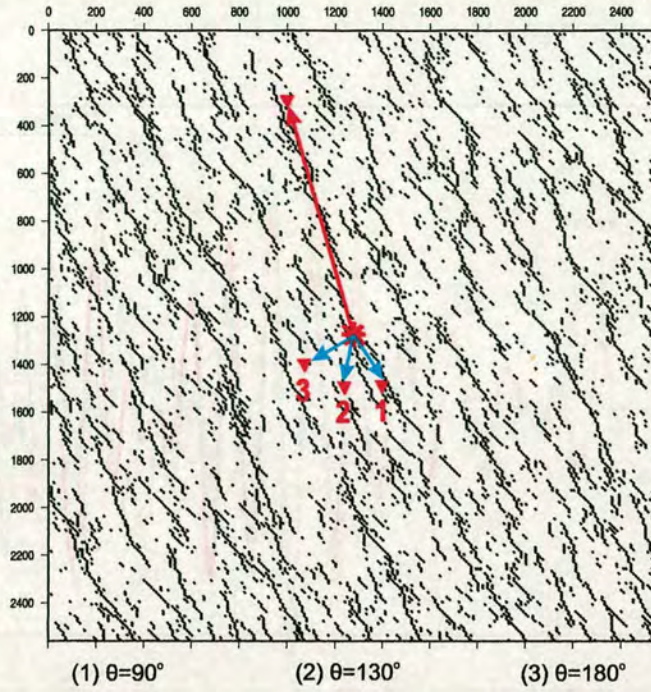
Figure 9.2: Configuration of the model used for seismic modelling at consecutive stages of fluid injection. The source is located at the centre of the model ($x = 1280m$, $y = 1280m$) and the single receiver where we record the seismic waves is located at $x = 1000m$ and $y = 300m$. Also the receivers used to examine azimuthal dependence are shown together with the azimuths for each case.

contrast, the S-wave and the coda waves exhibit strong amplitude changes which can be uniquely attributed to the pore pressure changes, since all other parameters remain constant. This is in agreement with the results presented by Liu et al. (2002). Angerer et al. (2002) also showed that P-waves are less affected by pore pressure changes compared to S-waves during CO_2 injection. In details, for the S-waves we can say that there is almost a similar pattern; as the pore pressure gets higher the amplitude of the wave gets higher. We can see that the orange wavelet has the higher amplitude, which represents the state at 100 hours after fluid injection, when the pore pressure is higher compared with the rest of the cases. On the contrary, for the coda waves (after 0.65 sec), they seem to be affected by pore pressure in an opposite way. So it has higher amplitude at the pre-injection stage (black wavelet) and lower amplitude when the pore pressure

is the greater (orange wavelet).
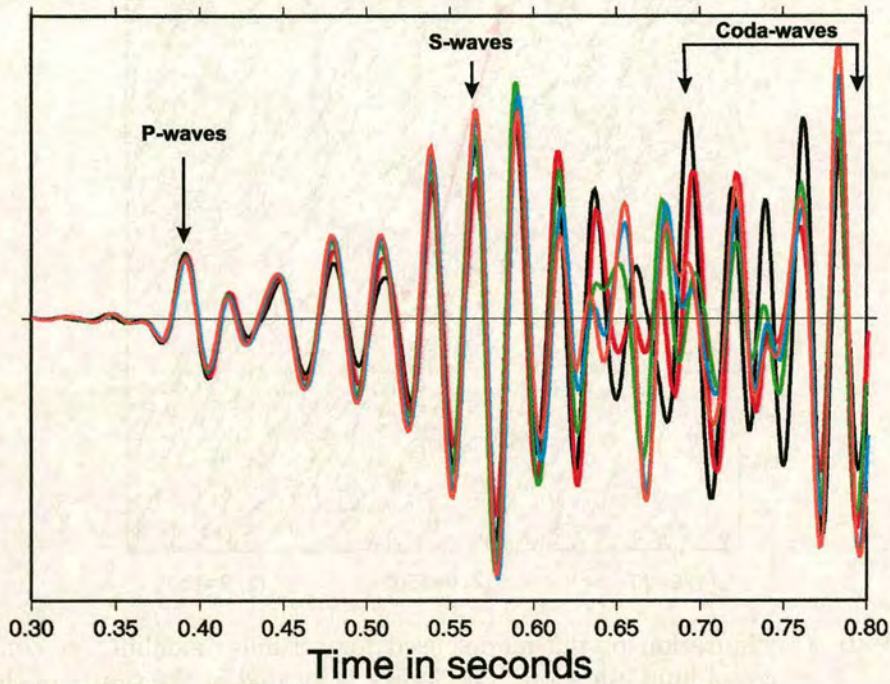
Figure 9.3: Wavelets recorded at an individual receiver for consecutive pore pressure stages. The black wavelet represents the pre-injection stage, and red, green, blue, and orange represent stages of the fluid injection at 10, 40, 70, and 100 hours after the injection, respectively.

To examine further the effects of pore pressure on the wavelet, we show in Figure 9.4 the spectrum of each of the wavelets presented in Figure 9.3. We can see a significant shift of the peak frequency towards lower frequencies as the injection proceeds. Starting from the pre-injection point where the most energy is near 40 Hz, we end up in the stage 100 hours after the injection where most of the energy is at 30 Hz. This indicates a systematic increase of attenuation with the increase of pore pressure. The magnitude of the peak frequency shift is about 10 Hz. Another feature seen in the spectrum is that at the initial stages of the injection, at 10 and 40 hours after the initialisation the energy is distributed in two frequency ranges compared to the rest of the cases where the energy is concentrated in a certain frequency range. This may be because the initial stages are a sort of a transition state of the system between the pre-injection and the

after-injection states.
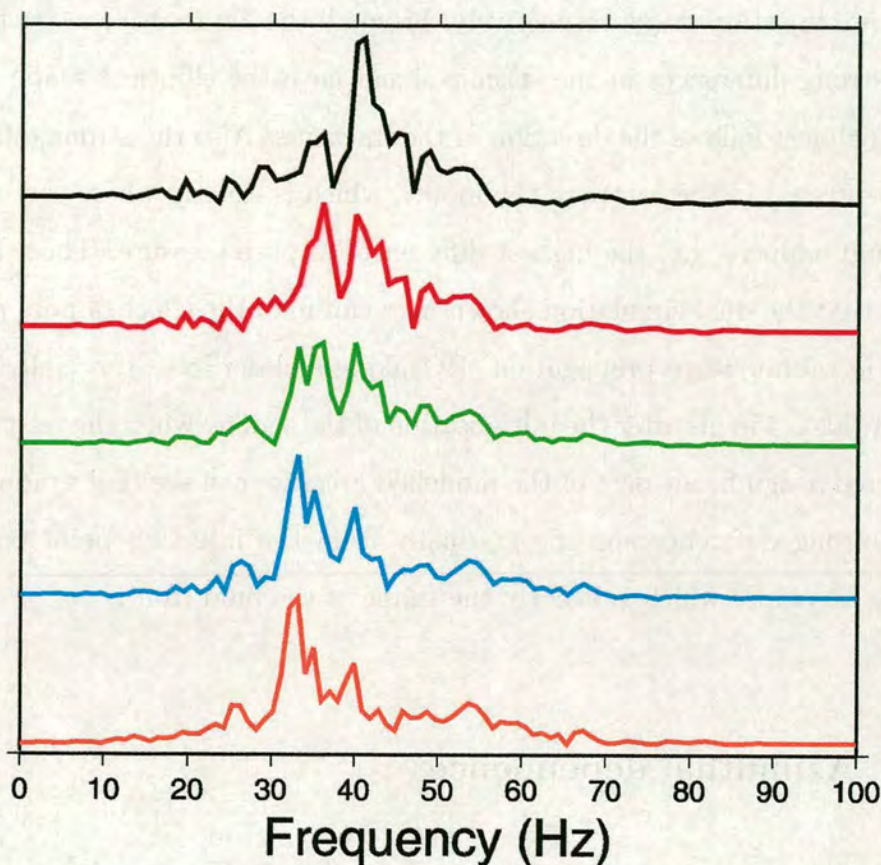
Figure 9.4: Spectrum of the waveforms shown in Figure 3, representing seismic waves recorded at different stages of the fluid injection. The colour code corresponds to the one used in Figure 3.

It is a usual practice in time-lapse seismic monitoring to examine the difference of measurements for two consecutive time-steps, in order to evaluate the effect of pore pressure changes. For the model shown in Figure 9.2, we conduct forward modelling for the pre-injection state, and the states 10, 40, 70, and 100 hours after the fluid injection. From each simulation snapshots of the seismic wave are generated at 150 ms, 250 ms, 350 ms, and 450 ms, after the initialisation of the source. To examine the effect of pore pressure changes, we take the pre-injection stage as a reference stage and find the difference between the snapshots of each stage after injection and the pre-injection stage. Figures 9.5, 9.6, 9.7, and 9.8 show the snapshots at consecutive time steps, which are the results of the difference

between the simulation stages at 10, 40, 70, and 100 hours after the fluid injection
and the pre-injection stage, respectively. From all the figures we can see that the
area of strong differences in the seismic signal have the elliptical shape that its
long axis almost follows the direction of the fractures. Also the strong differences
are concentrated in the centre of the model, which is exactly where the injection
of the fluid happens, i.e. the highest differences in pore pressure. Those features
indicate that the dual simulation shown here can map the effect of pore pressure
changes in seismic wave propagation. By taking a closer look, especially at each
snapshot taken 450 ms after the initialisation of the source, when the seismic wave
has covered a significant part of the modelled area, we can see that gradually the
area of strong difference spreads gradually from the injection point outwards,
following an ellipse which is exactly the shape of the fluid front.

9.3.2 Azimuthal dependence

Another important aspect of the pore pressure effect is the azimuthal dependence
on seismic signatures. We conduct the same simulations as above and record the
seismic waves at three receivers, at the same distance from the source, so we will
have almost the same attenuation due to the distance travelled by the seismic
wave, and at 90°, 130° and 180°, from the fracture normal. This is repeated for
each of the four states of the fluid flow simulation shown in Figure 9.1. Figure
9.9 shows the differences in the horizontal components recorded at the three
receivers at each azimuth. The differences are computed between: (a) 10 and 40
hours after injection, (b) 10 and 70 hours after injection, and (c) 10 and 100 hours
after injection. Figure 9.10 shows the corresponding difference in the frequency
spectra.

In general, this is another confirmation that P-waves are not greatly affected in
contrast to S-waves and coda (or scattered) waves. Along the fractures (azimuth

90°) we can see the strongest difference in S-waveforms, while at direction normal
to the fractures (azimuth 180°), the strongest difference is in coda (or scattered)
waveforms. As the pore pressure increases further, this effect becomes stronger,
as expected. It is interesting to note that there is a variation of the frequency
content with azimuth. The greatest frequency shift occurs at an azimuth of 180°
where a significant amount of energy is shifted from 50-60 Hz towards 30-40 Hz.
At 130° azimuth, energy moves between the same frequency ranges, but in a
smaller degree. Finally, at 90° azimuth there is a much more limited shift of
energy, and in addition there is significant energy present at the range of 50-
60 Hz. In this case the energy is redistributed to both low and high frequencies,
in a transition phase, before it shifts to systematically lower frequencies as angle
increases from the fracture normal.
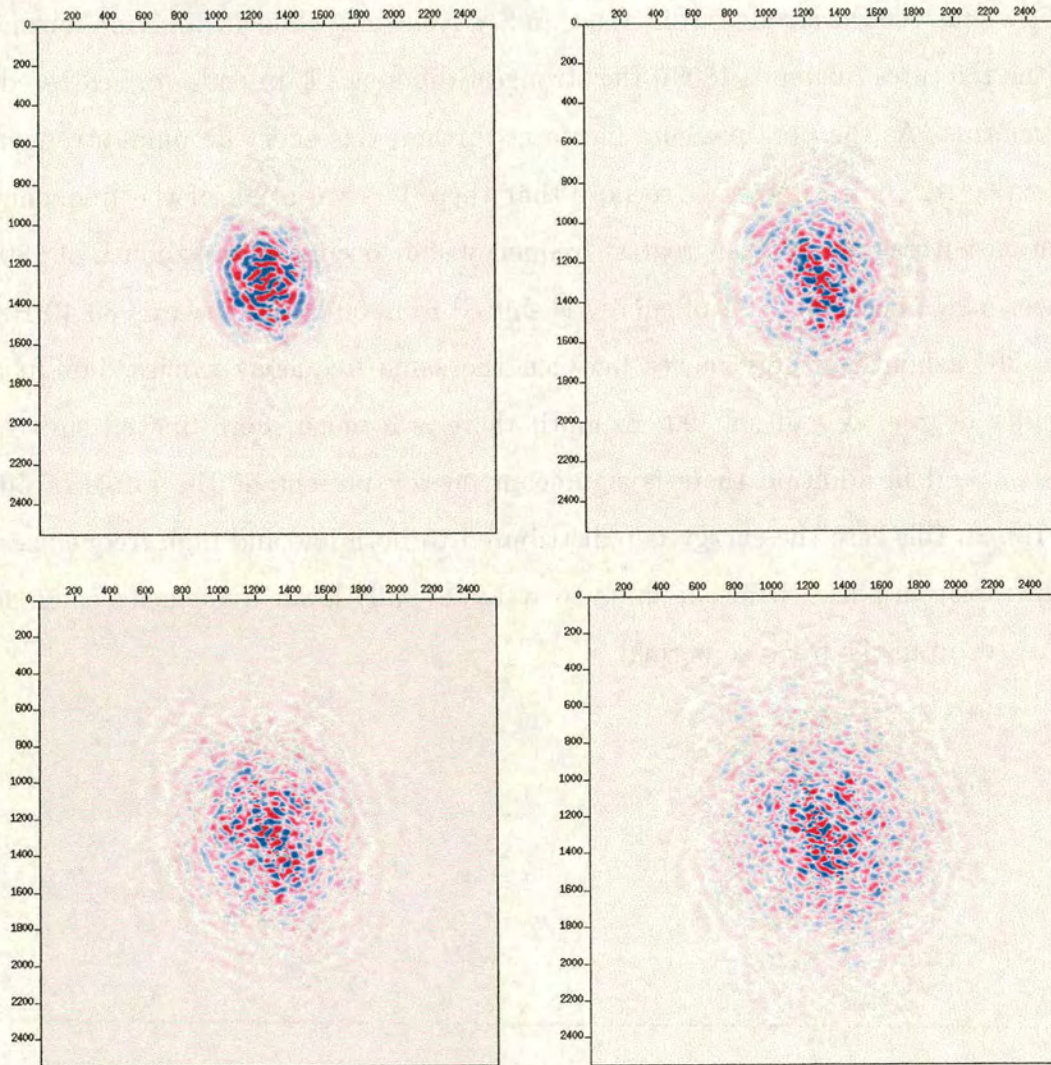
Figure 9.5: Snapshots at consecutive time steps (150 ms, 250 ms, 350 ms, 450 ms
after the source initialisation), which show the difference between the
simulation of the medium 10 hours after the injection of the fluid and
the pre-injection stage.
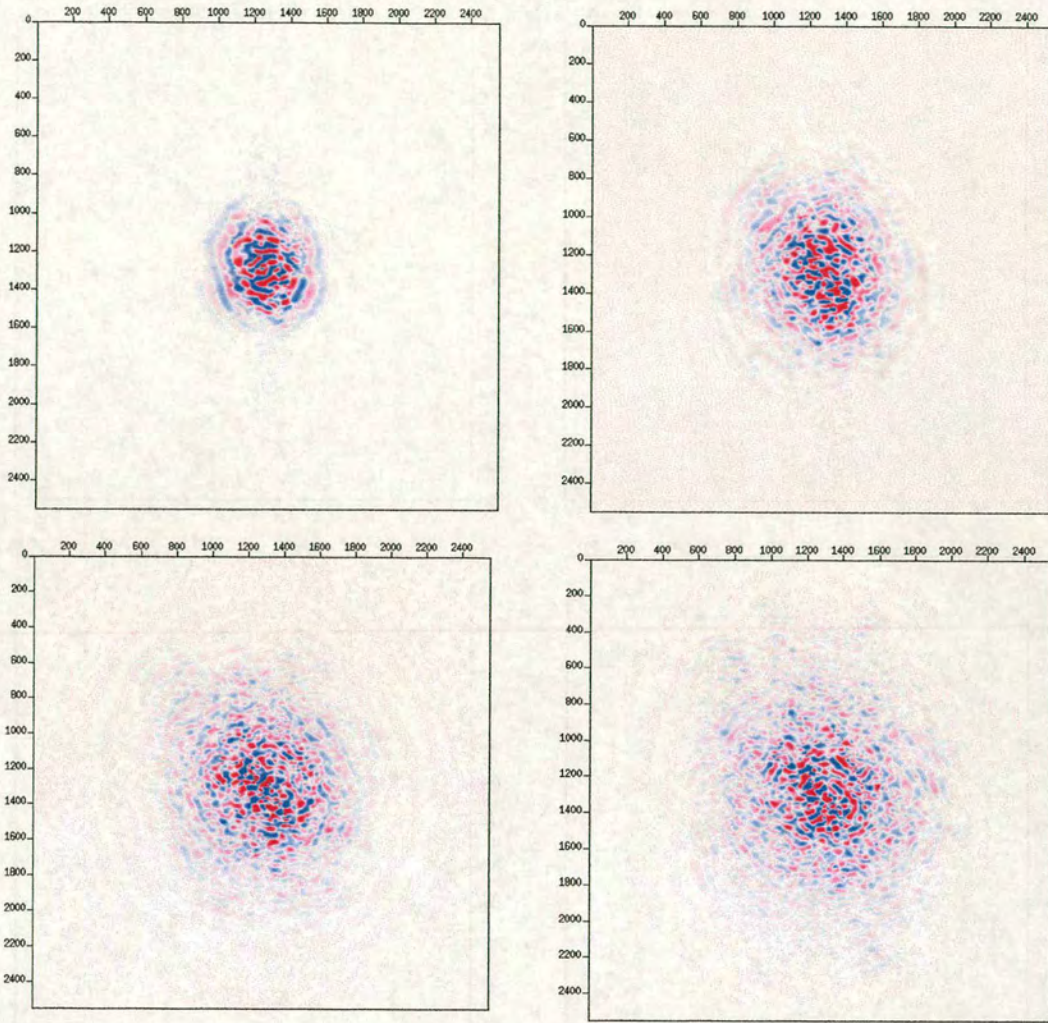
Figure 9.6: Snapshots at consecutive time steps (150 ms, 250 ms, 350 ms, 450 ms
after the source initialisation), which show the difference between the
simulation of the medium 40 hours after the injection of the fluid and
the pre-injection stage.
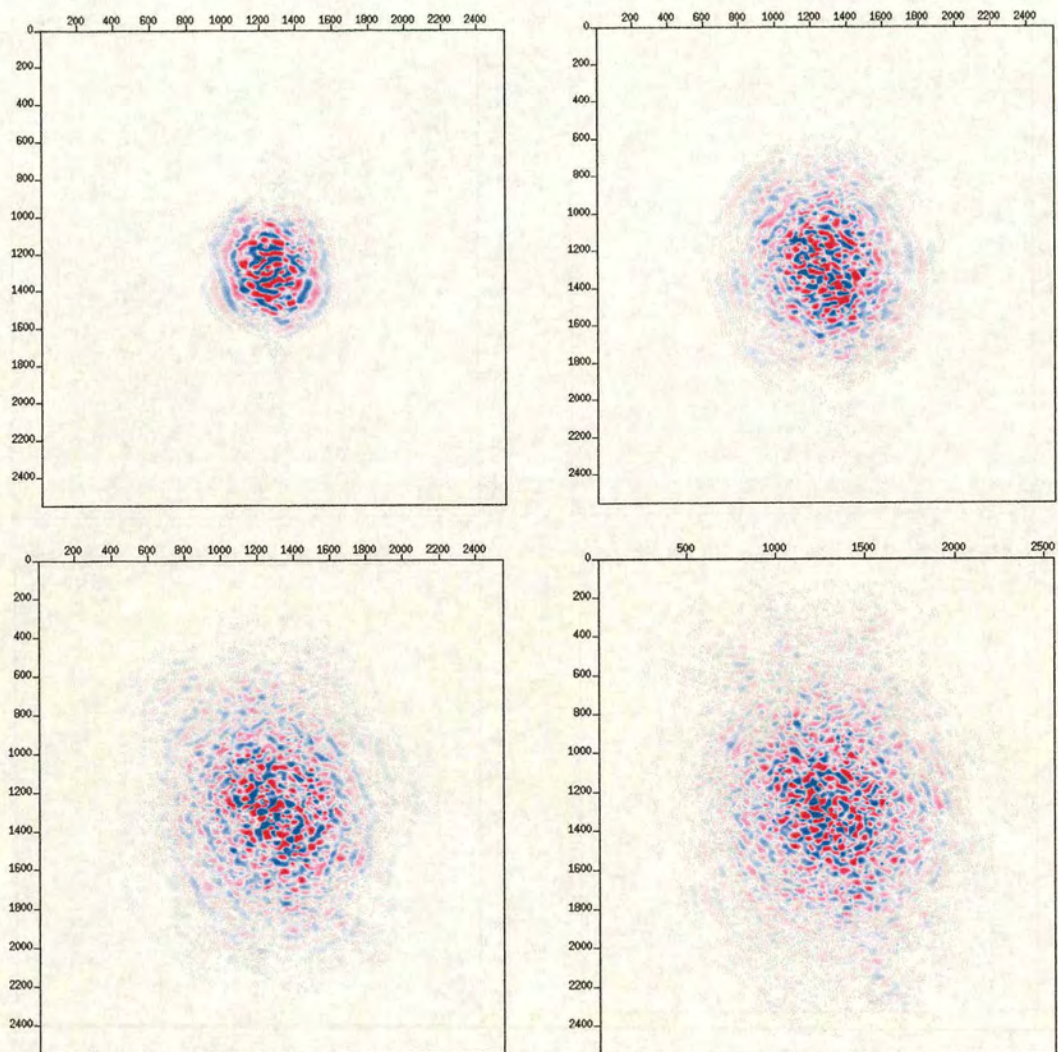
Figure 9.7: Snapshots at consecutive time steps (150 ms, 250 ms, 350 ms, 450 ms
after the source initialisation), which show the difference between the
simulation of the medium 70 hours after the injection of the fluid and
the pre-injection stage.
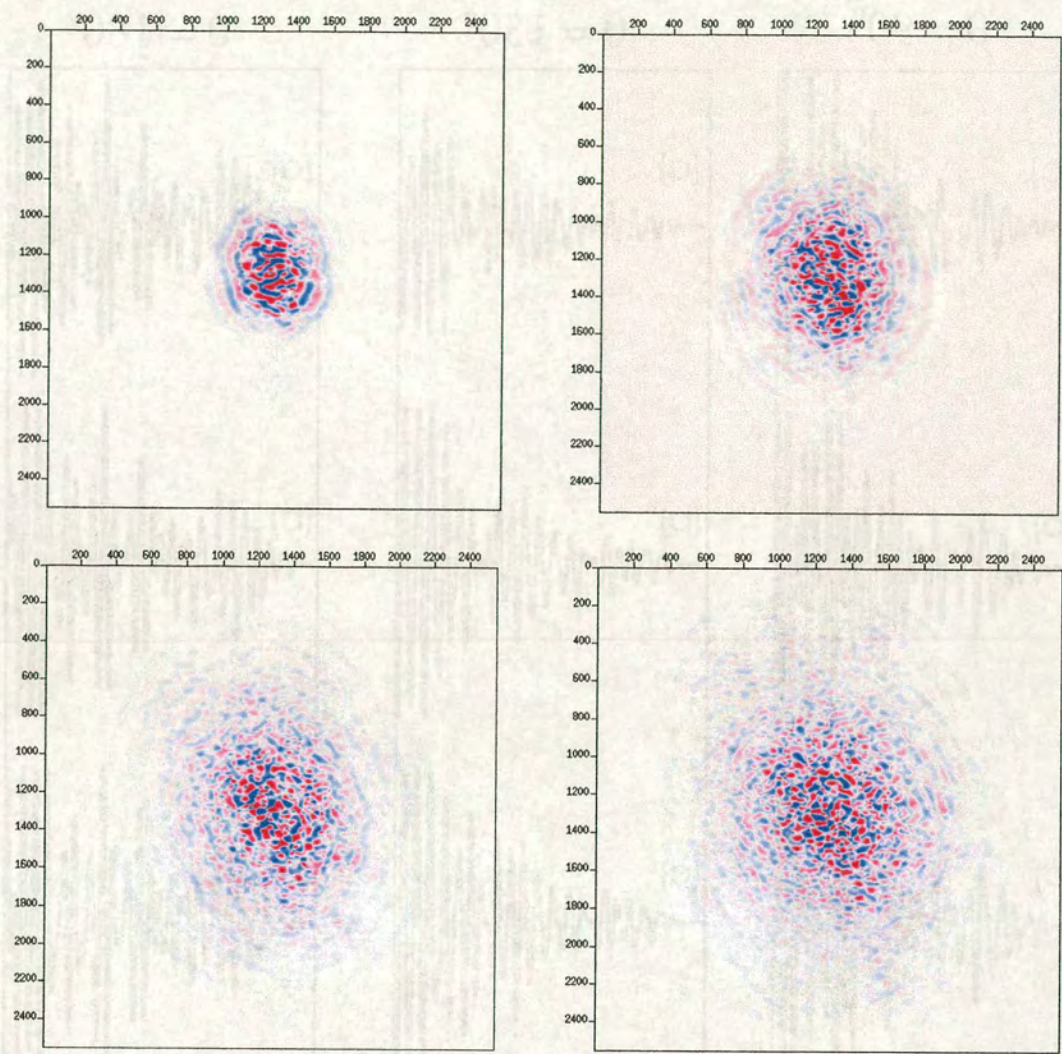
Figure 9.8: Snapshots at consecutive time steps (150 ms, 250 ms, 350 ms, 450 ms
after the source initialisation), which show the difference between the
simulation of the medium 100 hours after the injection of the fluid and
the pre-injection stage.
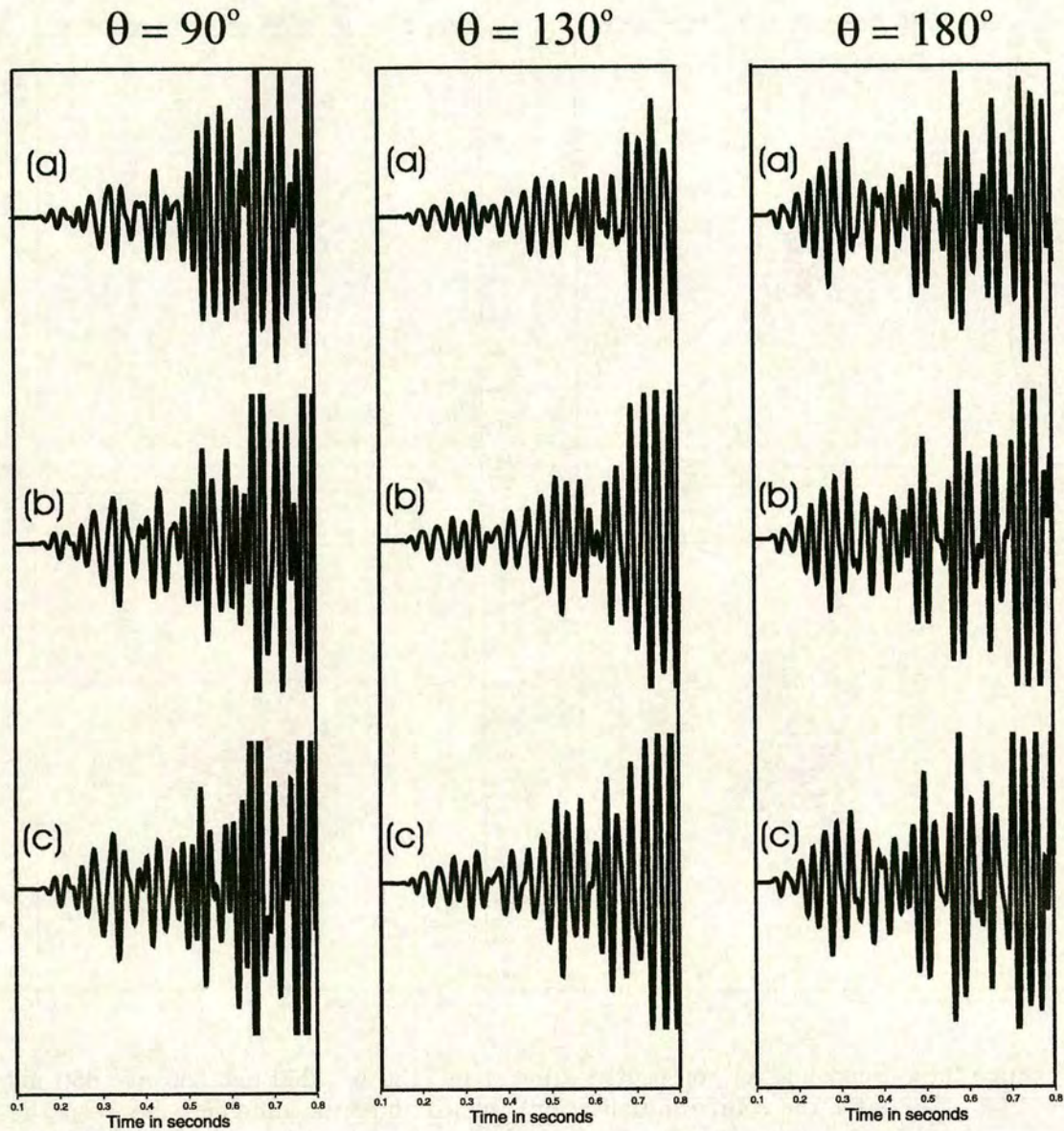
Figure 9.9: Differences in horizontal components recorded at receivers having different azimuths from the fracture normals. Figures (a), (b), and (c) correspond to the differences between pore pressure 10 and 40 hours, 10 and 70 hours, and 10 and 100 hours after injection, respectively.

9.4   Summary

We have conducted systematic dual numerical simulations of fluid flow and seismic wave propagation. For the fluid flow simulation the fluid is injected at the centre

$$\theta = 90° \qquad \theta = 130° \qquad \theta = 180°$$
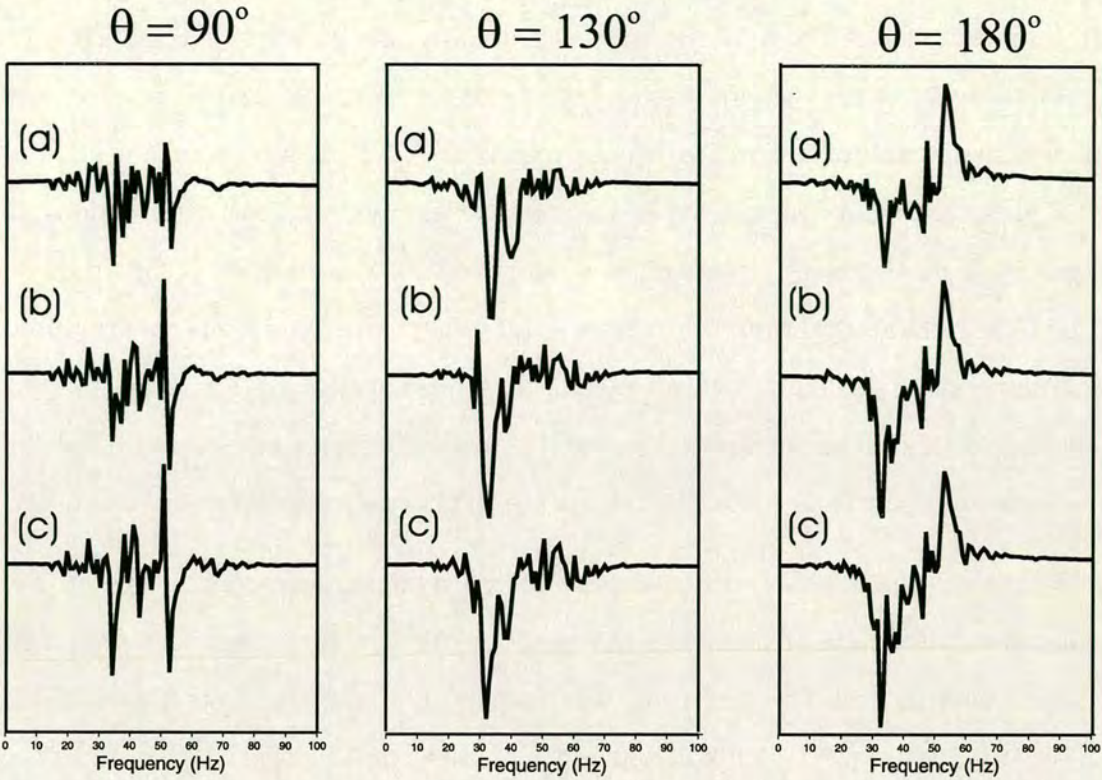
Figure 9.10: Differences in frequency spectra of the signals corresponding to the same cases as in Figure 9.9. (a), (b) and (c) represent increasing time difference between the examined stages as in Figure 9.9

of the model and at selected time steps after the injection information about pore pressure is collected. Variations in pore pressure lead to variations in the effective stress. We use an empirical relationship between the effective stress changes and respective changes in the compliance of the rock. Therefore, at each selected time step of the fluid simulation, we obtain complete information about the updated elastic properties of the medium, and use them to perform seismic simulation. This process gives seismic data at consecutive time steps when pore pressure changes, which is synthetic time lapse seismic data. The simulations in the thesis focused on the examination of the effects of pore pressure changes on seismic wave attributes.

These initial simulations show a different response between P-waves and S- and coda-waves to pore pressure changes. P-waves seem to be less affected or affected

in a limited way, while S- and coda-waves are strongly affected. We see that the amplitudes increase with increasing pore pressure. Also the frequency spectrum shows significant variations with pore pressure. There is an important shift of the peak frequency towards lower frequencies (implying strong attenuation) as pore pressure increases. However, it is possible that this frequency shift may be due to normal attenuation. Throughout the consecutive time steps the fractured medium does not change, which means that normal attenuation would be the same in all cases. Therefore when we find the differences in frequency spectra between different time steps, the results are solely due to the effects of fluid flow.

We also examined the effects of pore pressure changes on seismic signatures, related to the angle of incidence of seismic waves. In the simulation presented in this chapter fractures comprise the main path where the fluid moves in the reservoir, that is why the fluid front is an ellipse with its long axis parallel to the fracture orientation. Parallel to the fracture orientation we observe very strong amplitude difference in the S-waves as pore pressure changes, while normal to that direction the strong difference is observed in the coda (or scattered) waves. Finally, we show that the greater shift of energy in frequency happens when seismic waves travel normal to the flow path.

Finally, we presented snapshots of seismic waves at different stages of the fluid flow process. The snapshots show significant amplitude variations on seismic waves, that accurately describe the evolution of the fluid front. This indicates the validity of the technique we presented.

In the real field variations in fluid flow properties are examined with time-lapse seismic monitoring. It is a newly established tool for reservoir process observation and improved reservoir management. Commonly, several 3-D seismic surveys of the same reservoir at different times are compared. Differences in reflection amplitude or impedance are interpreted in terms of reservoir changes. In addition

to surface seismic surveys, high frequency (lower kilohertz range) crosshole data
are used for monitoring reservoir processes. Also under development are active
seismic reservoir monitoring techniques by permanently installed downhole source
and receivers.

To conclude, we have exhibited that our study can help to provide a greater
insight in the systematic effects of pore pressure changes on seismic waveforms and
attenuation, and to identify potential ways to estimate pore pressure changes from
seismic data. The results presented here form part of our strategy to establish
a direct link between pore pressure changes and potentially diagnostic variations
on seismic waves.

CHAPTER 10

Discussion and Conclusions

10.1 Summary of the main results

The aim of this thesis was to investigate the characterisation of fluid flow in fractured reservoirs, directly from seismic data. We concentrated on the theoretical investigation of the subject and tried to establish theoretical formula that link fluid flow properties with elastic properties of the medium, which can be identified directly from seismic wave attributes. The examination was based on numerical modelling both of seismic wave propagation and of fluid flow.

We started the examination from the numerical modelling of seismic waves. There is a number of techniques available for modelling wave propagation. Analytical methods describe in details and accurately the physics of the wave propagation in a medium and the interaction with a single fracture. However, when we deal with a complicated network of fractures those methods have serious limitations. On the other hand numerical modelling techniques can describe complicated cases successfully, but the resulting waveform has the properties of the mean effect of the fractures. Therefore we miss important information regarding the effects of each single fracture in a multiple fracture environment. We introduced a technique that uses a combination of the two methods. We used the pseudospectral method to model the wave propagation in the whole medium. Lo-

cally at each grid cell in the finite difference grid, we used an equivalent medium representation of the elastic properties. This new method by combining the two techniques, does not have the limitations of each individual technique and proves to be a reliable method for numerical modelling.

This new method needed to be validated and examined for the results. The grid spacing of the finite difference grid is limited from the maximum source frequency and the minimum wave velocity. In general, the wavelength should be about five times larger than the grid size, in order to have clear reflections without noise interference. We also examined grid spacing compared to fracture size. We concluded that the maximum grid size should be equal to the size of the fractures examined. To conclude this part, we examined the vertical and lateral resolution of the technique. For the vertical resolution, a vertical distance of a quarter of a wavelength between two fractures, is sufficient in order to distinguish between the reflections coming from the two fractures. On the other hand, lateral resolution depends on frequency, velocity and the depth of the reflecting interface. Also lateral uncertainty always exceeds vertical uncertainty by a factor of at least two. Generally, those limitations are valid for any fracture orientation, but they may vary slightly depending on the source and receiver deployment

Following we examined how fracture parameters affect seismic wave propagation. First, we examined spatial distribution of fractures. Spatial distribution affects clustering which is a parameter that controls scattering. In areas of heavily populated fracture clusters, there is strong and coherent energy. Also high fracture clustering results in high local fracture densities, which can cause the energy to be trapped in a certain area (localisation processing). We also observed that various spatial distributions of fractures give different frequency spectra on the recorded wavefield. Another parameter that affects the behaviour of fractures is fracture size. We found that fractures act as single scatterers and they become sources of secondary wavefield when their size is smaller than the wavelength. On

the contrary, when fractures are longer than the wavelength they act as interfaces and they generate strong reflections.

We examined the evolution of such a fracture network and investigated multiple scattering at each consecutive stage. At the initial stages of the evolution the size of fractures is less than the wavelength and fracture density is low. We examined scattering attenuation and we found that the attenuation factor shows global and local maximum values that correspond to certain frequencies. As fractures become longer the maximum values of attenuation appear at higher frequencies. When the system reaches the percolation threshold, fracture density becomes high thus leading to significant scattering and the waveform becomes elliptical. At the percolation threshold, we have no maximum values of the attenuation factor. After the percolation threshold, the system gets reorganised, the generation of new fractures stops and the existing ones start interacting to form longer fractures. Scattering attenuation factor is smaller in this case compared to the cases before the percolation threshold and it does not exhibit significant variations with frequency. At the final stages, we have the formation of a major fault. The size of the fault is bigger than the wavelength, which results in strong reflections rather than scattering.

We continued the examination of scattering attenuation but in this case by averaging the effect of the fractures. To do so we used the meanfield theory. The results showed that scattering attenuation becomes higher as the normalised wavenumber rises until it reaches $k\alpha = 4.41$, and at this point the fracture size becomes larger than the wavelength. After that point scattering attenuation declines (i.e. $k\alpha = 6.3$). For high frequencies each fracture excites scattered waves of significant amplitude with the largest corresponding to wavelengths comparable to the fracture size. For low frequencies, that correspond to wavelengths much larger than the size of the fractures, the waves excited by each fracture are negligible but the fractured medium excites a reflected wave as if it was one het-

erogeneous medium of some effective thickness. Finally, we examined the effect of the angle of incidence of the seismic wave on scattering attenuation. We found that scattering attenuation rises constantly from 0° to 90°, where the angle is measured from the fracture normal. That means that 0° is the crack normal and 90° is the fracture plane. It is interesting to note that the highest value is for 70° and not for 90°.

When we examined the effect of fracture parameters, we assumed that fractures are dry. In order to make our models more realistic, we introduced a fluid flow simulation technique for single-phase fluid. We presented a theoretical formula that links pore pressure changes due to fluid flow with corresponding changes in the elastic properties of the fractured medium. We used the fluid flow simulator in conjunction with the seismic modelling technique to examine the effect of pore pressure changes on seismic waves. The results showed a different response of P-waves, S-waves and coda-waves to pore pressure changes. P-waves seem to be less affected or affected in a limited way, while S-waves and coda-waves are strongly affected. We recognised that the amplitude of the seismic waves increases with increasing pore pressure. Also, an important shift of the peak frequency towards lower frequencies (implying strong attenuation) is present, as pore pressure increases. Those results refer to a single azimuth case. It is very important to examine what happens when the seismic waves travel at different angles towards the fractures. We examined the azimuthal dependence of the effects of pore pressure changes, for three different angles. We observed that parallel to the fracture orientation there are very strong differences in the amplitude as pore pressure changes, while normal to that direction the strong differences are in the coda waves. In addition to the amplitude variations, we also notice variations in the frequency content. There is redistribution of energy to lower frequencies due to scattering as pore pressure rises. The greater shift of energy in frequency happens when seismic waves travel normal to the flow path, that is normal to the

fractures.

10.2   Discussion of the results and implications

In this thesis we have introduced a new technique for the numerical modelling of wave propagation in a fractured medium. The method can deal with multiple scattering cases without having any limitations on the number of fractures present in the medium. The representation of the wavefield is highly accurate as long as sufficient grid elements are available. However, numerical modelling techniques in general have a limit in the maximum size of fractures they can deal with compared to the grid size. That poses serious limitations in the cases of long fractures. If we use very wide gridcells to include the fractures inside them, then in order to have high accuracy we will have constraints on the source wavelengths we can use. In order to avoid this scenario, we divide long fractures into smaller ones, that can be included in smaller grid cells. That can be easily done because the elastic properties of each grid cell are represented by the equivalent medium. When adjacent fractured cells have the same elastic properties, then the seismic wave will recognise them as a continuous fracture, no matter how we implement it on the numerical model.

The most important characteristic of the technique, is the combination of a numerical technique with an analytical method. Therefore we have the accuracy and the exact solution of the wave equation that an analytical method gives, together with the lack of limitations in the properties of the fractures provided by the numerical method. This method can be a useful tool in the understanding of the important role of fractures and their effects on wave propagation. The knowledge gained by such studies may ultimately lead to the extraction of valuable information concerning the fracture distributions in natural rocks, directly from seismic data. Such a study of different fracture distributions was presented

in this thesis. It showed that scattering is strongly dependent on the spatial distribution of fractures. When we have fractures that are distributed in such a way that leads to high local fracture densities, the wavefield is complex and that makes individual phases and their identification very complicated. Having in mind that we examined 2-D models, it is clear that strongly fractured areas should be investigated by 3-D techniques. The limitations introduced by 2-D modelling compared to 3-D modelling was briefly examined in a previous chapter. In the 2-D approximation the source is a line source of infinite length. There are ways of making a correction to our synthetic seismograms so as to resemble synthetic seismograms resulting from a point source. As shown by Vidale et al. (1985) an approximate SH source seismogram can be obtained by convolving the line source seismograms with $1/\sqrt{t}$ and differentiation with respect to time. This is equivalent to a deconvolution with $1/\sqrt{t}$, an approach used by other authors (e.g. Crase et al., 1990).

Our investigation showed that another critical parameter is frequency. We have shown that the frequency content of the wavefield depends on spatial distributions. That also is in agreement with findings from other researchers, who found that frequency-dependent seismic scattering depends on fracture spatial distribution. Therefore the usual examination of seismic data at certain frequency is not enough. Depending on the spatial distribution of the fractures, we may loose a lot of information, if we examine the wrong frequency range. Therefore a thorough investigation of seismic scattering should cover a wide range of frequencies. For example, lets take the case of coda waves, which is one of the usual effects of scattering. Coda waves is the result of energy that is redistributed to frequencies other than the source frequency. In real earth we have complicated spatial distributions and in some cases fractures have also power law or fractal size distributions. Such an environment gives very strong coda waves and very complicated waveforms. If we limit our examination in a certain frequency range,

we will loose all the information included in the coda waves.

In the initial stages of the investigation we examined fracture networks of certain properties. In the earth fracture networks are not static but they are evolving with time. We have conducted a systematic numerical study of scattering attenuation in such an evolving fracture network. Once more the examination showed that scattering attenuation is frequency dependent. However, that dependence varies with the frequency range examined. Also the relationship between scattering attenuation and frequency has significant variations at different stages of the fracture evolution. The parameters that vary while a fracture network evolves are fracture density and fracture size. The results indicate that one of those parameters or both of them, control frequency dependence. It is demonstrated that there is a proportional relationship between scattering attenuation and fracture density, because scattering becomes stronger as fracture density becomes higher. Following, strong scattering leads to the generation of coda waves and to a shift in frequency of a significant amount of energy. In addition, the mechanism of scattering is also sensitive to fracture scalelength. The results showed that scattering attenuation has in some cases maximum values at certain frequencies. Those frequencies possibly correspond to wavelengths comparable to the dominant scalelength of the fractures. That is visible in most of the evolution stages, especially at the later stages when we have few dominant scalelengths. At the percolation threshold, where we have no dominant scalelength, we have no indication of a maximum scattering attenuation at any frequency range. Although the combined effect of fracture density and scalelength on frequency dependence is very complicated to analyse with a single examination, this study showed the potentials of using scattering attenuation as a means of describing the properties of a medium and identifying dominant scalelengths of fractures. Although in real data it is not easy to discriminate between scattering attenuation and intrinsic attenuation, we believe that attenuation measurements can be used successfully

towards a more detailed characterisation of a fractured reservoir.

In seismic exploration, for a typical seismic dataset with a source that generates a range of wavelengths, the wavefield will interact with the various heterogeneity distributions. The resulting data will represent a mixture of the scattering regimes. Heterogeneities of smaller scales are usually larger in number than large-scale features. However, both features may contribute equally to the data. So the question that arises is what feature, if any, dominates the seismic response, and how can we recognise that feature? Two parameters that control the response are the scattering strength of the individual scatterers and the wavetype that is analysed. For example, when we have compressional waves, dry open fractures dominate over those with a water, oil or cement fill. On the contrary, for shear-waves the directional scattering is more distinctive for thin fractures than those with a larger aspect ratio. Therefore, the multicomponent seismic response of each group of heterogeneities may be different. Such results are important in interpreting the multicomponent seismic response, as not all reservoir features can be satisfactorily correlated to productivity. The seismic response also depends upon the way each class of heterogeneity such as pores and fractures, are organised within the medium. However, spatial distribution of heterogeneities of different scalelengths is not random. Small-scale features must be constrained to some extent by the distribution of larger scale features. Therefore the reservoir could be organised into groups of entities determined by the largest physical scalelength downwards. On the other hand, there is evidence of a fractal distribution for some aspects of a fracture network (Yielding et al., 1992). No matter how the heterogeneities of various scalelengths are distributed, the main question is how the various scattering processes combine, and what information do we get from seismic?

The idea of a simple anisotropic system as a basic building block for the effective seismic response of a medium containing many different heterogeneities is of high

importance to data processing and interpretation. However the question remains on how we can image reservoir features and what rules are there available for the interpretation. We can get results through a selection of appropriate data, where certain features are known clearly to dominate. One such case, is the detection of fracture swarms known to exist in the Austin Chalk in Texas, using shear wave amplitudes (Mueller, 1992). In that case a direct correlation was made between the anisotropic shear-wave behaviour and natural fracture distributions. Another approach used was the combination of anisotropic analysis with standard 3D reservoir seismic (Davis et al., 1993) to provide an integrated multicomponent interpretation. It is clear that numerical modelling technique is of great value and if used in conjuction with real data it can be a powerful tool. However, it may be necessary to design appropriate experiments to properly "tune in" the method to the distributions we are interested in according to the case we examine. This must be achieved using geophysical and engineering data, as well as knowledge of temporal variations of the anisotropic behaviour. Such experiments may help to give us an answer to the question about which wavefield characteristic indicates the reservoir properties, and how can we take full advantage of seismic anisotropy for reservoir characterisation.

In the last chapters of the thesis we examined the effect of the presence of fluid in wave propagation. Fluid flows in the rock pores and inside fractures. Here we assumed that the main path of the fluid is through fractures. Usually we have the presence of more than one fluid phases, but here for simplicity we used single phase fluid. An immediate effect of fluid is that it changes the elastic properties of a fracture. The elastic properties are directly affected by pore pressure changes. As a result the seismic signature of the fracture will change following the variations of pore pressure. That is the basic idea of time-lapse seismic data. Such data are used today to examine fluid flow and relevant pore pressure changes. We investigated such cases and we found out that S-waves and coda-waves are the

ones affected more. That means that the exploration techniques for such cases should be based more on S-wave records in order to be able to find even small changes in pore pressure. Such small changes can be very important in cases of CO_2 injection. Frequency also is a critical tool, because frequency shift is strong as pore pressure increases. Once more, data that cover wide frequency ranges are needed. There is also azimuthal dependence of the observed variations. S-waves are more affected parallel to the flow path while coda-waves normal to that path. To sum up, numerical time lapse seismic data can give a clear view of the fluid front, as we have shown, which is of great importance. However, fluid affects in a different manner each kind of wave. To limit the uncertainties of our findings we need the combination of P and S wave data. It is very important to extend the frequency range of the recorded data to include energy that is shifted in frequency due to scattering. The effect is expected to be different on P and S waves. Finally, our data should cover a variety of azimuths. Based on the results we will be able to determine the direction of flow and therefore the direction of fracturing. The combination of such data with numerical modelling results like the ones presented here, can give detailed information about the effect of fluid flow on seismic waves.

Time-lapse (or 4D) seismic data have proven their value in reservoir management. Time-lapse seismic is the comparison of 3D seismic surveys at two or more points in time. Successive time-lapse images give better understanding of the movement of fluid phases, the spacial changes in pore fluid saturation and in volumetric pressure. Also they help in the identification of by-passed oil and in-fill drilling opportunities. Finally, 4D data are used to constrain reservoir models, predict flow units and flow, and improve the performance of enhanced oil-recovery programs. One of the most successfull 4D projects to date was carried out in the Draugen field, offshore Norway for operator Shell and its partners. That involved a 1990 base survey and a 1998 monitor survey to obtain the results. The conclu-

sions were that a very clear time-lapse signal could be observed on the difference data set. Also time-lapse yielded information on the location of the waterfronts and seismic history matching of the dynamic reservoir model reduced uncertainties in the forecast for the production profile. Finally, time-lapse results impacted the location of a new production well within six months of the completion of the acquisition. This success story was the result of the combination of time-lapse data and a simulator that was updated by the real data. It is clear how important is the use of a simulating tool and how succesfull it can be when it is combined with real data. Another case where 4D time-lapse seismic played an important role is the Foinaven Active Reservoir Management Project. Foinaven, 190 km west of the Shetland Islands, is the first producing field in the deep water Atlantic Margin basin. It is a joint venture between BP, Shell and Schlumberger. One of the most obvious features in this study was the overall strengthening of amplitudes which was attributed to evolution of gas in the reservoir.

4D seismic modelling is also used as part of integrated tools for reservoir engineering, when it is combined with time-lapse seismic and production data. In such a study by Huang (2001) an initial static reservoir description is used for simulator model building. The simulator model is used to generate synthetic time-lapse seismic data which in turn are compared to measured time-lapse data in a model optimisation loop. Model optimisation is accomplished through numerical minimisation of an objective function formed from the errors between the data measured in the field and the ones predicted by the current model state. That is called seismic history matching. The potentials of 4D time-lapse seismic modelling was also shown by Olden et al. (2001) in a work that examined the effect of fluid flow and stress change in a hydrocarbon reservoir. They concluded that time-lapse seismic method could solve significant operational problems.

To finalise, the purpose of time-lapse seismic measurements is to be able to monitor the reservoir during production or improved oil recovery by detecting

induced changes in the seismic attributes. In time-lapse simulations, the aim is to develop a realistic reservoir model, which agrees with all available static and dynamic information from which we can make accurate future predictions about reservoir performance and plan further developments. Also time-lapse modelling is important because it helps us understand how changes in pore pressure and saturation, impact on the PP and PS waves.

10.3   Suggestions for future work

The results presented in this thesis form a part of a strategy to establish a direct link between pore pressure changes and variations on seismic signatures. The idea is to identify potentially diagnostic variations on seismic waves. The initial examination presented in this thesis shows some promising results for the further use of numerical modelling techniques to evaluate fracture and fluid flow properties. However, there are still steps forward to be taken to make the method more accurate and realistic. Starting from the numerical modelling technique, an important issue is the limitation of boundary reflections. We applied an absorbing boundary but still in some cases the synthetic seismograms showed reflected waves from the boundaries. A solution to that problem may be the implementation of the PML (Perfectly Matched Layer) technique in the boundaries of the finite difference grid.

So far in seismic modelling we considered 2-D cases. One of the priorities should be to extend the technique to 3-D, in order to be able to capture more efficiently fracture properties. Such a tool will give the ability to examine other effects of fractures, such as shear-wave splitting, that is not possible with a 2D model. Also, it would be possible to have a more detailed image of the fracture network, taking into account all the possible interactions between fractures.

The introduction of fluid flow in the fractured network gave us the chance to examine the effect of pore pressure changes on seismic signatures. That is an initial step towards a complete model that can produce accurate numerical time-lapse data. In the fluid flow modelling technique the assumption that the fluid has the same bulk modulus with the solid needs modification. Also further examination is needed for the relationship between pore pressure changes and the variations they cause to the elastic properties of the fractures. Detailed testing of this relationship is critical for the accuracy of the model. Finally the implementation of multi-phase fluid, will make the model correspond more closely to what happens in real earth, where we have cases of two-phase and even three-phase fluid (water, gas and oil).

To conclude, the 3D seismic modelling technique will also require the extension of the fluid flow model to 3D. The combination of both models can be used for forward modelling of heterogeneous reservoirs to identify the likely responses that might be observed. It will provide the ability to model fractured reservoirs where complex geometries result in unusual and often highly anisotropic flow regimes. It will make it possible to capture the complex spatial distributions and connectivity of fractured reservoirs. The models could be integrated with available well based fracture data by comparing the geometry of the intersected fractures with real core or image based fracture data. The ability to perform dynamic simulations through discrete fracture network models in conjunction with information of the pressure derivative can be used to help resolve such properties as fracture connectivity, lengthscale and permeability, which are the controlling factors of fluid flow in fractured reservoirs.

References

Achenbach, J., Gautesen, A., and McMaken, H., 1982, Ray Methods for Waves in Elastic Solids: Pitman, London.

Akaike, H., 1978, Bayesian analysis of the minimum aic procedure: Annals of the Institute of Statistical Mathematics, **30**, 9–14.

Aki, K., and Richards, P., 2002, Quantitative Seismology: University Science Books, Sausalito, California, second edition.

Aki, K., 1980, Scattering and attenuation of shear waves in the lithosphere: J. Geophys. Res., **85**, 6496–6504.

Alford, R., Kelly, K., and Boore, D., 1974, Accuracy of finite-difference modelling of the acoustic wave equation: Geophysics, **39**, 834–842.

Anderson, D., Minster, B., and Cole, D., 1974, The effect of oriented cracks on seismic velocities: J. Geophys. Res., **79**, 4011–4015.

Angerer, E., Crampin, S., Li, X.-Y., and Davis, T., 2002, Processing, modelling and predicting time-lapse effects of overpressured fluid-injection in a fractured reservoir: Geophys. J. Int., **149**, 267–280.

Atkinson, B. K., and Meredith, P. G., 1987, The theory of subcritical crack growth with applications to minerals and rocks, *in* Atkinson, B., Ed., Fracture Mechanics of Rock: Academic Press, 111–166.

267

Atkison, B. K., 1984, Subcritical crack growth in geological material: J. Geophys. Res., **89**, 4077–4114.

Balberg, I., Berkowitz, B., and Drachsler, G., 1991, Application of a percolation model to flow in fractured hard rock: J. Geophys. Res., **96**, 10015–10021.

Barker, J., 1988, A generalized radial-flow model for pumping tests in fractured rock: Water Resour. Res., **24**, 1796–1804.

Barley, B., Hudson, J., and Douglas, A., 1982, S to P scattering at the 650 km discontinuity: Geophys. J. R. astr. Soc., **69**, 159–172.

Barton, N., Bandis, S., and Bakhtar, K., 1985, Strength, deformation and conductivity coupling of rock joints: Int. J. Rock Mech. Min. Sci. and Geomech. Abstr., **22**, 121–140.

Bear, J., 1972, Dynamics of Fluid in Porous Media: American Elsevier Publishing Company, Dover, New York.

Bell, M., and Nur, A., 1978, Strength changes due to reservoir-induced pore pressure and stresses and application to lake oroville: J. Geophys. Res., **83**, 4469–4483.

Benites, R., Aki, K., and Yomogida, K., 1992, Multiple scattering of SH waves in 2-D media with many cavities: Pure and Appl. Geophys., **138**, 353–390.

Berenger, J., 1994, A perfectly matched layer for the absorption of electromagnetic waves: J. Comput. Phys., **114**, 185–200.

Berkowitz, B., and Balberg, I., 1992, Percolation approach to the problem of hydraulic conductivity in porous media: Transport in porous media, **9**, 275–286.

Biot, M., 1941, General theory of three-dimensional consolidation: J. Appl. Phys., **12**, 155–164.

Biot, M., 1956a, Theory of propagation of elastic waves in a fluid-saturated porous solid-I: Low frequency range: J. Acoust. Soc. Am., **28**, 168–178.

Biot, M., 1956b, Theory of propagation of elastic waves in a fluid-saturated porous solid-I: Higher frequency range: J. Acoust. Soc. Am., **28**, 179–191.

Bleistein, N., Cohen, J., and Stockwell, J., 2001, Mathematics of multidimensional seismic imaging, migration and inversion: Springer.

Bonnet, E., Bour, O., Odling, N., Davy, P., Main, I., Cowie, P., and Berkowitz, B., 2001, Scaling of fracture systems in geological media: Rev. Geophys., **39**, 347–383.

Boore, D., 1972, Finite-difference methods for seismic wave propagation in heterogeneous materials, *in* Alder, B., Fernbach, S., and Rotenberg, M., Eds., Methods in computational physics: Academic Press, 21–22.

Boore, D., 1981, Constitutive properties of faults with simulated gouge:, *in* Mechanical Behaviour of Crustal Rocks, AGU Gophys. Monogr. AGU, 24, 103–120.

Bourke, P., Durrance, E., Hodgkinson, D., and Heath, M., 1985, Fracture hydrology relevant to radionuclide transport: Report AERE-R 11414 of the Atomic Energy Research Establishment, Harwell.

Budiansky, B., and O'Connell, R., 1976, Elastic moduli of a cracked solid: Int. J. Solids Struct., **12**, 81–97.

Cacas, M., Ledoux, E., De Marsily, G., and Tillie, B., 1990, Modelling fracture flow with a stochastic discrete fracture network: calibration and validation 1: The flow model: Water Resour. Res., **26**, 479–489.

Carcione, J., Herman, G., and ten Kroode, A., 2002, Y2K Review Article - Seismic modeling: Geophysics, **67**, 1304–1325.

Carcione, J., 1994, The wave equation in generalized coordinates: Geophysics, **59**, 1911–1919.

Carmeliet, J., Delerne, K., Vandersteen, K., and Roels, S., 2004, Three-dimensional liquid transport in concrete cracks: Int. J. Numer. Anal. Meth. Geomech., **28**, 671–687.

Cerjan, C., Kosloff, D., Kosloff, R., and Reshef, M., 1985, A nonreflecting boundary condition for discrete acoustic and elastic wave equations: Geophysics, **50**, 705–708.

Chapman, C., and Drummond, R., 1982, Body-wave seismograms in inhomogeneous media using maslov asymptotic theory: Bull. Seism. Soc. Am., **72**, 277–317.

Charlaix, E., Guyon, E., and Roux, S., 1987, Permeability of a random array of fractures of widely varying apertures: Transport in Porous Media, **2**, 31–43.

Chernov, L., 1960, Wave Propagation in a Random Medium:.

Chew, W., and Liu, Q., 1996, Perfectly matched layers for elastodynamics: A new absorbing boundary condition: J. Comp. Acoust., **4**, no.4, 72–79.

Chew, W., and Weedon, W., 1994, A 3-D perfectly matched medium for modified Maxwell's equations with stretched coordinates: Microw. Opt. Technol. Lett., **7**, 599–604.

Clayton, R., and Engquist, B., 1977, Absorbing boundary conditions for acoustic and elastic wave equations: Bull. Seism. Soc. Am., **67**, 1529–1540.

Coates, R., and Schoenberg, M., 1995, Finite-difference modeling of faults and fractures: Geophysics, **60**, 1514–1526.

Cohen, J., Hagin, F., and Bleistein, N., 1986, Three-dimensional born inversion with an arbitrary reference: Geophysics, **51**, 1552–1558.

Collino, F., and Tsogka, C., 2001, Application of the perfectly matched absorbing layer model to the linear elastodynamic problem in anisotropic heterogeneous media: Geophysics, **66**, 294–307.

Crampin, S., and Bamford, D., 1977, Inversion of P-wave velocity anisotropy: Geophys.JR. astr. Soc., **49**, 123.

Crase, E., Pica, A., Noble, M., McDonald, J., and Tarantola, A., 1990, Robust elastic nonlinear inversion: application to real data: Geophysics, **55**, 527–538.

Darcy, H., 1956, Les fontaines publiques de la ville de dijon: Dalmont, Paris.

Davis, T., Shack, E., and Benson, R., 1993, Coalbed methane multicomponent 3D reservoir characterization study, Cedar Hill, San Juan Basin, New Mexico: Expanded Abstracts, **63rd SEG Meeting**, 175–180.

Eggleston, W., 1948, Summary of oil production from fractured rock reservoirs in California: Bull. Am. Assoc. Petrol. Geol., **2**, 1352–1355.

Emmermann, R., and Lauterjung, J., 1997, The German Continental Deep Drilling Program KTB: Overview and major results: Geophys. J. Int., **102**, 18179–18201.

Englman, R., Gur, Y., and Jaeger, Z., 1983, Fluid flow through a crack network in rocks: J. Applied Mechanics, **50**, 707–711.

Eshelby, J., 1957, The determination of the elastic field of an ellipsoidal inclusion and related problems: Proc. R. Soc. Lond. A., **241**, 376–396.

Fagin, S., 1992, Seismic modeling of geological structures: Applications to exploration problems: Geophysical Development Series, 2: Society of Exploration Geophysicists.

Foldy, L., 1945, The multiple scattering of waves. I. General theory of isotropic scattering by randomly distributed scatterers: Phys. Rev., **67**, 107–119.

Fornberg, B., 1987, The pseudospectral method: comparisons with finite differences for the elastic wave equation: Geophysics, **52**, 483–501.

Fornberg, B., 1988, The pseudospectral method: accurate representation of interfaces in elastic wave calculations: Geophysics, **53**, 625–637.

Frankel, A., and Clayton, R., 1984, A finite difference simulation of wave propagation in two-dimensional random media: Bull. Seismol. Soc.Am., **74**, 2167–2186.

Frankel, A., and Clayton, R., 1986, Finite difference simulations of seismic scattering: Implications for the propagation of short-period seismic waves in the crust and models of crustal heterogeneity: J. Geophys. Res., **91**, 6465–6489.

Frenje, L., and Juhlin, C., 2000, Scattering attenuation:2-D and 3-D finite difference simulations vs. theory: J. Appl. Geophys., **44**, 33–46.

Frenkel, J., 1944, On the theory of seismic and seismo-electric phenomena in moist soils: J. Phys. USSR, **8**, 230–241.

Garbin, H., and Knopoff, L., 1973, The compressional modulus of a material permeated by a random distribution of circular cracks: Q. appl Math., **30**, 453–464.

Garbin, H., and Knopoff, L., 1975, Elastic moduli of a medium with liquid-filled cracks: Q. appl Math., **33**, 301–303.

Gawith, D., and Gutteridge, P., 1996, Seismic validation of reservoir simulation using a shared earth model: Petroleum Geoscience, **2**, May.

Gazdag, J., 1981, Modeling the acoustic wave equation with transforms methods: Geophysics, **54**, 195–206.

Gottlieb, D., and Orszag, S., 1977, Numerical analysis of spectral methods: Soc. Ind. Appl. Math.

Greaves, R., and Fulp, T., 1987, Three dimensional seismic monitoring of an enhanced oil recovery process: Geophysics, **52**, 1175–1187.

Gueguen, Y., and Dienes, J., 1989, Transport properties of rocks from statistics and percolation: Mathematical Geology, **21**, 1–13.

Hastings, F., Schneider, J., and Broschat, S., 1996, Application of the perfectly matched layer (PML) absorbing boundary condition to elastic wave propagation: J. Acoust. Soc. Am., **100**, 3061–3069.

He, J., and Liu, Q., 1999, A nonuniform cylindrical FDTD algorithm with improved PML and quasi-PML absorbing boundary conditions: IEEE Trans. Geosci. Remote Sensing, **37**, 1066–1072.

Hentschel, H., and Proccacia, I., 1983, The infinite number of generalised dimensions of fractals and strange attractors: Physica D, **8**, 435–444.

Hill, R., 1963, Elastic properties of reinforced solids: some theoretical principles: J. Mech. Phys. Solids, **11**, 357–372.

Hirsche, W., Sedgwick, G., and Wang, Z., 1990, Seismic monitoring in enhanced oil recovery: Internat. Tech. Mtg., CIM Petr. Soc./Soc. Petr. Eng., Preprints, **2**, 72-1–72-13.

Hsieh, P., Neuman, S., Stiles, G., and Simpson, E., 1985, Field determination of the three-dimensional hydraulic conductivity tensor of anisotropic media: 2.Methodology and application to fractured rocks: Water Resour. Res., **21**, 1667–1676.

Hsu, C.-J., and Schoenberg, M., 1993, Elastic waves through a simulated fractured medium: Geophysics, pages 964–977.

Huang, X., 2001, Integrating time-lapse seismic with production data: A tool for reservoir engineering: The Leading Edge, **20**, 1148–1153.

Hudson, J., and Heritage, J., 1981, The use of the born approximation in seismic scattering problems: Geophys. J. R. astr. Soc., **66**, 221–240.

Hudson, J., and Knopoff, L., 1989, Predicting the overall properties of composite materials with small-scale inclusions or cracks: Pure and Appl. Geophys., **131**, 551–576.

Hudson, J., and La Pointe, P., 1980, Printed circuits for studying rock mass permeability: Int. J. Rock. Mech. Min. Sci. and Geomech. Abstr., **17**, 297–301.

Hudson, J., and Liu, E., 1999, Effective elastic properties of heavily faulted structures: Geophysics, **64**, 479–485.

Hudson, J., 1967, Scattering surface waves from a surface obstacle: Geophys. J. R. astr. Soc., **13**, 441–458.

Hudson, J., 1980, Overall properties of a cracked solid: Math. Proc. Camb. Phil. Soc., **88**, 371–384.

Hudson, J., 1980b, A parabolic equation for elastic waves: Wave Motion, **2**, 207–214.

Hudson, J., 1981, Wave speeds and attenuation of elastic waves in material containing cracks: Geophys. J. R. astr. Soc., **64**, 133–150.

Hudson, J., 1986, A higher order approximation to the wave propagation constants for a cracked solid: Geophys. J. R. astr. Soc., **87**, 265–274.

Hudson, J., 1988, Seismic wave propagation through material containing partially saturated cracks: Geophys. J. Int., **92**, 33–37.

Hudson, J., 1994, Overall properties of materials with inclusions or cavities: Geophys. J. Int., **117**, 555–561.

Israeli, M., and Orszag, S., 1981, Approximation of radiation boundary conditions: J. Comput. Phys., **41**, 115–135.

Jenkins, F., and White, H., 1957, Fundamentals of Optics: McGraw-Hill, New York.

Jenkins, S., Waite, M., and Bee, M., 1997, Time-lapse monitoring of the Duri steamflood: A pilot and case study: The Leading Edge, **16**, September.

Jing, L., and Stephansson, O., 1997, Network topology and homogenisation of fractured rocks, *in* Jamtveit, B., and Yardley, B., Eds., Fluid Flow and Transport in Rocks: Mechanisms and Effects: Chapman and Hall, 192–202.

Johnson, D., McKenny, R., Verbeek, J., and Almond, J., 1998, Time-lapse seismic analysis of fulmar field: The Leading Edge, **16**, October.

Johnson, O., 1984, Three-dimensional wave equation computations on vector computers: Proc. IEEE, **72**, 90–95.

Johnston, D., 1997, A tutorial on time-lapse seismic reservoir monitoring: J. Petr. Tech., **49**, 473–475.

Jones, M., Pringle, A., Fulton, I., and O'Neill, S., 1999, Discrete fracture network modelling applied to groundwater resourse exploitation in southwest Ireland, *in* McCaffrey, K., Lonergan, L., and Wilkingson, J., Eds., Fractures, Fluid Flow and Mineralization: Geological Society, Special Publications, 155, 83–103.

Kashanov, M., 1984, Elastic solids with many cracks and related problems: Adv. Appl. Mech., **30**.

Keller, J., 1964, Stochastic equations and wave propagation in random media: Proc. Symp. appl. Math., **16**, 145–170.

Kelner, S., Bouchon, M., and Coutant, O., 1999, Numerical simulation of the propagation of p waves in fractured media: Geophys. J. Int., **137**.

Knopoff, L., and Hudson, J., 1964, Scattering of elastic waves by small scale inhomogeneities: J. acoust. Soc. Am., **36**, 338–343.

Koehler, A., and Murphree, E., 1988, A comparison of Akaike and Scwarz criteria for selecting model order: Appl. Stats., **37**, 187–195.

Kosloff, D., and Baysal, E., 1982, Forward modeling by the fourier method: Geophysics, **47**, 1402–1412.

Kosloff, D., and Kessler, D., 1989, Seismic numerical modeling:, *in* Oceanographic and geophysical tomography, 249–312.

Kosloff, R., and Kosloff, D., 1986, Absorbing boundaries for wave propagation problems: J. Comp. Phys., **63**, 363–376.

Kosloff, D., Reshef, M., and Loewenthal, D., 1984, Elastic wave calculations by the fourier method: Bull. Seism. Soc. Am., **74**, 875–891.

Kuster, G., and Toksoz, M., 1974, Velocity and attenuation of seismic waves in two-phase media: Part 1. Theoretical formulations: Geophysics, **39**, 587–606.

Landers, T., and Clearbout, J., 1972, Numerical calculations of elastic waves in laterally inhomogeneous media: J. Geophys. Res., **77**, 1476–1482.

Leary, P., and Abercrombie, R., 1994, Frequency dependent crustal scattering and absorption at 5-160 hz from coda decay observed at 2-5 km depth: Geophys. Res. Lett., **21**, 971–974.

Leary, P., 1995a, The cause of frequency-dependent seismic absorption in crystal rock: Geophys. J. Int., **122**, 143–151.

—— 1995b, Quantifying crustal fracture heterogeneity by seismic scattering: Geophys. J. Int., **122**, 125–142.

Lee, C., Deng, B., and Chang, J., 1995, A continuum approach for estimating permeability in naturally fractured rocks: Engineering Geology, **39**, 71–85.

Leonard, T., and Hsu, J., 1999, Bayesian methods: Cambridge University Press, New York.

Lerche, I., and Petroy, D., 1986, Multiple scattering of seismic waves in fractured media: Velocity and effective attenuation of the coherent components of P waves and S waves: Pure and Appl. Geophys., **124**, 975–1019.

Lerche, I., 1985, Multiple scattering of seismic waves in fractured media: Cross-correlation as a probe of fracture intensity: Pure and Appl. Geophys., **123**, 503–542.

Liao, Z., Wong, H., Yang, B., and Yuan, Y., 1984, A transmitting boundary for transient wave analysis: Sci. Sinica A, **27**, 1063–1076.

Liu, Q., and Tao, J., 1997, The perfectly matched layer for acoustic waves in absorptive media: J. Acoust. Soc. Am., **102**, 2072–2082.

Liu, E., and Zhang, Z., 2001, Numerical study of elastic wave scattering by cracks or inclusions using the boundary integral equation method: J. Comp. Acoust., **9**, 1039–1054.

Liu, E., Crampin, S., and Queen, J., 1991, Fracture detection using crosshole surveys and reverse vertical seismic profiles at the Conoco Borehole Test Facility, Oklahoma: Geophys. J. Int., **107**, 449–463.

Liu, E., Hudson, J., and Pointer, T., 2000, Equivalent medium representation of fractured rock: J. Geophys. Res., **105**, 2981–3000.

Liu, E., Tod, S., and Li, X.-Y., 2002, Effects of stress and pore pressure on seismic anisotropy in cracked rock: GSEG Recorder, **September**, 93–98.

Liu, Q., 1997, An FDTD algorithm with perfectly matched layers for conductive media: Microw. Opt. Technol. Lett. , **14**, 134–137.

Liu, Q., 1999, Perfectly matched layers for elastic waves in cylindrical and spherical coordinates: J. Acoust. Soc. Am., **105**, 2075–2084.

Long, J., and Witherspoon, P., 1982, Porous media equivalents for networks of discontinuous fractures: Water Resour. Res, **18**, 645–658.

Long, J., and Witherspoon, P., 1985, The relatonship of the degree of interconnectivity to permeability in fracture networks: J. Geophys. Res., **90**, 3087–3098.

Long, J., 1996, Rock Fractures and Fluid Flow - Contemporary Understanding and Applications: National Academy Press, Washington.

Lynn, H., Simon, K., Bates, R., and Van Dok, R., 1996, Azimuthal anisotropy in P-wave 3-D (multiazimuth) data: Leading Edge, **15**, No.8, 923–928.

Lysmer, J., and Drake, L., 1972, A finite element method for seismology:, *in* Methods in computational physics II, Seismology Academic Press, 181–216.

Mahrer, K. D., 1986, An empirical study of instability and improvement of absorbing boundary conditions for elastic wave equation: Geophysics, **51**, 1499–1501.

Maillot, B., and Main, I., 1996, A lattice BGK model for the diffusion of pore fluid pressure, including anisotropy, heterogeneity, and gravity effects: Geophys. Res. Lett., **23**, 13–16.

Maillot, B., Nielsen, S., and Main, I., 1999, Numerical simulation of seismicity due to fluid injection in a brittle poroelastic medium: Geophys. J. Int., **139**, 263–272.

Main, I., Peacock, P., and Meredith, P., 1990, Scattering attenuation and the fractal geometry of fracture systems: Pure and Appl. Geophys., **133**, 283–304.

Malin, P., and Phinney, R., 1985, On the relative scattering of p and s waves: Geophys. J. R. astr. Soc., **80**, 603–618.

Massonnat, G., Umbhauer, F., and Odonne, F., 1994, The use of 3-D seismic in the understanding and monitoring of waterflooding in a naturally fractured gas reservoir: AAPG Bulletin, **78,no.7**, 1155.

Mavko, G., and Nur, A., 1978, The effect of nonelliptical cracks on the compressibility of rocks: J. Geophys. Res., **83**, 4459–4468.

Mavko, G., Mukerji, T., and Dvorkin, J., 1998, The rock physics handbook: Tools for seismic analysis in porous media: Cambridge University Press.

McCoy, J., 1977, A parabolic theory of stress-wave propagation through inhomogeneous linearly elastic media: J. Appl. Mech., **44**, 462–468.

McNaughton, D., 1953, Dilatency in migration and accumulation of oil in metamorphics rocks: Bull. Am. Assoc. Petrol. Geol., **37**, 217–231.

Menéndez, B., David, C., and Darot, M., 1999, A study of the crack network in thermally and mechanically cracked granite samples using confocal scanning laser microscopy: Phys. Chem. Earth A, **24**, 627–632.

Michie, U., 1996, The geological framework of the sellafield area and its relationship to hydrogeology: Quarterly J. Engineering Geology, **29**, S13–S27.

Mikhailenko, B., 1985, Numerical experiment in seismic investigation: J. Geophys., **58**, 101–124.

Mikhailenko, B., 2000, Seismic modeling by the spectral-finite difference method: Phys. Earth. Planet. Inter., **119**, 133–147.

Mueller, M., 1992, Using shear-waves to predict lateral variability in vertical fracture intensity: Geophysics, **12**, 29–35.

Muir, F., Dellinger, D., Etgen, J., and Nichols, D., 1992, Modeling elastic wave-fields across irregular boundaries: Geophysics, **57**, 1189–1193.

Narteau, C., in press, Formation and evolution of a population of strike-slip faults in a multiscale cellular automaton model: Geophys. J. Int.

Nelson, R., 1985, Geologic Analysis of Naturally Fractured Reservoirs: Gulf Pub. Co., Book Division, Houston.

Neretnieks, I., 1985, Transport in fractured rocks: Proceedings, Memories of the 17th Int. Cong. Of IAH, Int. Assoc Hydrogeolog, Tucson, Arizona, USA, **Vol.17**, 301–318.

Nielsen, S., and Tarantola, A., 1992, Numerical model of seismic rupture: J. Geophys. Res., **97**, 15291–15296.

Nielsen, S., Knopoff, L., and Tarantola, A., 1995, Model of earthquake recurrence: role of elastic wave radiation, relaxation of friction, and inhomogeneity: J. Geophys. Res., **100(B7)**, 12423–12430.

Nihei, K., and Myer, L., 2000, Natural fracture characterisation using passive seismic waves: Gas Tips.

Nihei, K., Nakagawa, S., and Myer, L., 2000, VSP fracture imaging with elastic reverse-time migration: VSP fracture imaging with elastic reverse-time migration:, 1784–1751.

Nihei, K., Nakagawa, S., Myer, L., and Majer, E., 2002, Finite difference modelling of seismic wave interactions with discrete, finite length fractures: 72th Annual Internat. Mtg., Soc. Expl. Geophys., Expanded Abstracts, 1963–1966.

Nishizawa, O., 1982, Seismic velocity anisotropy in a medium containing oriented cracks - transversely isotropic case: J. Phys. Earth, **30**, 331–347.

Nolte, D., Pyrak-Nolte, L., and Cook, N., 1989, The fractal geometry of flow paths in natural fractures in rock and the approach to percolation: PAGEOPH, **131**, 111–138.

Nur, A., and Byerlee, J., 1971, An exact effective stress law for elastic deformation of rock with fluids: J. Geophys. Res., **76**, 6414–6419.

Nur, A., 1971, Effects of stress on velocity anisotropy in rocks with cracks: J. Geophys. Res., **76**, 2022–2034.

O'Connell, R., and Budiansky, B., 1974, Seismic velocities in dry and saturated cracked solids: J. Geophys. Res., **79**, 5412–5426.

O'Connell, R., and Budiansky, B., 1977, Viscoelastic properties of fluid-saturated cracked solids: J. Geophys. Res., **82**, 5719–5735.

Oda, M., Hatsuyama, Y., and Ohnishi, Y., 1987, Numerical experiments on permeability tensor and its application to jointed granite at Stripa mine, Sweden: J. Geophys. Res., **92**, 8037–8048.

Oda, M., 1986, An equivalent continuum model for coupled stress and fluid flow analysis in joined rock masses: Water Resour. Res., **22**, 1845–1856.

Odling, N., 1997, Fluid flow in fractured rocks at shallow level in the Earth's crust: An overview, *in* Holness, M., Ed., Deformation-enhanced Fluid Transport in the Earth's Crust and Mantle: Chapman and Hall, 289–320.

Olden, P., Corbett, P., Westerman, R., Somerville, J., Smart, B., and Koutsabeloulis, N., 2001, Modeling combined fluid and stress change effects in the seismic response of a producing hydrocarbon reservoir: The Leading Edge, **20**, 1154–1163.

Ozdenvar, T., McMechan, G., and Chaney, P., 1996, Simulation of complete

seismic surveys for evaluation of experiment design and processing: Geophysics, **61**, 496–508.

Pekeris, C., 1947, Note on the scattering of radiation in an inhomogeneous medium: Phys. Rev., **71**, 268.

Pointer, T., Liu, E., and Hudson, J., 1998, Numerical modeling of seismic waves scattered by hydrofractures: application of the indirect boundary element method: Geophys. J. Int., **135**, 289–303.

Pollard, D. D., and Aydin, A., 1988, Progress in understanding jointing over the past century: GSA Bull., **100**, 1181–1204.

Press, W., Teukolsky, S., Vetterling, W., and Flannery, B., 1997, Numerical Recipies in Fortran 77: the Art of Scientific Computing (Vol.1 of Fortran Numerical Recipies: Cambridge University Press, Cambridge.

Pyrak-Nolte, L., Myer, L., and Cook, N., 1990, Transmission of seismic waves accross single natural fractures: J. Geophys. Res., **95**, 8617–8638.

Queen, J., and Rizer, W., 1990, An integrated study of seismic anisotropy and the natural fracture system at the conoco borehole test facility: J. Geophys. Res., **95**, 11255–11273.

Quian, Y., D'Humieres, D., and Lallemand, P., 1992, Lattice BGK model for Navier-Stokes equation: Europhys. Lett., **17**, 479–484.

Reshef, M., Kosloff, D., Edwards, M., and Hsiung, C., 1988, Three-dimensional elastic modeling by the fourier method: Geophysics, **53**, 1184–1193.

Reynolds, A. C., 1978, Boundary conditions for the numerical solution of wave propagation problems: Geophysics, **43**, 1099–1110.

Rice, J., and Cleary, M., 1976, Some basic stress diffusion solutions for fluid-saturated elastic porous media with compressible constituents: Rev. Geophys. Space Phys., **14**, 227–241.

Richards, P., and Menke, W., 1983, The apparent attenuation of a scattering medium: Bull. Seismol. Soc. Am., **73**, 1005–1022.

Ricker, N., 1977, Transient Waves in Visco-elastic Media: Elsevier, Amsterdam.

Ringdal, F., and Husebye, E., 1982, Application of arrays in the detection, location, and identification of seismic events: Bull. Seismol. Soc. Am., **72**, S201–S224.

Roth, M., and Korn, M., 1993, Single scattering theory versus numerical modelling in 2-D random media: Geophys. J. Int., **112**, 124–140.

Rueger, A., 1996, Variation of P-wave reflectivity with offset and azimuth in anisotropic media: SEG Annual Meeting Abstracts, **66**, 1810–1813.

Ryzhik, L., Papanicolaou, G., and Keller, J., 1996, Transport equations for elastic and other waves in random media: Wave Motion, **24**, 327–370.

Saenger, E., and Shapiro, S., 2002, Effective velocities in fractured media: a numerical study using the rotated staggered finite-difference grid: Geophysical Prospecting, **50**, 183–194.

Sahimi, M., 1987, Hydrodynamic dispersion near the percolation threshold: Scaling and probability densities: J. Phys. A. Math. Gen., **20**, L1293–L1298.

Sanderson, D., and Zhang, X., 1999, Critical stress localisation of flow associated with deformation of well-fractured rock masses, with implications for mineral deposits:, *in* Fractures, Fluid Flow and Mineralization Geological Society Special Publication, 155, 69–81.

Sato, H., 1982, Amplitude attenuation of impulsive plane waves in random media based on traveltime corrected mean wave formalism: J. Acoust. Soc. Am., **71**, 564–599.

Sayers, C., and Kachanov, M., 1995, Microcrack-induced elastic wave anisotropy of brittle rocks: J. Geophys. Res., **100**, 4149–4156.

Sayers, C., 1988, Inversion of ultrasonic wave velocity measurements to obtain the microcrack orientation distribution function in rocks: Ultrasonics, **26**, 73–77.

Schneider, W., 1978, Integral formulation for migration in two and three dimensions: Geophysics, **43**, 49–76.

Schoenberg, M., and Sayers, C., 1995, Seismic anisotropy of fractured rock: Geophysics, **60**, 204–211.

Schoenberg, M., 1980, Elastic wave behaviour across linear slip interfaces: J. Acoust. Soc. Am., **68**, 1516–1521.

Schoenberg, M., 2002, Time dependent anisotropy induced by pore pressure variation in fractured rock: J. Seismic Exploration, **11**, 83–105.

Scholz, C., 1990, The Mechanics of Earthquakes and Faulting: Cambridge University Press, Cambridge.

Shapiro, S., and Kneib, G., 1993, Seismic attenuation by scattering: theory and numerical results: Geophys. J. Int., **114**, 373–391.

Sheriff, R., and Geldart, L., 1980, Exploration Seismology: Cambridge University Press.

Sheriff, R., 1977, Limitations on resolution of seismic reflections and geologic detail derivable from them:, *in* Seismic Stratigraphy - Applications to Hydrocarbon Exploration AAPG Memoir 26, Tulsa: American Association of Petroleum Geologists, 3–14.

Smith, L., and Schwartz, F., 1984, An analysis of the influence of fracture geometry on mass transport in fractured media: Water Resour. Res., **20**, 1241–1252.

Smith, J., 1951, The Cretaceous limestone producing areas of the Mara and Maracaibo district, Venezuela: Proc. Thirld World Petrol Cong., 56–71.

Smith, W. D., 1974, A nonreflecting plane wave boundary for wave propagation problems: J. Comp. Phys., **15**, 492–503.

Smith, G., 1985, Numerical solution of partial differential equations: Finite difference methods: Clarendon Press.

Sochacki, J., Kubichek, R., George, J., Fletcher, W., and Smithson, S., 1987, Absorbing boundary conditions and surface waves: Geophysics, **52**, 60–71.

Sonneland, L., Signer, C., Veire, H., and Pedersen, L., 1997, Four-dimensional seismic on Gullfaks: J. Petr. Tech., **49**, 497.

Sorbie, K., and McDougall, S., 1998, The fundamentals of single and multiphase flow through porous media: Course presented at the Department of Petroleum Engineering, Heriot-Watt University.

Sornette, D., Miltenberger, P., and Vanneste, C., 1994, Statistical physics of fault patterns self-organized by repeated earthquakes: Pure and Appl. Geophys., **142**, 491–527.

Stacey, R., 1988, Improved transparent boundary formulations for the elastic-wave equation: Bull. Seism. Soc. Am., **78**, 2089–2097.

Stauffer, D., 1985, Introduction to Percolation Theory: Taylor and Francis, London.

Stearns, D., and Friedman, M., 1972, Reservoirs in fractured rock in stratigraphic oil and gas fields classification, exploration methods and case histories: Am. Assoc. Petroleum Geologists, **Mem. 16**, 82–106.

Terzagi, K., 1943, Theoretical soil mechanics: Wiley.

Tessmer, E., and Kosloff, D., 1994, 3-D elastic modeling with surface topography by a Chebychev spectral method: Geophysics, **59**, 464–473.

VanBaren, G., Mulder, W., and Herman, G., 2001, Finite-difference modeling of scalar-wave propagation in cracked media: Geophysics, **66**, 267–276.

Vidale, J., Helmberger, D., and Clayton, R., 1985, Finite-difference seismograms for SH waves: Bull. Seis. Soc .Am., **75**, 1765–1782.

Waite, M., and Sigit, R., 1997, Seismic monitoring of the Duri steamflood: Application to reservoir management: The Leading Edge, **16**, September.

Walsh, J., and Grosenbaugh, M., 1979, A new model for analysing the effect of fractures on compressibility: J. Geophys. Res., **84**, 3532–3536.

Walsh, J., 1965, The effect of cracks on the compressibility of rock: J. Geophys. Res., **70**, 381–389.

Wesley, J., 1965, Diffusion of seismic energy in the near range: J. Geophys. Res., **70**, 5099–5106.

Wu, R.-S., and Aki, K., 1985, Scattering characteristics of elastic waves by an elastic heterogeneity: Geophysics, **50**, 582–589.

Wu, H., and Lees, J., 1997, Boundary conditions on a finite grid: Applications with pseudospectral wave propagation: Geophysics, **62**, 1544–1557.

Wu, C., Harris, J., and Nihei, K., 2002, 2d finite-difference seismic modelling of an open fluid-filled fracture: comparison of thin-layer and linear-slip models: 72th Annual Internat. Mtg., Soc. Expl. Geophys., Expanded Abstracts, 1959–1962.

Wu, R.-S., 1982, Attenuation of short period seismic waves due to scattering: Geophys. Res. Lett., **9**, 9–12.

Wu, R.-S., 1994, Wide-angle elastic wave one-way propagation in heterogeneous media and an elastic wave complex-screen method: J. Geophys. Res., **99**, 751–766.

Yamashita, T., 1990, Attenuation and dispersion of SH waves due to scattering by randomly distributed cracks: PAGEOPH, **132**, 545–568.

Yielding, G., Walsh, J., and Watterson, J., 1992, The prediction of small scale faulting in reservoirs: First Break, **10**, 449–460.

Yomogida, K., and Benites, R., 2002, Scattering of seismic waves by cracks with the Boundary Integral Method: Pure and Appl. Geophys., **159**, 1771–1789.

Yomogida, K., Benites, R., Roberts, P., and Fehler, M., 1997, Scattering of elastic waves in 2-D composite media II. waveforms and spectra: Phys. Earth Planet. Inter., **104**, 175–192.

Zeng, Y., He, J., and Liu, Q., 2001, The application of the perfectly matched layer in numerical modeling of wave propagation in poroelastic media: Geophysics, **66**, 1258–1266.

Zhang, X., and Sanderson, D., 1994, Fractal structure and deformation of fractured rock masses:, *in* Fractal and Dynamic Systems in Geoscience Spring-Verlag, 37–52.

Zhang, X., and Sanderson, D., 1995, Anisotropic features of geometry and permeability in fractured rock masses: Engineering Geology, **40**, 65–75.

Zhang, X., and Sanderson, D., 1996, Numerical modelling of the effects of fault slip on fluid flow around extensional faults: J. Struct. Geol., **18**, 109–119.

Zhang, X., and Sanderson, D., 1998, Numerical study of critical behaviour of deformation and permeability of fractured rock masses: Marine and Petrol. Geol., **15**, 535–548.

Zhang, X., and Sanderson, D., 2001, Evaluation of instability in fractured rock masses using numerical analysis methods: the effects of fracture geometry and loading direction: J. Geophys. Res., **106**, 26689–26706.

Zhang, X., Sanderson, D., Harkness, R., and Last, N., 1996, Evaluation of the 2-D permeability tensor for fractured rock masses: Int. J. Mech. Min. Sci. and Geomech. Abstr., **33**, 17–37.

Zhang, X., Powrie, W., Harkness, R., and Wang, S., 1999b, Estimation of permeability for the rock mass around the shiplocks of the Three Gorges Project, China: Int. J. Mech. Min. Sci. and Geomech. Abstr., **36**, 381–397.

APPENDIX A

Effects of fracture tips

An important parameter in the accurate modelling of natural fractured rocks is the realistic implementation of the effects of fractures in wave propagation. The main issue is the realistic representation of the finite extent of a fracture, and especially the two fracture tips. To exhibit the end of the fracture at both tips, we should have no displacement outside those points, thus the compliance tensor Z should be 0. A way of expressing the change in the compliance is to keep the compliance constant along the fracture and drop to 0 at the crack tips. However, the sudden drop of the value is not very realistic, and there is no similar case in natural systems that demonstrates extreme changes of values. We believe that it is more realistic to represent the changes in Z as a gradual reduction towards 0 at the fracture tips. Following Kashanov (1984) the compliance at each point of the fracture is given by:

$$Z = Z_{max}[1 - (x/l)^2]^{1/2}, \qquad (A.1)$$

where Z_{max} is the maximum value of the compliance in the centre of the fracture, l is half the length of the fracture and x is the x-coordinate of the position of a point in the fracture. The coordinates of the right and the left fracture tips are $+l$ and $-l$, respectively. From Equation A.1, for the centre of the fracture ($x = 0$) the compliance is $Z = Z_{max}$, whilst for the fracture tips ($x = \pm l$) the compliance is $Z = 0$. So the value of compliance is maximum in the centre of the fracture

and reduces gradually following a hyperbolic function until it reaches 0 in both fracture tips. As we can see from Equation A.1 the rate of reduction depends on the size $2l$ of the fracture, so the larger the fracture, the more gradually the compliance reduces.

In Appendix A we described the implementation of fractures in the finite difference grid and the calculation of the effective compliance of a fractured medium. Equation 2.28 calculates the excess compliance tensor, that expresses the fracture influence. The excess compliance tensor is estimated for each of the fractured grid cells of the medium, thus the value of the compliance Z should remain constant inside each grid cell. To calculate the compliance for each of the grid cells, from Equation A.1 we find the values of the compliance for the two nodes of each cell, and take the average of the two values as the effective value of the compliance throughout the cell. That is illustrated in Figure A.1, where the curve represents the value of the compliance following Equation A.1, and the stepped line is the average value of the compliance we use for each grid cell. In the case where a grid cell is intersected by multiple fractures (or parts of fractures) the compliance is taken to be the average value of the compliances due to each of the fractures independently.

To understand the effect of the fracture tips on the wavefield, we model the case of a single fracture in which, in the first case, the compliance remains constant throughout the fracture and drops to 0 at the tips, and, in the second case, the compliance reduces following our implementation. The model we use is presented in FigureA.2.

For the two cases we compare the wavelets of a number of traces and the results are presented in Figure A.3. The wavelets presented in Figure A.3 do not include direct waves, because they are not affected by the fracture tips, and so are identical. Also, the amplitude of the wavelets is normalised between the several traces.

However, the relative amplitude between the wavelets for each individual trace remains accurate. From the comparison between the wavelets, we first observe that there is a time difference between the SS-waves when we have constant compliance and when the compliances reduce gradually, with SS-waves of the latter case being slower. That may be due to the sensitivity of S-waves in changes of anisotropy. By changing the compliance from constant to variable, we effectively change anisotropy, and that is only visible in the SS-wavelets. However, when
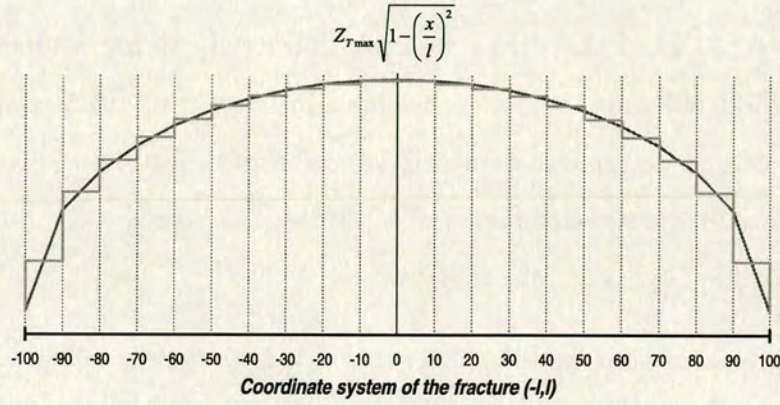
$$Z_{T\max}\sqrt{1-\left(\frac{x}{l}\right)^2}$$

-100 -90 -80 -70 -60 -50 -40 -30 -20 -10 0 10 20 30 40 50 60 70 80 90 100
Coordinate system of the fracture (-l,l)

Figure A.1: Schematic representation of the reduction of the value of compliance Z along a fracture. The red line represents the value of compliance following Equation A.1 by Kachanov (1984). The green line represents the way we approximate that function in our implementation.
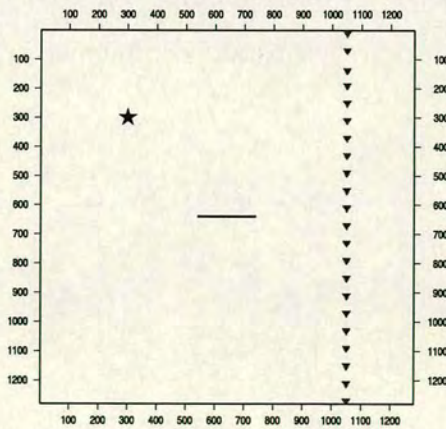
Figure A.2: Model used to examine the effect of the fracture tips on the wavefield

we observe the wavelets from traces 100 and 120 we see that the time difference in the SS-waves disappears. The waves observed at those receivers come from waves diffracted from the crack tips and from waves refracted at the fracture, in contrast with the rest of the receivers, where we have diffracted and reflected waves. Also, we can observe variations in the amplitude. In traces 20, 40, and 60, where the receivers are above the fracture, so we have reflected and diffracted waves, the amplitude of the waves when the compliance is constant is higher than the amplitude when the compliance follows our implementation. On the other hand, in trace 80, when the waves are only diffracted, we have opposite results. Finally, in traces 100 and 120, where we have refracted and diffracted waves, the amplitudes seem to be almost identical. We see that reflection and refraction are decisive factors in the wavelet pattern. More research needs to be done on those topics to examine how they affect the waves.

Another parameter that we have not examined is the effect of the length of the fracture. From Equation A.1 we can see that if we have a fracture of short length l then the reduction of the compliance would be severe, whilst when the fracture is very large we will have a very smooth reduction that can approximate the case of the constant compliance throughout the fracture. That has to be tested by modelling various sizes of fractures and the respective wavelets, to find out at what point the approximation of constant compliance is satisfactory.
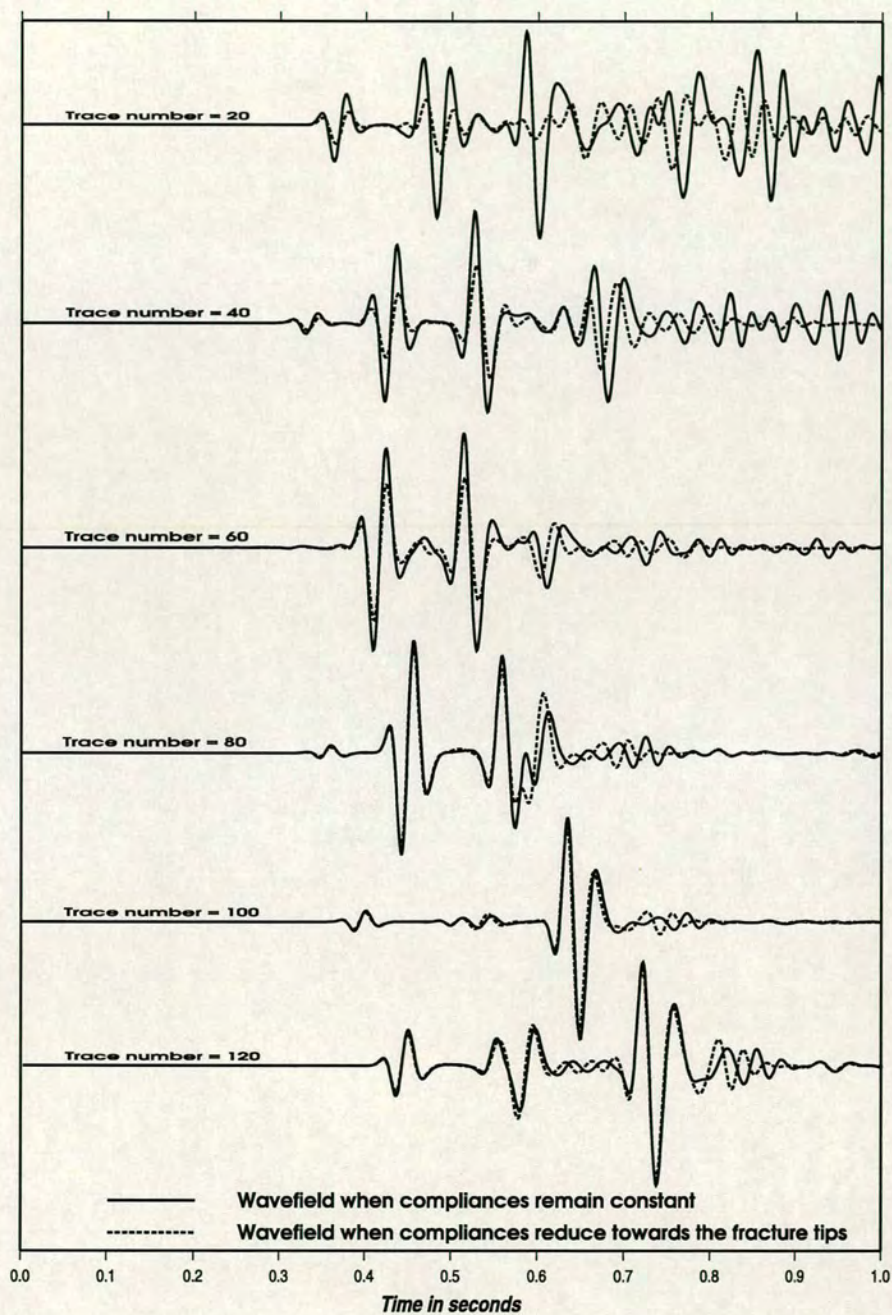
Figure A.3: Comparison of the wavefields generated by two different implementations of the fracture compliance. Solid-line wavelets represent the case of a constant compliance that drops to 0 at the fracture tips, while dotted-line wavelets represent our implementation, based on Kachanov's (1984) concept, where compliance reduces gradually. The trace numbers correspond to depths 200, 400, 600, 800, 1000 and 1200 m.

Appendix B

Fracture evolution

At the smallest scale, the dynamical system is determined by a time dependent stochastic process with two states of fracturing (active and stable). In the active state, the fracture segment interacts with adjacent active segments, while in the stable state, the fracture segment does not interact with adjacent active segments. At larger scale, the state of fracturing is determined by purely geometric rules of fracture interaction based on fracture mechanics. In addition to these short range interactions, a redistribution mechanism in the neighbourhood of active fractures ensures long range interactions. Thus, non-linear feedback processes are incorporated in the fracture growth mechanism. It is possible to distinguish different phases in the evolution of fault patterns, which are the nucleation, growth, coalescence and interaction, concentration, and branching phases.

In the initial stages of the nucleation phase we have isolated active fracture segments. Since fracture interaction is negligible, these fracture nuclei have a random homogeneous spatial distribution, and their number increases at a constant rate. The strain rates remain virtually uniform and only small fluctuations can be distinguished in the neighbourhood of the fracture nucleus. Nevertheless, they favour the accumulation and the concentration of the strain rates on the fracture segment and at the fracture tips while they impede it on each side of the fault.

While the nucleation process continues, the strain rates are primarily concentrated at the process zones of the fracture nucleus. In these process zones, the intensity of the micro-fracturing process increases and fractures at all scales may organise themselves more efficiently. During the growth phase, the fracture tips move faster as the fracture gets bigger. During the growth phase, new fracture segments always interact positively with fracture nucleus to form larger faults. The new fractures have an orientation close to the main direction.

When the nucleation process is almost nonexistent and as the growth process continues, the ratio between the length of the fractures and their distance increases and the fractures begin to interact. There are three types of interaction: (i) Overlap of process zones when two fractures propagate towards the same zone, (ii) overlapping shadow zones when two parallel fractures propagate simultaneously, and (iii) overlap of shadow and process zones in any step-like discontinuity. These interactions can efficiently modify the geometry of the fracture network and new fracture patterns emerge. The fracture population will have a dense composition of fractures with different lengths. Fractures may coalesce and form bend patterns while other fractures may produce en-echelon patterns.

From the hierarchy established at the end of the interaction phase, the fracture network evolves toward a stable system based on the coexistence of major faults. During this period within the evolution of the fracture network, major fractures in steady interaction increase their strain rates by removing the strain rates from minor fractures. The active fracture network becomes less compact. Major fractures of different lengths emerge with increasing simpler geometry. Branching and step-overs disappear but bends between regular segments may persist. The strain rates remain concentrated on the major fractures. During this concentration phase, the longest fractures have larger strain rates. Along these fractures, the strain rates are more uniform and may vary according to the alignment of the fracture segment with respect to the main direction and structural irregularities.

The fracture network may also evolve differently under a higher tectonic loading. For a larger amplitude of tectonic loading the nucleation phase activates a larger number of fracture nuclei. From this multitude of fracture nuclei, the growth phase initially produces a denser fracture network. The larger number of fractures and the higher amplitude of the tectonic loading results in a more complex distribution of the strain rates and a more irregular fracture geometry. That phase of evolution is called the branching phase.

Multi-phase fluid flow in porous media

In Chapter 8 we discussed the main concepts of single phase fluid flow. Also we introduced a numerical simulation technique for single phase fluid flow in a fractured network. The simulation can be extended to include multi phase fluid flow, but this is not in the scope of this thesis. In this Appendix, we will present the fundamental theoretical concepts for multi phase fluid flow.

C.1   Fluid flow in fractured systems

The basic features that describe single phase fluid flow, are also valid for each phase in multi phase fluid flow. Those features are described in section 8.4. In addition, when we have multiple fluid phases, we have to describe the interaction between the phases.

The interaction between fluids during fluid flow in a fractured system is described by miscible displacement. Whereas oil and water are immiscible fluids (i.e. they do not mix and are separated by an interface), some fluids are fully miscible (i.e. they mix freely in all proportions). When a gas (or other fluid) is injected into an oil reservoir and the fluids are miscible, this is referred to as a

miscible displacement. When a miscible solvent (s) displaces an oil (o), the pressure in each and the local pressure gradients are the same (there is no capillary pressure since there is no interface). The mixing between the solvent and the oil can occur locally by dispersion and by fingering. The displacement is described by a generalised convection-dispersion equation where the mixing viscosity, $\eta(c)$ is a function of the concentration of the solvent, c (or oil). Often, the solvent viscosity is below that of the oil (i.e. $\eta_s < \eta_o$) which tend to cause an instability to develop in the displacement known as viscous fingering.

C.2   Multi phase rock/fluid properties

In the case of multi phase flow some of the properties that describe the flow are the same but they have different meaning compared to the single phase and there are also some new properties. We will describe in this section saturation, residual saturation, relative permeability, capillary pressure, mobility, and the fractional flow.

The saturation refers to a single phase (oil, water, gas) and is the fraction of the pore space that it occupies (not of the total rock and the pore space volume). The symbols we use are S_w, S_o, and S_g respectively for oil, water, and gas. For a certain medium we have $S_w + S_o + S_g = 1$. The residual saturation of a phase is the amount of that phase (fraction of pore space) that is trapped or is irreducible; e.g. after many pore volumes of water displace oil from a rock, we reach residual oil saturation, S_{or}. At the residual saturation the corresponding relative permeability of that phase is zero. Typically, in a moderately water wet sandstone, $S_{or} \sim 0.2$-0.35. The amount of trapped or residual phase depends on the permeability and wettability of the rock.

The relative permeability is a quantity that describes the amount of impairment

to flow of one phase on another. It is defined in the two phase Darcy law and depends on the saturation of the phase. The wettability is a measure of the preference of the rock surface to be wetted by a particular phase. The wettability of a porous medium determines the form of the relative permeabilities and capillary pressure curves. The usual cases are water wet, oil wet and intermediate wet systems. Where water is the preferential wetting phase we refer to a water wet system. Water occupies the smaller pores and forms a film over all of the rock surface, even in the pores containing oil. Where oil is the preferential wetting phase we refer to an oil wet system. Oil occupies the smaller pores and forms a film over all of the rock surface - even in the pores containing water. Finally, an intermediate wet formation is where some degree of water wetness and oil wetness is shown by the same rock. Some different types of intermediately wet system have been identified known as mixed wet and fractionally wet.

The difference in pressure between two (immiscible) phases is the capillary pressure. It is defined as the non wetting phase pressure minus the wetting phase pressure. It depends on the saturation and for two faces the capillary pressure is, $P_c(S_w) = P_o - P_w$ (for a water wet porous medium). A typical capillary pressure and relative permeability curve is shown in Figure C.1. This example is for a moderately water-wet system. In the figure residual saturations are evident (S_{wc} and S_{or}).

The mobility of a phase (e.g. λ_w or λ_o) is defined as the ratio of the effective permeability of that phase (e.g. k_w=k $\cdot k_{rw}$; k_o=k $\cdot k_{ro}$) divided by the viscosity of that phase ($\lambda_w = (k \cdot k_{rw})/\mu_w$; $\lambda_o = (k \cdot k_{ro})/\mu_o$). Finally, the fractional flow of a phase is the volumetric flow rate of the phase under a given pressure gradient, in the presence of another phase. The symbols for water and oil fractional flow are f_w and f_o and they depend on the phase saturation, S_w: $f_w = Q_w/Q$; $f_o = Q_o/Q$. The fractional flows play a central part in Buckley-Leverett theory of linear displacement which starts from the conservation equation: $\partial S_w/\partial t = -\partial f_w/\partial x$;
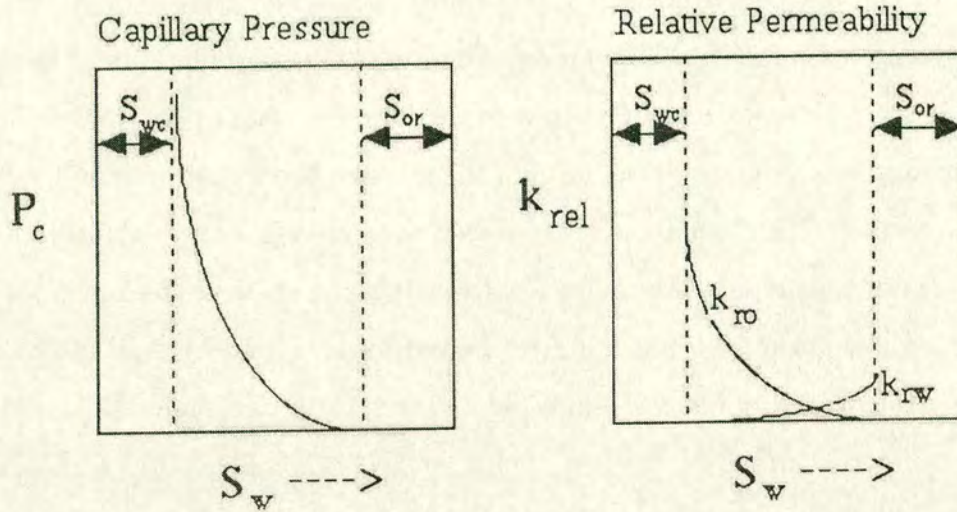
Figure C.1: Schematic figures for capillary pressure (left figure) and relative permeability (right figure) for a water wet system.

$$\partial S_o / \partial t = -\partial f_o / \partial x.$$

C.3 Differential equations for two phase fluid flow

In reservoir simulations, we are primarily concerned with modelling the displacement, within a porous medium, of oil by either water or gas. While the displacing fluid may be immiscible with the fluid being displaced, within the porous medium simultaneous flow of the two fluids takes place. The fluid that wets the porous medium is the wetting phase (and we use the subscript w) and the other is the nonwetting phase fluid (and we use the subscript n). In a water-oil system, water is most often the wetting phase; in an oil-gas system, oil is the wetting phase.

Because of surface tension and the curvature of the interfaces between the two fluids within the small pores, the pressure in the nonwetting fluid is higher than the pressure in the wetting fluid. The difference between these two pressures is

the capillary pressure, P_c:

$$P_c = P_n - P_w. \tag{C.1}$$

We accept, as an empirical fact, that the capillary pressure is a unique function of saturation:

$$P_n - P_w = P_c(S_w). \tag{C.2}$$

C.3.1 Darcy's law in two phase flow

Darcy's law is extended to multiphase flow by including the phase pressures and describe how they are involved in causing each fluid to flow. The superficial velocities for the nonwetting (V_n) and wetting fluids (V_w) are:

$$V_n = -\frac{K_n}{\eta_n}(\nabla P_n - \rho_n g \nabla D), \tag{C.3}$$

$$V_w = -\frac{K_w}{\eta_w}(\nabla P_w - \rho_w g \nabla D), \tag{C.4}$$

where η_n and η_w are the respective viscosities, and ρ_n and ρ_w the respective densities. K_n and K_w are the effective permeabilities for flow for each of the two fluids. Because the simultaneous flow of the two fluids causes each to interfere with the flow of the other, these effective permeabilities must be less than or equal to the single-fluid permeability, K, of the medium. Relative permeabilities are therefore defined by:

$$k_{rn} = \frac{K_n}{K}, \tag{C.5}$$

$$k_{rw} = \frac{K_w}{K}. \tag{C.6}$$

Again we accept as an empirical fact that these relative permeabilities are unique functions of the saturation. Typical relative permeability curves are shown in Figure C.2.

We rewrite Darcy's law now, using the relative permeabilities:

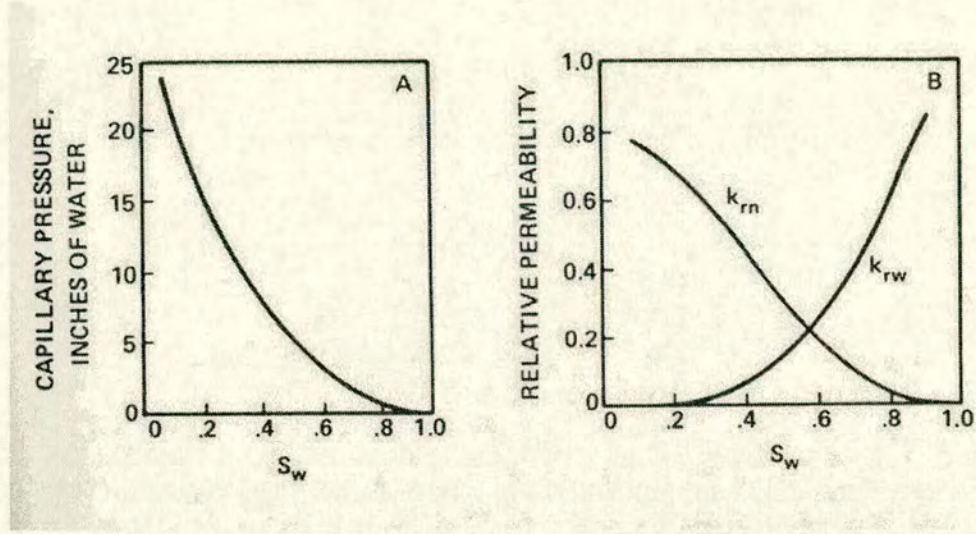$$V_n = -\frac{K k_{rn}}{\mu_n}(\nabla P_n - \rho_n g \nabla D), \tag{C.7}$$

Figure C.2: Typical curves for two-phase data. A.Capillary pressure. B.Relative permeabilities for the wetting and non-wetting phases (after Sorbie and McDougall, 1998)

$$V_w = -\frac{Kk_{rw}}{\mu_w}(\nabla P_w - \rho_w g \nabla D),$$ (C.8)

C.3.2   Conservation of each phase

Except for the accumulation term, the same considerations that were applied in the single phase flow are also applied here to derive a differential equation of flow for each phase. To obtain the accumulation term, we note that the amount of mass of each phase in a differential volume is the product of the volume of the differential element, the porosity, the density of the phase, and the saturation of the phase. The rates of accumulation for the 1-D case are for the nonwetting phase $A\frac{\partial(\phi\rho_n S_n)}{\partial t}\Delta x$ and for the wetting phase $A\frac{\partial(\phi\rho_w S_w)}{\partial t}\Delta x$. Hence the continuity equation for two phase flow is:

$$-\nabla \cdot (\alpha\rho_n V_n) + \alpha q_n = \alpha\frac{\partial(\phi\rho_n S_n)}{\partial t},$$ (C.9)

$$-\nabla \cdot (\alpha\rho_w V_w) + \alpha q_w = \alpha\frac{\partial(\phi\rho_w S_w)}{\partial t},$$ (C.10)

where α is a geometric factor.

C.3.3   The differential equations for two-phase flow

By combining Equations (C.7) with (C.9) and Equations. (C.8) with (C.10), we a set of simultaneous differential equations that describe two-phase flow:

$$\nabla \cdot \left[\frac{\alpha \rho_n K k_{rn}}{\mu_n}(\nabla P_n - \rho_n g \nabla D)\right] + \alpha q_n = \alpha \frac{\partial(\phi \rho_n S_n)}{\partial t}, \qquad \text{(C.11)}$$

$$\nabla \cdot \left[\frac{\alpha \rho_w K k_{rw}}{\mu_w}(\nabla P_w - \rho_w g \nabla D)\right] + \alpha q_w = \alpha \frac{\partial(\phi \rho_w S_w)}{\partial t}. \qquad \text{(C.12)}$$

These equations are extremely general in their applicability, including the effects of compressibility, capillary pressure, and the relative permeability, as well as spatial variations of the absolute permeability and the porosity.

C.3.4   Pressure differential equation

Equations (C.11) and (C.12) are not the only ones that describe the two phase flow problems. There are alternative pairs of equations that concentrate on different properties of the medium. The first of this pair is a pressure equation that primarily describes how pressure varies with time and position. The primary objective in deriving the pressure differential equation is to eliminate the time derivatives of saturation. To do this, we begin by expanding the time derivatives of Equations (C.9) and (C.10) to obtain:

$$-\nabla \cdot (\alpha \rho_n V_n) + \alpha q_n = \alpha[\rho_n S_n \partial \phi \partial t + \phi S_n \frac{d\rho_n}{dP_n}\frac{\partial P_n}{\partial t} + \phi \rho_n \frac{\partial S_n}{\partial t}], \qquad \text{(C.13)}$$

$$-\nabla \cdot (\alpha \rho_w V_w) + \alpha q_w = \alpha[\rho_w S_w \partial \phi \partial t + \phi S_w \frac{d\rho_w}{dP_w}\frac{\partial P_w}{\partial t} + \phi \rho_w \frac{\partial S_w}{\partial t}]. \qquad \text{(C.14)}$$

We divide Equation (C.13) by $\alpha \rho_n$ and Equation (C.14) by $\alpha \rho_w$, and add the resulting equations. Then using the fact that $S_n + S_w = 1$, we obtain:

$$-(1/\alpha \rho_n)\nabla \cdot (\alpha \rho_n V_n) - (1/\alpha \rho_w)\nabla \cdot (\alpha \rho_w V_w) + Q_t = \frac{\partial \phi}{\partial t} + \phi S_n c_n \frac{\partial P_n}{\partial t} + \phi S_w c_w \frac{\partial P_w}{\partial t},$$

$$\text{(C.15)}$$

where:

$$Q_t = (q_n/\rho_n) + (q_w/\rho_w), \tag{C.16}$$

is the total volumetric injection rate, and

$$c_n = \frac{1}{\rho_n}\frac{d\rho_n}{dP_n} \tag{C.17}$$

$$c_w = \frac{1}{\rho_w}\frac{d\rho_w}{dP_w} \tag{C.18}$$

are fluid compressibilities, analogous to the single-phase compressibility. Note that time derivatives of saturation are absent from Equation (C.15). We can also use an average pressure defined by:

$$P_{avg} = (P_n + P_w)/2, \tag{C.19}$$

so the individual phase pressures are defined in terms of the average pressure and the capillary pressure by:

$$P_n = P_{avg} + \frac{1}{2}P_c, \tag{C.20}$$

$$P_w = P_{avg} - \frac{1}{2}P_c. \tag{C.21}$$

We also use the phase mobilities, λ_n and λ_w that are given by:

$$\lambda_n = Kk_{rn}/\eta_n, \tag{C.22}$$

$$\lambda_w = Kk_{rw}/\eta_w. \tag{C.23}$$

P_c is usually quite small relative to P_{avg}. We can also ignore the variation of $\alpha\rho_n$ and $\alpha\rho_w$ with position. Then Equation (C.15) can be simplified to:

$$\nabla \cdot (\lambda_n + \lambda_w)\nabla P_{avg} + Q_t \approx \phi c_t \frac{\partial P_{avg}}{\partial t}. \tag{C.24}$$

where c_t is a total compressibility defined by:

$$c_t = (1/\phi)(d\phi/dP_{avg}) + (S_n c_n + S_w c_w). \tag{C.25}$$

C.3.5 Saturation differential equation

The other alternative pair of equations is the saturation differential equation. In deriving the saturation equation we can focus on either the wetting or the non-wetting phase. Here we choose, quite arbitrarily, the wetting phase. Assuming that the solution to Equation (C.24) is known, P_w may be obtained from Equation (C.21) and then V_w obtained from Equation (C.8). Equation (C.10), which involves V_w, may then be used for the saturation equation.

However, a more significant saturation equation can be obtained, one that involves the total velocity ($V_t = V_n + V_w$). To this end, we first obtain the wetting phase velocity in terms of the total velocity. From Equations (C.1), (C.7), (C.8), (C.22), and (C.23), we get:

$$\nabla P_c = \nabla P_n - \nabla P_w, \tag{C.26}$$

$$V_n = -\lambda_n(\nabla P_n - \rho_n g \nabla D), \tag{C.27}$$

$$V_w = -\lambda_w(\nabla P_w - \rho_w g \nabla D). \tag{C.28}$$

Combination of the these three equations and rearrangement yields:

$$\lambda_n \lambda_w \nabla P_c = -\lambda_w V_n + \lambda_n V_w + \lambda_n \lambda_w (\rho_n - \rho w) g \nabla D. \tag{C.29}$$

We define a total velocity by:

$$V_t = Vn + V_w. \tag{C.30}$$

Using Equation (C.30) to eliminate V_n, we obtain:

$$(\lambda_n + \lambda_w)V_w = \lambda_w V_t + \lambda_n \lambda_w [\nabla P_c + (\rho_w - \rho_n)g \nabla D]. \tag{C.31}$$

Let us define the following functions of saturation:

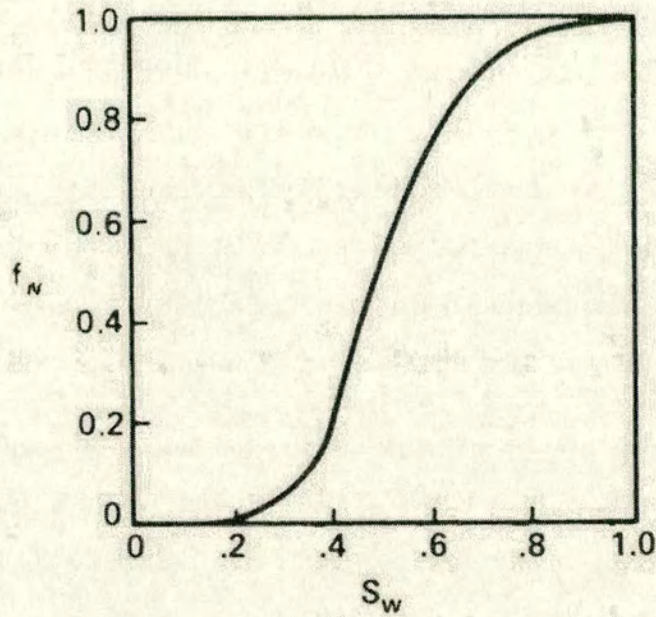$$f_w = \frac{\lambda_w}{\lambda_n + \lambda_w}. \tag{C.32}$$

Figure C.3: Typical curve of f_w vs. S_w (after Sorbie and McDougall, 1998)

$$h_w = -\frac{\lambda_n \lambda_w}{\lambda_n + \lambda_w} \frac{dP_c}{dS_w}. \tag{C.33}$$

A typical curve of f_w vs. S_w is shown in Figure C.3.

The negative sign is included in the definition of h_w to keep it positive, since P_c is a decreasing function of S_w. Equation (C.31) then becomes:

$$V_w = f_w V_t - h_w \nabla S_w + \lambda_n f_w (\rho_w - \rho_n) g \nabla D. \tag{C.34}$$

and Equation (C.10) can be written in the following final form for the saturation equation:

$$\nabla \cdot (\alpha \rho_w h_w \nabla S_w) - \nabla \cdot (\alpha \rho_w f_w)[V_t + \lambda_n (\rho_w - \rho_n) g \nabla D] + \alpha q_w = \alpha \frac{\partial (\phi \rho_w S_w)}{\partial t}. \tag{C.35}$$

The first term (which involves the capillary pressure) strongly suggest that it is essentially parabolic in nature, unless capillary effects are unimportant. In that

case, the two centre terms that involve velocity and gravity become important, but their significance is not so obvious.

In the region of the reservoir we take $q_w = Q_t = 0$ and we have

$$V_w = f_w V_t - h_w \nabla S_w + \lambda_n f_w (\rho_w - \rho_n) g \nabla D. \qquad (C.36)$$

and Equation (C.35) can be simplified to:

$$(1/\alpha)\nabla \cdot (\alpha h_w \nabla S_w) - \frac{df_w}{dS_w} V_t \cdot \nabla S_w = \phi \frac{\partial S_w}{\partial t} + (1/\alpha)\nabla \cdot (\alpha G_w \nabla D), \qquad (C.37)$$

where

$$G_w = f_w \lambda_n (\rho_w - \rho_n) g, \qquad (C.38)$$

is another function of saturation. Equation (C.37) may be either parabolic or hyperbolic in nature, depending on the importance of the capillary pressure term relative to the convection term. When capillary pressure effects dominate, h_w is large, and Equation (C.37) behaves like a parabolic problem. When capillary pressure effects are small or absent or, more importantly sometimes, when velocities are large, then the convection term dominates, and the equation approaches the first-order nonlinear hyperbolic equation:

$$-\frac{df_w}{dS_w} V_t \cdot \nabla S_w = \phi \frac{\partial S_w}{\partial t} + (1/\alpha)\nabla \cdot (\alpha G_w \nabla D). \qquad (C.39)$$

C.3.6   Diffusion-convection equation

Equation (C.37) can be regarded as a non-linear variation of the diffusion-convection equation:

$$D\nabla^2 C - V \cdot \nabla C = \phi \frac{\partial C}{\partial t}, \qquad (C.40)$$

which governs multidimensional miscible displacement. Here D is diffusivity and C is concentration. The first term of the equation is the diffusion term and, when it dominates, it behaves like the parabolic heat conduction equation. On the other

hand, when the diffusion term is small, the centre term i.e. the convection term, dominates and the equation approaches the first-order hyperbolic equation:

$$-V \cdot \nabla C = \phi \frac{\partial C}{\partial t}. \tag{C.41}$$

The first-order character of Equation (C.40) may be made more clearly by expanding the left-hand side:

$$-V_x \frac{\partial C}{\partial x} - V_y \frac{\partial C}{\partial y} - V_z \frac{C}{\partial z} = \phi \frac{\partial C}{\partial t}. \tag{C.42}$$

Equation (C.42) can thus be seen to be a multidimensional equivalent of the one-dimensional equation.

Appendix D

Publications

D.1 Papers

The following pages include all the papers, both published and submitted:

1) Vlastos, S. and Liu, E. and Main, I.G. and Li, X.-Y., 2003, Numerical simulation of wave propagation in media with discrete distributions of fractures: effects of fracture sizes and spatial distributions, 152, 649-668, Geophysical Journal International.

2) Liu, E. and Vlastos, S. and Li, X.-Y. and Main, I.G. and Schoenberg, M., 2004, Modelling seismic wave propagation during fluid injection in a fractured network: Effects of pore fluid pressure on time-lapse seismic signatures, August 2004, 778-783, The Leading Edge.

3) Liu, E. and Vlastos, S., 2003, A method to generate fracture patterns with different distributions and orientations, submitted in March 2003 in Computers and Geoscience.

4) Vlastos, S. and Narteau, C. and Liu, E. and Main, I.G., 2003, Numerical study of scattering attenuation in fractured media: the effects of scalelength on multiple scattering attenuation, submitted in May 2003 in Geophysical Journal International.

5) Vlastos, S. and Schoenberg, M. and Maillot, B. and Liu, E. and Main, I.G. and Li, X.-Y., 2004, Dual simulation of fluid flow and seismic wave propagation in a fractured network: Effects of changes in pore pressure on seismic signature, submitted in May 2004 in Geophysical Journal International.

D.2   Expanded Abstract

The following pages include expanded abstracts presented at the Annual International Meeting of the Society of Exploration Geophysicists, at the EAGE Conference and Exhibition and at two other conferences:

1) Vlastos, S. and Liu, E. and Li, X.-Y. and Main, I.G., 2002, Numerical study of seismic wave propagation in rock with scale length (size) and spatial distributions of fractures, Expanded Abstracts of the EAGE 64th Conference and Exhibition, Florence, Italy, 27-30 May.

2) Liu, E. and Vlastos, S., 2002, Finite difference simulation of seismic wave propagation in 2D solids with distribution of discrete fractures, 5th ISMST Congress, Winterthur, Switzerland, 26-29 May.

3) Vlastos, S., 2002, Numerical simulation of wave propagation in rocks with discrete fractures, LMS Durham Symposium, Computational Methods for wave propagation in direct scattering, Durham, UK, 15-25 July.

4) Vlastos, S. and Narteau, C. and Liu, E. and Main, I.G., 2003, Numerical study of scattering attenuation in fractured media: frequency dependence and effects of characteristic scale lengths, Expanded Abstracts of the EAGE 65th Conference and Exhibition, Stavanger, Norway, 2-5 June.

5) Vlastos, S. and Schoenberg, M. and Maillot, B. and Main, I.G. and Liu, E. and Li, X.-Y., 2003, Fluid flow simulation in a fractured medium: effects of pore pressure changes on seismic waves, Expanded Abstracts of the EAGE 65th Conference and Exhibition, Stavanger, Norway, 2-5 June.

6) Vlastos, S. and Narteau, C. and Liu, E. and Main, I.G., 2003, Numerical study of scattering attenuation in fractured media: the effects of scalelength on multiple scattering attenuation, Expanded Abstracts of the 73rd Annual International SEG Meeting, Dallas, Texas, 26-31 October.

7) Vlastos, S. and Schoenberg, M. and Maillot, B. and Main, I.G. and Liu, E. and Li, X.-Y., 2003, Dual simulation of fluid flow and seismic wave propagation in a fractured network: effects of changes in pore pressure on signature of seismic waves, Expanded Abstracts of the 73rd Annual International SEG Meeting, Dallas, Texas, 26-31 October.

Appendix E

Reprints of published papers

The following pages include reprints of the following two published papers:

1) Vlastos, S. and Liu, E. and Main, I.G. and Li, X.-Y., 2003, Numerical simulation of wave propagation in media with discrete distributions of fractures: effects of fracture sizes and spatial distributions, 152, 649-668, Geophysical Journal International.

2) Liu, E. and Vlastos, S. and Li, X.-Y. and Main, I.G. and Schoenberg, M., 2004, Modelling seismic wave propagation during fluid injection in a fractured network: Effects of pore fluid pressure on time-lapse seismic signatures, August 2004, 778-783, The Leading Edge.

Numerical simulation of wave propagation in media with discrete distributions of fractures: effects of fracture sizes and spatial distributions

S. Vlastos,[1,2] E. Liu,[1] I. G. Main[2] and X.-Y. Li[1]

[1]*British Geological Survey, Murchison House, West Mains Road, Edinburgh EH9 3LA, UK. E-mail: svl@bgs.ac.uk*
[2]*Department of Geology and Geophysics, University of Edinburgh, Grant Institute, West Mains Road, Edinburgh EH9 3JW, UK*

SUMMARY

We model seismic wave propagation in media with discrete distributions of fractures using the pseudospectral method. The implementation of fractures with a vanishing width in the 2-D finite-difference grids is done using an effective medium theory (that is, the Coates and Schoenberg method). Fractures are treated as highly compliant interfaces inside a solid rock mass. For the physical representation of the fractures the concept of linear slip deformation or the displacement discontinuity method is used. According to this model, the effective compliance of a rock mass with one or several fracture sets can be found as the sum of the compliances of the host (background) rock and those of all the fractures. To first order, the background rock and fracture parameters can be related to the effective anisotropic coefficients, which govern the influence of anisotropy on various seismic signatures. We test the validity of the method and examine the accuracy of the synthetic seismograms by a comparison with theoretical ray traveltimes. We present three numerical examples to show the effects of different fracture distributions. The first example shows that different spatial distributions of the same fractures produce different wavefield characteristics. The second example examines the effects of variation of fracture scale length (size) compared with the wavelength. The final example examines the case of fractures with a power-law (fractal) distribution of sizes and shows how that affects the wavefield propagation in fractured rock. We conclude that characterization of fractured rock based on the concept of seismic anisotropy using effective medium theories must be used with caution. Scale length and the spatial distributions of fractures, which are not properly treated in such theories, have a strong influence on the characteristics of wave propagation.

Key words: cracked media, effective medium theory, fractures, finite-difference methods, wave propagation.

1 INTRODUCTION

Numerical modelling techniques are now becoming very common for understanding the complicated nature of seismic wave propagation in fractured rocks. The scientific community has shown an increasing interest in this subject, and currently there are a variety of approaches for forward modelling. Analytic expressions for the description of elastic wave propagation in the presence of fractures are only available for rather simple cases, that is, single cracks with simple geometries (Mal 1970), and in most cases are only valid in the far field (Liu *et al.* 1997). In complex situations, solutions based on Born or Rytov approximations may be used (Wu & Aki 1985). These approximations become accurate in the limit of low-frequency wave propagation and low contrast between scatters and the host rock. However, they have limitations when dealing

with large-scale inclusions or fractures such as those encountered in hydrocarbon reservoirs. On the whole, several non-numerical approaches exist for the computation of elastic wavefields that take into account multiple scattering, but few are valid for large sizes and short wavelengths. When the size of inclusions is substantially less than the wavelength, various equivalent medium theories are available (see the review by Liu *et al.* 2000). However, the presence of spatial correlations of different systems cannot be accounted for with any effective medium theory. Therefore, the use of numerical methods seems to be the only way that is capable of providing accurate solutions without a restriction of the size-to-wavelength ratio.

The numerical techniques employed so far to study seismic wave scattering problems include the Maslov theory (Chapman & Drummond 1982), the finite-difference method (FD) (van Baren

650   *S. Vlastos* et al.

et al. 2001; Saenger & Shapiro 2002), the pseudospectral method (PS) (Fornberg 1988), the finite-element method (FE) (Lysmer & Drake 1972), the boundary element method (Benites *et al.* 1992; Pointer *et al.* 1998; Liu & Zhang 2001) and the spectral finite-difference method (Mikhailenko 2000). In this study we use the pseudospectral method to simulate wave propagation in media with discrete distributions of fractures. In contrast with the widely used FD method, the PS method substitutes the spatial difference scheme with a Fourier and inverse Fourier transform pair. A minimum of two nodes per wavelength (theoretically) is needed to obtain an accurate derivative, compared with FD which normally requires 10–20 nodes per wavelength (Alford *et al.* 1974). This is one of the major

advantages of the PS method. However, there is a drawback in the use of the PS method. It intrinsically treats all physical quantities as spatially periodic and, as a result, all energy transmitted and reflected through the boundary will travel back into the grid. These artefacts often mask important features of real modelled signals. This deficiency can be mitigated by modifying the wavelet near the grid boundary in such a way that the wave amplitude is attenuated.

Fractures with a vanishing width in the 2-D finite-difference grids are implemented using an effective medium theory (following Coates & Schoenberg 1995). In the literature, there have been several such theories that attempt to predict effective properties of a rockmass containing distributed fractures. In this paper,
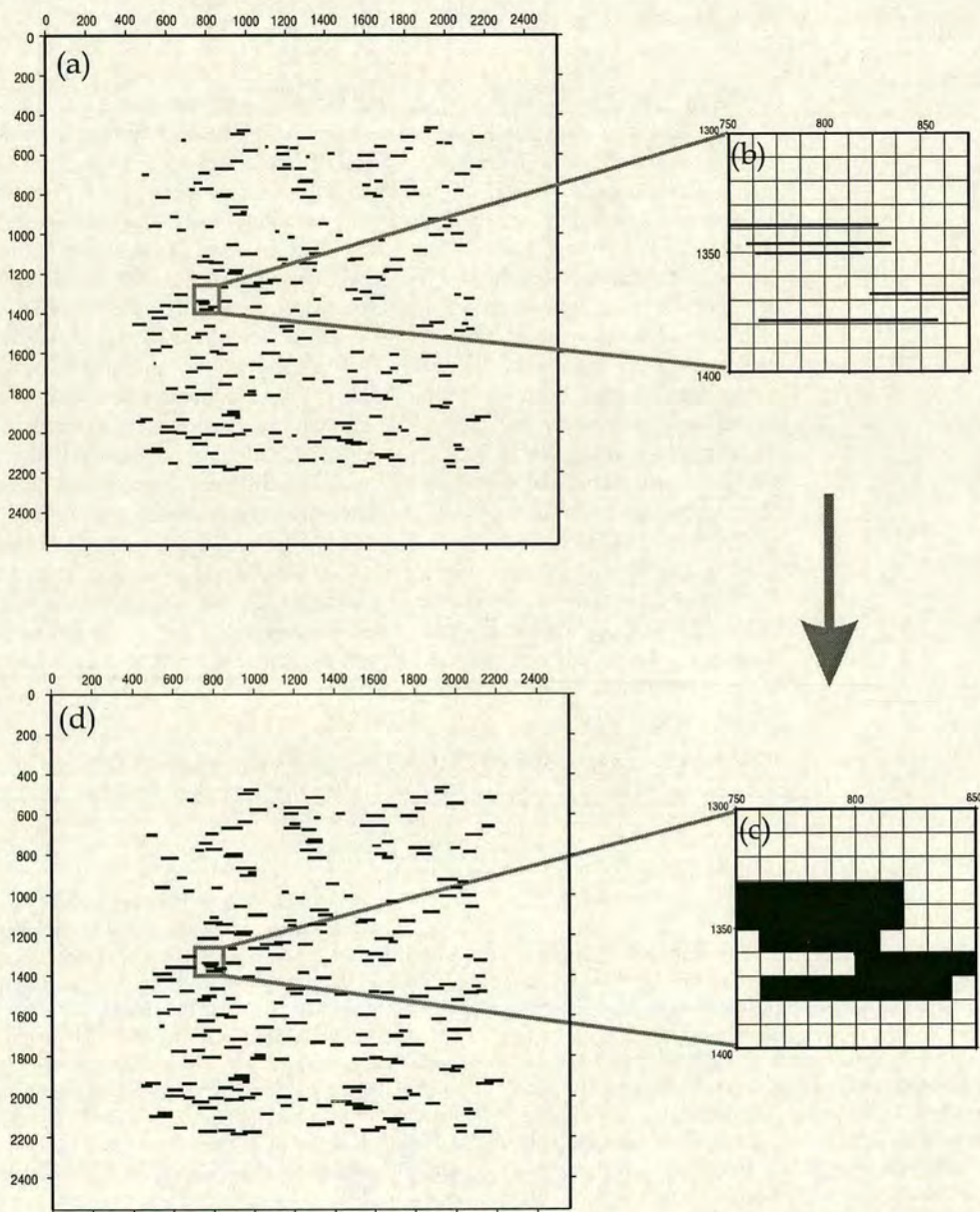

Figure 1. Schematic illustration of fracture discretization in the finite-difference grid. In (a) we show the fractured medium that we want to examine. In (b) we present a very small area of the whole model and (c) shows the same area discretized in the FD grid. Finally, (d) shows again the whole medium where, this time, the fractures are discretized. By comparing (a) and (d) we can see the high accuracy of the discretization.

fractures are treated as highly compliant interfaces inside a solid rock mass. We represent the fractures using the displacement discontinuity method (DDM) by Schoenberg (1980). We examine the validity of the method, and test the accuracy of the synthetics pro-
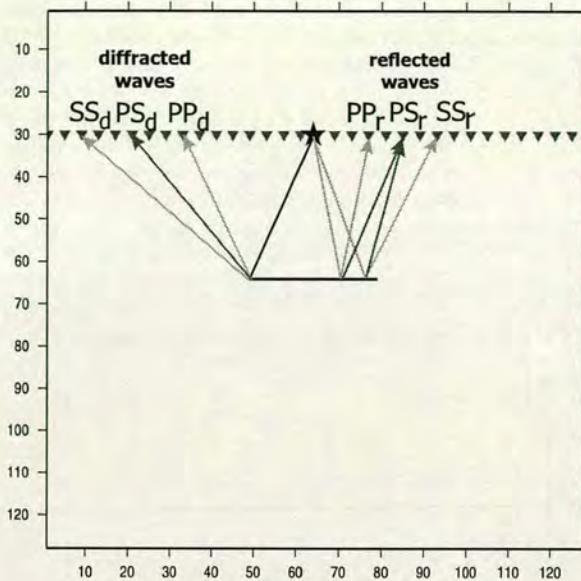
duced from the modelling. We choose a simple case to model and compare the synthetic seismograms with the theoretical ray traveltimes. After testing the method, we present some numerical examples. First, we examine the effect of the spatial distribution of fractures on the wavefield propagation. Secondly, we examine different sizes of fractures, having the same spatial distribution, and we attempt to associate the different features of the waveforms with the attributes of the fractures, and in particular their sizes. Finally, we model the scattering of the wavefield by fractures with a scale length distribution. The fractures in our model follow a power-law or fractal distribution up to a maximum length smaller than the model space, that is, below the percolation threshold. Power-law size distributions are the most common form encountered in natural data sets where a broad bandwidth of data is available (Bonnet *et al.* 2001).

Figure 2. Schematic representation of the model used for the testing of the accuracy of the modelling method, and representation of the ray paths of the different kind of waves generated by the source that interact with the fracture.

2 IMPLEMENTATION OF FRACTURES (THE COATES AND SCHOENBERG METHOD)

To obtain the effective parameters of fractured media, fractures are treated as infinitely thin highly compliant interfaces inside a solid rockmass. Following the concept of the linear slip deformation or displacement discontinuity model of Schoenberg (1980), a fracture can be represented as a boundary across which the displacements are discontinuous, whereas the stresses remain continuous. To first order the displacement discontinuity and the tractions are linearly related, i.e.

$$[u] = Z\tau, \tag{1}$$

where $[u]$ is the average displacement discontinuity, τ is the traction acting across the fracture and Z is called the fracture compliance
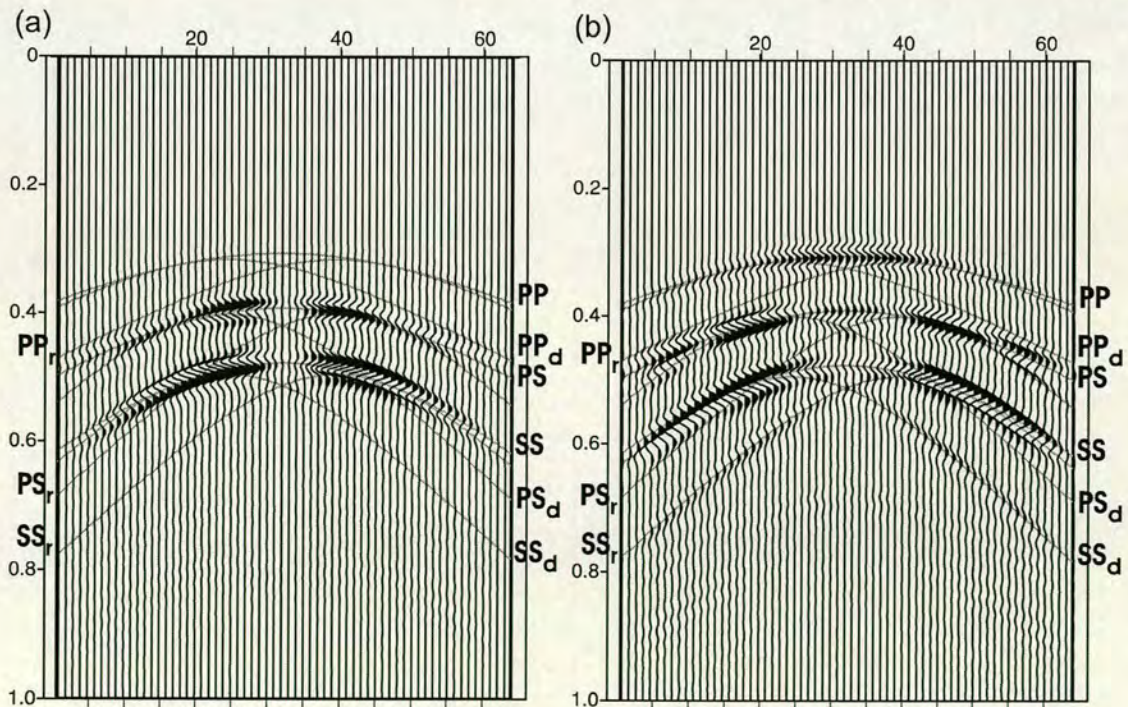

Figure 3. Comparison between the theoretical ray traveltimes and the synthetic seismograms generated by the modelling method. We present (a) the horizontal (*x*) and (b) the vertical (*z*) components of the seismograms. As we can see from the figure they are in very good agreement with the theoretical traveltimes, thus verifying the accuracy of the method.

652   *S. Vlastos* et al.

tensor, which is an elastic parameter of the medium. This linear relationship is consistent with the usual seismic approximation of infinitesimal strain. In addition, there has been some experimental verification of the DDM model by Pyrak-Nolte *et al.* (1990) and Hsu & Schoenberg (1993). Essentially, eq. (1) is a boundary condition of the fracture surfaces. In a finite-difference algorithm, the relationship can be implemented by requiring a displacement jump across gridpoints on either side of the interface, proportional to the local (continuous) stress traction. The implementation of the displacement jump is relatively simple, even with Z being a function of position on the fault plane, providing the interface lies along a given plane of the finite-difference grid. In nature, fractures have finite length. To implement a finite fracture we take $Z = 0$ at locations on the plane exterior to the fracture. The question that remains is how to implement the constraint that $Z \rightarrow 0$ on the tips of the fracture. We taper off the value of Z following the formulation of the

crack-opening displacement introduced by Kachanov (1984). The value of Z has its maximum value in the centre of the fracture and reduces to 0 at both fracture tips following a hyperbolic pattern. The rate at which the value of compliance reduces depends strongly on the length of the fracture.

In the finite-difference method, the medium is discretized into small rectangular grids and we find the elastic parameters of the equivalent medium for each grid cell. For each grid intersected by a fracture (or portion of fracture), the elastic medium within the cell surrounding the fracture, together with the embedded segment of the fracture, are replaced by an equivalent anisotropic medium. Muir *et al.* (1992) showed how the elastic parameters could be found for a cell enclosing an interface between two elastic media. The discretization of the fracture in the finite-difference grids is shown schematically in Fig. 1. This method was first used by Coates & Schoenberg (1995), and therefore it is referred to as the Coates and
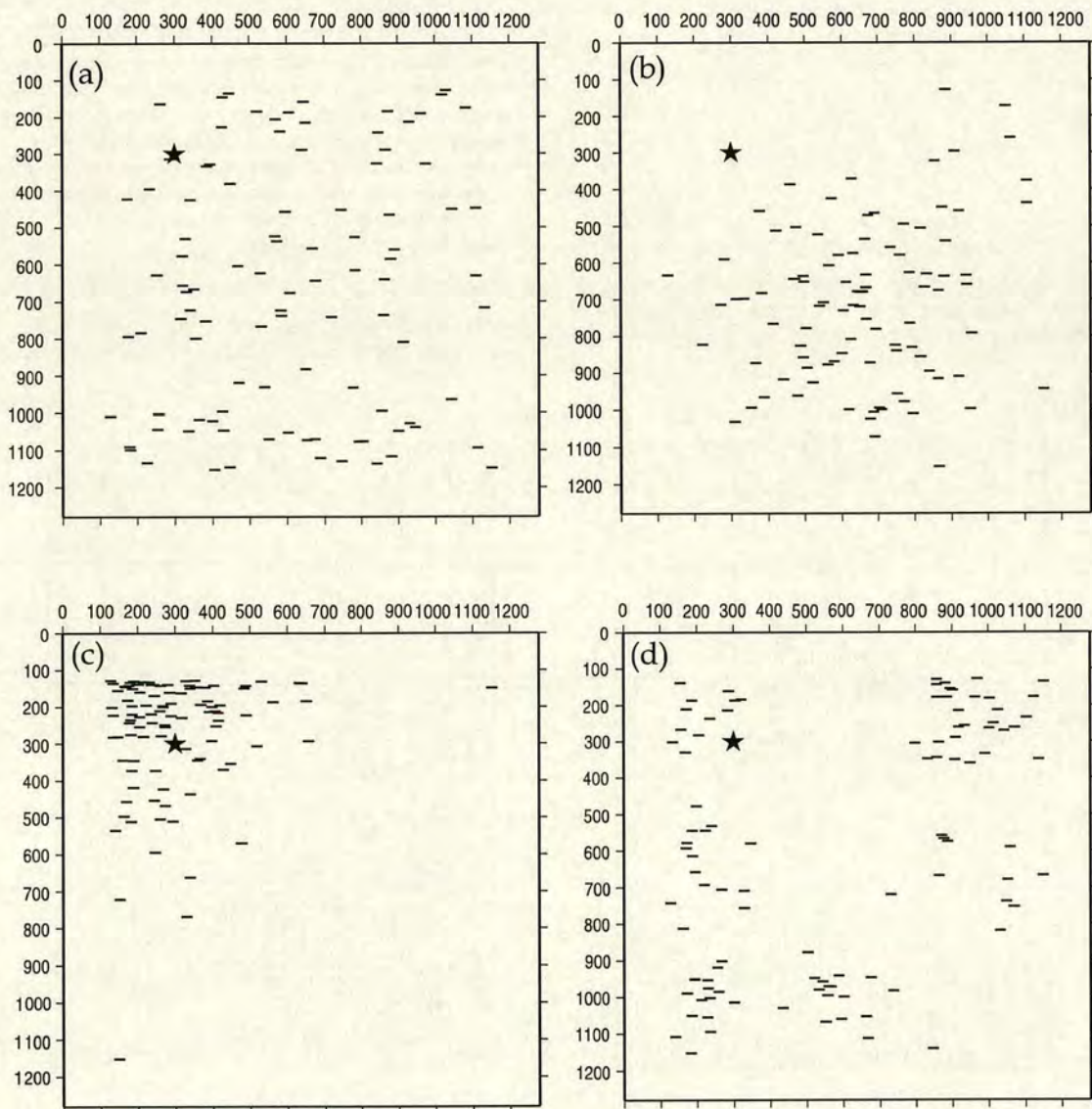

Figure 4. Example 1: model used to compute snapshots from spatially distributed fractures. The four different models, (a)–(d), illustrate different statistical distributions of fractures. *P* and *S* waves are generated at the source (represented by a star) and travel inside the medium.

Schoenberg method in this paper. In Fig. 1(a) we show the whole fractured medium. Then we take a very small area of the medium in Fig. 1(b), to show how the fractures are represented in the finite-difference grid. Fig. 1(c) shows the discretization of the fractures in the grid, where the shaded areas are the finite-difference grid cells intersected by one or more fractures, whilst the plain areas are the cells that include only the background rock. Finally, in Fig. 1(d) we show the whole medium again, but this time each cell is either shaded or plain, depending on whether fractures are present. By comparing Fig. 1(d) with Fig. 1(a), where we show the medium with the actual fractures, we can see that the discretization of the fractures is very accurate. In the numerical examples presented in this paper we use in some cases a grid size of 128×128 and in other cases 256×256. The grid cell size is very important for the discretization of the fractures. To achieve high accuracy, we choose grid sizes smaller than or equal to the size of the smallest fractures.

Thus any size of fracture can be represented accurately by the elastic parameters of the effective medium in each finite-difference grid cell. The variables required for the effective medium calculation in each cell are the length of the fracture, its orientation and the local value of the fracture compliance tensor. In the numerical models that will be presented later, fractures are represented as finite lines for which we know the starting and the ending points. Using simple algebra we can define the equation of any line that passes between two points. Knowing the equation that describes each fracture, we can locate the intersections of the fractures with the horizontal and vertical boundaries of each cell (if any) and calculate the length and orientation of the fracture segment lying in each cell. The effective medium for each cell may then be calculated using these values and the method for estimating the fracture compliance tensor outlined in Appendix A. The tapering of the value of the fracture compliance Z is explained in detail in Appendix B.
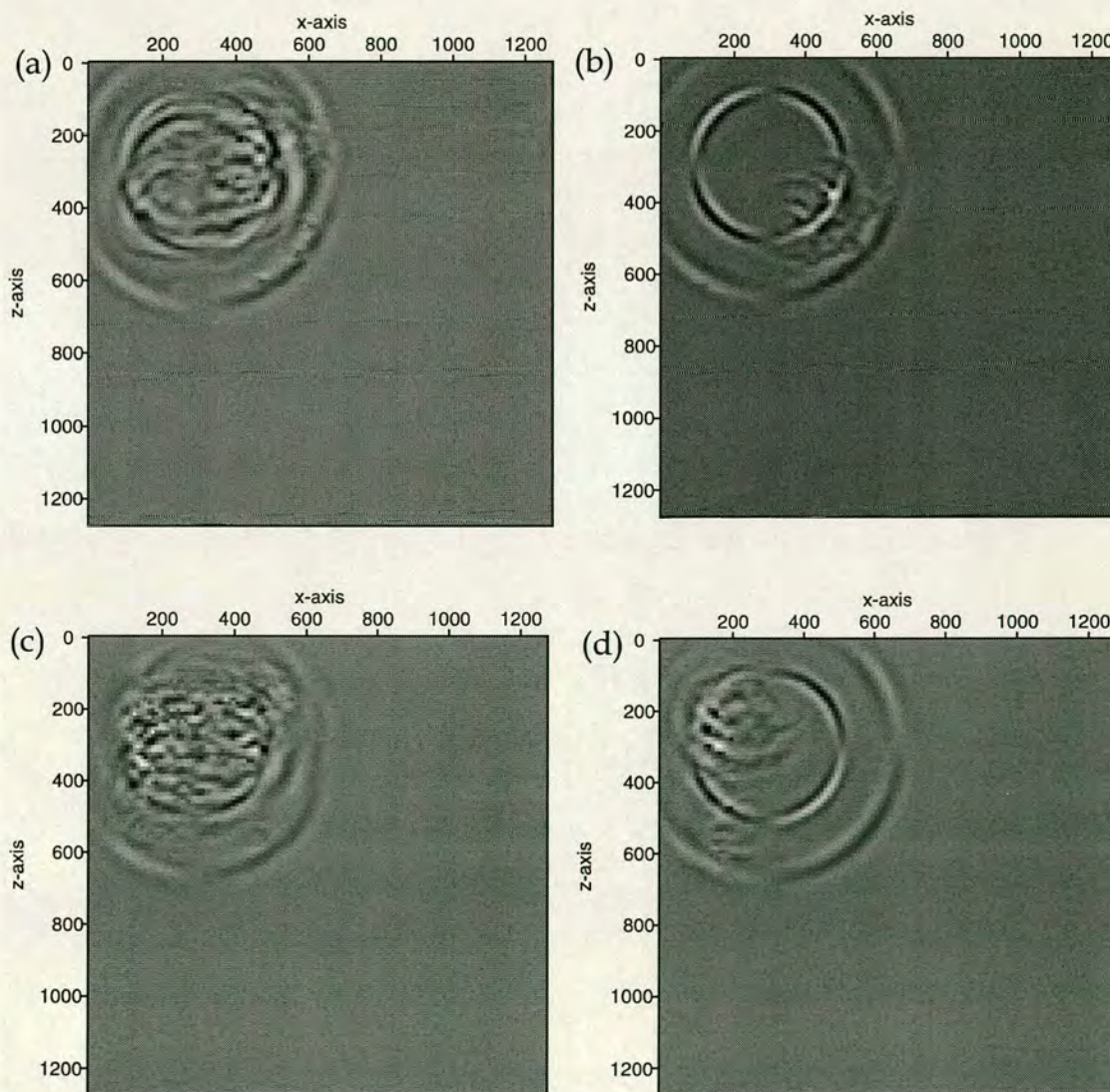

Figure 5. Snapshots taken at $t = 100$ ms. (a)–(d) correspond to fracture distributions (a)–(d) in Fig. 4. The numbers on the top and on the left-hand side of the snapshots are the model dimensions. We present the x-component of motion.

654   *S. Vlastos* et al.

3 VALIDATION

The first step is to compare results generated by our modelling method with those obtained by another method. This has been done by Coates & Schoenberg (1995), Nihei & Myer (2000) and Nihei *et al.* (2000), who compared the synthetic seismograms from the Coates and Schoenberg method described with the exact solutions using boundary element methods. We assess the accuracy by comparing the synthetic seismograms generated by the modelling with the ray theoretical traveltimes.

The model geometry used for accuracy testing is shown in Fig. 2. The source, receivers and fracture are situated in an ideal elastic ($V_P = 3300$ m s^{-1}, $V_S = 1800$ m s^{-1}, $\rho = 2200$ kg m^{-3}) full space. The receiver array at which vertical and horizontal particle displacements are recorded is horizontal and 340 m above the fracture. The fracture is 300 m long. The source is located at the centre of the receiver array. The source type is a vertical force. The source signal is a Ricker wavelet (Ricker 1977) with a peak frequency of 25 Hz

and a pulse initial time of 0.1 s. Fig. 2 also shows the different kinds of waves created by the interaction of the waves generated by the source and the fracture. The source generates both P and S waves. When they reach the fracture boundary those waves are reflected and we have PP_r, PS_r, SP_r, and SS_r waves. PP_r-waves will be the first to arrive at the receivers. Those are waves that travel both before and after the reflection as P waves. The next arrivals will be the PS_r and SP_r waves. The PS_r waves travel as P waves from the source to the fracture, and as S waves from the fracture to the receivers. In the case of the SP_r waves, the case is the complete opposite. The arrival of those two different types of waves happens at the same time, because the source–fracture and fracture–receiver distances are equal. As a result, the distance that they travel as P and as S waves is exactly the same in both cases, so we present both of them as PS_r waves in Fig. 2. Finally, the SS_r waves arrive at the receivers, which travel both legs as S waves. In addition to the reflected waves, there are waves diffracted from the crack tips. We have P- and S-wave diffractions, and also conversion from P to S waves and vice versa, which are
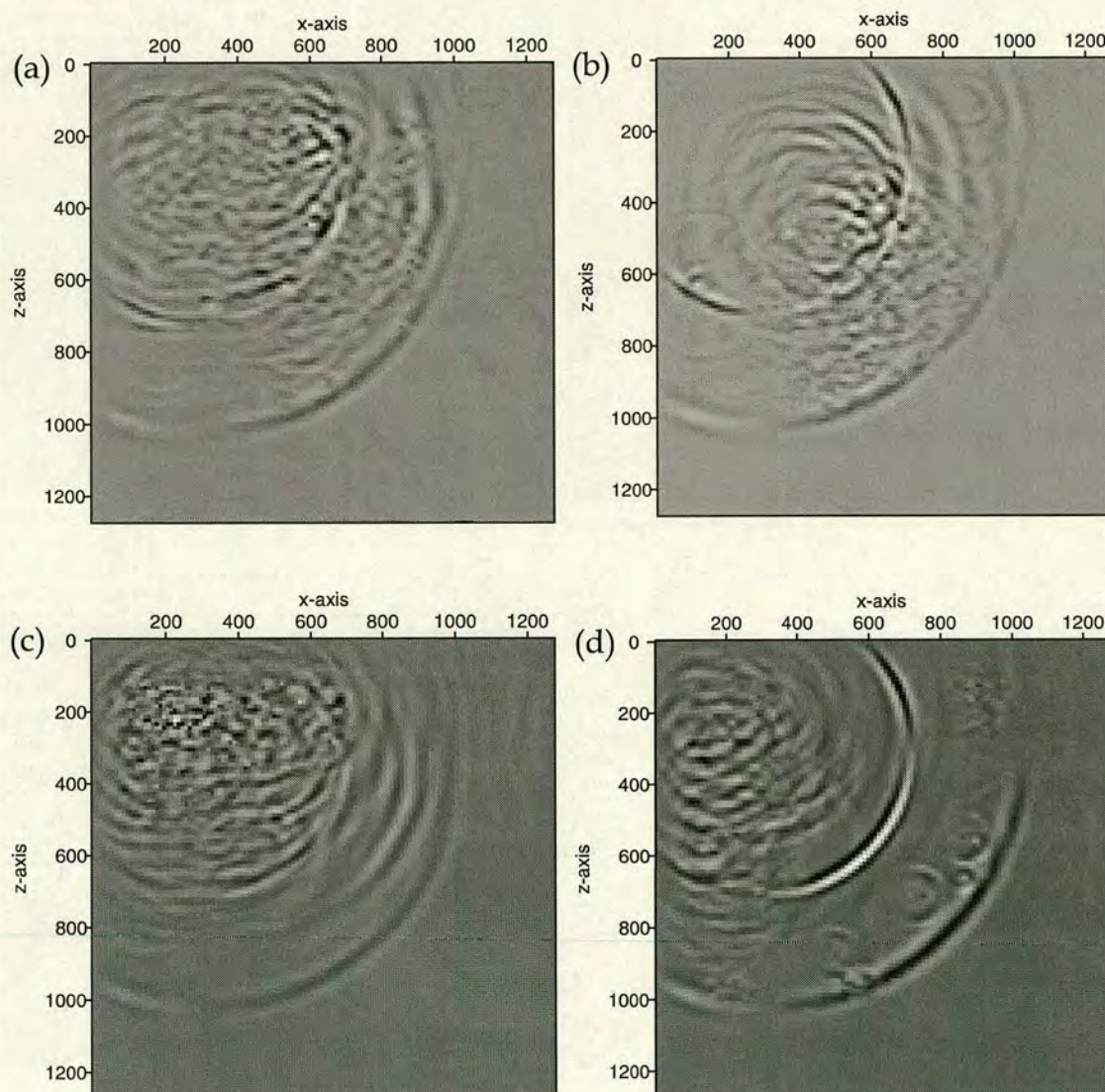

Figure 6. Snapshots taken at $t = 200$ ms.

diffracted from the tips of the fracture. These waves are presented in Fig. 2 as PP_d, PS_d, SP_d and SS_d waves.

We calculate the theoretical ray traveltimes and overlap them on the synthetic seismograms. Figs 3(a) and (b) show the horizontal (x) and the vertical (z) components, respectively, of the synthetic seismograms together with the theoretical ray traveltimes. As we can see from both figures, we have very good agreement between the theoretical ray traveltimes and the synthetic seismograms. All types of waves are accurately represented in the synthetic seismograms. Owing to the type of source that we implement, we have strong arrivals at short offsets on the horizontal component and strong arrivals at long offsets on the vertical component. In addition to that, the diffracted waves from the tips of the fracture and the PP_r and PP_d waves are not visible in the horizontal component, but they are very clearly demonstrated in the vertical component and follow the theoretical traveltimes. This is expected because the source causes vertical displacements on the medium, so very close to the source and very far away from it, the horizontal displacement is negligible.

Another aspect of the comparison between the theoretical and the modelled data is that they give us further insight into the waveform patterns. For instance, we can see in both Figs 3(a) and (b) that in the areas of superposition between the reflected waves from the fractures and the diffracted waves from the tips we have maximum amplitude in the wavefield, as a result of constructive interference. This gives us valuable information concerning the medium we are examining.

4 NUMERICAL EXAMPLES

The PS method has been used to model the seismic wavefield reflected and diffracted by fractures. We examine the influence of different fracture parameters on the displacements. In particular, we are interested in understanding the effects of spatial distributions, the scale length distribution of fractures and looking for characteristics in the wavefields owing to different distributions.
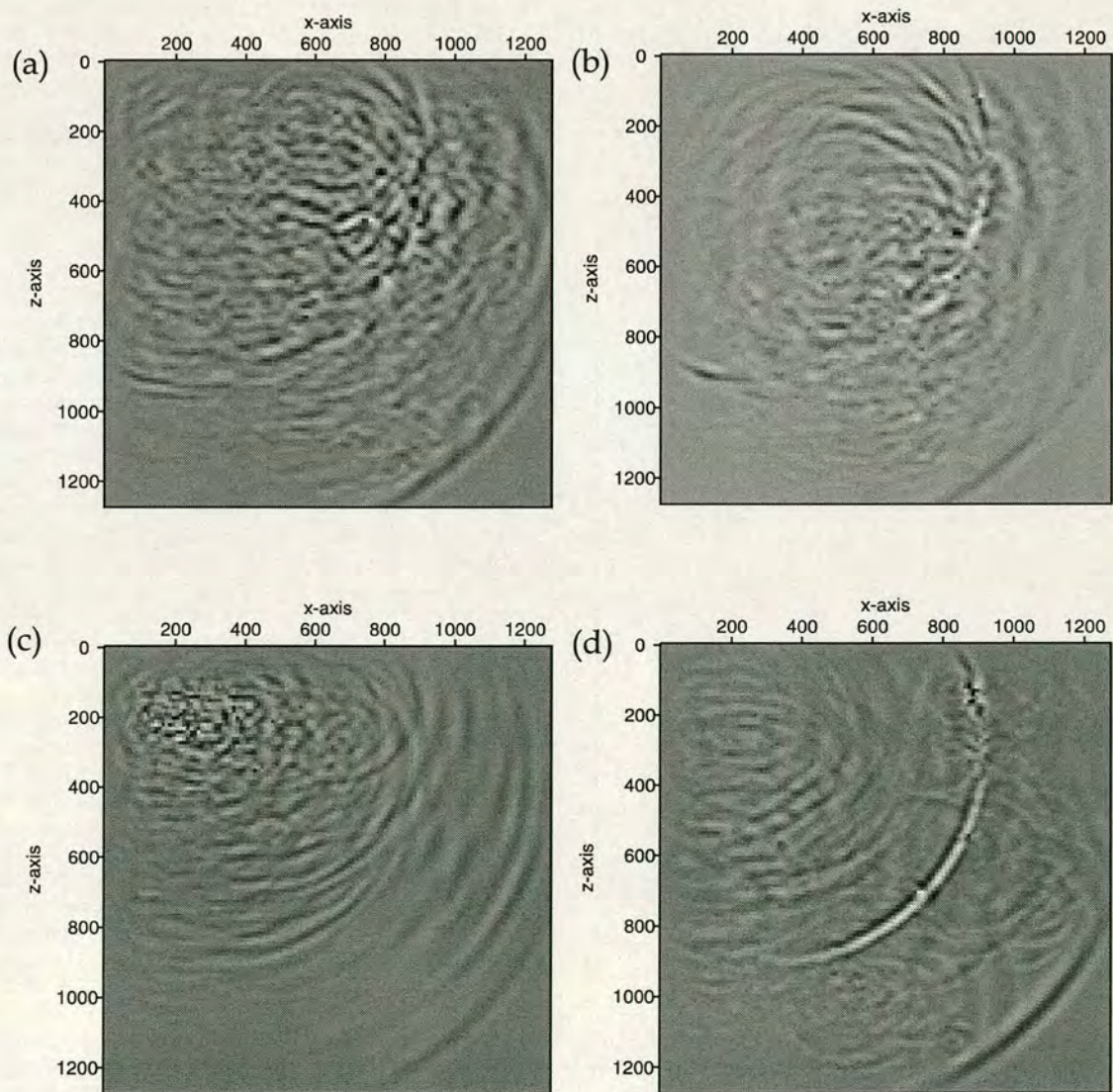

Figure 7. Snapshots taken at $t = 300$ ms.
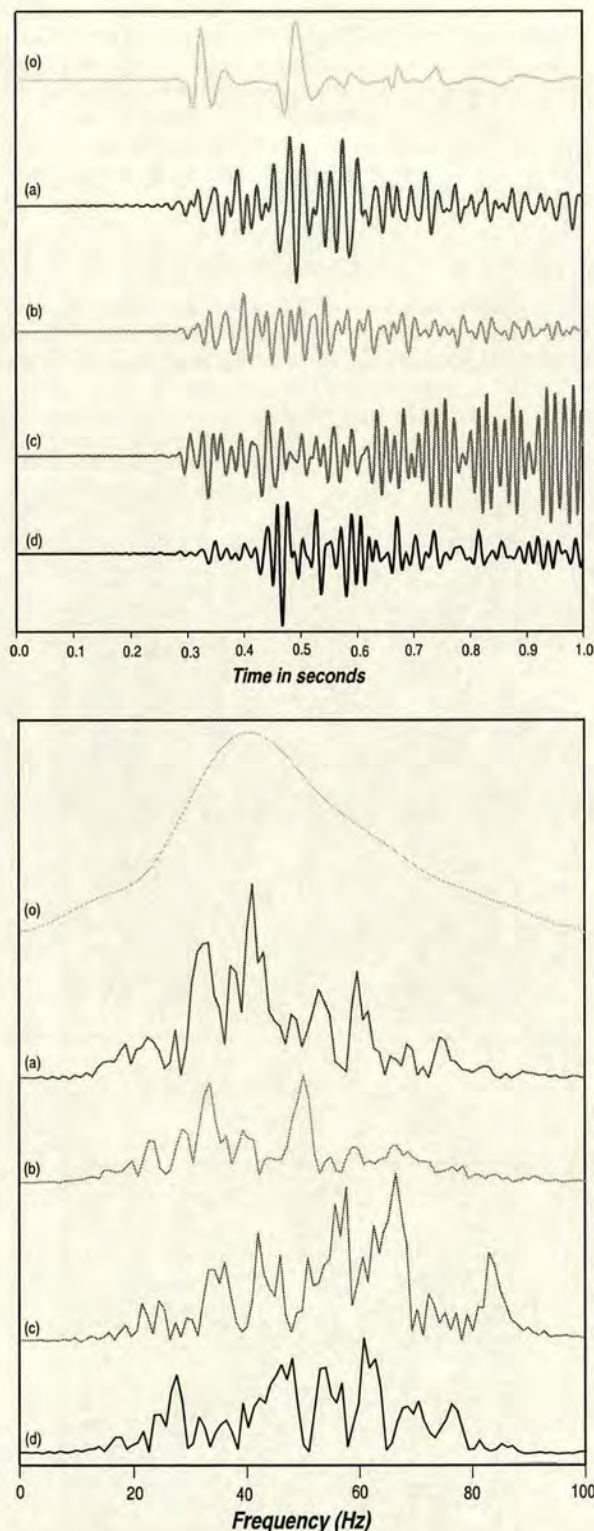
656   *S. Vlastos* et al.

Figure 8. Comparison of synthetic seismograms and corresponding spectra from various distributions of fractures: (o) no fractures, (a)–(d) correspond to the fracture distributions of Fig. 4 (trace number 100).

4.1 Fracture spatial distribution

The first example is given in Fig. 4, in which we attempt to model four different simulations of random fracture distributions. In each model, there are 100 fractures randomly distributed in a 1280 × 1280 m^2 area. To create the various random distributions of fractures we used an algorithm that generates four arbitrary distributions, featuring different qualitative characteristics. We use parent distributions for the fracture centre spacings that are (a) random uniform, (b) Gaussian, (c) exponential and (d) Gamma distribution. In the cases where we have overlapping of fracture positions, we remove the overlapping fractures and generate new fractures until the desired number of fractures is reached. As a result of this process, the final crack distribution is not necessarily random. Nevertheless, the purpose of this paper is to illustrate how different distributions affect multiple scattering. The generation of the different fracture distributions is presented in detail in Appendix C. In this simulation, each fracture has the same length, $2\alpha_c = 30$ m, where α_c is the radius or the half-length of the fracture. The surrounding solid (matrix) has P- and S-wave velocities $V_P = 3500$ m s^{-1}, $V_S = 2000$ m s^{-1} and density $\rho = 2200$ kg m^{-3}. The source is located at the left-hand corner of the model. The source type is a vertical force. A Ricker wavelet with a dominant frequency of 40 Hz is used, so that $k_p\alpha_c = 1.08$ and $k_s\alpha_c = 1.88$ (where $k_p = 2\pi f/V_P$ and $k_s = 2\pi f/V_S$ are the P and S wavenumbers), or equivalently $\lambda_p/2\alpha_c = 2.9$ and $\lambda_s/2\alpha_c = 1.67$ (where $\lambda_p = V_P/f$ and $\lambda_s = V_S/f$ are P and S wavelengths, respectively). For demonstration purposes, in all models in the paper we have used fracture compliance $Z_N = Z_T = 5.6 \times 10^{-10}$ G Pa^{-1} at the elementary scale.

The resulting snapshots taken at $t = 100$, 200 and 300 ms are given at Figs 5–7, respectively. As we can see from Fig. 4, fractures are more clustered in models (b) and (c), whereas they are more uniformly distributed or more scattered in models (a) and (d). In the extreme case of model (c), where the fractures are exponentially distributed, they are all concentrated in a small area around the source, forming a big cluster. This results in a lot of energy being trapped inside the cluster, between the various fractures. We observe the effect of the high clustering in the snapshots of the wavefield propagation at consecutive times, concentrating mainly on the mean wavefield. The wave fronts shown on the snapshots represent the statistical average effect of the fractures encountered throughout the wave path, thus resulting in a mean wavefield. The energy attenuation becomes clearer at 300 ms, where we see a lot of energy remaining in the area of the fracture cluster, whereas the mean wavefield almost does not exist. In model (b) where the fractures follow a Gaussian distribution, the fractures also form a big cluster in the centre of the model, but in this model they occupy more space and the distance between the various fractures is greater. In this case, similar to model (c), we have a significant amount of energy trapped in the fracture cluster. However, we can observe from the snapshots that there is more energy coming through the cluster, and that gives a fairly clear image of the mean wavefield of at least the P wave. The opposite case to the two previous ones is described in model (d). In this case the fractures follow a Gamma distribution (a power law with an exponential tail), thus forming a number of small clusters that are significantly distant from each other. It is observed in the snapshots that in this case the mean wavefield, for both P and S waves, is most clearly observed and has the highest amplitude compared with the rest of the cases. We believe that the small size of the clusters formed means that a lot of energy is not kept inside them, letting most of the energy propagate through the whole model. Finally, model (a)

where fractures are randomly uniformly distributed, describes a case where we do not have any clustering. The fractures are distributed throughout the whole medium. Although the snapshots show some trapped energy between the fractures, the mean wavefield propagation is quite clearly observed. To sum up the results, we can see that the wavefield propagates with the least energy attenuation when we have the least fracture clustering as shown in model (d), while attenuation increases with increasing clustering as shown in models (a)–(c), respectively.

In the following, we take the models of Fig. 4 and calculate the synthetic seismograms. The receivers are positioned along the *z*-direction and shifted by 1050 m in the *x*-direction. The cases we compare are (o) no fractures, (a) random uniform distribution, (b) Gaussian distribution, (c) exponential distribution and (d) Gamma distribution. Fig. 8 shows comparisons of waveforms of the *x*-component of motion from trace number 100, that corresponds to the depth of 1000 m, of each of the models and their corresponding Fourier spectra. In the figure we observe a noticeable shift of

energy to frequencies higher than the dominant frequency. If we compare the global maxima for all the cases examined, we can see in model (a) that the maximum energy is at approximately 40 Hz, which is the source dominant frequency, in model (b) it is at approximately 49 Hz, in model (c) it goes up to approximately 67 Hz, and in model (d) it is at 60 Hz. In terms of the distance that the wave travels between two consecutive scatterings, in model (a) we have the longest distance and in model (c) the shortest. Combining that with the observation that in model (a) we have no frequency shift of the energy, while in model (c) we have the maximum frequency shift indicates that there is a systematic shift of energy to higher frequencies when the multiple scattering dimension becomes shorter. Another feature of the spectra is the local minima of the amplitude. The first local minimum is observed at 30 Hz where the length of the fractures is approximately a quarter wavelength. There are also local minima at around 38, 58 and 70 Hz. These minima can be a result of the constructive or destructive interference of multiply scattered waves from the fractures. Finally, we notice that the
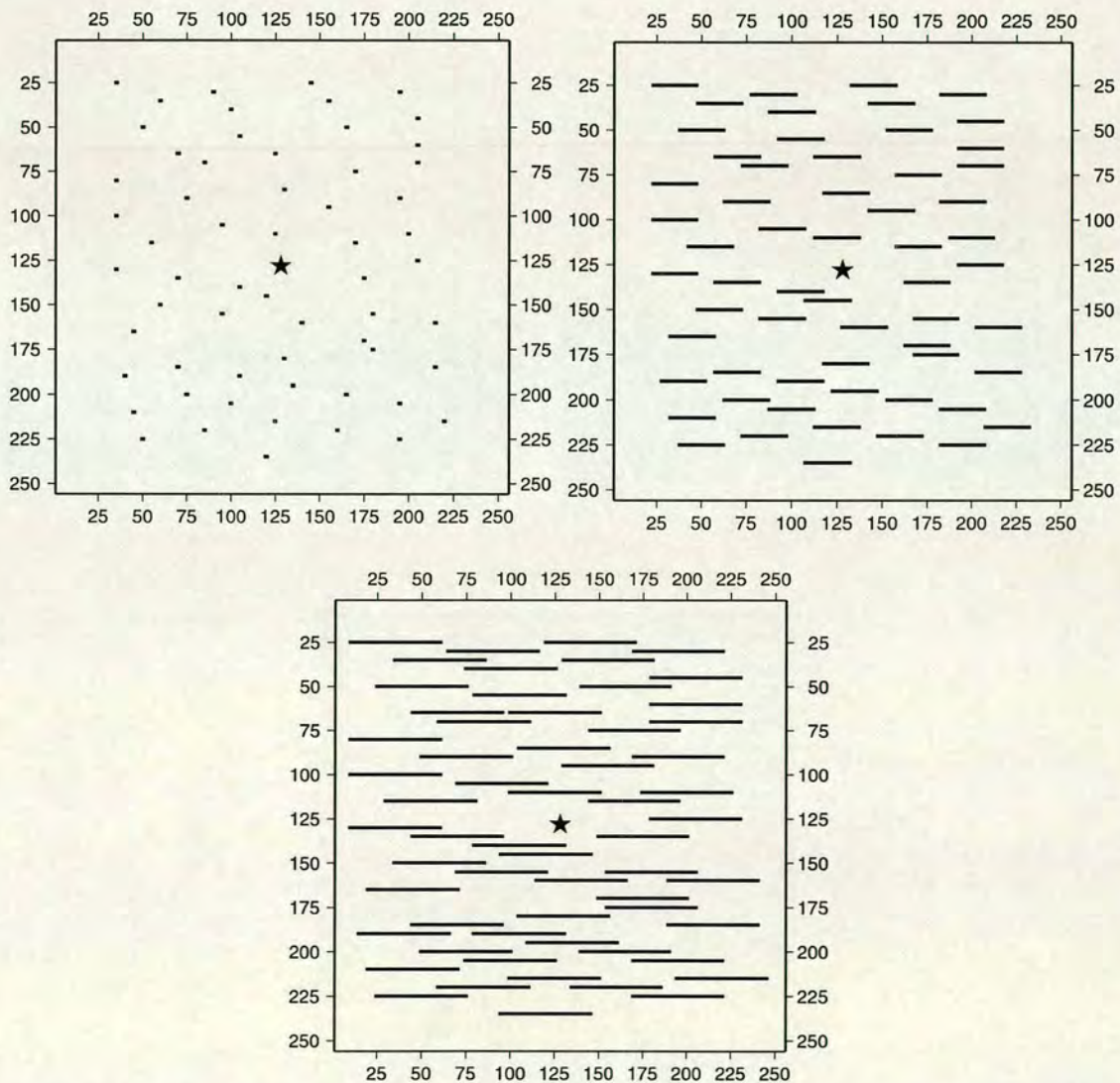

Figure 9. Example 2: model used to compute snapshots from randomly distributed fractures having different sizes compared with the source wavelength: (a) $\alpha = 0.1\lambda$, (b) $\alpha = \lambda$ and (c) $\alpha = 2\lambda$.

amplitude of the wavefield from distribution (b) is much smaller and has a relatively low-frequency content compared with the other distributions. This is possibly because in this case the local fracture density along the wave path towards the receivers is higher compared with the other cases. This example demonstrates clearly that different distributions of fractures have a significant influence on multiple scattering.

4.2 Effects of fracture scale length

The second example is used to examine wave scattering in a fractured medium where fractures have different sizes compared with the source wavelength. To ensure consistency of the results from different models we use the same background medium in all cases, which guarantees that any variation in the features of the wavefield is a result of the variation in the size of the fractures. The matrix parameters are $V_P = 3300$ m s^{-1} and $V_S = 1800$ m s^{-1} for the

P- and S-wave velocities, respectively, and the density is $\rho = 2.2$ g cm^{-3}. The source is a vertical force and is located at the centre for all the models. The source wavelet is a Ricker wavelet with a dominant frequency of 25 Hz and a initial pulse time at 0.1 s. We use a grid size of 256×256, with a spatial grid step of 10 m and a time step of 0.001 s. In all the models we have 50 fractures that follow a completely random distribution to avoid clustering patterns. We examine three different cases of fracture sizes, $\alpha_c = 0.1\lambda$, $\alpha_c = \lambda$ and $\alpha_c = 2\lambda$, where α_c is half the fracture length and λ is the wavelength.

Fig. 9 shows the models of the different sizes of fractures we examine, while Fig. 10 shows the respective snapshots taken at 350 ms. We observe in model (a) that when the wavelength is larger than the size of the fractures, we have a clear image of the propagation of P and S waves through the fractured medium, and each individual fracture acts as a point scatterer that becomes a secondary source. On the other hand, when the size of the fractures is equal to or larger
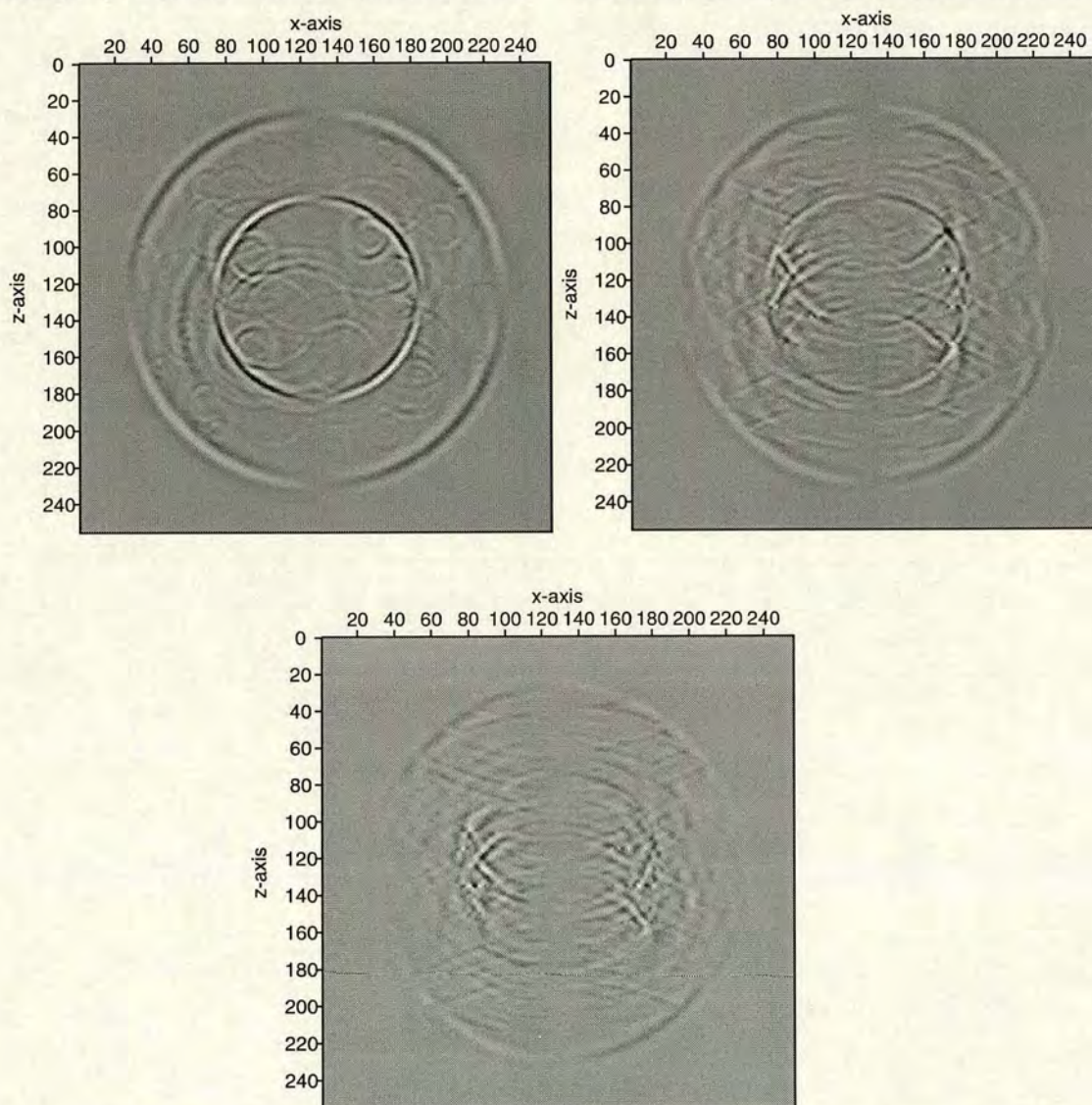

Figure 10. Snapshots taken at $t = 350$ ms. (a)–(c) correspond to fracture models (a)–(c) in Fig. 9. The numbers on the top and on the left-hand side of the snapshots are the model dimensions. We present the x-component of motion.

than the wavelength, they act almost as individual boundaries and the amplitudes of the reflected waves depend on the interference between the various reflections. In addition, following the results of the previous section on the effects of the fracture distribution together with the effects of the scale length, strong and coherent energy will be present in areas of high fracture clustering where fractures form large clusters and have a large size, thus acting as a single reflector.

4.3 Power-law (fractal) distribution of fracture sizes

The final example is used to model wave scattering from discrete fractures with a scale length distribution. The model we use is given in Fig. 11(a), where the variation of crack sizes follows a von Kármán correlation function, which gives a power-law distri-

bution (Wu 1982). We can also use other correlation functions, such as Gaussian or exponential functions. The model shown in Fig. 11(a) is generated with a correlation length of 40 m. In this model we have 400 fractures randomly distributed in a 2560×2560 m^2 area. The source is a vertical force and is located in the centre of the model, and is represented by a star in Fig. 11(a). The longest fracture is 100 m and the shortest is 10 m. The mean length of the fractures $\langle a \rangle$ is 27.5 m, and the fracture density of the medium $\varepsilon = N_f \langle a \rangle^2 / S$ is 0.046, where N_f is the number of fractures and S is the surface of the medium. The peak frequency is 40 Hz, which gives α ranging from 0.36 to 3.6 for P waves and from 0.63 to 6.3 for S waves, where k is the wavenumber, the P-wave velocity is 3500 m s^{-1} and the S-wave velocity is 2000 m s^{-1}. Figs 11(b)–(d), illustrate the attributes of the size distribution of the fractures. Fig. 11(b) shows the different sizes of fractures in the model of Fig. 11(a). Fig. 11(c)
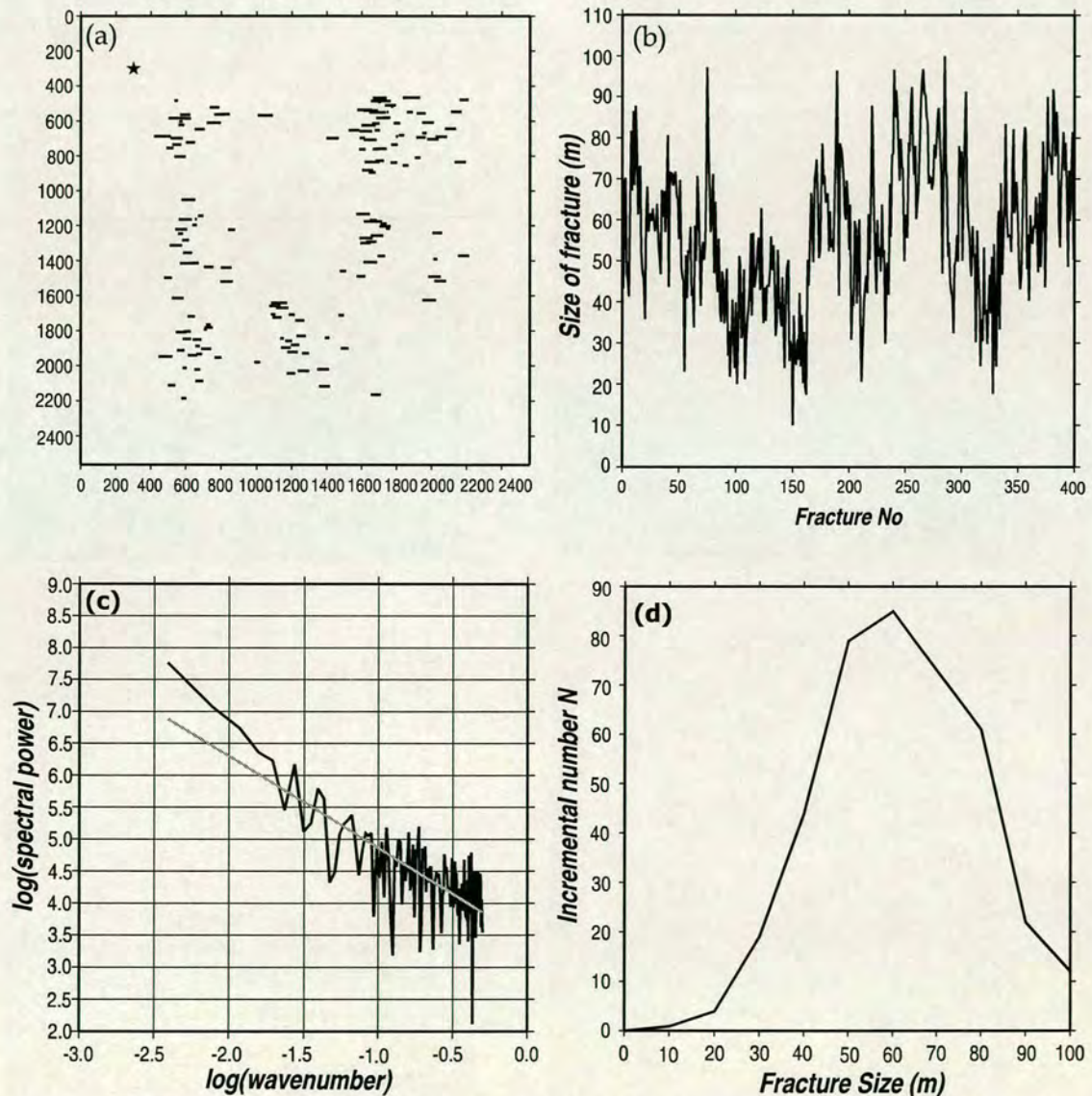

Figure 11. (a) Example 3: model used to compute synthetic seismograms from fracture distribution with power-law distribution of fracture sizes. (b) Illustration of the sizes of fractures in model (a), that follow a power-law distribution. (c) Power spectra of fracture size distributions shown in (a). (d) Cumulative number of the fractures of model (a) plotted against the fracture size.

shows the power spectrum of the fracture size distribution presented in Fig. 11(a) (plotted on a log–log scale). We see that the variation can be fitted with a straight line. Such a model (i.e. with a linear variation of the logarithm of the power spectrum with the logarithm of the spatial wavenumber) is a power-law distribution, often called a fractal (Bonnet *et al.* 2001). Fig. 11(d) shows the variation of the incremental number of the fracture population in the corresponding range of fracture sizes. To examine the behaviour of the wavefield arising from the fractal distribution of fractures in the medium, we take snapshots at consecutive times, $t = 200, 250, 300$ and 350 ms. The snapshots are presented in Fig. 12. As we can see from the snapshots, the behaviour of the wavefield is very complicated. Clearly, the P and S mean waves are fading away as they propagate through the medium. This can be attributed to the scattering taking place as the wavefield propagates through the high fracture density clusters. This is confirmed by the snapshots, where we can see high energy concentrated at the exact positions of the fracture clusters.

This is particularly clear in Fig. 12(d), where we have high amplitudes in the areas of fracture clusters resulting in strong coda waves, and at the same time low amplitudes of the mean P and S waves.

5 CONCLUSIONS

We have used the pseudospectral method to study the effect of different attributes of fractures on the wavefield characteristics. The fractures have been implemented in finite-difference grids using an effective medium theory. The method can deal with multiple scattering cases without having any limitations on the number of fractures included in the medium. The representation of the wavefield is highly accurate as long as sufficient grid elements are available, and in very good agreement with the theoretical ray travel-times. Note that in addition to our work presented in this paper, as far as we know the Coates and Schoenberg method has also been implemented by Nihei & Myer (2000) and Nihei *et al.* (2000) on
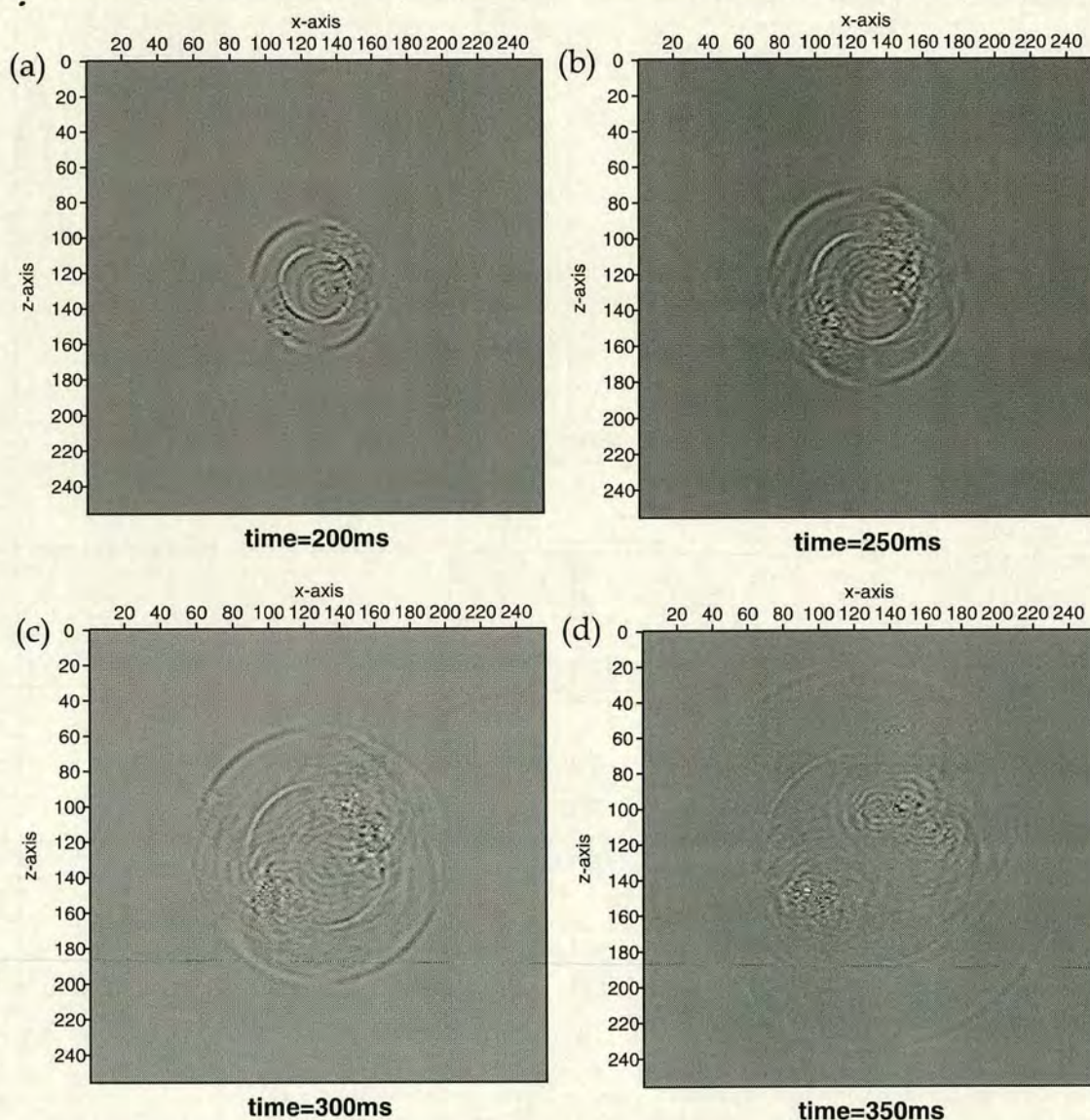

Figure 12. Snapshots from model in Fig. 11(a) taken at (a) $t = 200$ ms, (b) $t = 250$ ms, (c) $t = 300$ ms and (d) $t = 350$ ms.

staggered grid FDs, and by Chunlin Wu on variable grid FDs (Wu *et al.* 2002).

From the numerical examples we come to some interesting conclusions. First, we can see the importance of the spatial distribution of fractures in a medium. Our results show that in areas with fracture clustering, there is strong and coherent energy. Also, high clustering does result in high local fracture densities, which can cause the energy to be trapped in a certain area (localization processing), increasing the complexity of the wavefield and making individual phases and their identification very complicated. Also, we observe that different spatial distributions give different frequency content on the recorded wavefield. This as we might expect means that frequency-dependent seismic scattering depends on the spatial distribution of fractures (Leary & Abercrombie 1994). In addition, also of great importance is the fracture size relative to the wavelength, independent of the spatial distribution. It is demonstrated that when fractures are smaller than the wavelength, they act as single scatterers and generate secondary wavefields, whereas when the size approaches the wavelength they act as individual interfaces and the wavefield is more complicated. To complete our study, we examined the case of fracture sizes that follow a power-law or fractal distribution. The wavefield generated shows very strong coda waves and is very complicated. The observation confirms the importance of spatial and scale length distributions in modelling fractured rock.

Numerical modelling techniques, such as those presented here, can be a useful tool in the understanding of the important role of fractures and their effects on wave propagation. The knowledge gained by such studies may ultimately lead to the extraction of valuable information concerning the fracture distributions in natural rocks, directly from seismic data. In addition, our method may potentially provide a test of fracture imaging using seismic methods (as demonstrated by Nihei *et al.* 2000), and characterization of fractured reservoirs based on the concept of seismic scattering.

6 COLOUR ONLINE

Colour versions of Figs 2, 3, 8 and B1 are available online at Blackwell Synergy, www.blackwell-synergy.com.

ACKNOWLEDGMENTS

REFERENCES

Alford, R.M., Kelly, K.R. & Boore, D.M., 1974. Accuracy of finite-difference modelling of the acoustic wave equation, *Geophysics,* **39,** 834–842.

Benites, R., Aki, K. & Yomogida, K., 1992. Multiple scattering of *SH* waves in 2-D media with many cavities, *Pure appl. Geophys.,* **138,** 353–390.

Bonnet, E., Bour, O., Odling, N.E., Davy, P., Main, I., Cowie, P. & Berkowitz, B., 2001. Scaling of fracture systems in geological media, *Rev. Geophys.,* **39,** 347–383.

Chapman, C.H. & Drummond, R., 1982. Body-wave seismograms in inhomogeneous media using Maslov asymptotic theory, *Bull. seism. Soc. Am.,* **72,** 277–317.

Coates, R.T. & Schoenberg, M., 1995. Finite-difference modeling of faults and fractures, *Geophysics,* **60,** 1514–1526.

Fornberg, B., 1988. The pseudospectral method: accurate representation of interfaces in elastic wave calculations, *Geophysics,* **53,** 625–637.

Hentschel, H.G.E. & Proccacia, I., 1983. The infinite number of generalised dimensions of fractals and strange attractors, *Physica D,* **8,** 435–444.

Hill, R., 1963. Elastic properties of reinforced solids: some theoretical principles, *J. mech. Phys. Solids,* **11,** 357–372.

Hsu, C.-J. & Schoenberg, M., 1993. Elastic waves through a simulated fractured medium, *Geophysics,* **58,** 964–977.

Hudson, J.A. & Knopoff, L., 1989. Predicting the overall properties of composite materials with small-scale inclusions or cracks, *Pure appl. Geophys.,* **131,** 551–576.

Kachanov, M., 1984. Elastic solids with many cracks and related problems, *Adv. Appl. Mech.,* **30.**

Leary, P.C. & Abercrombie, R., 1994. Frequency dependent crustal scattering & absorption at 5–160 Hz from coda decay observed at 2–5 km depth, *Geophys. Res. Lett.,* **21,** 971–974.

Liu, E. & Zhang, Z., 2001. Numerical study of elastic wave scattering by cracks or inclusions using the boundary integral equation method, *J. comp. Acoust.,* **9,** 1039–1054.

Liu, E., Crampin, S. & Hudson, J.A., 1997. Diffraction of seismic waves with application to hydraulic fracturing, *Geophysics,* **62,** 253–265.

Liu, E., Hudson, J.A. & Pointer, T., 2000. Equivalent medium representation of fractured rock, *J. geophys. Res.,* **105,** 2981–3000.

Lysmer, J. & Drake, L.A., 1972. A finite element method for seismology, *Methods Computat. Phys.,* **11,** Academic Press, New York.

Mal, A.K., 1970. Interaction of elastic waves with a Griffith crack, *Int. J. eng. Sci.,* **8,** 763–776.

Mikhailenko, B.G., 2000. Seismic modeling by the spectral-finite difference method, *Phys. Earth planet. Inter.,* **119,** 133–147.

Muir, F., Dellinger, D., Etgen, J. & Nichols, D., 1992. Modeling elastic wavefields across irregular boundaries, *Geophysics,* **57,** 1189–1193.

Nihei, K.T. & Myer, L.R., 2000. Natural fracture characterisation using passive seismic waves, *Gas Tips,* Gas Technology Institute, US Dept. of Energy and Hart Publications Inc.

Nihei, K.T., Nakagawa, S. & Myer, L.R., 2000. VSP fracture imaging with elastic reverse-time migration, *70th Ann. Int. Mtg.: Soc. of Expl. Geophys.,* 1784–1751.

Pointer, T., Liu, E. & Hudson, J.A., 1998. Numerical modelling of seismic waves scattered by hydrofractures: application of the indirect boundary element method, *Geophys. J. Int.* **135,** 289–303.

Press, W.H., Teukolsky, S.A., Vetterling, W.T. & Flannery, B.P., 1997. *Numerical Recipes in Fortran 77: the Art of Scientific Computing (Vol. 1 of Fortran Numerical Recipies),* pp. 266–283, Cambridge University Press, Cambridge.

Pyrak-Nolte, L.J., Myer, L.R. & Cook, N.G.W., 1990. Transmission of seismic waves accross single natural fractures, *J. geophys. Res.,* **95,** 8617–8638.

Ricker, N.H., 1977. *Transient Waves in Visco-elastic Media,* Elsevier, Amsterdam.

Saenger, E.H. & Shapiro, S.A., 2002. Effective velocities in fractured media: a numerical study using the rotated staggered finite-difference grid, *Geophys. Prosp.,* **50,** 183–194.

Sayers, C.M. & Kachanov, M., 1995. Microcrack-induced elastic wave anisotropy of brittle rocks, *J. geophys. Res.,* **100,** 4149–4156.

Schoenberg, M., 1980. Elastic wave behaviour across linear slip interfaces, *J. acoust. Soc. Am.,* **68,** 1516–1521.

Schoenberg, M. & Sayers, C.M., 1995. Seismic anisotropy of fractured rock, *Geophysics,* **60,** 204–211.

662   *S. Vlastos* et al.

van Baren, G.B., Mulder, W.A. & Herman, G.C., 2001. Finite-difference modeling of scalar-wave propagation in cracked media, *Geophysics*, **66**, 267–276.

Wu, C., Harris, J.M. & Nihei, K.T., 2002. 2-D finite-difference seismic modelling of an open fluid-filled fracture comparison of thin-layer and linear-slip models, *72nd SEG Ann. Int. Mtg. Exp. Abs.: Soc. of Expl. Geophys.*, 1959–1962.

Wu, R.S., 1982. Attenuation of short period seismic waves due to scattering, *Geophys. Res. Lett.*, **9**, 9–12.

Wu, R.S. & Aki, K., 1985. Scattering characteristics of elastic waves by an elastic heterogeneity, *Geophysics*, **50**, 582–589.

APPENDIX A: EFFECTIVE COMPLIANCE OF A FRACTURED MEDIUM

Effective medium calculus is used to calculate the elastic parameters that are associated with a given cell through which a fracture passes. In the simple case of an unfractured cell, where the cell is occupied only by the background rock, the calculation of the compliance tensor is straightforward. Assuming that we know the elastic parameters of the host rock, we calculate the compliance tensor s^0_{ijkl} as follows:

$$\mu = \rho V_s^2,\tag{A1}$$

$$\lambda = \rho \left(V_P^2 - 2V_S^2\right),\tag{A2}$$

$$\left(s^0_{ijkl}\right)^{-1} = c_{ijkl} = \begin{bmatrix} \lambda + 2\mu & \lambda & \lambda & 0 & 0 & 0 \\ \lambda & \lambda + 2\mu & \lambda & 0 & 0 & 0 \\ \lambda & \lambda & \lambda + 2\mu & 0 & 0 & 0 \\ 0 & 0 & 0 & \mu & 0 & 0 \\ 0 & 0 & 0 & 0 & \mu & 0 \\ 0 & 0 & 0 & 0 & 0 & \mu \end{bmatrix}.\tag{A3}$$

where V_P and V_S are the P- and S-wave velocities in the medium, respectively, c_{ijkl} is the 6×6 matrix form of the stiffness tensor for the unfractured medium, and λ and μ are the Lamé constants.

In the presence of fractures the average strain ϵ in an elastic homogeneous solid with volume V containing N_f fractures with surfaces S_r ($r = 1, 2, \ldots, N_f$) can be written as

$$\epsilon_{ij} = \left(s^0_{ijkl} + s^f_{ijkl}\right)\sigma_{kl},\tag{A4}$$

where σ is the average stress tensor, s^0_{ijkl} is the matrix compliance tensor in the absence of the fractures and s^f_{ijkl} is the extra compliance tensor resulting from the fractures. The additional strain is given by (Hill 1963; Hudson & Knopoff 1989),

$$s^f_{ijkl}\sigma_{kl} = \frac{1}{2V}\sum_{r=1}^{N_f}\int_{S_r}([u_i]n_j + [u_j]n_i)\,dS,\tag{A5}$$

where u_i is the ith component of the displacement discontinuity on S_r and n_i is the ith component of the fracture normal. If all fractures are aligned with fixed normal n, we may replace each fracture in V by an average fracture having a surface area S and a smoothed linear slip boundary condition given by

$$[\bar{u}_i] = Z_{ip}t_p,\tag{A6}$$

where t_p is the traction on the fracture, $[\bar{u}_i]$ is the average displacement discontinuity on the fracture and the quantities $\{Z_{ip}\}$ depend on the interior conditions and infill of the fracture (Sayers & Kachanov 1995; Schoenberg & Sayers 1995). The traction t_p is linearly related to the imposed mean stress σ or, more precisely, to the traction $\sigma_{pq}n_q$

that would exist on the crack face if the displacements were constrained to be zero.

Liu *et al.* (2000) used a model of a simple fracture in an unbounded medium and proposed that the traction can be written as

$$t_p = \sigma_{pq}n_q,\tag{A7}$$

eq. (A6) becomes

$$[\bar{u}_i] = Z_{ip}\sigma_{pq}n_q.\tag{A8}$$

Inserting eq. (A8) into eq. (A5) and after some tensor algebra, we obtain

$$s^f_{ijkl}\sigma_{kl} = \frac{N_f S}{4V}(Z_{ik}n_l n_j + Z_{jk}n_l n_i + Z_{il}n_k n_j + Z_{jl}n_k n_i)\sigma_{kl},\tag{A9}$$

where S is the mean area of fracture; so the fracture induced excess compliance s^f_{ijkl} is

$$s^f_{ijkl} = \frac{D_f}{4}(Z_{ik}n_l n_j + Z_{jk}n_l n_i + Z_{il}n_k n_j + Z_{jl}n_k n_i),\tag{A10}$$

where D_f is

$$D_f = \frac{N_f S}{V}.\tag{A11}$$

If the fracture set is statistically invariant under rotations about n, only two terms in $\mathbf{Z}$ are required (Schoenberg & Sayers 1995); a normal fracture compliance Z_N and a tangential compliance Z_T. Thus

$$Z_{ij} = Z_N n_i n_j + Z_T(\delta_{ij} - n_i n_j) = Z_T\delta_{ij} + (Z_N - Z_T)n_i n_j,\tag{A12}$$

where δ_{ij} is the Kronecker delta. By inserting (A12) into (A10), we have

$$s^f_{ijkl} = \frac{D_f}{4}[Z_T(\delta_{ik}n_l n_j + \delta_{jk}n_l n_i + \delta_{il}n_k n_j + \delta_{jl}n_k n_i)$$
$$+ 4(Z_N - Z_T)n_i n_j n_k n_l].\tag{A13}$$

Following Coates & Schoenberg (1995), in the case of 2-D media in a grid cell intersected by a fracture, eq. (A11) becomes

$$D_f = \frac{N_f \Delta l}{\Delta A},\tag{A14}$$

where Δl is the length of the segment of the fracture lying within the cell and ΔA is the area of the 2-D cell. If L is defined for each cell intersected by a fracture so that

$$\frac{1}{L} \equiv \frac{\Delta l}{\Delta A},\tag{A15}$$

then eq. (A13) finally becomes

$$s^f_{ijkl} = \frac{N_f}{4L}[Z_T(\delta_{ik}n_l n_j + \delta_{jk}n_l n_i + \delta_{il}n_k n_j + \delta_{jl}n_k n_i)$$
$$+ 4(Z_N - Z_T)n_i n_j n_k n_l],\tag{A16}$$

which is the equation we use for the calculation of the excess compliance tensor. So the induced excess compliance tensor of a cell depends on the normal Z_N and the tangential Z_T fracture compliance, the number N_f of the fractures inside the cell, the length Δl of each fracture (or segment of fracture) and the orientation of each fracture estimated by the normals n. The total compliance tensor for the fractured cells is the effective compliance tensor s^{eff}_{ijkl}, which characterizes the cell and is

$$s^{\text{eff}}_{ij} = s^0_{ijkl} + s^f_{ijkl}.\tag{A17}$$

If we want to determine the stiffness c_{ijkl}, we transform s_{ijkl} to the conventional (two-subscript) condensed 6×6 matrix notation, $11 \rightarrow 1, 22 \rightarrow 2, 33 \rightarrow 3, 23 \rightarrow 4, 13 \rightarrow 5, 12 \rightarrow 6$, with factors of 2 and 4 introduced as follows: $s_{ijkl} \rightarrow s_{pq}$ when both of P, q are 1, 2, or 3; $2s_{ijkl} \rightarrow s_{pq}$ when one of p, q is 4, 5 or 6; and $4s_{ijkl} \rightarrow s_{pq}$ when p, q are any of 1, 2, 3, 4, 5 or 6. The inverse of the compliance matrix s_{pq} gives the effective elastic constants or stiffness matrix c_{pq}. Using the same transformation as for the compliance, we transform the stiffness from the condensed (two-subscript) to the normal notation $(c_{pq} \rightarrow c_{ijkl})$.

APPENDIX B: EFFECTS OF FRACTURE TIPS

An important parameter in the accurate modelling of natural fractured rocks is the realistic implementation of the effects of fractures in wave propagation. The main issue is the realistic representation of the finite extent of a fracture, and especially the two fracture tips. To exhibit the end of the fracture at both tips, we should have no displacement outside those points, thus the compliance tensor Z should be 0. A way of expressing the change in the compliance is to keep the compliance constant along the fracture and drop to 0 at the crack tips. However, the sudden drop of the value is not very realistic, and there is no similar case in natural systems that demonstrates extreme changes of values. We believe that it is more realistic to represent the changes in Z as a gradual reduction towards 0 at the fracture tips. Following Kachanov (1984) the compliance at each point of the fracture is given by

$$Z = Z_{max}[1 - (x/l)^2]^{1/2}, \tag{B1}$$

where Z_{max} is the maximum value of the compliance in the centre of the fracture, l is half the length of the fracture and x is the x-coordinate of the position of a point in the fracture. The coordinates of the right and the left fracture tips are $+l$ and $-l$, respectively. From eq. (B1), for the centre of the fracture ($x = 0$) the compliance is $Z = Z_{max}$, whilst for the fracture tips ($x = \pm l$) the compliance is $Z = 0$. So the value of the compliance is maximum in the centre of the fracture and reduces gradually following a hyperbolic function until it reaches 0 in both fracture tips. As we can see from
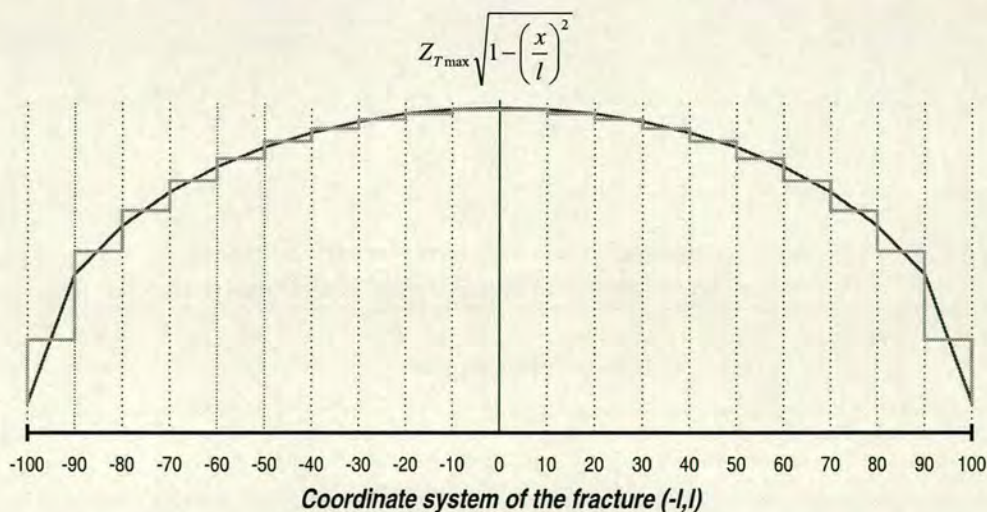

Figure B2. Model used to examine the effect of the fracture tips on the wavefield.

eq. (B1) the rate of reduction depends on the size $2l$ of the fracture, so the larger the fracture, the more gradually the compliance reduces.

In Appendix A we described the implementation of fractures in the finite-difference grid and the calculation of the effective compliance of a fractured medium. Eq. (A16) calculates the excess compliance tensor, which expresses the fracture influence. The excess compliance tensor is estimated for each of the fractured grid cells of the medium, thus the value of the compliance Z should remain constant inside each grid cell. To calculate the compliance for each of the grid cells, from eq. (B1) we find the values of the compliance for the two nodes of each cell, and take the average of the two values as the effective value of the compliance throughout the cell. This is illustrated in Fig. B1, where the curve represents the value of the compliance following eq. (B1), and the stepped line is the average

$$Z_{T\,max}\sqrt{1 - \left(\frac{x}{l}\right)^2}$$

Coordinate system of the fracture (-l,l)

Figure B1. Schematic representation of the reduction of the value of compliance Z along a fracture. The curve represents the value of compliance following eq. (B1) of Kachanov (1984). The stepped line represents the way we approximate that function in our implementation.
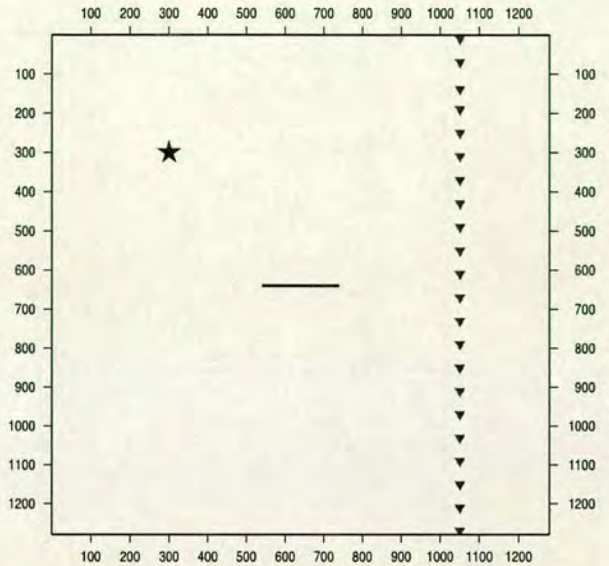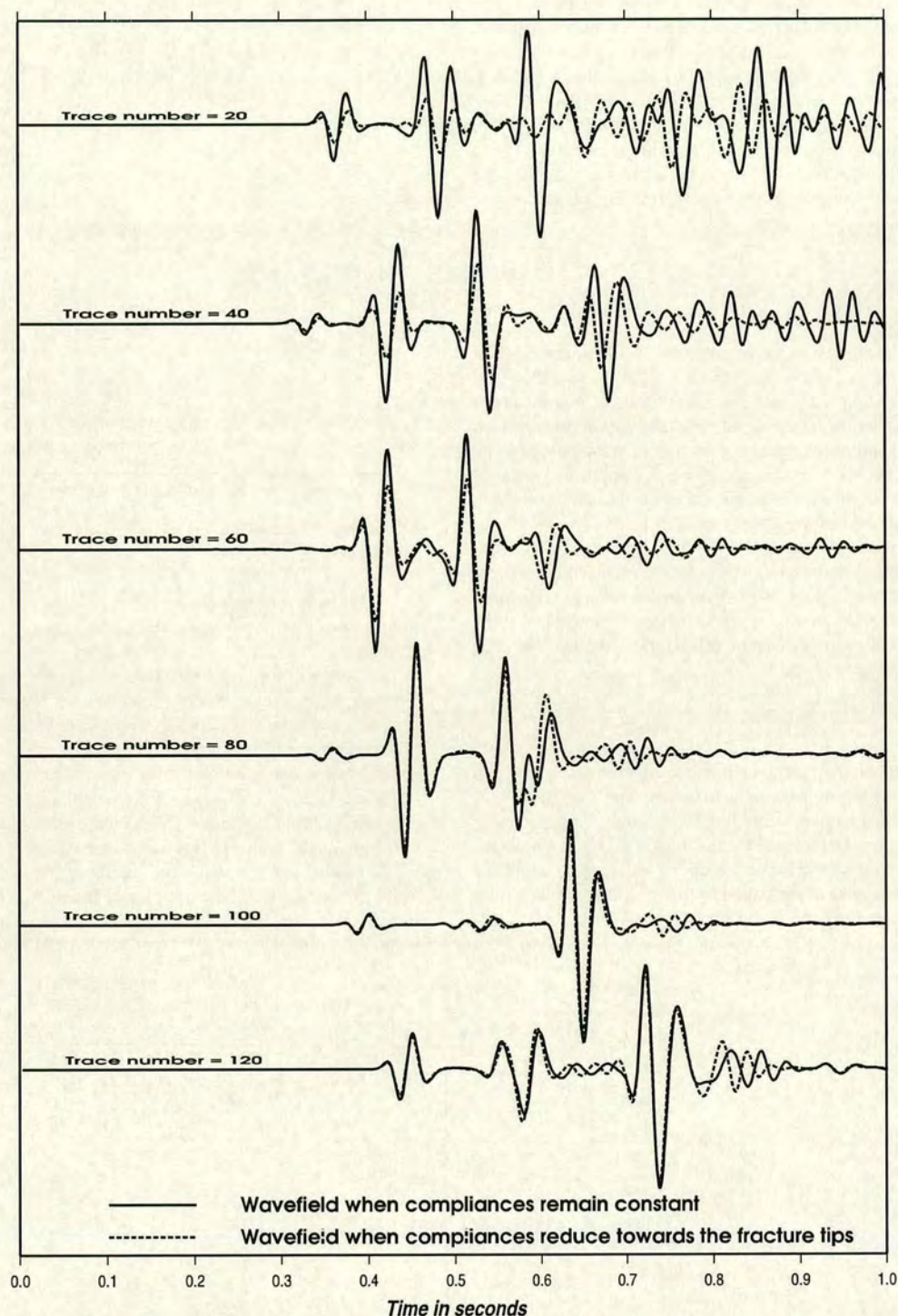
664   *S. Vlastos* et al.

Figure B3. Comparison of the wavefields generated by two different implementations of the fracture compliance. Solid-line wavelets represent the case of a constant compliance that drops to 0 at the fracture tips, while dotted-line wavelets represent our implementation, based on Kachanov's (1984) concept, where the compliance reduces gradually. The trace numbers correspond to depths 200, 400, 600, 800, 1000 and 1200 m.

value of the compliance we use for each grid cell. In the case where a grid cell is intersected by multiple fractures (or parts of fractures) the compliance is taken to be the average value of the compliances arising from each of the fractures independently.

To understand the effect of the fracture tips on the wavefield, we model the case of a single fracture in which, in the first case, the compliance remains constant throughout the fracture and drops to 0 at the tips, and, in the second case, the compliance reduces

following our implementation. The model we use is presented in Fig. B2. For the two cases we compare the wavelets of a number of traces and the results are presented in Fig. B3. The wavelets presented in Fig. B3 do not include direct waves, because they are not affected by the fracture tips, and so are identical. Also, the amplitude of the wavelets is normalized between the several traces. However, the relative amplitude between the wavelets for each individual trace remains accurate. From the comparison between the wavelets, we first observe that there is a time difference between the *SS* waves when we have constant compliance and when the compliances reduce gradually, with *SS* waves of the latter case being slower. This may be a result of the sensitivity of *S* waves to changes of anisotropy. By changing the compliance from constant to variable, we effectively change the anisotropy, and this is only visible in the *SS* wavelets. However, when we observe the wavelets from traces 100 and 120 we see that the time difference in the *SS* waves disappears. The waves observed at those receivers come from waves diffracted from the crack tips and from waves refracted at the fracture, in contrast to the rest of the receivers, where we have diffracted and reflected waves. Also, we can observe variations in the amplitude. In traces 20, 40 and 60, where the receivers are above the fracture, so we have reflected and diffracted waves, the amplitude of the waves when the compliance is constant is higher than the amplitude when the compliance follows our implementation. On the other hand, in trace 80, when the waves are only diffracted, we have opposite results. Finally, in traces 100 and 120, where we have refracted and diffracted waves, the amplitudes seem to be almost identical. We see that reflection and refraction are decisive factors in the wavelet pattern. More research needs to be done on these topics to examine how they affect the waves.

Another parameter that we have not examined is the effect of the length of the fracture. From eq. (B1) we can see that if we have a fracture of short length *l* then the reduction of the compliance would be severe, whilst when the fracture is very large we will have a very smooth reduction that can approximate the case of the constant compliance throughout the fracture. This has to be tested by modelling various sizes of fractures and the respective wavelets, to find out at what point the approximation of constant compliance is satisfactory.

APPENDIX C: GENERATION OF FRACTURE DISTRIBUTIONS

Scaling in fracture systems has become an active field of research over the previous 25 years motivated by practical applications. In the case of the hydrocarbon industry, scaling laws provide a key to predicting the nature of subseismic fracturing (below the limit of seismic resolution), which can significantly influence reservoir and cap rock quality, from seismically resolved faults. The numerous studies of fracture-system scaling in the literature do indeed suggest that scaling laws exist in nature. They also indicate, however, that such scaling laws must be used with caution and with due regard to the physical influences that govern their validity. Over recent years the power-law distribution has been increasingly employed to describe the frequency distribution of fracture properties and geometry. However, a power law is not an appropriate model in all cases, and other distributions that have been used include the log-normal, gamma and exponential laws.

In the main part of this paper, we examine the effect of different spatial distributions of fractures on the wave propagation. The fractures are distributed as follows: (a) a random uniform, (b) a Gaussian, (c) an exponential and (d) a Gamma distribution, as shown in Fig. 4. The algorithm utilizes a different random number generator (Press *et al.* 1997), which varies according to the distribution we want to simulate. For each distribution, the generator is applied once to give *x*-coordinates, and completely independently once more to give *z*-coordinates. Both *x*- and *z*-coordinates are afterwards normalized to the grid size of the model.

These pairs of *x*- and *z*-coordinates are the centres of the distributed fractures. The resulting distribution of fractures, without any alterations, is the parent spatial distribution. The size and orientation of the fractures are given as an input to the algorithm. In this paper all the fractures are parallel to the grid. Subsequently, the algorithm examines the fractures for any overlapping cases. We define overlapping as the case where the distance between the centres of two fractures is less than a predefined value. In the current application of the algorithm, we examined only the horizontal distances between pairs of fracture centres having the same *z*-coordinate. For simplicity in this paper we deliberately avoid modelling intersected cracks, that is, conjugate fracture sets. However, in theory, such a case can also be modelled with the method we use. In this case, the second overlapping fracture is excluded from the distribution. After testing for overlapping, the remaining number of distributed fractures is counted. If that number is less than desired, the resulting distribution of fractures is rejected. The number of fractures following the parent spatial distribution is raised by 5. A new group of fractures, spatially distributed according to the parent distribution, is chosen. The new group of fractures follows the same procedure that we described above. This process continues until the desired number of non-overlapping spatially distributed fractures is reached. A flow chart of the filtering algorithm is presented in Fig. C1. The final spatial distribution of the fractures is a result of the parent distribution after applying data filtering, so we call this the daughter spatial distribution. The spatial correlation in the daughter population is then determined by the two-point correlation function of the fracture centre locations in two dimensions. Figs C2–5 show the independent probabilities $P(x)$ and $P(z)$ as a function of the *x*- and *z*-coordinates of the centres of the fractures, for the daughter distributions (a)–(d) of Fig. 4. In the same figures we show the two-point correlation function $C(r)$, for each of the four parent distributions, defined as

$$C(r) = \frac{1}{N^2} N_d(r), \tag{C1}$$

where *N* is the total number of points and N_d is the number of pairs of points where the distance is less than *r* (Hentschel & Proccacia 1983).

The probability plots in Figs C2–5 confirm that the random number generator does create random uniform, Gaussian, exponential and Gamma distributions, respectively, of centres of fractures along the two grid directions. The two-point correlation functions of the parent spatial distributions, are shown in Figs C2(c), C3(c), C4(c) and C5(c). The random uniform distribution has correlations that peak in the medium range, the Gaussian and the exponential peak in the short range, and the Gamma is the most broad-band distribution. Thus the ratio of wavelength to correlation length will be greatest for the random uniform distribution, and smallest for the Gamma distribution.
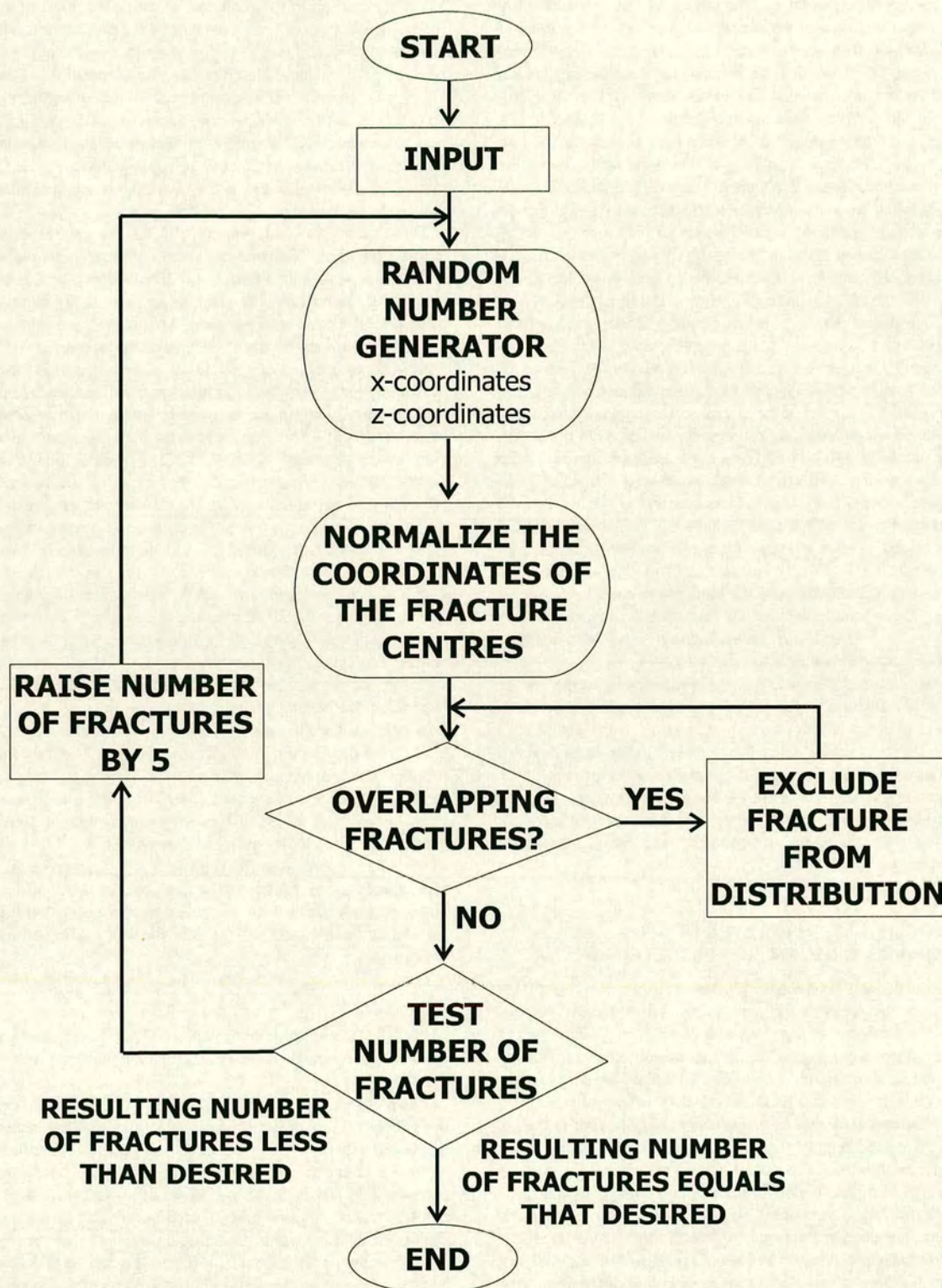
666   *S. Vlastos* et al.

Figure C1. Flow chart of the algorithm used to generate the four spatial distributions of fractures shown in Fig. 4.
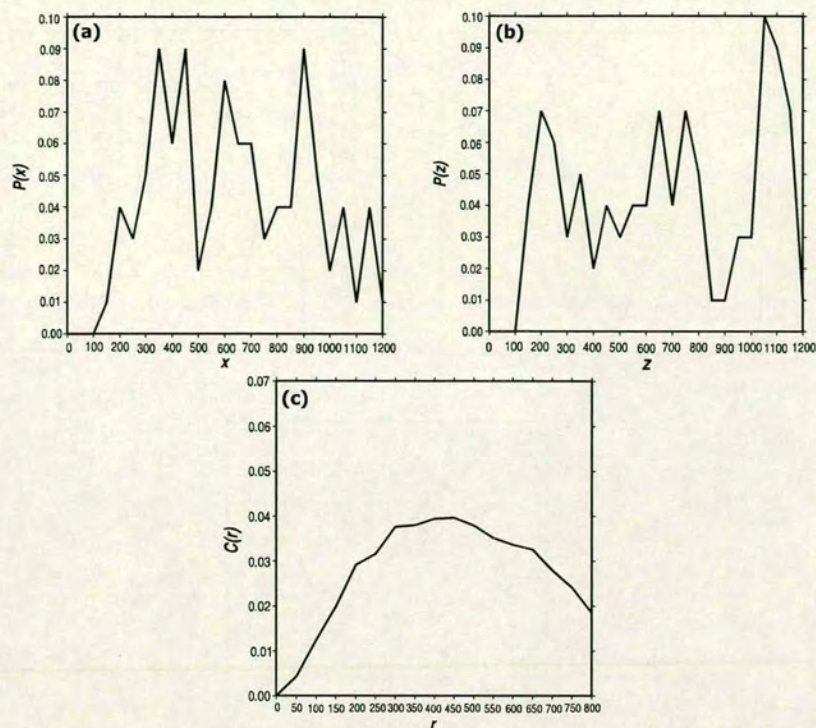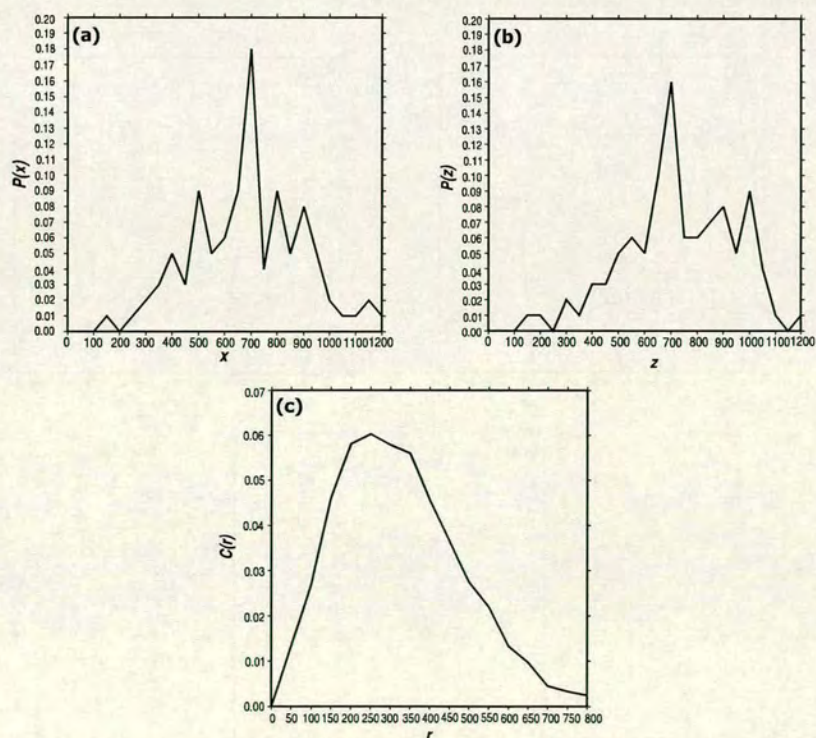
Figure C2. Statistical properties of the random uniform distribution of fractures in Fig. 4(a). (a) Probability plot of the coordinate of the centre of fractures along the *x*-direction, (b) probability plot of the coordinate of the centre of fractures along the *z*-direction, (c) two-point correlation function of the parent distribution of fractures.

Figure C3. Statistical properties of the Gaussian distribution of fractures in Fig. 4(b). (a) Probability plot of the coordinate of the centre of fractures along the *x*-direction, (b) probability plot of the coordinate of the centre of fractures along the *z*-direction, (c) two-point correlation function of the parent distribution of fractures.
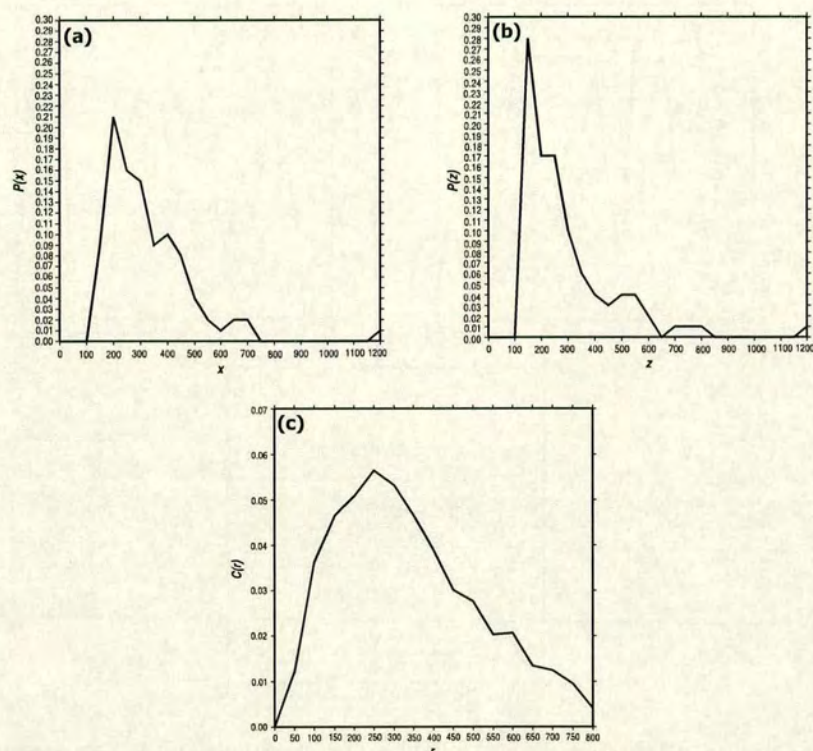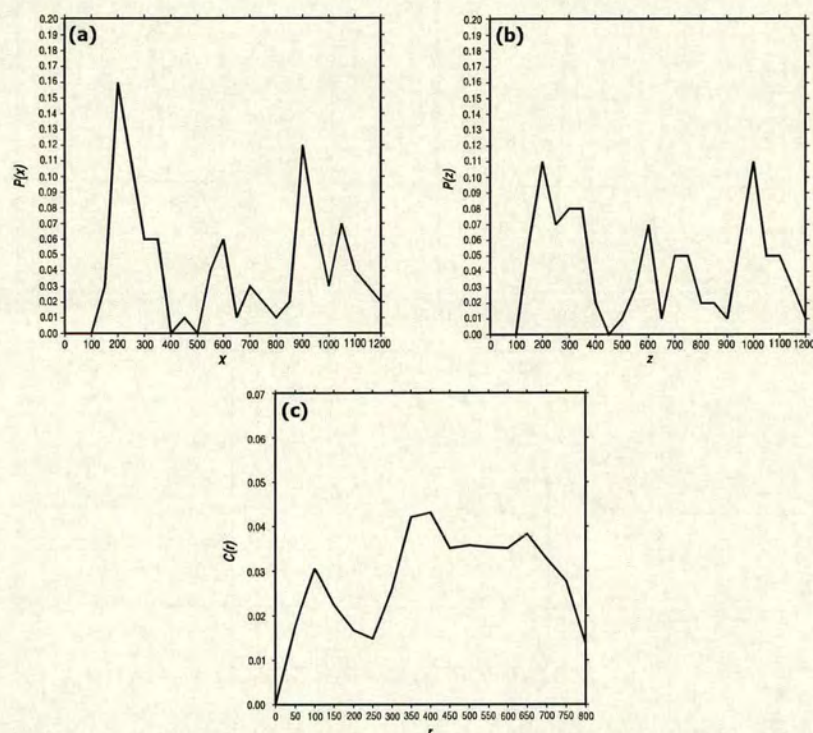
668   *S. Vlastos* et al.

Figure C4. Statistical properties of the exponential distribution of fractures in Fig. 4(c). (a) Probability plot of the coordinate of the centre of fractures along the x-direction, (b) probability plot of the coordinate of the centre of fractures along the z-direction, (c) two-point correlation function of the parent distribution of fractures.

Figure C5. Statistical properties of the Gamma distribution of fractures in Fig. 4(d). (a) Probability plot of the coordinate of the centre of fractures along the x-direction, (b) probability plot of the coordinate of the centre of fractures along the z-direction, (c) two-point correlation function of the parent distribution of fractures.

Modeling seismic wave propagation during fluid injection in a fractured network: Effects of pore fluid pressure on time-lapse seismic signatures

ENRU LIU, SERAFEIM VLASTOS, and XIANG-YANG LI, Edinburgh Anisotropy Project, British Geological Survey, U.K.
IAN G. MAIN, School of GeoSciences, University of Edinburgh, U.K.
MICHAEL SCHOENBERG, Lawrence Berkeley National Laboratory, California, U.S.

Fluid flow in the earth's crust plays an important role in a number of geologic processes. In carbonate reservoirs, fluid flow is thought to be controlled by open macrofractures. The movement of fluids in the fractured media results in changes in the pore pressure and consequently causes changes in the effective stress, traction, and elastic properties. Many recent examples in time-lapse or 4D seismic surveys have demonstrated that seismic waves can be used to monitor changes in oil or gas reservoirs as a function of time (e.g., Landrø, 2002; Angerer et al., 2002).

During production from a reservoir, the movement of fluids is accompanied by substantial change in the pore pressure field. As fluids drain, pore pressure decreases, which increases the effective pressure on fractures, grain boundaries, and microcracks. Higher static load on these surfaces decreases their compliance nonlinearly and decreases fracture opening and/or pore throat size, thus increasing the stiffness of the rock (by increasing compressional and shear velocities) and decreasing permeability (Schoenberg, 2002). Conversely, pore pressure buildup due to injection leads to a decrease in effective pressure and an increase in rock compliance.

Fractured rock is often modeled as a relatively rigid, defect-free, "background" medium with embedded sets of linear slip interfaces. A linear slip interface is a surface across which anomalously large strain occurs due to the passage of a wave. In linear slip deformation theory, the large strain is approximated by a displacement discontinuity across the surface that is linearly related to the dynamic traction acting on the interface (to the first order). The dynamic elastic properties of the rock are determined by adding the compliance tensor of the background to an excess fracture compliance tensor associated with the fractures (e.g., Liu et al., 2000). The linear parameters governing the infinitesimal slip on these planes have been shown to depend on the static stress state in a highly nonlinear and most likely hysteretic manner. If such relations are established, we may begin to be able to predict static effective stress based on dynamic properties (wave speeds and their associated polarizations) and ultimately explore the pore pressure field changes induced by reservoir drainage or other fluid movement.

The main purpose of this study is to examine the effect of pore pressure changes on seismic wave propagation (i.e., amplitude, frequency, etc.). This is achieved by using a dual simulation of fluid flow and seismic propagation in a common fracture network (developed by Vlastos et al., 2004). The flow simulation updates the pore pressure at consecutive time steps, and thus the elastic properties of the rock, for the seismic modeling. The simulation allows us to effectively evaluate the validity of inferring changes in fluid properties directly from seismic data. Our results indicate that P-waves are not as sensitive to pore pressure changes as S-waves or coda (scattered) waves. The increase in pore pressure causes a shift of the energy toward lower frequencies, as shown by changes in the spectrum (as a result of attenuation). In addition, the fluid effects on the wavefield vary significantly with the source-receiver direction (i.e., the azimuth relative to the fracture orientation).

Simulation of fluid injection. At a macroscopic scale, fluid flow in porous rocks and fracture zones can be considered an anisotropic diffusive process that varies spatially and temporally by several orders of magnitude. At this scale, pore pressures can also have high local variations. Injecting fluids into a porous rock mass at sufficiently high pressures results in two possible fracture processes—hydraulic fracturing or induced seismicity—depending on the fluid and rock properties and the local stress field. However, because changes in the fracture network will complicate the identification of pore pressure changes in seismic signatures, we have chosen to keep the fracture network unchanged. This type of model is "static" in terms of the stress field, and the fracture network is used only to account for the porosity and permeability. We assume that both fluid and solid phases are chemically inert and at constant temperatures, that the implicit void spaces are fully connected and that the porosity ϕ is uniform and constant. Only the single phase of fluid is considered. We combine mass conservation, Darcy's law and a linear equation of state [$\rho_f = \rho_{f0}(1+\rho/K_s)$], to obtain the time evolution of the fluid pressure ρ:

$$\frac{\partial \rho}{\partial t} = \frac{\partial}{\partial x_i}\left(D_{ij}\frac{\partial \rho}{\partial x_j}\right) \qquad (1)$$

where ρ_{f0} is the fluid density at the initial stress state, ρ_f is the fluid density at pressure ρ, and K_s is the bulk modulus of the solid.

$$D_{ij}(x,y,t) = \frac{K_s}{\phi\eta}K_{ij}(x,y,t) \qquad (2)$$

Equation 2 is the diffusivity tensor, and η and $K_{ij}(x,y,t)$ are the viscosity of the fluid and the permeability tensor of the matrix, respectively. We use the lattice Boltzmann method to solve equation 1, which is valid for the most general media with anisotropic, heterogeneous and time-dependent diffusivity.

In the examples presented below, we have implemented the fluid flow model in 2D using a 256 x 256 "d2q9" lattice for the BGK diffusion model. Following the terminology of Quian et al. (1992), a "d2q9" lattice is a 2D square lattice where each node is connected to eight neighbors; four horizontally and vertically, and four at 45°. The boundary conditions are periodic, where the top side of the grid links to the bottom side, and the left side to the right side. The plane of computation is horizontal, justifying the absence of a gravity term in equation 1. An injection well is inserted in the center. The dimension of the model is characterized by the length scale L that represents the overall extent of the grid, and the timescale T that represents the duration of
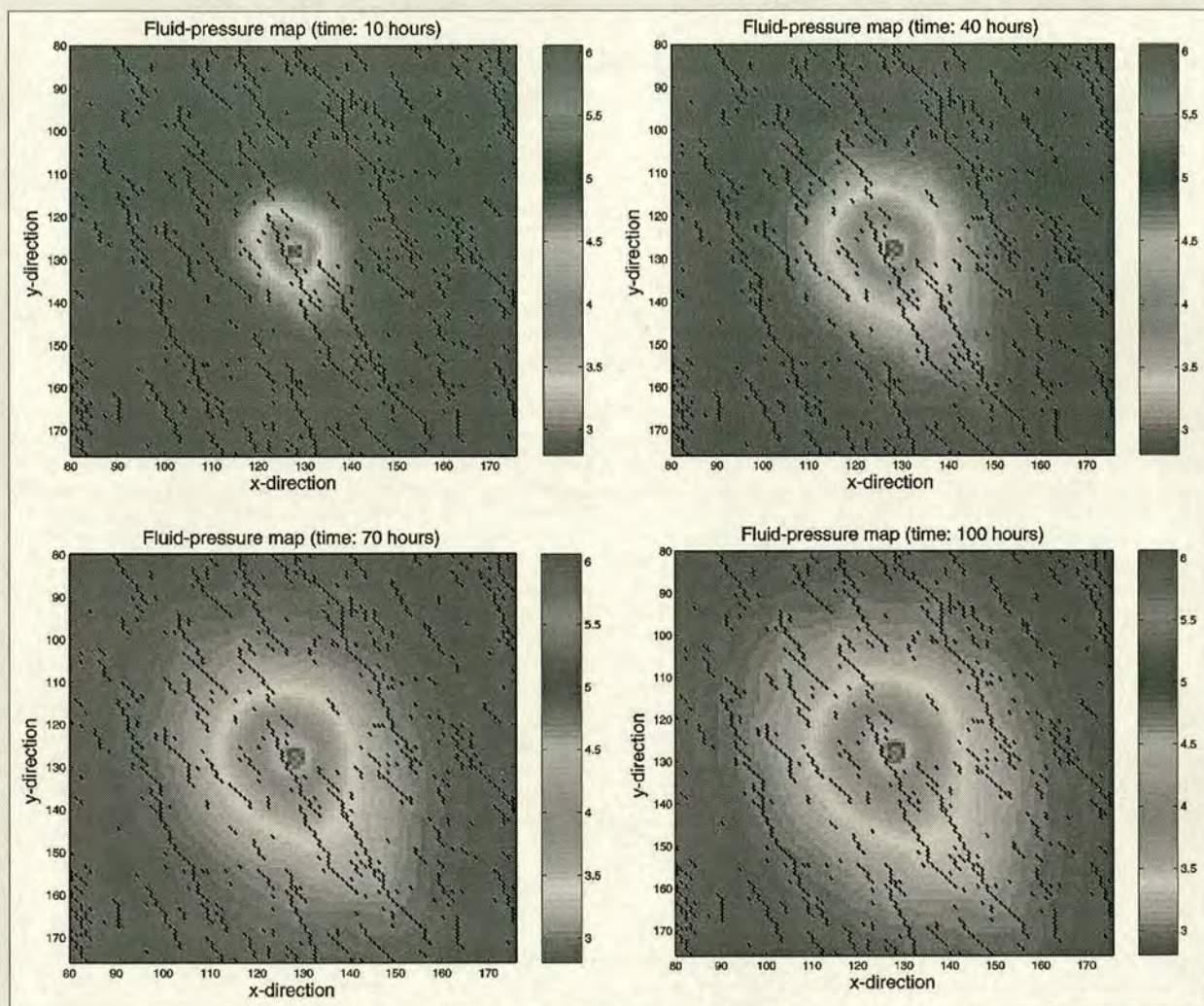
Figure 1. Pore-pressure maps in a small area around the injection point (1000 × 1000 m) at four consecutive times, 10, 40, 70, and 100 hours, after the initialization of the injection of the fluid. The black lines are the pre-existing fractures.

the fluid injection at the well. The spatial discretization is Δx=10 m, and therefore the dimension of the model is 2560 x 2560 m. In the model, the diffusivity for unfractured (isotropic) background rock is D=10^{-3}m^{2}s^{-1}. In the fractures, the principal components are D_1 along the local direction of the fractures and D_2 normal to the fractures, with D_1=10^4D and D^2=10^2D. The time step is Δt_d=1 s.

We examine the case of a pre-existing, hydraulically conductive, fracture network with fluid injected in the center of the model. Figure 1 shows the resulting pore-pressure maps at 10, 40, 70 and 100 hours after the initialization of the injection.

Effects of pore pressure on fracture compliance. Fracture surfaces, grain boundaries, microcracks and joint faces are much more compliant and thus sensitive to stress than intact rock. Fractured rock properties therefore are analyzed based on fracture compliance. Fracture anisotropy that changes as the traction on the fractures varies with pore pressure properties of the intact background rock are assumed to be constant. During fluid injection, pore pressure generally increases, resulting in a decrease in the effective pressure on fractures, grain boundaries and micro cracks. Lower static load on such surfaces increases the compliance in a non-

linear way and increases fracture opening and/or pore throat size, thus decreasing the stiffness of the rock (decreasing compressional and shear velocities) and increasing permeability (Schoenberg, 2002). The model that we examine here has nearly parallel 2D fractures, i.e., the fracture direction lies in the (1,2)-plane (Figure 1). We consider the effects on this model when subjected to an anisotropic external stress field with principle external stresses denoted by σ_x, σ_y and σ_z in the 1-, 2-, and 3-directions, respectively.

As a simple assumption, let the fracture compliances at any angle be independent of the tangential component of effective stress traction on the fracture faces and dependent on the normal component, $\tau \perp (\theta)$, given by:

$$\tau_\perp(\theta) = -\rho + \frac{\sigma_x + \sigma_y}{2} + \frac{\sigma_x - \sigma_y}{2} cos2\theta \qquad (3)$$

where θ is the angle relative to the normal direction of fractures, ρ is the pore pressure, and σ_x and σ_y the principal stresses in the horizontal 1- and 2-directions. We assume highly compliant fractures at low normal stress with fracture compliances asymptotically approaching low values as normal stress becomes large (Schoenberg, 2002). Approximating such dependence by an exponential decay function (neglecting any hysteretics) yields:
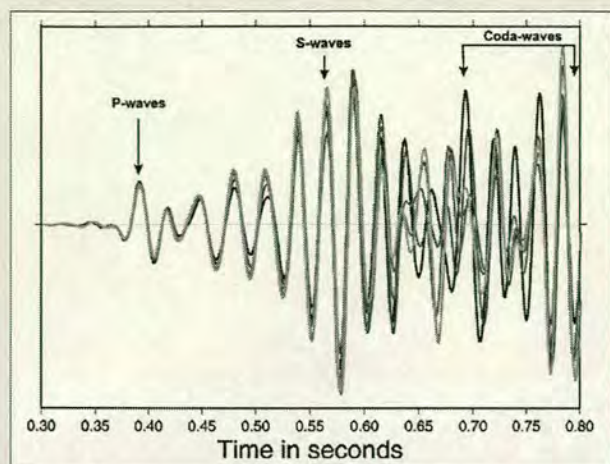
Figure 2. Wavelets recorded at a receiver located at x=1000 m and y=300 m for consecutive pore pressure stages. Black represents the pre-injection stage, and red, green, blue, and orange represent 10, 40, 70 and 100 hours after the injection, respectively.
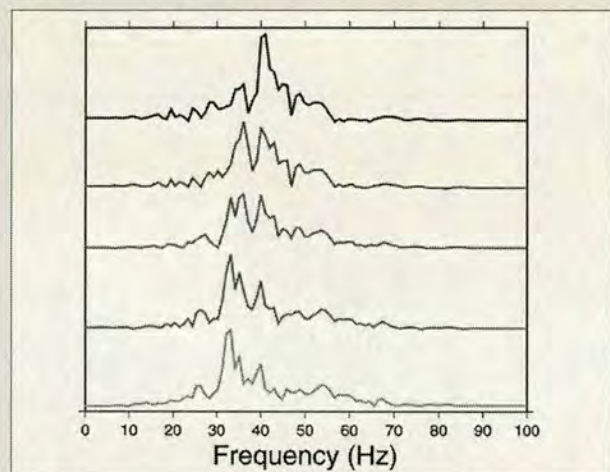

Figure 3. Spectrum of the waveforms shown in Figure 2 representing different stages of the fluid injection. The color code corresponds to the one used in Figure 2.

$$Z_N(\theta) = Z_{N_\infty}(\theta) + [Z_{N_0}(\theta) - Z_{N_\infty}(\theta)]e^{-\tau L(\theta)/\tau_N(\theta)} \qquad (4)$$

$$Z_T(\theta) = Z_{T_\infty}(\theta) + [Z_{T_0}(\theta) - Z_{T_\infty}(\theta)]e^{-\tau L(\theta)/\tau_T(\theta)} \qquad (5)$$

for a general case where the parameters governing the exponential decay functions are themselves functions of θ. However, in the model examined, $\tau_T, \tau_N, Z_{T_0}, Z_{T_\infty}, Z_{N_0}$ and Z_{N_∞} are not functions of θ. The coefficients τ_T and τ_N have been empirically set to 1.35 MPa. The compliances at zero stress are $Z_{T_0} = 5.681 \cdot 10^{-9} GPa^{-1}$ and $Z_{N_0} = 2.8409 \cdot 10^{-10} GPa^{-1}$, and the compliances at infinite stress are $Z_{T_\infty} = Z_{T_0}/5$ and $Z_{N_\infty} = Z_{N_0}/2$.

Seismic simulation using finite difference method. From equations 4 and 5, we compute the effect of the pore pressure changes on fracture compliance, from which we can compute the dynamic effective elastic properties of the rock (e.g., Liu et al., 2000).

Then we use a finite-difference method that can simulate wave propagation in complicated fractured networks with fractures at arbitrary angles (Vlastos et al., 2003) to examine the potential of extracting information about the pore pressures directly from seismic waves.

Figure 2 shows an example of the *x*-component of the waves recorded at a receiver located at *x*=1000 m and *y*=300 m at consecutive stages of the injection numerical simulation. The source of the seismic waves is located at the center of the medium (*x*=1280 m, *y*=1280 m), exactly at the same position as the fluid injection point, so the waves traveling to the receivers will be greatly affected by pore-pressure changes. In the y-direction, the source-receiver angle is 16° while the average fracture direction angle is 30°. The source-receiver angle relative to the fracture normal direction averages 104°. The waveform in black (Figure 2) is recorded at the pre-injection stage when pore pressure is equal throughout the model (used as a reference). The waveforms in red, green, blue and orange are recorded at 10, 40, 70, and 100 hours after the initialization of the fluid injection, respectively. Generally we can see variations on the features of the waves as pore pressure changes. The direct P-wave at 0.37 s does not seem significantly affected by pore pressure changes. In contrast, the shear wave and the coda waves exhibit strong amplitude changes attributed to the pore pressure changes. In addition, pore pressure affects the spectrum (Figure 3). As pore pressure builds, there is a gradual shift of shear-wave energy towards lower frequencies, indicating systematic increase of attenuation. The magnitude of the peak frequency shift is about 10 Hz. The P-wave amplitudes are less affected when compared to the shear-waves, which agree with the laboratory results of Prasad (2002).

It is common in time-lapse seismic monitoring to examine the difference in measurements for two consecutive time-steps, to evaluate the effect of pore pressure changes. We conducted forward modeling for the pre-injection state, and the states 10, 40, 70, and 100 hours after the fluid injection. Snapshots of the seismic wave are generated for each simulation at 150, 250, 350, and 450 ms, after the initialization of the source. To examine the effect of pore pressure changes, we determine the difference between the pre-injection stage and the snapshots of each stage after injection. Figures 4 and 5 show examples of the snapshots at consecutive time steps, which are the results of the difference between the simulation stages at 70 and 100 hours after the fluid injection and the pre-injection stage, respectively. From Figures 4 and 5 we can see that the area of strong differences in the seismic signal have an elliptical shape with the long axis paralleling the fracture direction. Also, the strongest differences are concentrated in the center of the model, or the injection site, with the highest differences in pore pressure. The results indicate that the dual simulation shown here can accurately map the effect of pore pressure changes in seismic wave propagation. Specifically, when the seismic wave has covered a significant part of the modeled area (at 450 ms after source initialization), the area of strong difference spreads gradually from the injection point outwards, following an ellipse exactly the shape of the fluid front.

Finally, we examine the azimuthal dependence of seismic waves on fluid pressure. The waveforms are recorded at three receivers, at almost the same distance from the source, and at 90°, 130° and 180° from the fracture normal. This is repeated for each of the four states of fluid flow simulations shown in Figure 1. Figure 6 shows the differences in the horizontal components recorded at the three receivers at each azimuth. The differences are computed between: (a) 10 and 40 hours after injection, (b) 10 and 70 hours after injection, and (c) 10 and 100 hours after injection. Figure 7 shows the corresponding difference in the frequency spectra. In general, the P-waves are not greatly affected in contrast to shear-waves and coda or scattered waves as shown in Figure 6. Along the fractures (azimuth 90°), we can see the strongest differences in shear
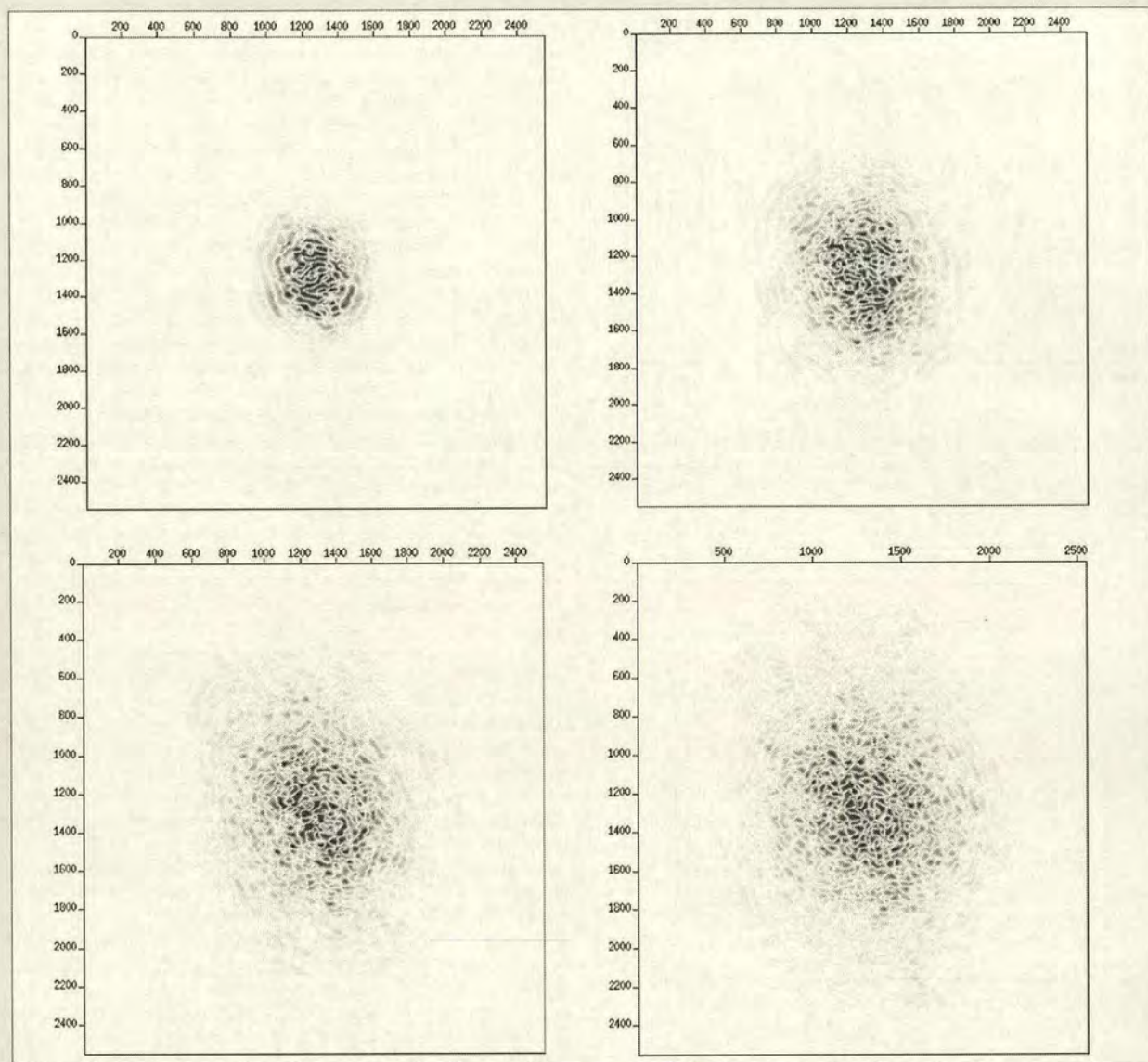
Figure 4. Snapshots at consecutive time steps (150, 250, 350, amd 450 ms after the source initialization), which show the difference between the simulation of the medium 70 hours after the injection of the fluid and the pre-injection stage.

waveforms, while at normal to the fractures (azimuth 180°) the strongest difference is in coda or scattered waveforms. As the pore pressure increases, this effect becomes stronger. It is interesting to note that there is a variation of the frequency content of the waveforms with azimuth. The greatest frequency shift occurs for an azimuth of 180° where a significant amount of energy is shifted from 50-60 Hz towards 30-40 Hz. At an azimuth of 130°, energy moves between the same frequency ranges are much smaller (negligible).

Finally, at a 90° azimuth there is a much more limited shift of energy, but significant energy present at the range of 50-60 Hz. In this case the energy is redistributed to both low and high frequencies, in a transition phase, before it shifts to systematically lower frequencies as angle increases from fracture normal.

Discussion and conclusions. We have conducted systematic dual numerical simulations of fluid flow and seismic wave propagation in a common fractured network. For the fluid flow simulation the fluid is injected in the center of a horizontal

fractured layer, and at selected time steps after the injection, information about pore pressure is collected. Variations in pore pressure lead to variations in the local effective stress. We use an empirical relationship between the effective stress changes and respective changes in the compliance of the rock. Therefore, at each selected time step of the fluid simulation, we obtain complete information about the updated elastic properties of the medium, and use these to perform seismic simulation. This process gives results in seismic data at consecutive time steps with varying pore pressures, or synthetic time lapse seismic data.

Our results show a different response between P, shear-, and coda waves to pore pressure changes. P-waves seem to be less affected or affected in a limited way, while shear- and coda waves are strongly affected, which supports the theoretical results of Liu et al. (2002) and field evidence of Angerer et al. (2002). Also, the amplitudes increase with increasing pore pressure and the frequency spectrum shows significant variations with pore pressure. There is an important shift of the peak frequency towards lower frequencies (implying strong
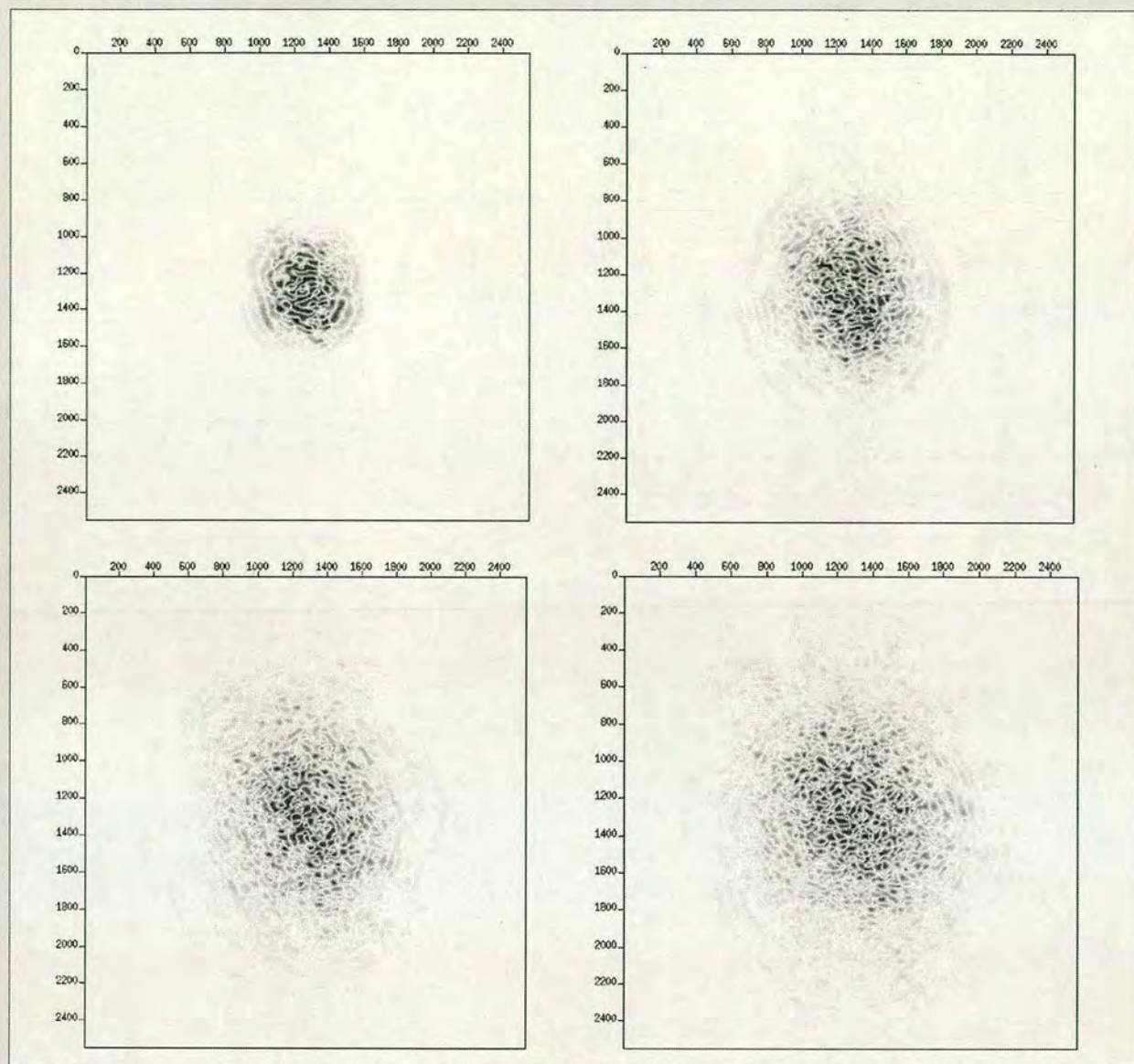
Figure 5. Snapshots at consecutive time steps (150, 250, 350, and 450 ms after the source initialization), which show the difference between the simulation of the medium 100 hours after the injection of the fluid and the pre-injection stage.

attenuation) as pore pressure increases. Another important aspect of our study is the azimuthal dependence of these effects. Fractures comprise the main path where the fluid moves in the reservoir, which is why the fluid front is an ellipse with its long axis oriented parallel to the fracture orientation. We also observe very strong amplitude differences in the shear-waves parallel to the fracture orientation and the coda waves normal to the fracture orientation, as pore pressure changes. Finally, we show that the greater shift of energy in frequency happens when seismic waves travel normal to the flow path. We conclude that significant diagnostic interpretation may be made by examining time-lapse shear-waves and coda-wave data, especially prior to any study that analyzes wave attenuation.

Suggested reading. "Discrimination between pressure and fluid saturation changes from time-lapse seismic data" by Landrø (*GEOPHYSICS*, 2001). "Processing, modelling and predicting time-lapse effects of overpressured fluid-injection in a fractured reser-

voir" by Angerer et al. (*Geophysical Journal International*, 2002). "The effects of stress and pore fluid pressure on seismic anisotropy in cracked rocks" by Liu et al. (*Canadian SEG Recorder*, 2002). "Equivalent medium representation of fractured rock" by Liu et al. (*JGR*, 2000). "A lattice BGK model for the diffusion of pore fluid pressure, including anisotropy, heterogeneity, and gravity effects" by Maillot and Main (*Geophysical Research Letters*, 1996). "Acoustic measurements in unconsolidated sands at low effective pressure and overpressure detection" by Prasad (*GEOPHYSICS*, 2002). "Lattice BGK models for Navier-Stokes equation" by Quian et al. (*Europhysical Letters*, 1992). "Time dependent anisotropy induced by pore pressure variation in fractured rock" by Schoenberg (*Journal of Seismic Exploration*, 2002). "Numerical simulation of wave propagation in media with discrete distribution of fractures: effects of fracture sizes and spatial distributions" by Vlastos et al. (*Geophysical Journal International*, 2003). "Dual simulation of fluid flow and seismic wave propagation in a fractured network: effects of pore pressure on seismic signature" by Vlastos et al. (*Geophysical Journal International*, 2004). T|E

Figure 7: Differences in frequency spectra of the signals corresponding to the same cases as Figure 6. (a), (b) and (c) represent increasing pore pressure as before.

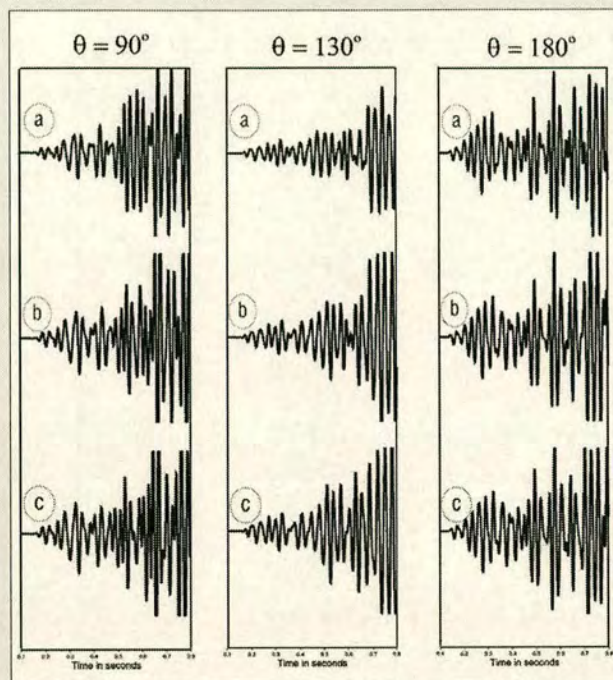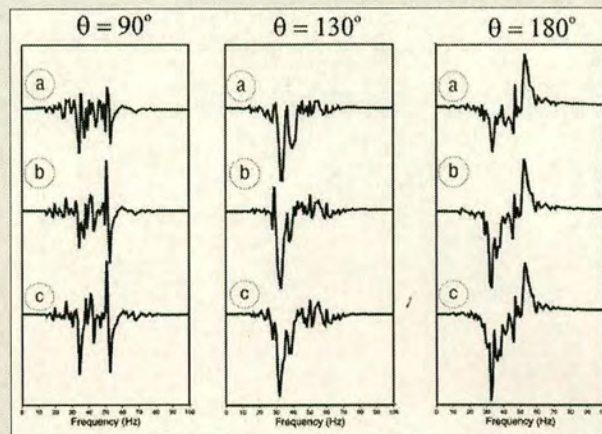Corresponding author: E.Liu@bgs.ac.uk

Figure 6. Differences in horizontal components recorded at receivers having different azimuths from the fracture normal. (a), (b) and (c) correspond to the differences between pore pressure 10 and 40 hours, 10 and 70 hours, and 10 and 100 hours after injection, respectively.